Fabrication of hierarchical cell carrier matrices for tissue regeneration by directional solidification

Dissertation zur Erlangung des
naturwissenschaftlichen Doktorgrades
der Julius-Maximilians-Universität Würzburg

vorgelegt von

Dipl.-Ing. Kai Stuckensen

aus Würzburg

Würzburg 2016

Eingereicht bei der Fakultät für Chemie und Pharmazie am

_____

Gutachter der schriftlichen Arbeit

1. Gutachter: _____
2. Gutachter: _____

Prüfer des öffentlichen Promotionskolloquiums

1. Prüfer: _____
2. Prüfer: _____
3. Prüfer: _____

Datum des öffentlichen Promotionskolloquiums

_____

Doktorurkunde ausgehändigt am

_____

This work was conducted at the Department for Functional Materials in Medicine and Dentistry (FMZ) of the University of Würzburg from October 2010 until March 2016 under the supervision of Prof. Dr. Jürgen Groll.

Lao-Tse, Tao Te Ching - Wang Bi Manuscript, Section 71

"Knowing not knowing is strength,

not knowing knowledge is sickness."

"The wise man is not sick,

because he is sick of sickness."

Translation of Lao-Tse, Tao Te Ching, Section 71, 1 and 3

Contents

Table of Figures:

Table of Abbreviations

ACD	Adjustable Cryostructuring Device
ANI	Anisotropic porous structured bone scaffold
BV	BioVaSc (decellularized porcine jejunal segment)
CAD	Computer-aided design
CaP	Calcium phosphate
cdw	Collagenous dry weight
CD	Deep chondral zone
CM	Middle chondral zone
CMI	Collagen meniscus implant (commercial available)
CS	Superficial chondral zone
EDX	Energy dispersive X-ray spectroscopy
EDC	1-Ethyl-3-(3-dimethylaminopropyl)-carbodiimide
ELISA	Enzyme linked immunosorbent assay
EWC	Equilibrium water content
FMZ	Department for Functional Materials in Medicine and Dentistry; University of Würzburg
FT-IR	Fourier transform - infrared spectroscopy
FWC	Free water content
GAG	Glycosaminoglycan
HMDI	1,6-Hexamethylene diisocyanate
hMSCs	Human mesenchymal stem cells

IAG	Inner assembly group of Adjustable Cryostructuring Device
IM	Inner meniscus zone
ISO	Isotropic porous structured bone scaffold
ISOCS	Isotropic bone scaffold containing chondroitin sulphate
µ-CT	Micro computer tomography
MES	2-(N-Morpholino)ethanesulphonic acid
m/mo	Residual mass
NHS	N-Hydroxysuccinimide
OAG	Outer assembly group of Adjustable Cryostructuring Device
OM	Outer meniscus zone
PE	Peltier element
rh-BMP-2	Recombinant human bone morphogenetic protein 2
rpm	Rotations per minute
SEM	Scanning electron microscope
SIS	Small intestine submucosa
v_s	Solidification velocity
wt%	Weight percent
XRD	X-ray diffraction
3D	Three-dimensional
$\vec{\nabla} T$	External temperature gradient

1 Introduction

A hierarchical structure, in terms of composition and architecture, represents an important functional feature inherent of tissues in the human body, including the musculoskeletal system[1,2]. The ambition to regenerate damaged tissues by cellular approaches is the motive behind the discipline of tissue engineering[3]. Since dedicated two dimensional cell culture is unable to recreate the complex structural properties of cell environments[4], approaches in three dimensions (3D) are favoured[5]. Therefore, 3D cell carrier matrices, namely scaffolds, are engineered to resemble the native cellular environment and to act as an artificial extracellular matrix.

Many different strategies to address musculoskeletal defects have been researched intensively[6]. Due to the similarity with native environments, the use of biodegradable hydrogels is especially promising[7]. Moreover, the desired regrowth of functional tissue occurs to replace the degrading biomaterial, which is the ultimate goal in tissue engineering[8]. In order to be used as scaffolds, hydrogels are conventionally processed to gels[9], films[10], fibre meshes[11], stacked lattice structures[12,13] and sponges[14]. Some of these processing techniques produce scaffolds with interconnected porosity; a mimicking of compositional differences in the tissue and its mechanical properties is attempted too. But still, the ability to mimic the sophisticated hierarchical organization of functional tissue is yet to be achieved[15] when the scaffolds are seeded with cells. However, the required extent in mimicking the complexity of natural extracellular matrix remains a key question for biomimetic materials[16]. Most of the modern synthetic biomaterials represent “oversimplified” mimics of these native cell environments, lacking the essential spatial complexity of the latter[17].

While films and meshes bare obvious, production conditional limitations to serve as matrices with larger extensions in all three dimensions, dense gels commonly do not feature a porosity in the micrometer range, which would allow a proper cellular migration and nutrient supply inside larger structures. Currently, additive manufacturing approaches of hydrogels are either working with the extrusion of thick strands[18], or are facing difficulties with extending the third dimension in the range of multiple millimeters[19]. If they are applied for the creation of larger 3D scaffolds,

only box like pores with diameters in the range of several hundred micrometers are producible. Furthermore, common sponge matrices exhibit the desired interconnected pore structure with various possible pore sizes[20], but they do not reproduce the anisotropic character of many native tissues.

The **hypothesis** that a closer approximation of the hierarchical, compositional and structural anisotropic, properties of musculoskeletal tissues would lead to an improved cellular response and thus a better healing quality appears obvious. However, an evaluation of this hypothesis remains problematic using established fabrication processes, since the resulting scaffolds lack the required degree of mimicry.

Nevertheless, cell carrier matrices, featuring a controlled internal macro- and microstructure that allow the transport of oxygen and nutrients deep into the scaffold are demanded. In order to facilitate a direct use for regenerative therapies, these should also possess the ability to promote cell attachment, growth and proliferation[21]. Furthermore, a scaffold pore size of approx. 80 µm is thought to be beneficial for holistic cellular infiltration[22]. Directional solidification of collagenous hydrogels appears to be a promising candidate to meet this need, since collagen represents a mayor constituent of native cellular environments. Additionally, an anisotropic porosity would address the structural properties of many tissues as well as the mentioned cellular migration and supply. One component sponges with unidirectional porosity have already been fabricated by controlled freezing of collagen I solutions[23]. In this approach, porous matrices were produced by directional growth of ice crystals and subsequent, lyophilisation. But a mimicking of the compositional changes that are occurring inside many parts of the musculoskeletal system may not be addressed by this method.

Therefore, the **key challenges of this thesis** are: The development of a new, solidification based procedure for the production of hierarchical scaffolds. These scaffolds should feature an anisotropic porosity and zonal compositions that mimic the structural architecture and the biochemical components of the native extracellular matrix. Subsequently, their effect on cells in tissue engineering applications is to be used for the validation of the above mentioned hypothesis.

Initially, the state of the art has to be researched concerning components, structure, function and existing tissue engineering approaches of bone, osteochondral and meniscus tissue. Different crosslinking methods of hydrogels and solidification phenomena are to be considered additionally (**Chapter 2**). Collagens and calcium phosphates have to be prepared to serve as raw materials. Therefore, isolation and purification protocols of collagenous materials need to be established (**Chapter 3**).

Furthermore, the scaffold production by directional solidification shall be build up as a field of research activity. A production of scaffolds, which may be applied in multiple parts of the musculoskeletal system, requires a high versatility in the fabrication process that is to be developed. Due to this fact, a solidification apparatus needs to be devised, evaluated and optimized so that it facilitates a variable control over the solidification structures and sample dimensions (**Chapter 4.1**). Furthermore, the used raw materials have to be examined and the influences of freezing parameters on the resulting structures have to be investigated and understood (**Chapter 4.2**).

Moreover, the process should enable the fabrication of scaffolds with different zonal compositions and pore architectures to mimic the ones of native tissues. In detail, scaffolds for bone (**Chapter 4.3**), meniscus (**Chapter 4.4**) and osteochondral (**Chapter 4.5**) applications should be developed. The resulting scaffolds are to be characterized by material scientific methods (**Chapter 3.5**). Among these investigations, especially pore structure, composition, degradation and mechanical behaviour of the produced matrices are to be considered. Supplementary to this, properties of the solidifying precursors, cytokine release kinetics and a scaffold modification by electrostatically spun fibres and 3D printed calcium phosphates should be addressed.

Musculoskeletal tissues, like articular cartilage, are commonly mechanically tested by unconfined or confined compression[24]. Due to incorrect results by negligence of change in cross sectional area during unconfined measurements, a measurement in liquid under confinement is to be preferred. Conventional confined, porous measurement systems that allow a circulation of liquid during testing are known for problematic sample alterations[25]. Thus, the development of a modified confined compression setup, which overcomes this drawback, represents desirable (**Chapter 4.6**). Finally, the biological performances of the scaffolds as well as further applications of the process are to be presented (**Chapters 4.7** and **4.8**).

2 State of the Art

Parts of the following chapter are published analogously within other text documents. Fractions of **Chapter 2.1**, **Chapter 2.3** and **Chapter 2.5** are shared with the diploma thesis of the author[26]; a moiety of **Chapter 2.5** may be also found in the Patent EP2788171A2[27].

2.1 Bone and Calcium Phosphates

Bone tissue is composed of cells (osteoblasts and osteocytes) that are embedded in an extracellular matrix[28], which represents as a hierarchical network assembled from two major components: collagen I fibrils and hydroxyapatite nanocrystals distributed along the collagen fibrils. These collagen fibrils feature a length of ca. 300 nm with an approximate diameter of 1.5 nm, while the plate-shaped hydroxyapatite crystals span an area around 50 nm × 25 nm with a height between 1.5 nm and 4 nm[29,30]. For human bones, the proportion of the matrix components is commonly about: 35 vol% of mineral compounds, ca. 37 vol%, of organic components and 28 vol% water[31]. A simplified scheme, depicting the hierarchical structure of bone, is displayed in **Figure 2.1** a) - d). The macroscale arrangements are composed out of compact / cortical bone at the surface and spongy / trabecular bone in the interior (**Figure 2.1** d)). Trabecular bone features a foam-like microstructure with approx. 100 µm thick struts. Compact bone consists of aligned osteons and Haversian canals, which surround blood vessels (**Figure 2.1** c)). Osteons feature a lamellar channel structure, whereby fibres arranged in geometrical patterns build individual lamellas. These fibres comprise numerous mineralized collagen fibrils (**Figure 2.1** b)). These fibrils in turn are composed of triple helical collagen molecules (tropocollagen) and hydroxyapatite nanocrystals which are interlinked by an organic phase to form fibril arrays (**Figure 2.1** a)).

This categorisation might be sufficient for a principal understanding of the bone structure. However, on a more detailed consideration of the different structural levels of bone, a significantly more complex organization is revealed (**Figure 2.1** e)): Macro-molecular components assemble structural units, which build arrays that are arranged in distinct patterns to form a superstructure. At these levels, the materials feature either an ordered (green) or a disordered structure (blue).

Above the level of superstructures, ordered and disordered materials are combined to yield higher structural levels. The colourless box depicts other members of the bone family which still need to be investigated with respect to the presence of both material types.

At the level of material patterns, these two materials combine into lamellar bone[32] and parallel fibered bone[33]. The level of tissue elements corresponds to the lamellar packets (trabecular bone material), the cylindrically shaped lamellar bone (osteonal bone), and a fibrolamellar unit (primary hyper-calcified layer), the parallel fibered bone and the lamellar bone[33].

Hydroxyapatite nanocrystals have been reported to be preferentially oriented with their c axis parallel to the collagen fibrils, while being arranged in a periodic, staggered array along the fibrils[29,30]. If also the disordered bone material is taken into account, divagating crystal orientations are present too. Those divagations are attributed to the differently oriented collagen fibrils in the disordered structure and / or the presence of crystals which are not associated with collagen fibrils[32]. Generally, the orientation of apatite crystals in the bone, seems to be mediated by water through an amorphous calcium phosphate like layer that coats the crystalline bone apatite[34].

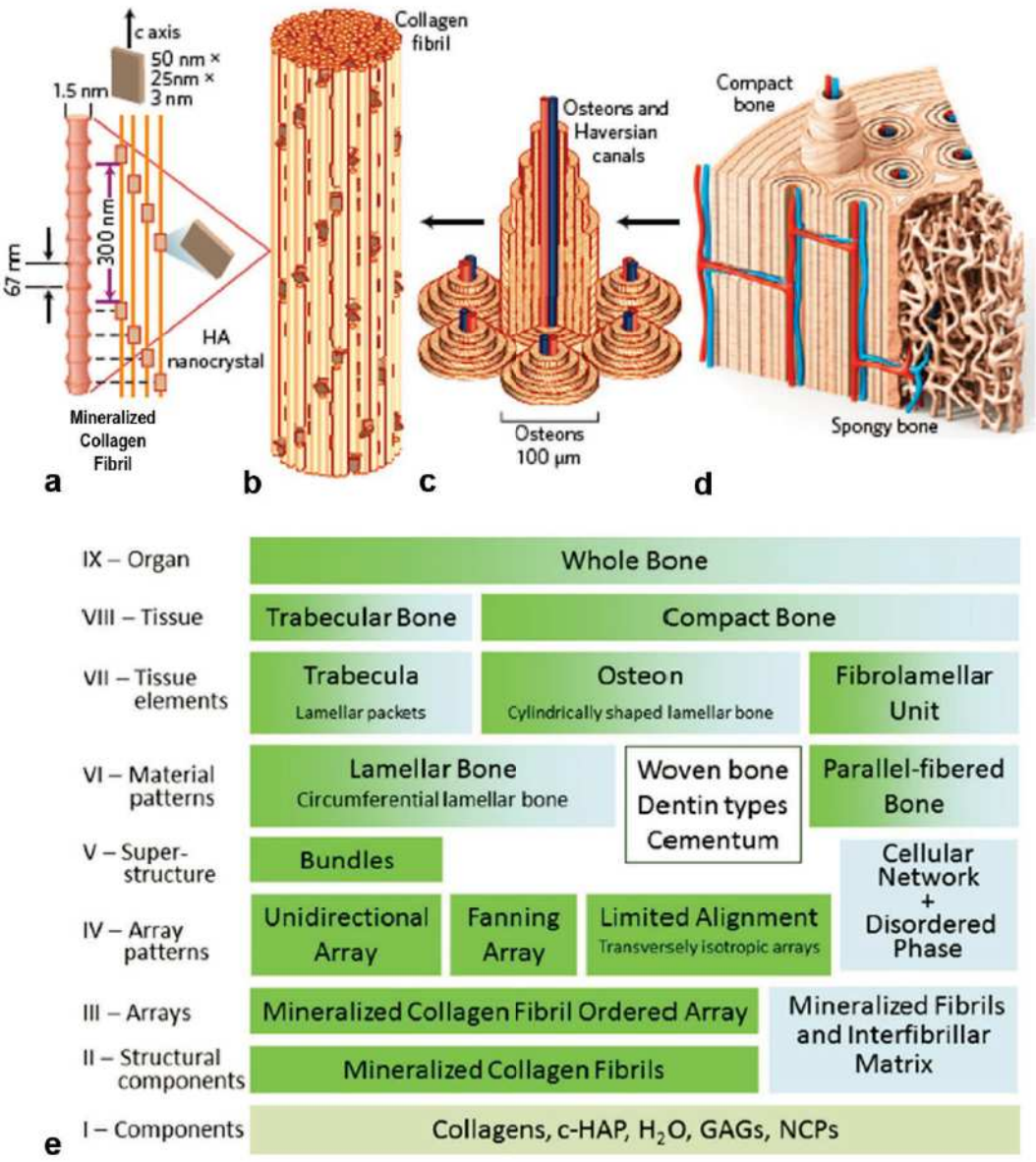

Figure 2.1: Structural organization of bone tissue. a)-d) Simplified scheme of hierarchical organization from mineralized collagen fibrils (a)) that are forming arrays (b)), which build tissue elements (c)) forming the entire bone (d)) (HA: hydroxyapatite; modified from[29]). e) Complex organization of bone in multiple structural levels (I – IX). These hierarchical levels divide into ordered and disordered materials, as displayed in green and blue respectively. (c-HAP: carbonated hydroxyapatite; GAGs: glycosaminoglycans; NCPs: non-collagenous proteins)[2]

Due to the presence of bone morphogenetic proteins (BMPs) and osteogenic proteins (e.g. collagen, osteonectin, osteopontin, bone sialoprotein) in the extracellular matrix, bone tissue features osteoinductive properties[35]. Osteoinduction of a material is defined as the ability to induce the formation of new bone (osteogenesis) by the stimulation of immature cells to develop into pre-osteoblasts[36]. Thereby, bone tissue can also been formed at non-skeletal implantation sites.

Since calcium phosphates (CaPs) represent the majority of the mineral phase of bone tissue, they are particularly suitable as a material for bone replacement purposes[37]. Besides CaP granules, the use in form of various CaP cements found its way into biomedical applications[38]. Hydraulic setting CaP cement materials were proposed within the early 1980s[39,40] and are currently applied as mineral bone cements. Because of their small mechanical stability, compared to the replaced bone material, they are used in low load bearing defect sites like craniofacial surgery and dental applications[41]. The reinforcement of CaP cements for load bearing applications represents a significant aspect of current research[42]. These cements may be tuned to feature controlled drug release capabilities[43] or improved injectability[44,45]. Another field of biomedical application is represented by 3D powder printed CaPs[46,47], which also may be used for drug release[48].
Unlike other synthetically produced materials, CaPs show direct and rapid ingrowth of bone tissue without the formation of fibrillary connective tissue when implanted to bone[49]. Although CaPs are sometimes claimed to be osteoinductive, their properties are more correctly expressed as osteoconductive[35]. Osteoconductivity is defined as a surface property, which permits bone growth on the surface or down into topographical structures (like pores, channels etc.)[36]. Those “intrinsic” osteoinductive properties claimed in *in vivo* experiments are rather to be attributed to topographical and geometrical features, which allow the entrapment of circulating bone morphogenic proteins (BMPs) and osteoprogenitor cells[35]. Therefore CaPs are generally not to be considered as osteoinductive in the first instance; they are mainly considered as osteoinductive[50].

A degradation or resorption of CaPs in *in vitro* or *in vivo* conditions implies cell-mediated degradation. The cellular activity creates acidic conditions, which affect solubility and extent of dissolution, respectively (**Figure 2.2** a)).The enrichment of the microenvironment by dissolving CaPs in turn affects the proliferation and activities of the cells. The concentration increase by release of calcium and phosphate ions promotes the formation of carbonate apatite which is similar to bone apatite[51].
As mentioned above, the degradation behaviour of CaPs is dominantly dependent on the solubility of the individual phases within the present pH conditions of the environment. The solubility phase diagram of several CaP phases is displayed in **Figure 2.2** a):

The presented isotherm curves describe the solubility, expressed as the calcium concentration of the saturation solution. At a given pH value, a CaP phase, whose isotherm proceeds below the one of another phase, is less soluble and therefore more stable. In a pH range between 4.2 and 10.0, as found in physiologic conditions, hydroxyapatite represents the least soluble CaP phase. For this reason, the main mineral components of native or artificial CaPs convert over time into (impure) hydroxyapatite phases in physiological environments, as found in *in vitro* and *in vivo* conditions. These solubility observations are also considered as the major driving force behind the setting reactions of CaP cements[52].

2.1.1 Brushite

Brushite (calcium hydrogen phosphate dihydrate) represents a resorbable mineral from the CaP family[53], which is also found in minor amounts inside urinary and dental calculi inside the human body[54]. Besides this, brushite particles have been reported to be present inside non-collagenous organic matter around non-mineralized, ordered collagen fibrils to represent an ion reservoir for subsequent mineralization[55]. Brushite can be synthesized by precipitation of hydrogen phosphate ions with calcium ions in aqueous solutions[56].

$$HPO_4^{2-} + Ca^{2+} + 2H_2O \rightarrow CaHPO_4 \cdot 2H_2O \qquad (1)$$

After this reaction brushite is attained as a white, crystalline precipitate. The crystal morphologies that occur can be categorized into five manifestations: irregular crystals, regular and asymmetric crystals, symmetric crystals, twin crystals and crystallite aggregates. Which of the respective morphologies is mainly produced depends only slightly on the supersaturation of the solution. The concentrations of precipitants and the pH represent the most important factors[57].
However, whether the nucleation of brushite occurs in general, is dependent on the super saturation. A low supersaturation of the solution above a certain critical value is required for the nucleation of brushite to take place as the first and only phase. If the saturation point in solutions with lower concentrations ($c \leq 0.05$ mol/l) of precipitation reagents is exceeded, the formation of amorphous CaPs will result[57].

The pH value necessary for the precipitation of brushite decreases proportional to the logarithm of the phosphate ion concentration. The higher the concentration of the precipitating reagents, the wider is the pH range in which brushite nuclei can be induced[58].

If the crystallization reaction is taking place at a pH value of 5 with high concentrations of the precipitating reagents, plate-shaped brushite crystallites will result[57]. **Figure 2.2** b) displays a schematic illustration of a possible appearance of a plate-shaped brushite crystal. The respective surfaces are crystallographic indexed. The surface of the plate shaped crystals corresponds to the (010) plane in the crystal lattice.
A projection of the brushite crystal structure on the (010) crystal plane is shown in **Figure 2.2** c). Corrugated (010) layers of $CaPO_4$ are separated from each other by H_2O inclusions[54]. The individual water molecules are aligned in such a way that the overall dipole moment orthogonal to the surface disappears[57]. In the forming crystal structure, each Ca^{2+} ion is octahedral coordinated. Brushite crystals show bidental growth characteristics, so that the crystal is most likely to grow the length at the $(\bar{1}0\bar{1})$ and the $(\bar{1}1\bar{1})$ surfaces. These are nearly orthogonal to the [010] direction. Due to the released energy associated with the integration into the crystal lattice, the crystal growth occurs preferably by formation of the strongest bonds. These run mainly along the (010) surfaces of the crystal[54]. Therefore, the surface growth mechanism of brushite is highly anisotropic. The (010) surface shows a screw dislocation growth mechanism, while other areas almost exclusively grow by surface nucleation[57]. This results in preferential growth morphology of plate shaped crystallites.

Since the biologically mediated resorption of brushite *in vivo* proceeds complete or at least extensively[59], it was chosen as the appropriate CaP phase for fabrication of fully resorbable scaffolds in this thesis. As explained above, brushite converts into hydroxyapatite phases under physiological conditions. Commonly this conversion is occurring via an intermediate phase of octa-calcium phosphate[54] (OCP in **Figure 2.2** a)).

2.1.2 Hydroxyapatite

Biological apatite represents the main mineral constituent of bone and teeth tissue[60]. This form of hydroxyapatite is represented by a poorly crystalline ion-substituted CaP phase, whereby calcium often is substituted by carbonation[61]. Since sintered hydroxyapatite shows a very slow degradation rate under physiological conditions, so that the bulk of implants persists within the body for years after implantation[62], precipitated hydroxyapatite crystals, that show a comparably faster degradation[63], were used within this thesis.

Besides the use for biomedical applications, hydroxyapatite is also employed for catalysis, fertilizers, pharmaceutical products, chromatography, and water treatment[64]. Alternatively to other production methods (solid state reactions, plasma techniques, crystal growth under hydrothermal conditions, layer hydrolysis of other calcium phosphate salts, and sol-gel crystallization)[64,65], hydroxyapatite can be produced precipitation reaction (modified from literature[66]):

$$6\,HPO_4^{2-} + 10\,Ca^{2+} + 2OH^- + 6\,H_2O \rightarrow Ca_{10}(PO_4)_6(OH)_2 + 6\,H_3O^+. \qquad (2)$$

In this representation, hydroxyapatite is displayed as $Ca_{10}(PO_4)_6(OH)_2$ to indicate, that the elementary cell of the crystal lattice contains two $Ca_5(PO_4)_3(OH)$ units. This reaction is favoured by an increase in temperature. Since the pH value decreases during the precipitation reaction, the addition of basic agents is necessary to maintain the pH value at a constant level. A lack of pH control could result in nonstoichiometric apatites[66].

The resulting crystals are formed by a nucleation – aggregation - agglomeration growth process, whereby especially the aggregation is ruled by surface energy minimization[67]. The schematic crystal structure of hydroxyapatite is depicted in **Figure 2.2** d), as a projection onto the {0001} crystal plane. It may be described as a three-dimensional tetrahedral network of PO_4^{3-} groups, which are interlinked by columns of nine fold coordinated “Ca1” atoms. This network is penetrated by channels containing triangles of sevenfold coordinated “Ca2” atoms.[60] By substitution of PO_4^{3-} by CO_3^{2+} and of OH^- by CO_3^{2+} or Cl^- or F^- inside the crystal lattice, non-stoichiometric forms of hydroxyapatite are obtained[60]. Additionally, numerous other ionic substitutions may take place[64].

All of these substitutions can already occur during the precipitation reaction, so that special choices of environments and reactants[68] may be made in order to obtain a stoichiometric hydroxyapatite with a Ca : P ratio of 1.667. Hydroxyapatite crystals also feature a certain adsorption potential for divalent cations, which may be incorporated in the crystal lattice to build new mineral phases. This way, heavy metal ions can be removed from aqueous solutions[69].

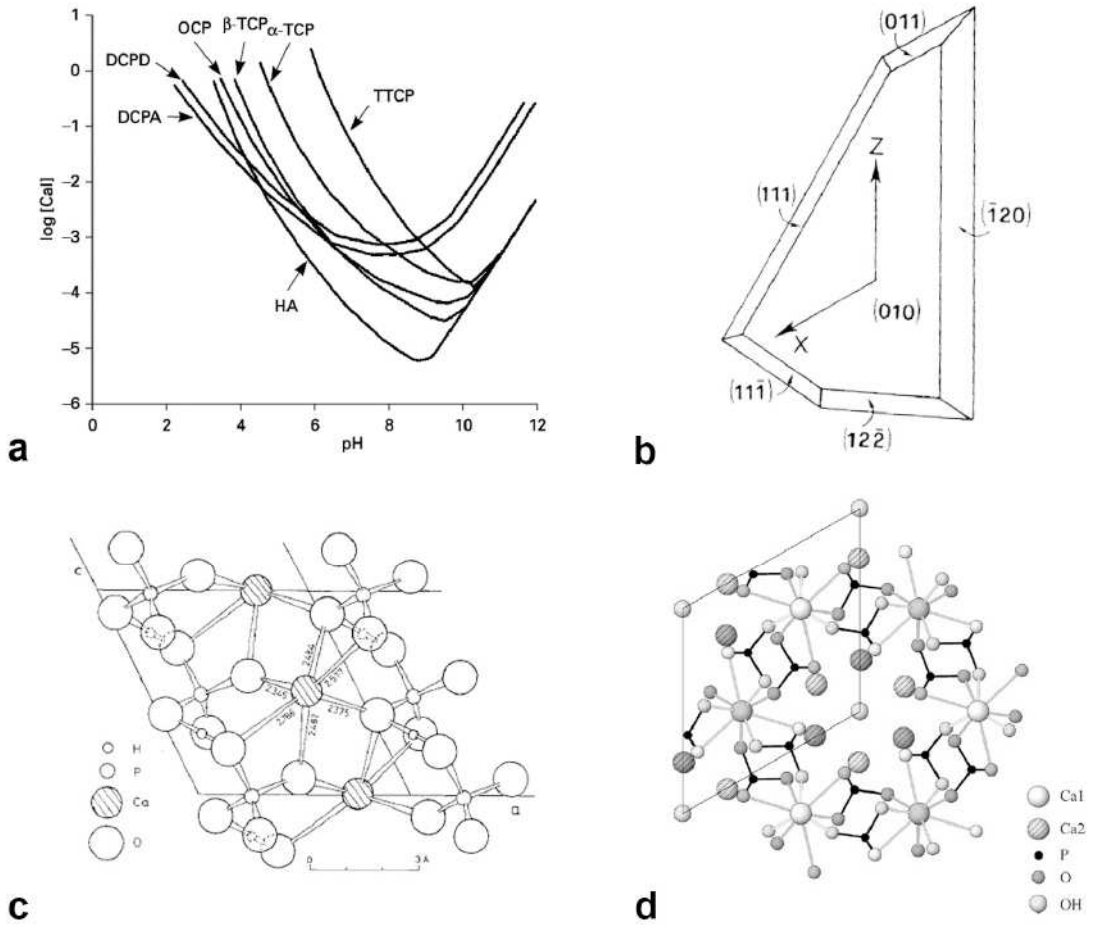

Figure 2.2: Solubility isotherms and crystal structures of calcium phosphates. a) Solubility isotherms at 25 °C[52]. HA (hydroxyapatite), DCPA (dicalcium phosphate anhydrous / monetite), DCPD (dicalcium phosphate dihydrate / brushite), OCP (ocatcalcium phosphate), α-TCP (α-tricalcium phosphate), β-TCP (β-tricalcium phosphate) and TTCP (tetracalcium phosphate). b) Schematic illustration of the crystal planes of brushite[57]. c) Projection of the brushite crystal structure on the (010) crystal plane[54]. d) Projection of the crystal structure of hydroxyapatite onto the {0001} crystal plane[60].

2.2 Collagens and Cartilage

Prior to the production of cartilage substitute materials, a consideration of the natural conditions i.e. the structure and peculiarities of cartilage tissue is indicated. Originating from the mayor components of the extracellular matrix in cartilage, this chapter will give an insight into articular cartilage and meniscus tissues. Both represent important constituents of the musculoskeletal system, which often need to be addressed in surgical procedures[70,71].

Collagen embodies the main component of the non-aqueous parts of the extracellular matrix in cartilage tissues and features a hierarchical structure which is expressed over several length scales[1,72,73]. Inside the body it is used to maintain the structural integrity of numerous functional units[73,74]. Essentially, collagen may be considered as a long polypeptide of amino acids which is referred to as a protein. An exemplary primary structure of a polypeptide chain is depicted in **Figure 2.3** a). The peptide bond is to be considered as stiff and planar due to mesomeric effects, but in between the peptide bonds a rotation is possible[75]. During the biosynthesis of collagen also disulphide links influence the formed structures[76].
Thereby, the formation of a secondary structure in form of a left-handed helix, with three residues per circulation, may occur[75] (**Figure 2.3** b) left). The collagen protein structure features a unique, repeating tri-peptide-sequence out of glycine and two further amino acids[75,77]. An identical helix is depicted again beside the ball stick model in form of a calotte model. Three of those helices combine to a right-handed triple helix (**Figure 2.3** b) middle), which is also referred to as “tropocollagen”[78] or collagen fibers. The combination between the respective molecular amino acid sequence and helical secondary structure determines which sequence parts of the collagen fibril are buried inside, or accessible to the extracellular matrix and cells[79]. An illustration of this is given at the right hand side of **Figure 2.3** b). Here, a horizontal cross section of the alongside standing triple helix is presented where the red coloured residues of the amino acid glycine are buried inside the triple helix[75]. Depending on the sequence of amino acids that are bound together to form the polypeptide chains, they are denoted as numbered “α chains”. The common collagen I molecule, which is found in skin, bone and tendons, is build up out of two α1 type I chains and one α2 chain (designated as $[\alpha1(I)]_2\alpha2$),

while the collagen II molecule, which is predominately found among cartilage tissues, consists of three α1 type II chains (designated as $[\alpha1(II)]_3$)[80].

Slight differences on the molecular level may lead to significant different properties and behaviour of the respective collagens. A variating combination of 18 amino acids[72] leads to 28 different forms of collagens[73]. Although all collagens feature anisotropic viscoelastic properties[9,73,81], some tend to form fibres and fibrils, while others do not show this behaviour[73,82]. The collagens I and III form fibres which can be found in tendons or blood vessels[83] while cartilage fibrils are heterotypically assembled from collagens II, IX and XI[84].

Although all the mechanisms that are responsible for elastic energy storage in collagenous tissues are not entirely understood[77], a considerable proportion of the dampening behaviour in cartilage tissues is to be attributed to the presence of glycosaminoglycans (GAGs) and their attached sulphate groups, respectively. In cartilage tissues, the GAGs are predominantly found as proteoglycan aggregates (**Figure 2.3** c)): Bottle brush like structures are formed by non-covalent attachment of the core protein aggrecan to a hyaluronic acid backbone via link proteins. Each aggrecan molecule bares covalently attached keratan sulphate (displayed blue) and chondroitin sulphate (displayed orange) molecules[75]. Here, chondroitin sulphate represents the most abundant GAG. Proteoglycans are large (~$1*10^6$ Da) hydrophilic molecules that can entrain 50 times their weight of water in free solution[85]. In the hydrated state, the negatively charged sulphate groups repulse themselves mutually[86], which generates a resilient force upon mechanical displacement relative to each other. In addition to this, they attract many positive counter-ions, which further enhances the ability of the tissue to resist compressive loads[85]. This mechanism is also referred to as osmotic properties of cartilage[87]. The bio-characteristics of GAGs include binding and modulation of growth factors and cytokines, as well as the inhibition of proteases[88]. Furthermore, GAGs have been implicated to be involved in the migration, proliferation and differentiation of cells[74].

Due to its relevance for cartilage functionality, the structural composition of a cartilage fibril is considered in more detail (**Figure 2.3** d)): A core of quarter-staggered collagen XI triple helices (inner cylinder) is enclosed by collagen II triple helices (outer cylinder) to form a fibril. On the surface, partly helical collagen IX molecules are attached, whereby non-helical domains are represented by spheres.

Chondroitin sulphate chains (illustrated by polygons) are attached to some of these non-helical domains.[89] Within the cylindrical displayed fibril, the individual ends of triple helices are separated to each other by regular gaps[80,82]. The overlap of individual triple helices is responsible for the characteristic cross-striation patterns, with a periodicity of 64-67 nm[73], which may be observed in electron microscopic investigations of native collagen fibrils[80,90,91].

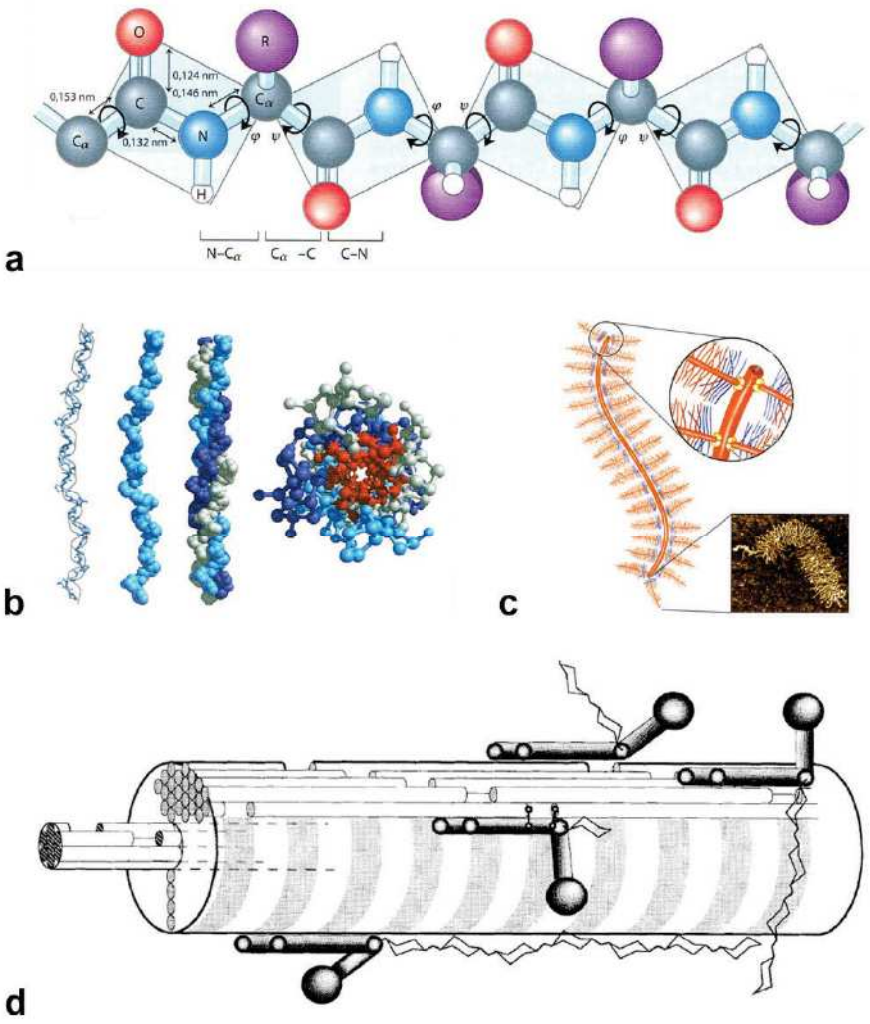

Figure 2.3: Hierarchical structure of collagenous cartilage fibres and fibrils. Collagen peptide chains (a)) assemble to triple helical collagen fibres (b)). Together with glycosaminoglycans (c)) they build up the majority of the extracellular matrix in cartilage tissues. Cartilage fibrils are formed from fibres of collagen XI, which are surrounded by collagen II; on the outside, glycosaminoglycans (displayed as polygon chains) are attached through collagen IX molecules (d)). (a), b) and c) adopted and modified from pages 154, 164 and 338 of literature [75], copyright 2009 with permission of Springer; d) adopted from literature [89])

Based on such cartilage fibrils, different manifestations of cartilage tissues may be found. Depending on the respective structure and composition, hyaline cartilage, elastic cartilage and fibrocartilage are distinguished[86,87].

2.2.1 Osteochondral Tissue

Articular cartilage represents as a member of hyaline cartilage. Hyaline cartilage contains per definition[92] only collagen II, as well as minor amounts of collagen IX and XI[1]; therefore it is distinguishable from other cartilage tissues. Due to its viscoelastic properties, it ensures a uniform force transmission between the joints[93]. Its structure and composition locally reflect special mechanical properties[92]. The joint cartilage can be structurally divided into two zones:

The chondral zone serves essentially as an elastic buffer, while the subchondral zone represents a transition from cartilage to bone tissue. These two different zones may be observed within **Figure 2.4** a), where a hematoxylin staining of an articular cartilage cross section from the trochlea joint is displayed[93]: The upper brighter part represents the chondral zone, while the dark ribbon in the downer part depicts the calcified subchondral zone, which is merging into the bone. A more detailed investigation shows the presence of more or less aligned holes throughout the tissue. These holes are attributed to associations of cartilage cells, so called chondrocytes, which are not individually displayed due to preparative issues related to the staining. Depending on the location inside the cartilage they are arranged in clusters, so called chondrons, composed of 1–13 cells[94]. The tissue in between the chondrons is primarily responsible for the mechanical properties of cartilage and is called inter-territorial matrix[95]. Upon consideration of the spatial alignment of this inter-territorial matrix and the chondrons, a columnar alignment, approximately perpendicular to the joint surface, is to be found in dominant volume parts of both cartilage zones (**Figure 2.4** a).

An even more detailed contemplation of the cartilage tissue reveals that it comprises stratified zones where resident chondrocytes differ in morphology and biosynthetic activity[96]. Usually it is subdivided into a tangential zone (“s” in **Figure 2.4** b)), a transitional zone (“m” in **Figure 2.4** b)) and a radial zone (“d” in **Figure 2.4** b)) with cartilage columns orthogonal to the surface[93]. The nomenclature is representative of the preferential alignment of the collagenous fibres inside the tissue zones in relation

to the joint surface. As illustrated in the left part of **Figure 2.4** b)[97], flat cells in horizontal chondrons are found in the superficial zone (s), while round cells are present in columnar chondrons in the deep zone (d). The orientation of the collagen fibres remind on the architecture of gothic cathedrals[98]. These are indicated by dashed blue lines that proceed parallel to the surface in the superficial zone and perpendicular to the subchondral bone in the deep zone[97]. In average, a mean thickness of ca. 0.2 mm for the superficial, ca. 0.6 mm for the middle and ca. 1.1 mm for the deep chondral zone was reported[99]. The so called "tidemark"[95] separates the chondral from the subchondral zone and is indicated as bright blue line in left hand side of **Figure 2.4** b).

Together with the compressive modulus, the GAG content increases from the superficial to the deep zone, as shown by EPIC- micro computer tomography (µ-CT) in the right hand side of **Figure 2.4** b)[97]. Collating literature results[97,100-102] the GAG concentration inside the cartilage zones may be summarized as follows: inside the superficial chondral zone no or only negligible amounts of GAGs are found. In the middle chondral zone ca. 15 % and in the deep chondral zone ca. 20 % of the cartilage's collagenous dry weight (cdw) is present as GAGs, respectively. Of cause these represent approximate numbers, since the individual amounts change with age[102] and degeneration[100] of the cartilage. This depth-wise increase of spatial GAG concentration in cartilage[99,101] is also described as a decrease in collagen density[103].

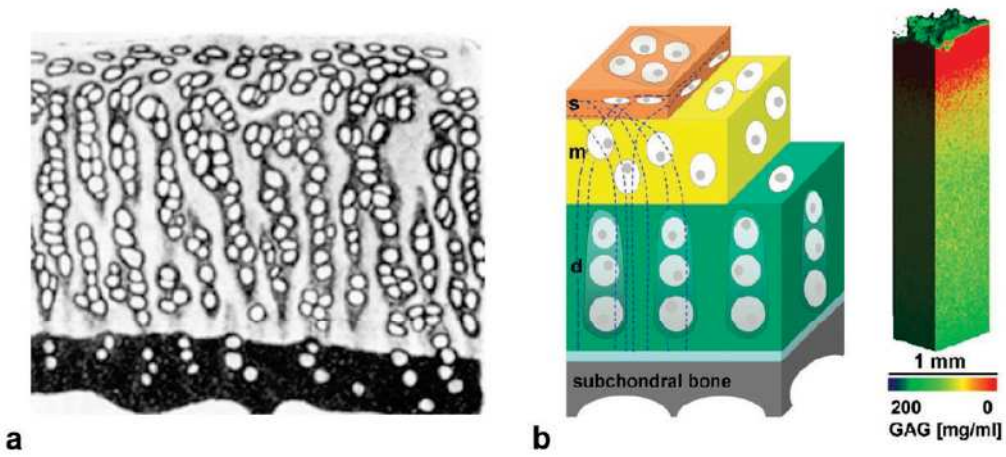

Figure 2.4: Structure of osteochondral tissue. a) Hematoxylin staining of articular cartilage from trochlea[93] showing predominately a columnar organization within the chondral and subchondral areas. b) Left: Schematic illustration of the zonal architecture of osteochondral tissue in superficial (s), middle (m) and deep (d) zones. Blue dashed lines indicate preferential directions of collagen fibres. Right: Glycosaminoglycan (GAG) content according to EPIC-µ-CT.[97]

Articular cartilage shows the lowest volumetric cell density of any human tissue; chondrocytes occupy only about 1 % of the total volume, while the remaining 99 % are consisting out of the previously described extracellular matrix, which has been produced by them[104]. Chondrocytes originate from mesenchymal stem cells (MSCs) that are found in the bone marrow[95]. During embryogenesis, the MSCs start to differentiate into chondrocytes and secrete a cartilaginous matrix whereby they continue to divide. But when they reach the state of mature chondrocytes, they are unable to proliferate and show only a very limited migration potential because of a complete enclosure in extracellular matrix[95].
Due to this fact, in combination with the avascular nature of this tissue and the lack of access to potent reparative cells, articular cartilage bares a very limited ability for cell renewal and tissue regeneration; therefore, defects are usually irretrievable[105]. Although, there is a minor potential for tissue repair, the build fibrocartilage[106] represents only a suboptimal solution, since its biochemical and mechanical properties do not equal those of native cartilage, resulting in a gradual failure and subsequent erosion[107]. Thus, articular cartilage defects only heal poorly and lead to catastrophic degenerative arthritis[108].

Although the material properties of cartilage may be investigated by several methods, they are commonly determined by confined compression testing[86]. This compression testing under lateral confinement is typically performed using porous platens or indenters for compression and or bedding together with a non-permeable confinement[109-114]. Thereby, the compressive modulus of human glenohumeral cartilage was determined to ca. 0.1 MPa[113]. Noticeably, the compressive modulus of bovine articular cartilage was demonstrated to be significantly higher for immature cartilage (ca. 0.40 MPa) than for mature articular cartilage (ca. 0.26 MPa)[114].

2.2.2 Meniscus Tissue

The meniscus inside the knee joint represents as a fibrocartilage[115]. In contrast to articular cartilage, which contains almost exclusively collagen II, meniscal fibrocartilage is predominately made up out of collagen I, which distinguishes the fibrocartilage of menisci from hyaline cartilage[85].

Analogously to articular cartilage, the material properties of menisci are determined by their biochemical composition and by the organization and interaction of the major tissue constituents: water, proteoglycans, and collagen[85].

Being located in the medial and lateral areas of the joint between the femoral condyle and tibia plateau, the menisci may be subdivided into two areas of different composition[116]. While the inner third (IM in **Figure 2.5** a)) appears more like hyaline cartilage regarding gross appearance and histological examination, the outer two-thirds (OM in **Figure 2.5** a)) are fibrocartilaginous[116]. Makris et al.[117] also described the inner meniscus zone (IM) as the “white white zone” and the outer meniscus zone (OM) as the “red red zone”. The dry weight content of collagens inside the meniscal zones, were found to be approx. 70 % for the IM and ca. 80 % for the OM[116,117]. While the IM bears a collagenous composition of 60 % collagen II and 40 % collagen I, collagen I is predominantly found inside the OM with other collagen variants (type II, III, IV, VI, and XVIII) present at less than 1 %[116-120]. The entire extracellular matrix is composed primarily of water (72 %) and collagen (22 %); proteoglycans, non-collagenous proteins and glycoproteins account for the remaining weigh[121].

Meniscus tissue features a highly oriented collagen ultrastructure, which makes the tissue anisotropic in tension, compression and shear[85]. The complex architecture of the meniscus in three distinct cross section layers has been described by Petersen et al.[122]: The tibial and femoral meniscus surfaces are covered by a fibrillary meshwork. Underneath, a layer of lamella-like collagen fibril bundles is found. Collagen fibrils, which are arranged in a radial direction, proceed in the external circumference of the anterior and posterior segments, while collagen fibril bundles intersect at various angles in all other parts. The dominant fraction of collagen fibrils is located in the central region of the meniscus. Here the collagen fibril bundles are orientated in a circular manner (**Figure 2.5** b)[122]. In other words, parallel to the peripheral border, the collagen fibers are oriented circumferentially[121] assembling a lamellar network over the majority of the meniscus tissue.

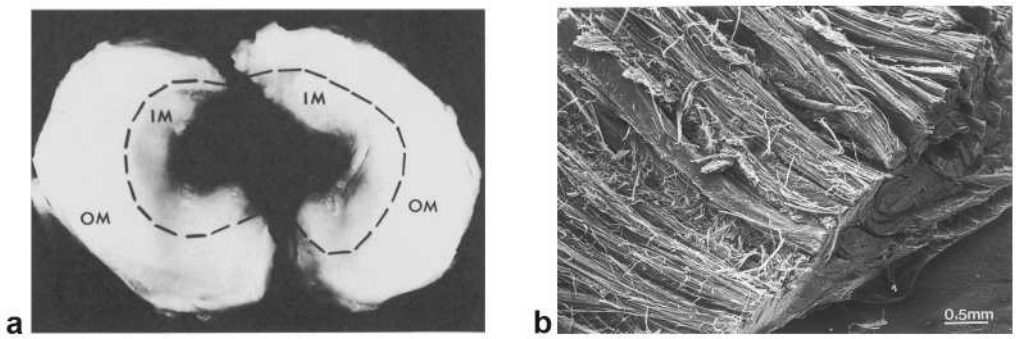

Figure 2.5: Structure of meniscus tissue. a) Zonal composition of meniscus tissue in a hyaline cartilage-like inner meniscus zone (IM) and a fibrocartilage-like outer meniscus zone (OM)[116]. b) Lamellar inner fibril texture of the meniscus[122].

During development, the menisci are formed between joint surfaces of femur and tibia by condensation of an intermediate layer of mesenchymal tissue, which is building attachments to the surrounding joint capsule[121]. In coherence with the hyaline and the fibrocartilaginous nature of the inner and outer meniscus zones, also the presence of GAGs changes throughout the meniscus. According to the literature, the GAG content, measured as cdw, accounts up to 10 % for the inner and less than 1 % for the outer meniscus zone, respectively[115,121]. More precise sources reported values of 2 % cdw GAGs for the IM and 0.8 % cdw GAGs for the OM[123]. Thereby chondroitin sulphate represents as the most abundant GAG in all zones, accounting for about 80 % of all GAGs in the inner and 50-56 % in the outer zone[123].
The developing menisci are highly cellular and vascular, with the blood supply entering from the periphery and extending through the entire width of the menisci, but within mature menisci only the peripheral 10 % to 30 % have blood supply[121]. The cells of the menisci are referred to as “fibrochondrocytes” since they represent a mixture of fibroblasts and chondrocytes in their appearance[120,124].

Meniscal tears are the most common knee injuries and have a poor ability of healing. Since the meniscus consists of a vascularized part at the outer seam and an inner avascular part, lesions of the vascularized area have the greatest capacity for repair. Meniscal tears are usually located in the inner avascular zone of the meniscus and are unable to heal by themselves[125]. Furthermore, long persisting damage leads to joint degeneration which may manifest as osteophyte formation, articular cartilage degeneration, joint space narrowing and symptomatic osteoarthritis[121].

Osteoarthritic menisci show an increased expression level of collagen I and II genes when compared to healthy tissue, but the cellular matrix synthesis is only modestly enhanced[126]. A severe decrease in collagen content within the entire meniscus, suggesting an increased collagen-degrading enzymatic activity, was observed in osteoarthritic menisci[127].

2.3 Tissue Engineering of Bone and Cartilage

Since the technologies available currently, or in the near future, are most likely not able to compete with the highly complex native tissue structures described in the previous chapters, the use of autografts (healthy tissues that are harvested from the patient to replace damaged parts) is still to be considered as the gold standard[50,70,128,129]. But due to a lack of availability in combination with surprisingly high failure rates, alternatives are needed[50,107]. Allografts and xenografts (tissues that are harvested from cadavers of the same species or from different species to replace damaged parts) are alternatively applied, but they bare problematic issues due to immunological reactions and disease transmission potential in combination with poor repair results and even higher failure rates than autografts[107,129,130]. Therefore the discipline of tissue engineering is seeking to fulfil the demand for functional tissue replacement by a combination of scaffolds, suitable cells and an appropriate environment[131].

Tissue engineering requires highly porous scaffolds to host mammalian cells while guiding tissue growth and regeneration in 3D[132]. Because of their lack in mechanical properties in combination with a common absence of interconnected channels, existing three-dimensional scaffolds are considered “less than ideal” for actual applications[132]. This is reasoned by the fact that tissue ingrowth affecting factors like pore size, shape and tortuosity are insufficiently controlled when established processing techniques are used[132]. Therefore a need for new manufacturing methodologies is present[132] since conventional biological tissue culture may not fulfil the tasks of engineered production processes[21].

As reviewed recently, inherent material properties may be engineered to dictate stem cell fate decisions[133]. Although stem cells react to multiple material inputs simultaneously, the variety of potentially relevant material properties aggravates the control of material-induced stem cell responses in complex microenvironments[133].

A desirable approach in scaffold design has to be able to fabricate hierarchical porous structures in order to create the required mechanical function and mass transport (permeability and diffusion) properties[5]. Furthermore, the approach has to enable the production of scaffolds with arbitrary complex three-dimensional anatomical shapes[5]. The underlying mechanisms, on which tissue specific reconstruction and the regeneration of functional tissue rely, are yet not well understood and the importance of the interplay between the scaffolds composition and structure is controversy discussed[134]. But there is reasonable evidence to confirm that structural[135] and functional properties play essential roles for the biological response[134].

Consequently, anisotropic and hierarchical build tissue mimetic scaffolds are presumed to be beneficial for the healing performance, but the realization of an adequate scaffold fabrication process is still lacking. Since a description of all of the numerous relevant approaches in musculoskeletal tissue engineering is way beyond the scope of this thesis, only the ones with close relations to the developed scaffolds are addressed. Therefore, selected strategies and issues for tissue engineering with the focus on bone, osteochondral and meniscus tissue will be presented in the following paragraphs:

Alginate as Hydrogel for Tissue Engineering

The anionic polysaccharide alginate is produced by brown algae for the commercial use and is widely applied within the field of biomedical applications[136,137]. Besides the use as encapsulation polymer[138] or bead[107] in cell culture, it is applied in the form of fibre meshes[139,140], films[141] and 3D scaffolds[142] for tissue engineering applications. In particular, alginate is also used for osteochondral scaffolds[143]. By blending with other polymers also high performance materials may be created[10].

Alginate represents a high molecular weight copolymer of β-D-mannuronic acid (M) and α-L-guluronic acid (G) in 1,4-connection[144]. These monomers assemble into blocks, which in turn form macromolecular sequences (**Figure 2.6** a)). For the use as hydrogel, alginate is commonly transferred from the sol to the gel state by complexation. Possible geometric arrangements of alginate bonding with divalent metal ions (M) forming a chelate complex are shown in **Figure 2.6** b). A chelate complex bond within an alginate chain leads to a planar geometry, as it may be observed in the left hand side of the scheme. If two alginate chains

or one curved chain are bound by a chelating ion, non-planar geometries are resulting as depicted in the middle and right part of the figure[145]. Within the chelate complex bonding with divalent cations, such as the Ca^{2+}-ion, the central ion is usually eightfold coordinated. The bonds, which do not connect to carboxyl or hydroxyl groups, are known to coordinate with water[146]. The formation of a complex bond can take place with several different divalent cations. However, the strength of the chelate complex bonding varies with the metal ion involved[146]. A possible arrangement of antiparallel running alginate chains which are bound together by the presence of divalent cations is depicted in **Figure 2.6** c). Hereby, the black spheres represent complex-forming cations.

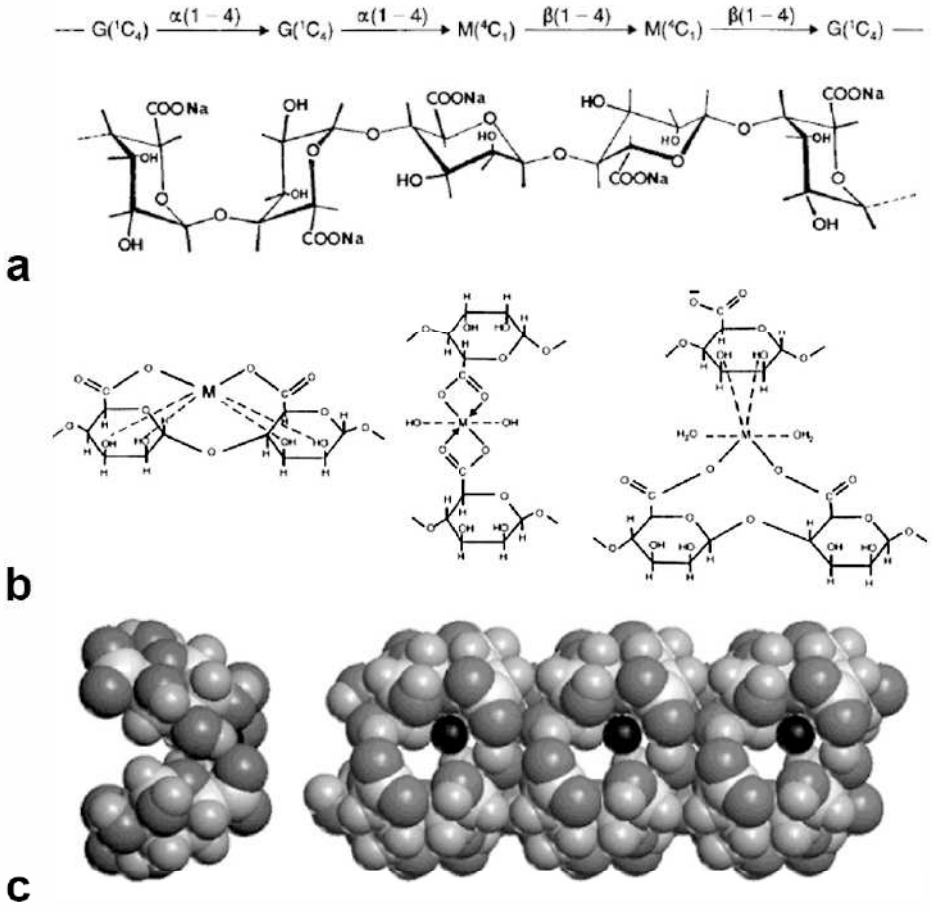

Figure 2.6: Molecular structure of alginate. a) Sodium alginate is composed out β-D-mannuronic acid (M) and α-L-guluronic acid (G) in 1,4-connection, which form an unbranched binary copolymer[144]. b) Chelation of divalent metal (M) alginate complexes[145]. c) Van der Waals structure of cross-linked, anti-parallel and helical arranged alginate chains (Adapted with permission from Literature [146]. Copyright 2001 American Chemical Society).

In the resulting gel structure, the complex bound alginate molecules are oriented parallel to each other[147]. The reaction of a calcium ion with sodium alginate may be formally described in the following manner:

$$2\ \mathrm{NaAlginate} + \mathrm{Ca}^{2+} \leftrightarrow \mathrm{Ca\ (Alginate)}_2 + 2\mathrm{Na}^{+} \quad (3)$$

The process is reversible, so that the equilibrium is shifted to the left hand side of equation 3 on addition of monovalent ions, which leads to a reaction back to the sol state and thus the dissolution of the gel structure. This feature is responsible for the degradation behaviour of the gel structure *in vivo* by ion exchange[147].

A diffusion of polyvalent cations in alginate solutions may lead to the formation of a primary membrane, followed by the separation of gel phase and deliberated water[148]. The process of polyvalent cations diffusing unidirectional into an alginate sol is described as ionotropic gelation: Immediately a sparingly soluble salt is formed as a gel membrane, which separates the alginate sol from the electrolyte solution. Ions and electrolytes of the alginate sol may diffuse through this membrane. However, because of its size the alginate polyanion is not able to penetrate the gel membrane, which features a thickness of about 1 micron and pores smaller than 5 nm. Due to the size and the respective charge of the different ions, they diffuse at different rates so that a diffusion potential is build up. The coiled alginate chains are elongated by the formed electric field. They are arranged orthogonally to the ion current, and finally consolidated into an anisotropic gel.[148]

This mechanism of ionotropic gelation may be also applied for the generation of self-aligned precipitating crystals in multilayer biocomposites[149]. Depending on diffusion processes caused by temperature gradients (thermodiffusion) and concentration gradients (interdiffusion) ionotropic capillaries may be formed in shape of cylindrical pores inside the gel phase. A theoretical description of the emergence of ionotropic capillaries in alginate gels was performed by H. Treml and H.-H. Kohler et al.: By integration of a diffusion-reaction model in a hydrodynamic model a reasonable agreement with experimental findings was achieved. The formation of ionotropic capillaries requires certain ion concentrations as well as a critical value of the gel contraction velocity which lead to hydrodynamic circular convective streams.[147,150,151]

Bone Tissue Engineering

Deville et al. used a unidirectional freeze casting of slurries to produce porous hydroxyapatite scaffolds for bone tissue engineering applications, exhibiting high compressive strengths up to 145 MPa[152]. Although it was possible to attain an anisotropic porous structure within the upper regions of the scaffold, two other zones featuring an isotropic pore structure and a non-porous dense structure were always formed in the downer scaffold regions[152]. Thus, a consecutive anisotropic pore structure could not be achieved. Gelinski et al. developed porous scaffolds consisting of collagen I which is mineralized by nano-crystalline hydroxyapatite[153]. The scaffolds were prepared by freezing and following lyophilisation before they were cross linked by 1-Ethyl-3-(3-dimethylaminopropyl)-carbodiimide (EDC)[153]. Thereby an isotropic porosity, with pore sizes of approx. 200 µm, was generated, which showed a low cell density in the centre of the scaffold after cell seeding[153]. In cyclic unconfined compression testing, the scaffolds reached a compressive strength of ca. 11.5 kPa at 20 % compression in simulated body fluid[153]. Similar problems with an effective cellular penetration were often observed in various types of synthetic and natural scaffolds, so that an unfavourable restriction of cellular ingrowth commonly appears after some 100 µm below the scaffold surface[154-156].

As reviewed by Geiger et al. an optimal approach in bone healing involves the local delivery of an osteoinductive differentiation factor, like bone morphogenetic protein (BMP), which is released by an adequate matrix[50]. These scaffolds should prolong the residence time of the loaded proteins and act as support for invading osteoprogenitor cells[50,157]. But extremes like a burst release, or prolonged low level release are not considered to be beneficial to bone induction[157]. Especially collagen sponges are seen as adequate matrices[50]. A demineralized rat bone matrix, which was loaded with a low (1.4 µg) and a high (11 µg) dose of BMP-2 was used to treat 5 mm femoral defects in rats[158]. Whereas no instances of union were observed for the low dose, 80 % of the defects were bridged for the high dose, but the histological evaluation of the regrown tissue did not return a very native impression[158]. Regarding the mechanical properties[155], it was demonstrated that bone regeneration may be influenced by the hydrogel's elasticity[159]. An "optimal" bone formation was registered at an elastic modulus of 60 kPa, which demonstrated the ability of biophysical cues to direct stem cell behaviors in situ[159].

Osteochondral Tissue Engineering

Harley et al. created osteochondral scaffolds by layering of a calcium phosphate mineralized collagen I/GAG suspension and a collagen II/GAG suspension that was purchased from Geistlich Biomaterials[160]. Both were allowed to interdiffuse and placed into a freeze drier before they were cross linked by EDC[160]. Thereby, a bi-layered osteochondral scaffold was produced without large areas of delamination at the interface, which featured irregular spongy pore sizes between 350 µm and 700 µm[160]. Elastic moduli of the scaffolds were measured in cyclic unconfined compression with a clearly visible change in cross section area that persisted after deformation[160]. Independently on the situation *in vivo* the scaffolds were measured in dry state and showed zonal Young moduli of ca. 30 kPa for the cartilage replacement and ca. 760 kPa for the bone replacement area of the scaffolds[160]. A decrease of these values by two orders of magnitude was denoted for hydrated scaffolds, but exhibiting comparable mechanical properties to native tissues was not seen as a requirement for optimal regenerative capacity[160].

Tampieri et al. combined three layers of different composition by pressing them onto each other to produce one collagen scaffold, which was subsequently subjected to a freeze-drying process.[161] Prior to this, the individual layers were cross linked separately by 1,4-butanediol diglycidyl ether[161]. The top layer consisted of pure collagen I and served as replacement for the chondral zone while the subchondral bone was replaced by collagen I that was mineralized by precipitated hydroxyapatite with a mineral matrix ratio of 70/30 wt%[161]. An, similarly mineralized, intermediate layer with a mineral matrix ratio of 40/60 wt% was supposed to represent the tide mark[161]. The dimensions of the intermediate layer clearly exceed the tide mark dimensions of the native osteochondral tissue for orders of magnitude[161]. A cell seeding of the spongy porous scaffolds turned out to be problematic, since only a small cell migration with a non-uniform distribution was observed in the interior of the cartilage replacement zone[161]. The region in the centre of the scaffolds remained essentially acellular[161]. A commercially available class III osteochondral scaffold based on this proceeding is represented by “MaioRegen®” (Finceramica, Faenza, Italy). As revealed by the associated patent EP 1858562 B1, the individually produced zones that were compressed together afterwards, may show delamination issues on rehydration of the freeze dried matrices[162]. Histological results of animal experiments indicated that only fibrous cartilage material,

without any morphological connection to native articular cartilage tissue, was found in the treated cartilage area[162]. Fibrous cartilage differs from native cartilage tissue in structure and functionality. It is also formed in the meagre, natural and incomplete self-healing processes of cartilage.

Another, more synthetic based, osteochondral scaffold in medical use is represented by "Trufit CB®" (Smith & Nephew, Hamburg, Germany). The chondral replacement zone is composed out of a polylactide-co-glycolide copolymer and the bone replacement area is made out of polyglycolide fibres, calcium sulphate and a surfactant. Since histologic analysis of revision surgery biopsy specimens revealed a fibrous vascularized repair tissue with the presence of foreign-body giant cells inside the articular cartilage, the clinical results are to be rated as "modest"[163]. When applied in a medical study within human knees, no significant differences have been observed between the scaffold treated group and the control/empty defect group[164]. Moreover, 20.0 % of the patients showed persistent clinical symptoms or even more clinical symptoms[163].

An insight in approaches using directional solidification to create anisotropic porous scaffolds that might be also relevant for osteochondral tissue engineering is to be found within **Chapter 2.5.4.**

Meniscus Tissue Engineering

Gastel et al. used folded and compressed layers of porcine small intestine submucosa (SIS) to replace the inner meniscus zone in rabbits[165]. SIS is known to contain GAGs as well as growth factors like fibroblast growth factor, vascular endothelial cell growth factor, and transforming growth factor-β; moreover it features the common issues of xenogenic grafts[166]. Although this approach represents rather simple, the filled defect was infiltrated by apparent fibrochondrocytes and a considerable replacement of the SIS material occurred by connective tissue that appeared similar to the host tissue[165].

A co-culture of meniscus cells and synovium derived stem cells in a fibrin gel on SIS that was supplemented with transforming growth factor β-1 and insulin-like growth factor I was used by Tan et al.[166]. By the incubation in chondrogenic medium, a differentiation into chondrogenic phenotypes, which expressed GAG, collagen II, and Sox 9 but relatively low collagen I, was achieved by the cost of decreasing cell numbers during culture[166].

Müller et al. investigated in vitro the influence of two types of freeze dried scaffolds with spongy pores on meniscus cells[167]. The first type consisted of collagen I and chondroitin sulphate (GAG), while the second type was made out of collagen II and chondroitin sulphate[167]. In case of the collagen II/GAG matrix, the cells were forming a loose network on the outside of the scaffold, but they were also inhomogenously distributed on the inside[167]. The collagen I/GAG sponge was densely encapsulated, with a layer up to 15 cells thick, and hardly any cells were found within the scaffold[167]. Moreover a shrinkage of ca. 54 % was denoted during cell culture for the collagen I/GAG scaffolds[167]. On both kinds of scaffolds, the cells were shown to produce collagen I[167].

A complete meniscus scaffold from electrospun collagen I fibre mats, was developed by Bahcecioglu et al.[168]. These mats were dehydrothermal cross linked, before they were layered and infiltrated with poly (L-lactic acid) / poly (lactic acid-co-glycolic acid) solution[168]. After freeze drying, the meniscus constructs were further treated with oxygen plasma resulting in random pore structures with diameters of ca. 130 µm[168]. After a 21 day culture with fibrochondrocytes, the cells had produced collagen I, collagen II and aggrecan as extracellular matrix components[168].

From a current clinical point of view, meniscus allografts and the collagen meniscus implant (CMI Menaflex®, ReGen Biologics, New Jersey, USA) are the only options that are close to represent a sufficient scaffold for the treatment of larger meniscus defects[169]. CMI consists out of purified bovine Achilles tendons together with hyaluronic acid and GAGs; the scaffold is cross linked by glutaraldehyde and dehydrothermal treatment[169-171]. However, CMI may only be used for a partial meniscus replacement, since a stable rim of native meniscus is still needed[169]. Although the use of CMI did not show a significant benefit shortly after implantation, the ingrowth of repair tissue was observed in second-look-arthroscopies and the knee cartilage degeneration did not increase one year after the treatment[169].

Current repair techniques only succeed in repairing the peripheral vascularized area of the meniscus and a uniform cell infiltration still represents to be problematic[117]. Summarized, the use of extracellular matrix molecules are often favorited, but collagen II/GAG scaffolds promote more meniscus cell proliferation, GAG deposition and less contraction than collagen I/GAG matrices[117]. There is a controversial discussion about appropriate pore sizes of scaffolds for meniscal repair.

While pore sizes between 100 µm and 150 µm have been reported to be favourable for meniscus cells[117], pores between 150 µm and 500 µm were demonstrated to be optimal for ingrowth and incorporation of partial or complete meniscus scaffolds[172].

Ddespite decades of intensive research, matching the special peculiarities of the respective zones of cartilage tissue and thus the formation of functional tissue, which may enable a true regeneration, was not achieved jet[173,174]. For cartilage tissue engineering, an ideal scaffold should be chondroinductive, chondroconductive and guide the cells to differentiate along the right lineage[131]. Additionally the distinct structural properties, as well as the changing material composition inside the native tissues should be considered[98]. Especially the anisotropic structure of mature cartilage seems to play a key role for durable and functionally competent scaffold materials[174].

Besides the pore structure, also the pore size was demonstrated to have a noticeable effect on the cellular behaviour and acceptance: A decrease in pore size, in the range between 150 µm and 95 µm, led to a linear increase in cell attachment and viability for collagen I/GAG scaffolds with isotropic pores[175]. Cells seeded inside collagen I scaffolds with spherical pores showed the highest expression of collagen II and aggrecan for the smallest pores, which were investigated in the range between 150 µm and 500 µm[20].

In order to obtain a specific cell differentiation, cytokines are commonly used for tissue engineering[176]. But regarding clinical application, the use of such growth factors bares problematic regulatory aspects[177] as well as risks for growth factor related complications[178]. Thus, a material which is capable of inducing a zonal specific stem cell differentiation without the need for cytokines would be beneficial in terms of translational intentions. Although multiple attempts of chondrogenic differentiation of MSCs were undertaken, none of them recreated a fully functional articular hyaline cartilage without chondrocytes exhibiting a hypertrophic phenotype[179].

Since an integral cell ingrowth would be facilitated by a continuous pore system that, at best, also approaches the pathway of the collagen fibres in the native tissues, directional solidification seems to be a promising processing route to fulfil this need. Indeed, the use of controlled freezing was applied to generate scaffolds from collagen[14,180,181] and ceramics[152,182,183] for tissue engineering before, but so far a combination of tissue mimetic zonal adapted material composition together with aligned micropores was not achieved. In other words, the prior state of art does not allow creating a physical or (bio) chemical hierarchical, monolithic structure with multiple zones of different material compositions and continuous anisotropic pores.

2.4 Cross Linking of Collagens

In order to control the biodegradation rate and to prevent a rapid elution of the scaffold, collagen-based biomaterials are commonly further cross linked[184]. Thereby, the mechanical properties may be increased to a level where they can be handled or sutured conveniently[184]. Furthermore, cross linked collagen shows a bigger resistance to proteases and a lower degree of swelling than un-cross linked collagen[184]. In the following, the most common methods for cross linking of collagenous scaffolds will be addressed:

A physical way of cross linking is represented by using dehydration via a so called dehydrothermal treatment[185]. It involves subjecting collagen to increased temperatures ($T > 90$ °C) under vacuum[186]. Commonly, this treatment is carried out for an exposure period between 24 h and 120 h[186]. This way, water is removed from the collagen molecules, which results in the formation of intermolecular cross links. More precisely, condensation reactions are induced either by esterification or amide formation[72,185,186]. Although it seems preferable over alternative crosslinking methods, since the use of cytotoxic reagents is avoided[186], it is known to result in partial degradation of the collagen[187].
Further physical cross linking methods include the use of high energy irradiation. The application of gamma and electron beams is able create radicals[188]. These radicals may also lead to the establishment of covalent bonds throughout the scaffold, but since the radicals are formed very unselectively, there is little control over the occurring molecular changes.

In most cases, chemical ways of cross linking are carried out. Among the entire cross linking mechanisms that are driven by addition reactions, the use of isocyanates[11], and especially of 1,6-hexamethylene diisocyanate (HMDI) represents to be very popular. As a family member of the organic isocyanates, it reacts with hydroxyl groups in a sequence of reactions to give urethanes (carbamates), allophanates and isocyanurates[189]. Which product develops favourably, is depending on ratios of functional groups and the presence of eventual catalysts[189]. Additionally, a reaction with water, finally yielding amine groups at the former isocyanate molecule and liberated CO_2, may occur. Furthermore, HMDI is known to react with amine groups, e.g. of collagen, resulting in stable urea groups[190]. But since HMDI is very toxic to cells, a careful extraction[188] or full conversion is indicated.

A further, well established, cross linking method is represented by chemical reaction of complementary functional groups[188]. Therefore glutaraldehyde is commonly used, whereby the aldehyde groups react with amine groups to give covalent imine bonds. Because glutaraldehyde is a toxic compound that shows cell-growth inhibition, even at low concentrations, alternatives have been developed[188]:

The most prominent cross linking mechanism for collagen, by condensation reactions, is carried out by the use of 1-ethyl-3-(3-dimethylaminopropyl)-carbodiimide (EDC)[188]. The underlying cross linking mechanism is explained according to Damink et al. in **Figure 2.7**[191]: It involves the activation of carboxylic acid groups of amino acid residues in collagen (I) by EDC (II) to return 0-acylisourea groups (III)[191].

These 0-acylisourea groups may either react with an available amino group of collagen, or they may be hydrolytically split[192]. In the first case, zero length cross links, without an additional spacing between two collagen molecules (IV) are formed as peptide bonds[192] after nucleophilic attack of 0-acylisourea groups (III) by free amine groups of collagenous amino acids (I)[191]. Thereby, the water-soluble compound 1-ethyl-3-(3-dimethyl aminopropyl)urea (VIII) is liberated[191]. In the second case, water can act as a nucleophile on the 0-acylisourea group (III), resulting in a hydrolysis to return a substituted urea (VIII) and the starting carboxylic acid group of collagen (I)[191]. A rapid hydrolysis of carbodiimides in aqueous solutions can be observed in general, which is increased by the use of common buffers like phosphate-, acetate- and tris buffers[192]. Additionally, the highly reactive 0-acylisourea group may react to a stable N-acylurea group (V), which is referred to as an “N-acyl shift” that is independent on the presence of nucleophiles[191].

Since the normal lifetime of the 0-acylisourea groups (III) is extremely short, the cross linking effect can be quite low when EDC is used alone[192]. Reasoned by this, N-Hydroxysuccinimide (NHS (VI)) is often supplemented to the cross linking solution since it suppresses the unbeneficial side reactions of hydrolysis and N-acyl shift[191]. NHS can interact with the 0-acylisourea groups (III) to form an activated ester (VII), which is significantly more stable in aqueous solutions[192] and less susceptible to hydrolysis at acidic pH values[191]. This ester (VII) can then form a covalent bond with another collagen molecule (IV). After longer times, the ester (VII) may also hydrolyse, restoring the collagenous carboxyl group (I)[192]. Thus, by simultaneous application of EDC and NHS the 0-acylisourea groups (III) and the NHS-activated carboxylic acid group (VII) can both react with free amine groups of collagen (I)[191] and therefore, very high crosslink yields may be achieved[192].

The EDC derived cross links may be formed within one collagen α chain, between two α chains, or as intermolecular linkages between two collagen fibres/fibrils[192]. In comparison to glutaraldehyde, where each cross link requires two amino groups (with a maximum of 15 crosslinks per 1000 collagenous amino acid residues), EDC cross linking requires only one amino group (with a maximum of 20 crosslinks per 1000 residues) and leads to a higher mechanical stability of the product[192]. Since EDC is able to bind on carboxyl groups of sugar residues and proteins[192], it is also been used to attach GAGs to collagen[88]. The use of 2-(N-morpholino)ethanesulphonic acid (MES) may extend the half-life period of EDC to 20 h at a pH of 6.0[193], where the highest degree of cross linking may be achieved for GAG containing collagen matrices[194]. Porous collagenous matrices often collapse during EDC cross linking; under the presence of ethanol, a reduced tendency to collapse together with an increased incorporation of bioavailable GAGs can be obtained[88].

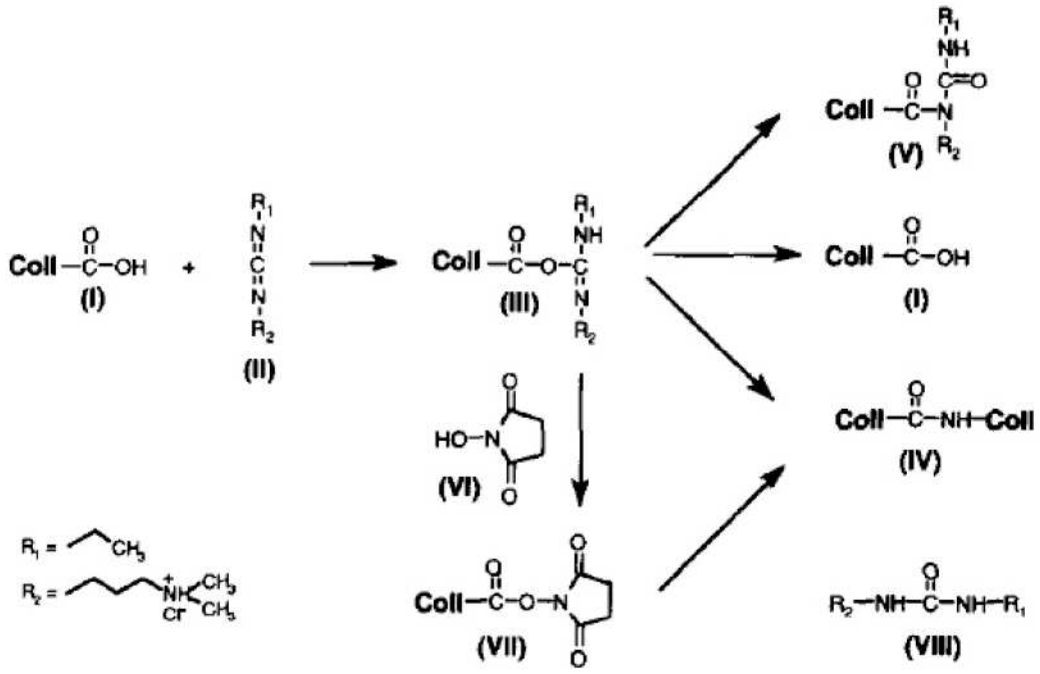

Figure 2.7: Collagen cross linking mechanism by carbodiimides. Carboxylic acid groups of collagen (I) are activated by 1-ethyl-3-(3-dimethylaminopropyl)-carbodiimide (EDC (II)), yielding 0-acylisourea groups (III). Covalent peptide bonds are formed between collagens (IV) after nucleophilic attack of III by free amine groups of I. Unwanted side reactions, to a N-acrylurea group (V) or hydrolysis of III resulting in collagen (I) and 1-ethyl-3-(3-dimethyl aminopropyl)urea (VIII), may be suppressed by the supplementation of N-Hydroxysuccinimide (NHS (VI)). Thereby, a more hydrolytically stable NHS activated carboxylic acid group (VII) is created which also can react together with I to build IV.[191]

2.5 Solidification Technologies

Solidification processes influence material structures in a very broad range of meltable materials on the macroscopic as well as the microscopic level. The directional form of solidification is yielding particularly interesting results, since the spatial orientation of the solidification progress may influence the material structure accordingly. On a macroscopic level, the directional solidification of lava melts was responsible for shaping entire land areas resulting in basalt columns with diameters in the meter range[195,196]. On the other hand, the directional solidification of melts traditionally represents a significant processing step in metalworking applications[197]. Thereby, the microstructure of solidified bodies and thus their mechanical properties can be influenced. For example, this is employed for the production of high-strength turbine blades[198] or single crystals out of metalloid melts to generate the raw material for silicon wafers[199].

In addition to these high temperature applications for metals and metalloids, directional solidification is also partially used in low temperature applications with materials in aqueous media. Therefore, the freezing characteristics of water are of special importance:

2.5.1 Solidification of Water

At atmospheric pressure and below 0 °C, water manifests in solid form of the stable ice phase I_h. In addition to I_h, currently twelve other crystal structures of ice are known which appear only under special circumstances[200]. Since the oxygen atom inside the H_2O molecule is sp^3 hybridized, each water molecule is linked tetrahedral via hydrogen bonds with four other water molecules. Growing I_h crystals in aqueous solutions preferably take the shape of hexagonal prisms. Therefore, the growth kinetics of ice I_h are suitably to be described in a hexagonal crystal system. The $\{0001\}$ plane corresponds to the base of the prism (basal plane). A side surface of the prism is e.g. described by the $\{10\bar{1}0\}$ plane (prism surface). The location of the $\{11\bar{2}0\}$ plane is illustrated together with the previously mentioned crystal planes in **Figure 2.8** a)[201].

The respective growth kinetics of individual crystal planes can be concluded from a consideration of the steric circumstances at a molecular level: The growth at the ice/water interface proceeds by rearrangement of the hydrogen bond network in the liquid phase. This occurs in two-dimensional form for the basal and in three-dimensional form for the prism and the $\{11\bar{2}0\}$ planes (**Figure 2.8** b)). From the basal plane water molecules are standing off, whereby the mutual distance is too large that they could be attached together via hydrogen bonds. More water molecules can only be bound stable by the establishment of hydrogen bonds to three already incorporated water molecules, resulting in a layer-wise growth mechanism. On the contrary, in case of the prism and $\{11\bar{2}0\}$ planes the steric circumstances are more advantageous for the incorporation of water molecules into the crystal lattice. Here, newly adhered water molecules have to establish less hydrogen bonds to enable a stable structure. This results in a higher growth rate compared to the basal plane[201].

Besides these steric considerations also the correlation between vacancy energies and corresponding dipole moments is of importance for an incorporation into the crystal lattice of ice[202]. A more detailed insight into the molecular dynamics of ice freezing, based on the circumstances in the hydrogen bond network, may be found in literature [203].

In addition to the growth of individual ice crystals, the macroscopic structure of ice is also produced by the sintering of crystallites. During the sintering process the inclusion of impurities, which may be present in all three aggregate states[204], determines the microstructural and mechanical properties of the formed ice[205,206]. The presence of impurities often results in a lowered freezing point of water[207]. While sintering in a liquid phase, the mass transport within his phase occurs mainly by diffusion and convection. Hereby, the convective transport is several orders of magnitude faster than the diffusive transport[208]. While water molecules are incorporated into the crystal lattice, other molecules, colloids and ions predominantly stay behind at the grain boundaries of the ice surface, which leads to an elevated concentration in the liquid phase ("cryoconcentration")[205].

2.5.2 Supercooling and Solidification Morphologies

When a liquid substance is cooled below its freezing temperature without being transferred to the solid state, it is called supercooled[209] or undercooled. The transfer to the solid aggregate state requires stable nucleation sites which depend on the difference of the chemical potentials of both states, as well as the interfacial free energy of the crystallite[210]. A detailed review on different solidification states of water may be found in literature [211]. The nucleation may be either driven by thermodynamic fluctuations or catalytic particles (extrinsic nucleation substrates), which feature a higher melting point than the nucleating phase[208]. As indicated by the naming, the energy barrier to pass is smaller in case of catalytic particles than for fluctuations. While impurities, which might act as catalytic particles, facilitate the nucleation on the one hand, an accumulation of those impurities by cryoconcentration will lower the temperature at which solidification can occur on the other hand. The local accumulation of particles increases the density of microstates, which results in increased entropy and energy dispersion when compared to the previous state[212].

This supercooling due to composition changes was defined as “constitutional supercooling” by Rutter and Chalmers[213]. In the 1950s they investigated the solidification processes of metals and metal alloys. This led to the establishment of a fundamental theory, in which the constitutional supercooling is occurring in an unstable liquid ahead of the solid liquid interface. Here the layer of liquid is below its equilibrium liquidus temperature, which also may be interpreted by a comparison of gradients: For a constitutional supercooled liquid, the gradient of the sample temperature at the solid liquid interface is smaller than the gradient of the liquidus temperature curve[214]. (**Figure 2.8** g) bottom panel)

For the mathematical description of these processes, complex models have been created based on the pioneering work of Mullins and Sekerka in the 1960s[215-217]. By perturbation theory calculations they derived a criterion for the morphological stability of a solid liquid interface. Originating from a slight, spatially regular disturbance, the solid liquid interface may become more unstable (**Figure 2.8** c)) or more stable (**Figure 2.8** d)) with progressing solidification. The scale bar is indicating typical projection sizes for the casting of alloys. Perturbations of the interface may be induced by a variety of fluctuations in temperature, composition, or pressure[208]. The circumstances of interacting concentration and temperature changes may be advantageous or disadvantageous the formation of forward-pointing solid projections[213] leading to morphological instability or stability, respectively. This represents a significant aspect for the solidification of metal melts since applications like single crystalline silicon wafers[199] require a stable solid liquid interface, while refined polycrystalline castings, e.g. for turbine blades[218], require a morphological instability of the interface.

Different possibilities of solidification morphologies, as well as respective concentration and temperature fields are displayed in **Figure 2.8** e)-h)[214]: Here, c_o represents the concentration of a further phase so that e) and f) depict the situation for pure substances ($c_o = 0$) while g) and h) represent alloys ($c_o > 0$). The upper panel depicts the solidification morphologies together with the corresponding mass diffusion fields (middle panel) and heat diffusion fields (bottom panel) along the dashed line in the upper panel. The temperature gradient at the solid liquid interface is expressed by G, which is imposed by the external heat flux.

Within the heat diffusion fields T_q represents the sample temperature while T_f and T_L stand for the melting point of a pure substance and the liquidus temperature of an alloy, respectively.

For a pure substance, a plane solidification front will form when a pronounced external temperature gradient is directing the solidification. Since the heat flow is progressing in the opposite direction of solidification, more heat will pass the tips of perturbations leading to their re-melting and a planar interface (**Figure 2.8** e)). If the external temperature gradient is small / approaching zero, an equiaxed crystal growth will occur in a supercooled melt (marked as cross hatched in the bottom panel). Due to the released latent heat, the area surrounding the equiaxial crystal is warmed which leads to a preferential growth of perturbations and a morphological unstable interface (**Figure 2.8** f)).

In the case of alloys, a columnar/dendritic solidification may occur for a pronounced external temperature gradient. If the slope of the liquidus temperature multiplied by the concentration gradient is bigger than the positive interface temperature gradient, the conditions of constitutional supercooling are matched and the interface becomes constitutional unstable. These circumstances are to be fulfilled to obtain an oriented microstructure by directional solidification (**Figure 2.8** g)). For small external temperature gradients, an equiaxed crystal growth will result again, since heat and the further phase are both accumulated in front of the unstable solid liquid interface (**Figure 2.8** h)).

Since a detailed description of the highly complex mechanisms of solidification processes is beyond the scope of this thesis, the interested reader is referred to the textbooks of Glicksman[208], Kurz and Fischer[214]. Although these models have been created for a description of solidifying metal melts, the general principles may be also transferred to the solidification of aqueous mixtures/alloys.

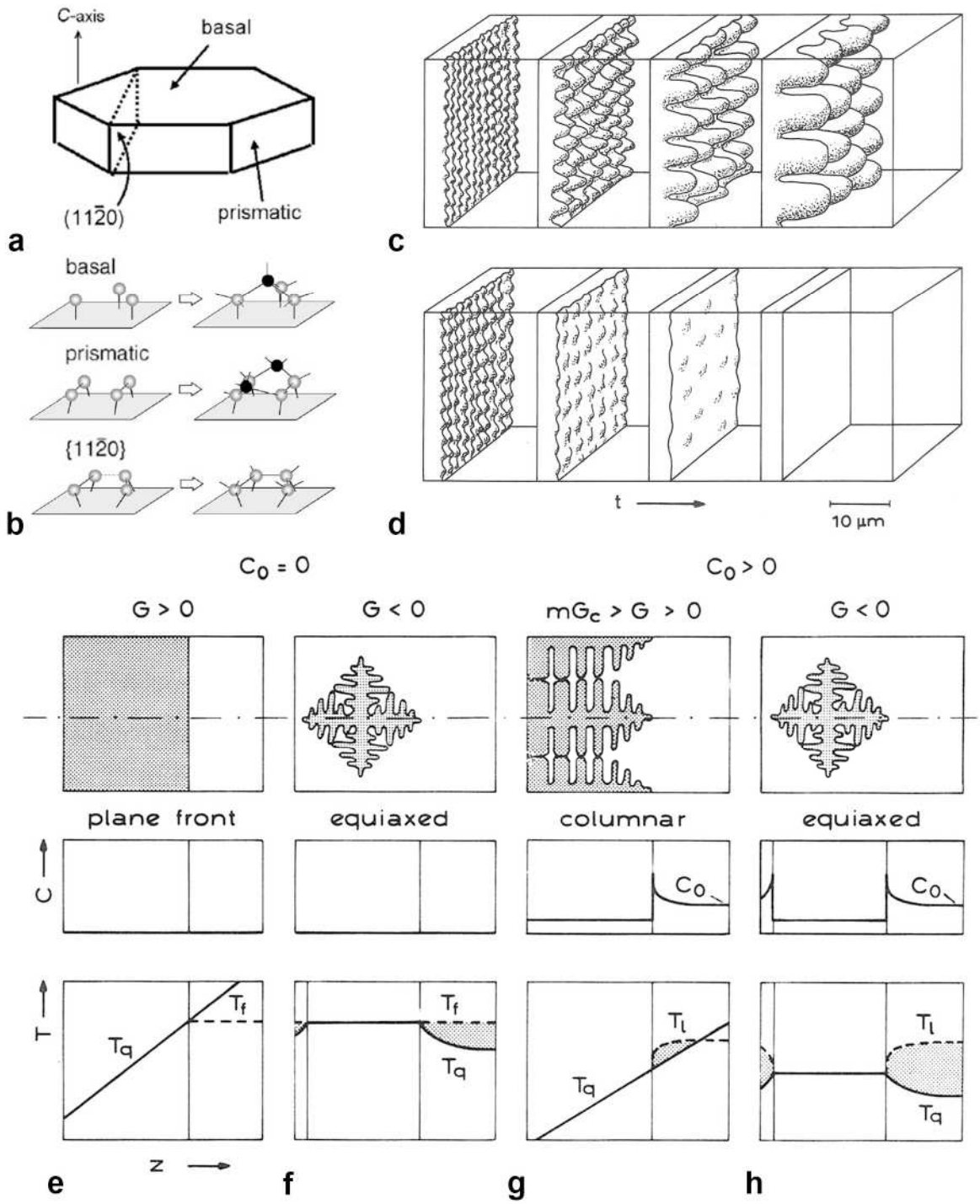

Figure 2.8: Solidification of water. a) Crystal planes of ice I_h[201]. b) Steric circumstances at adhesion sites of water molecules (modified from literature [201]). c), d) Temporal development of morphological stability for an unstable (c)) and stable (d)) solid liquid interface. e) - h) Different solidification morphologies for pure substances (e), f)) and alloys (g), h))[214]. Upper panel illustrates solidification morphologies, while middle and downer panel depict the corresponding mass and heat diffusion fields along the dashed line in upper panel. Circumstances to obtain an oriented microstructure by directional solidification under constitutional supercooling are described in g). (Abbreviations: c_o = concentration of a further phase, G = temperature gradient at the solid liquid interface, T_q = sample temperature, T_f = melting point of a pure substance and T_L = liquidus temperature of an alloy; Figures c) – h) modified from literature [214] with permission of Trans Tech Publications)

During the application of a unidirectional freezing process on aqueous colloidal suspensions different ice growth styles may occur, depending on the respective freezing parameters: In the case of slow freezing rates a flat ice front, which displaces the colloidal particles, is formed preferably[219]. An equiaxial ice crystal growth is manifesting in spherical ice crystals that are found for low external temperature gradients[220]. The dominant presence of equiaxial crystal growth finally leads to an isotropic solidification morphology.

A lamellar or dendritic (tree-like) morphology is established for a columnar form of solidification under higher external temperature gradients[220]. A lamellar morphology can be imagined as an arrangement of fins, while a columnar morphology corresponds to rod or prism-shaped appearances. Protrusions of the side surfaces of a lamellar or columnar morphology that branch out yield a dendritic solidified phase. Under conditions that produce unstable planar interfaces, the developing interface morphology may be cellular, but dendritic growth usually occurs when the degree of instability is large[221]. The dendritic branches run along preferred growth directions which correspond to low-indexed crystallographic directions of the crystal lattice[222] and decrease in size with increasing freezing rates[223]. All of these types of morphologies result in an anisotropic form of solidification.

Depending on the local variation of freezing parameters and thus, the corresponding primary spacing between the anisotropic morphologies, individual crystals tips may also be overgrown. On the other hand, a tip splitting or the growth of a tertiary arm may occur in cellular and dendritic patterns, respectively[224]. In general, all forms of solidification patterns may be perturbed by heterogeneities (particulates/dirt) which may lead to a variety of polycrystalline growth patterns[225]. These larger polycrystalline patterns may be also formed superimposed to the smaller underling solidification morphologies.

Freezing solutions, with ingredients that are likely to crystallize, show a eutectic freezing behaviour: if, for instance, water crystallizes in the form of ice, the remaining saturated solution is gradually more concentrated by further crystallization until the sample is completely solidified and present in the solid aggregate state[214]. Even sodium chloride solutions tend to show a eutectic solidification behaviour[226]. Other solutions, however, tend to supersaturation. They solidify as an amorphous glass, rather than crystallizing at the eutectic point[214].

2.5.3 Issues Related to Mathematical Descriptions of Solidification Processes

Due to the relevance for the metal working industry, the mathematical description of the solidification problem has been the field of intensive research[221,227-231]. A variety of relevant parameter functions are known for well characterized systems like metal and alloy melts. The direct transfer to arbitrary other systems remains problematic due to a lack of detailed information. Especially for complex systems, which may contain a mixture of solvents, polymers and particles, the correct ascertainment of values for the functions of numerous variables* represents a problematic issue. These variables often depend on multiple parameters, which also may change during the solidification process[232].

With respect to the solidification phenomena of the current work, the consideration of some material parameters of water and ice seems indicated: In the case of aqueous formulations, the fact that heat capacity and compressibility of liquid water increase dramatically when the supercooled region is approached[233], complicates a correct description. Furthermore, the parameter function of the latent heat of water was observed to show abnormalities for a solidification in the supercooled state[234]. By negligence of the temperature dependency of the thermal conductivity of water, whose value may change for ca. 58 % between 0 °C and – 100 °C[235], the heat flux through the solid liquid boundary may be underestimated by a factor of two[236]. Accordingly, this also results in a higher ice front velocity and cooling rate at the ice front[236].

Since the solidification is performed on materials in a non-solid aggregate state, the precursors in form of solutions, suspensions or gels are rather to be treated as present in the liquid aggregate state. Thus, the solidification of liquids would have to be described by mathematical models. In contrast to solid materials, which show a linear progression of the temperature profile in heat transfer situations, the situation in liquid materials is way more complicated: Besides heat conduction, which represents the dominant mechanism in solids, also convection inside the liquid has to be considered[237]. This aggravates a correct mathematical description heavily, since the temperature profile of a transition between a solid and a liquid material does not follow a linear behaviour[237].

* Diffusion coefficient, Gibbs-Thomson coefficient, Gibbs free energy, mixing entropy, wetting angle, viscosity, heat capacity, latent heat and thermal conductivity are examples of important functions for the for the theoretical description of solidification processes.

During the sintering of ice crystals, the mass transport in the liquid phase is carried out via diffusion and convection[205]. The convective transport proceeds several orders of magnitude faster than the diffusive transport[205] and adds up to the other convective processes, which are induced in the liquid phase: Depending on geometrical aspects, the temperature gradient, flow properties of the liquid and further parameters, convective processes occur, whereas turbulent streams cannot be excluded in real situations[237]. Obviously, a general theoretical description of this problem is far away from being trivial[238], whereby the assumptions of the boundary conditions should meet actual experimental conditions too. Additionally, the entropic changes during solidification represent a significant aspect for crystallisation processes.

Alternatively to this, most of the mathematical descriptions approximate heat transfer processes in already solidified liquids, under the negligence of convective heat transfer and the assumption of quasi stationary conditions. Moreover, the mathematical solution of “Neumann” represents the most prominent analytical approach to solve the solidification problem of differential equations. However, the necessary boundary condition of first order, which demands a constant temperature of the sounding container, is corresponding to a heat transition coefficient of infinite size, which will most likely not be fulfilled in practical conditions[239].
Due to the high complexity in combination with an incomplete general understanding of the interaction of all related phenomena, the actual solidification of a liquid is commonly not mathematically solved. The significance of the related issues becomes obvious, if the fact is considered that currently, even the crystallisation of pure water may be simulated only partially[240].

2.5.4 Directional Solidification in Biomedical Applications

Freeze structuring of ceramics was studied by Deville et al. via the solidification of slurries on a one-sided cooled cold finger, in order to achieve an anisotropic structuring[152,182,183,241-245]. By controlling the cooling and freezing rate, a unidirectional ice growth could be obtained, which resulted in a plane-parallel orientation of the ceramic particles that correlated with the structure of nacre[182].

In this way hydroxyapatite ceramics, intended for osseous tissue regeneration, were obtained which showed a compressive strength parallel to the ceramic layers of about 145 MPa despite a porosity of 48 %[152]. The process of cryostructuring is variable with respect to the achievable structures: In addition to the freezing rate, additives (e.g., salts, carbohydrates, alcohols) and template structures underneath the frozen slurries may exert control of the freezing process and thus the resulting ceramic structures[246].

Further applications that were carried out using an analogue experimental approach as mentioned above succeeded in the ice-templating of cellulose[247] and β-tricalcuim phosphate[231,248,249] with controlled ice front velocities. By infiltration with poly (caprolactone), the inner surface of the ice-templated ceramic structures was coated, which lead nearly to a duplication of the compressive strength for samples with low initial solid content[250].

The influence of initial pH values on the freezing characteristics of collagen dispersions was studied in literature [251], resulting in varying freezing temperature profiles for acidic and basic conditions. H. Schoof investigated the controlled directional solidification of collagen I suspensions[252]: Based on light microscopic investigations of the ice front, she determined acetic acid with concentrations between 1.5 wt% and 3.8 wt% as an appropriate solvent for the attainment of a cellular ice crystal morphology. By using the technology described in DE 19751031 A1[253], a controlled formation of an anisotropic pore structure could be generated in the range between 20 µm and 50 µm[14,23].
This technology[253] is also applied by the Matricel GmbH (Herzogenrath, Germany) to produce collagen I products. Besides collagenous membranes for the coverage of bone and cartilage defects, the anisotropic porous scaffold "OptiMaix 3D" is produced, which is not intended for use in humans yet. The freezing method is based on finger shaped ice crystals that grow through a collagen I dispersion, producing channel like structures. For this purpose, a freezing method has been designed in analogy to conventional methods for metal processing: A mixture of substances is solidified between two temperature controlled, parallel or concentrically arranged surfaces while the temperature gradient between the surfaces is kept constant.

Resulting scaffolds with pores of ca. 50 µm have been applied in research concerning preadipocyte transplantation[254], muscle cell differentiation[255] and nerve guidance[256,257].

Pot et al. used a different “wedge-based” system to create anisotropic porous scaffolds from collagen I[258]: By using two baths of liquid nitrogen and a dry ice / ethanol mixture, smaller pores of ca. 66 µm and larger pores of ca. 146 µm diameter could be generated, respectively. The variation of the concentrations of collagen and acetic acid as well as the incorporation of detergents led to a further slight alteration of attainable pore sizes.

3 Materials and Methods

Since the development of a novel process and the construction of a custom device, which is specialized for the fabrication of new scaffolds represented crucial elements of the thesis, these topics are described in detail within **Chapter 4** "Results and Discussion". Similarly, the development of a confined compression setup and evaluation method is more explicitly described in **Chapter 4**

3.1 Alginate

An alginate solution was produced in distilled water by dissolving 5.5 wt% Protanal LF 10/60, (G/M=70 %, MW=180 kDa; FMC Biopolymer, Drammen, Norway) a low viscosity alginate for wound dressings. Therefore a successive addition of sodium alginate was carried out under vortex appearance in order to prevent formation of alginate association colloids. The concentration of Ca^{2+} ions within the distilled water was determined by inductivity coupled plasma mass spectrometry (ICP-MS) to a value of 2.4 µmol/l, which shows a certain degree of inherent gelation potential of the solution.

3.2 Calcium Phosphates

3.2.1 Synthesis of Brushite

Brushite crystals (calcium hydrogen phosphate dihydrate) were synthesized by precipitation reaction of a 1 mol/l $(NH_4)_2HPO_4$ solution with an equimolar $Ca(NO_3)_2 \cdot 4H_2O$ solution:

$$(NH_4)_2HPO_4 + Ca(NO_3)_2 \cdot 4H_2O \rightarrow CaHPO_4 \cdot 2H_2O + 2NH_4^+ + 2NO_3^- + 2H_2O \qquad (4)$$

Upon contact of the two solutions, a milky turbidity, followed by sedimentation of white precipitate was instantly recognizable. The resulting mixture was filtered and washed several times with deionized water to remove residual ions, and water-soluble salts. After air-drying the remaining calcium phosphate slurry brushite crystals were derived.

3.2.2 Synthesis of Hydroxyapatite

For the synthesis of hydroxyapatite two solutions of 300 ml were prepared in desalinated water: A phosphate solution, containing 0.05 mol/l $(NH_4)_2HPO_4$, and a calcium solution, containing 0.03 mol/l $Ca(NO_3)_2 \cdot 4H_2O$, were produced. Both solutions were split into aliquots of 100 ml each. The first 100 ml of both solutions were combined inside a reaction vessel drop wise, afterwards the second parts were mixed slowly and finally the remaining solutions were rapidly poured together. Instantly, 40 ml of a 25 % NH_3 solution were supplemented and the reaction vessel was heated to 80 °C for 10 min before it was left to rest for 16 h.[259]

$$3\,(NH_4)_2HPO_4 + 5\,(\,Ca(NO_3)_2 \cdot 4H_2O\,) \;+\; NH_3 \rightarrow$$
$$Ca_5(PO_4)_3(OH) + 7\,NH_4^+ + 10\,NO_3^- +\; 18\,H_2O + 2\,H_3O^+ \qquad (5)$$

The suspension was filtered under suction and washed five times, each with 1 l deionized water to remove residual ions and water-soluble salts. After freeze drying (**Chapter 3.3.2**) of the calcium phosphate slurry, hydroxyapatite crystals were obtained. (The crystal phase was identified as hydroxyapatite by X-Ray Diffraction (XRD) analysis.)

3.2.3 3D Powder Printing of Calcium Phosphates

In order to produce the inorganic component of the osteochondral scaffolds as monolithic piece, 3D Powder Printing was applied. A CAD based bone replacement section was designed using “ThinkDesign suite 2008.1“ (think3; Bologna, Italy) and printed as cylindrical samples, with 30 mm diameter and 3 mm height as well as 11 mm diameter and 2 mm height, both penetrated by holes with 1.5 mm diameter on the lateral surface. The printing was performed by using α/β tricalcium phosphate powder and diluted phosphoric acid as binder like described in literature [46].

By sintering of $CaHPO_4$ (monetite) together with $CaCO_3$ at 1400 °C for 5 h, tricalcium phosphate was generated[†]:

$$2\ CaHPO_4 + CaCO_3 \rightarrow Ca_3(PO_4)_2 + CO_2 + H_2O \qquad (6)$$

After milling for 20 min a α/β tricalcium phosphate powder with a fraction size below 100 µm was derived. The powder was processed with a 3D powder printing system "ZPrinter 310" (Z Corporation; Burlington, Massachusetts, USA) which was controlled by the software "ZPrint 7.10.2-9" (Z Corporation; Burlington, Massachusetts, USA). For the 3D printing process, the most promising results were obtained using a layer thickness of 0.1 mm together with a saturation of 72 % for the shell and a saturation of 198 % for the core, both with a binder / volume ratio of 0.165. Monolithic brushite parts may be formed by hydraulic setting reaction together with 20 % phosphoric acid as binder:

$$Ca_3(PO_4)_2 + H_3PO_4 + 6\ H_2O \rightarrow 3\ CaHPO_4 \cdot 2H_2O \qquad (7)$$

After removal of the printed part from the build container and blowing off excessive powder with a pressure of ca. 2 bar, a post-curing with 20 % phosphoric acid was performed for 1 min.

3.3 Collagen

The raw materials for collagen suspensions were derived from processing collagenous tissues of animalistic origin. A mixture of collagen I and III[73,77,82] was isolated from murine tail tendon, while bovine knee cartilage represented the basis to isolate a mixture of collagen II, IX and XI[73,84,89,92,260,261].

Considering the dominant collagenous amounts in these mixtures, they are referred to as "collagen I" and "collagen II" in this thesis. Calf knees were purchased from "Brüninghoff Kalbfleisch" (Bocholt, Germany) while murine tails were kindly provided by the animal testing facility of the "Department for Functional Materials in Medicine and Dentistry" (FMZ, University of Würzburg, Germany).

[†] The production of the raw powder material was carried out by Ms. Isabell Biermann, technical assistant at FMZ.

3.3.1 Collagen Isolation

Murine tendons were harvested to isolate collagen I. Instead of pulling out single collagenous tendon fragments from cut of rat tail parts using tweezers, it was found to be more effective to derive the collagen I after the execution of the following protocol: Freeze stored rat tails were thawed in physiologic NaCl-solution. Using a medical clamp the tail was fractured in 2-3 cm distance from the tip of the tail. While holding the rest of the tail, the fractured piece was pulled out together with the attached tendons (**Figure 3.1** a), b)). The fracturing and pulling out was repeated in intervals of 2-3 cm until the entire tail was processed. The tendons were cut off the tail pieces with a scalpel and stored in physiological NaCl solution. In average, a yield of ca. 0.9 g tendon material per tail could be gained by this way of processing.

The tendons were disinfected twice for 10 min in 70 % ethanol and washed under stirring in 0.9 % NaCl for 12 h. The dissolution of the collagenous material was carried out by acidic fractioning with 100 ml of 0.1 % acetic acid per gram of tendon material.

The setup for the acidic fractioning is depicted in **Figure 3.1** c): A “RML6” cryostat (Lauda; Lauda-Königshofen, Germany), cooled by a 1:1 ethylene glycol water mixture, is coupled to a glass reactor. Inside the reactor, tendons are fractured for 28 days at 5 °C under stirring with an “E60” KPG stirrer (Heidolph; Schwabach, Germany) at 15 rotations per minute (rpm). Finally the collagen I was lyophilized and stored at - 20 °C.

Figure 3.1: Isolation of collagen I from murine tendon. a) Radial orientation of the tendons along a rat tail. b) Pulling out of collagenous tendon material. c) Setup for acidic fractioning of collagen I.

An analogous procedure applied to collagen II material did not produce a significant yield. Alternatively, a procedure corresponding to the patent DE 10157182 A1[262] was chosen, where various wet chemical purification steps were carried out for the isolation of collagen II. The removal of hydrophobic contaminants, the action of calcium chelating agents or enzyme inhibitors respectively, the leaching out of hydrogen bound contaminants, as well as the repeated storage in acids and bases represent the most concise steps involved.[262]

The isolation and purification of collagen II was carried out after the following protocol: Fresh, intact calf knees were dissected by cutting the lateral sinews of the patella from the femur to the tibia. After opening of the joint and cutting through the cruciate ligament the menisci and all surrounding tissue were removed before the articular cartilage of femur, tibia and patella was carved out with a scalpel. (**Figure 3.2**.) Special attention had to be paid that the collection of bone and periosteum material was avoided to ensure the purity of the collagen II. Hyaline articular cartilage produced squeaking noises during carving of the whitish tissue. If the tissue was reddish and did produce other sounds upon carving, it was discarded. The collected cartilage chips were inactivated and disinfected by placing 100 g cartilage in 500 ml of 0.5 mol/l NaOH for 2 h at 20 °C. A neutralization step was carried out with 0.3 mol/l HCl under stirring for 30 min.

Neutralization residues were removed by a washing step which was repetitively applied during this isolation protocol: The material to purify was triple washed in 1 l desalinated water for 30 min each, followed by discarding the supernatant after sieving through a 125 micron sieve.

Afterwards the cartilage material was fractioned together with crushed ice in a "Waring Laboratory Blender" (Waring; Connecticut, USA): 250 g of crushed ice, 250 ml of cooled desalinated water and the cartilage chips were subjected to 3 x 45 sec "LO" pulse; after supplementation of 60 g of crushed ice and 3 x 45 sec "HI" pulse the cartilage fragments were separated from the liquid by a 125 micron sieve. This cartilage mass together with 50 g of crushed ice and 150 ml of desalinated water was again subjected to a 45 sec "LO" pulse followed by 5 min of continuous operation on "HI", while adding 60 g of crushed ice every minute. After another sieving procedure the last fractioning step was repeated and the cartilage mass was sieved again.

A degreasing of the obtained collagen mass was performed by 3 times washing in 0.5 l of acetone each for 45 min to remove hydrophobic contaminants. The residues of the acetone were removed by another washing step, as described previously.

In the next step, calcium chelating agents and enzyme inhibitors were applied by washing the collagen mass threefold, each with 0.5 l of 27 mmol/l HEPES-buffered (pH ~ 5) 50 mmol/l NaCl solution, mixed with 7 mmol/l ethylenediaminetetraacetic acid (EDTA) (Sigma-Aldrich; Munich, Germany) each for 45 min. Hereinafter, the afore mentioned washing procedure was carried out.

To remove impurities bound by hydrogen bonds 250 ml of 4 mol/l urea solution were added to the collagen mass and left for 45 min reaction time. Another application of the washing step leads to the removal of urea residues.

For the avoidance of irreversible peptide bond cleavage, the collagen mass was stored in 500 ml of 0.1 mol/l NaOH for 24 h at pH values of 12 - 14. After neutralization with 100 ml of 0.1 mol/l HCl a further washing step was applied followed by storage of the collagenous mass in 500 ml of 0.1 mol/l HCl for 24 h at pH values between 0 and 3. After neutralization with 0.1 mol/l NaOH, a final washing step was applied followed by centrifugation of the supernatant. Afterwards, the collagen II was lyophilized and freeze fractured before it was stored at - 20 °C.

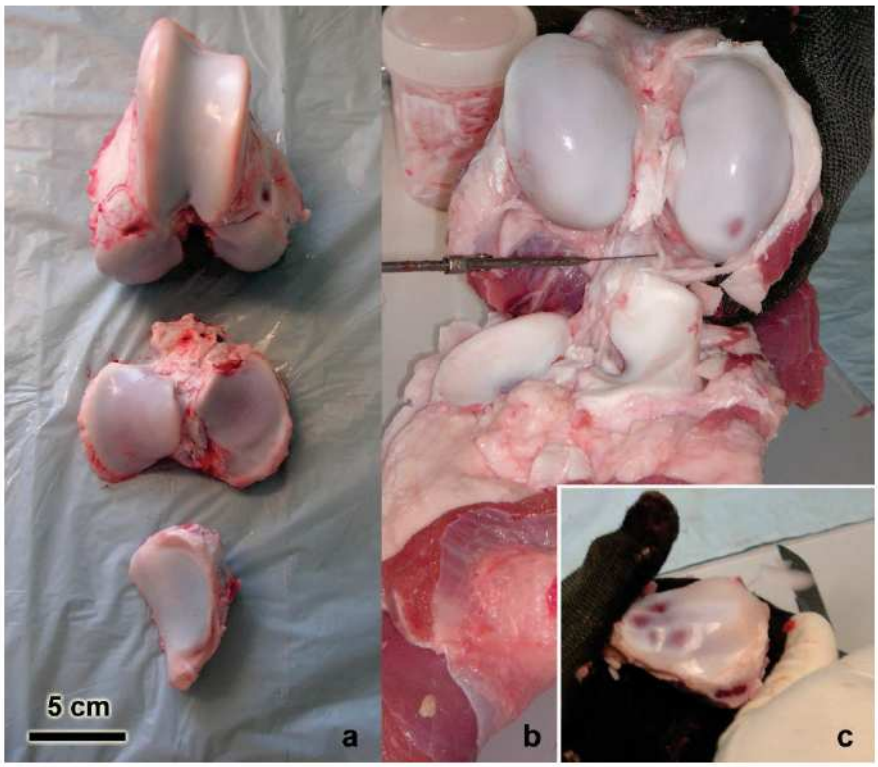

Figure 3.2: Isolation of collagen II from bovine knee cartilage. a) Articular cartilage is harvested from the knee joint surfaces of femur (top), tibia (middle) and patella (bottom). b) Dissection of cruciate ligament to access the hyaline cartilage tissue. c) Carving of cartilage chips from patella with a scalpel.

3.3.2 Lyophilisation

The freeze drying of all samples was performed with an "Alpha 1-2 LD" lyophilizator (Christ; Osterode, Germany). The specimens were frozen for 3 h at - 20 °C inside the glass vessels that were plunged onto the lyophilizator afterwards. If not specified otherwise the sublimation of the frozen solvent was generally carried out for 18 h, at a temperature of - 52 °C and a pressure of 70 µbar.

3.3.3 Cryogenic Fracturing

Since hyaline cartilage from bovine knee tissue represents an extraordinary rigid material a comminution to small particles by conventional methods would involve the risk of heat denaturation of the collagens as well as unsatisfactory fraction sizes. To avoid any risk of thermal denaturation, the collagen II was fractured cryogenically with an oscillating mill “CryoMill MM400” (Retsch; Haan, Germany) under cooling with liquid nitrogen supplied by an “autofill” Dewar unit.

A 25 ml zirconia milling container and a 20 mm diameter zirconia milling ball were used in order to prevent the contamination of the collagen by abrasion of metal particles. The following milling protocol was found to be most effective in reaching the smallest obtainable particle sizes while preventing denaturation:
The milling container was filled up with ca. 1.3 g freeze dried collagen II fragments and the milling ball. After mounting the container to the CryoMill a precooling step was carried out in “Auto” mode with 5 Hz oscillations. Thereby, the container was bathed by liquid nitrogen and the specimen was entirely frozen. For the actual fragmentation, 8 milling cycles with 25 Hz were each applied for 4 min each. In order to prevent heat denaturation during the milling procedure the above named cycles were interrupted by intermediate cooling cycles with 5 Hz for 1 min where liquid nitrogen was flushed through the system. This way, a bimodal particle size distribution (**Figure 9.1**), featuring peaks around 10 µm and 40 µm with a median value of ca. 14 µm was obtained.

3.4 Design and Manufacturing of Custom Devices

The individual parts of the custom devices used in this thesis were designed by using both computer-aided design (CAD) softwares “ThinkDesign suite 2008.1“ (think3; Bologna, Italy) and “SolidWorks Education Edition SP2.0” (Dassault Systèmes; Paris, France).
Preliminary parts were fabricated out of acrylonitrile-butadiene-styrene (ABS) by using the 3D printer "MakerBot Replicator 2X" (MakerBot Industries; Stuttgart, Germany). The 3D printing was carried out with a platform temperature of 110 °C and an extruder temperature of 218 °C, using a layer height of 0.25 mm and an extruding speed of 60 mm/s. Depending on the respective part, 3 - 5 shells were used together with an internal filling percentage of 20 - 100 %.
The manufacturing of the final parts was performed within the Workshop[‡] of the Department for Functional Materials in Medicine and Dentistry (FMZ, University of Würzburg). These components were used to assemble an Adjustable Cryostructuring Device as well as a confined compression setup in an iterative process. (**Chapters 4.1.1** and **4.6.1.1**)

[‡] The fabrication of custom build final parts was carried out by Mr. Harald Hümpfer and Mr. Anton Hofmann, precision mechanic masters at FMZ.

3.5 Scaffold Characterization

3.5.1 Cryostatic Sectioning

In order to prepare smooth cross section surfaces for the electron microscopic investigations, a cryostatic sectioning was performed using a “Cryostat MNT” cryomicrotome (SLEE, Mainz, Germany). The samples were frozen and fixated onto the sample rack by using water before they were trimmed in 20 µm steps and finally cut in 1 µm steps. Only the truncus of each sectioning was used for further evaluation in lyophilized form; the sections were discarded.

3.5.2 Scanning Electron Microscopy (SEM) and Energy Dispersive X-ray Spectroscopy (EDX)

Prior to the electron microscope studies, characteristic areas of freeze dried samples were prepared using a ceramic blade or cryostatic sectioning. The materials were fixed on the sample racks (Provac; Sprendlingen, Germany) by "Conductive Carbon Cement LEIT C" (Neubauer; Münster, Germany). After curing of the cement a two-fold, four-minute gold coating was applied in a "Emtech K550" (Emtech; Mannheim, Germany) DC sputtering system, each with 25 mA. A "Digital Scanning Microscope 940" (Zeiss; München, Germany) was used to accommodate the scanning electron microscope (SEM) images with an acceleration voltage of 5 kV.

In addition, SEM and EDX investigations were carried out at the Fraunhofer Institute for Silicate Research in Würzburg. An “Auriga 60” SEM (Zeiss; München, Germany) was used for recording high resolution images. The samples were thinly coated with carbon and platinum before they were scanned with 3 kV acceleration voltage. Energy dispersive X-ray spectroscopy (EDX) measurements of characteristic sample areas were performed within the “Auriga 60” SEM using an “Apollo XL SDD” detector. The EDX spectra were captured with 5 kV acceleration voltage at a resolution of 133 eV.

3.5.3 Mechanical Testing

The mechanical testing measurements were carried out in PBS at 25 °C using a "Eletroforce 3220" (Bose GmbH, Friedrichsdorf, Germany) with "Wintest 4.1" software. The scaffolds were tested in elastic response inside a custom build confined compression setup (**Chapter 4.6.1.1**) coupled to a 2.45 N load cell.
Cylindrical chondral, subchondral, osteochondral, inner meniscus and outer meniscus scaffolds were tested with an 8 mm diameter custom confined compression setup, while bone scaffolds with isotropic pores, anisotropic pores and isotropic pores with chondroitin sulphate were tested inside a 4 mm diameter setup. All measurements were performed with 5 samples for each scaffold type within a deformation interval of 10 % of the initial scaffold height, executing the following deformation protocols:

- Linear compression with 0.15 mm/sec
- Cyclic compression with physiological frequencies of 0.2 Hz and 2 Hz and a high frequency of 20 Hz; n= 5
- Instantaneous compression with a square function (0.2 Hz, n=3).

The apparent elastic modulus, the dissipation factor and the relaxation time were determined (**Chapter 4.6.1.2**). Measurement inaccuracies were determined by error propagation.

3.5.4 Micro Computer Tomography (µ-CT)

µ-CT-scans of freeze dried osteochondral scaffolds were performed[§] at the "SKZ Technology Centre" Würzburg. Prior to scanning, a ca 5 mm^3 cuboid sample was fixated by cyanoacrylate glue to a polyethylene sample rack. A "CT-Workstation exaCT S60" (Wenzel Volumetrik; Balingen, Germany) was used to capture and process the data. 360 ° CT- scans were recorded with a voxel size of ca. 7 µm.

[§] µ-CT scans were carried out by Mr. M. Eng. Sebastian Horlemann; SKZ Technology Centre Würzburg

3.5.5 Degradation Study

Osteochondral scaffolds (chondral, subchondral and osteochondral), meniscus scaffolds (inner meniscus, outer meniscus and combined meniscus scaffolds) and bone scaffolds (anisotropic, isotropic and isotropic with chondroitin sulphate) were subjected to lixiviation in PBS (137 mmol/l NaCl, 2.7 mmol/l KCl, 7 mmol/l Na_2HPO_4, 1.5 mmol/l KH_2PO_4) containing 3 mmol/l sodium azide. The degradation behaviour was monitored for 30 days at 37 °C and shaking with 25 rpm.

For osteochondral and meniscus scaffolds, the degradation was carried out with 6 cylindrical scaffolds of each type (8 mm diameter; 3 mm height) in 24 well plates, with 2 ml buffer per scaffold being exchanged every two days. In case of the bone scaffolds, 5 cylindrical scaffolds of each type (4 mm diameter; 6 mm height) were lixiviated in 96 well plates, where 0.5 ml buffer was exchanged in a two day interval. The initial dry weight, the wet weight and the drained weight of the gamma sterilized scaffolds were used to determine mass loss, free water content and equilibrium water content. Associated errors are represented by the respective standard deviations. The scaffolds were drained by placing each side for 4 seconds on tissue paper.

The obtained data was processed, to calculate residual mass (m/mo), equilibrium water content (EWC) and free water content (FWC). Although the degradation behaviour is not to be expected to proceed strictly linear, a linear fit was performed on the datasets to allow an approximated statement of the daily changes. Therefore, the software "Origin Pro 8.5.1 G" (OriginLab Corporation; Northampton, Massachusetts, USA) was used whereby the displayed errors represent the standard error of the linear fit.

3.5.6 Fourier Transform - Infrared Spectroscopy (FT-IR)

FT-IR measurements were performed with a “NICOLET iS10” (Thermo Fischer Scientific; Waltham, Massachusetts, USA) spectrometer. Freeze dried samples were measured within an interval between 500 cm^{-1} and 4000 cm^{-1} in triplicate, each with 32 scans at a resolution of 0.5 cm^{-1}. The determination of the maximal peak positions was carried out by using the software “OMNIC 8.2” (Thermo Fischer Scientific; Waltham, Massachusetts, USA). Hereby, the measuring inaccuracies were displayed as standard deviation.

3.5.7 Rheological Measurements

To investigate the viscosity of different precursors as an approximation for the initial cooling during the cryostructuring, rheological measurements were carried out with a temperature sweep. A “MCR301” rheometer (Anton Paar; Graz, Austria) was mounted with a “PP25-SN18294” measuring system against a circular plate with 25 mm diameter. The temperature was sweeped with a continuous ramp of 2 K/min between 20 °C and 0 °C. A precursor volume of ca. 490 µl was measured within a gap of 1 mm under 0.1 rpm. Temperature and viscosity were displayed by the software “RHEOPLUS/32 V3.40” (Anton Paar; Graz, Austria).

3.5.8 Electrostatic Spinning of Polymeric Solutions

In order to realize a fibre alignment parallel to the scaffold surface, electrostatic spinning of polymer solutions was applied. A spinning solution was prepared by dissolving 72.8 mg poly (D,L-lactic-co-glycolic acid) (PLGA) in a mixture of 225 µl acetone, 25 µl dimethyl sulfoxide (DMSO) and 5 µl of a tri-fluor acetic acid/water mixture (9 % TFA). The solution was filled into a 1 ml syringe which was mounted to an “AL-1000” syringe pump (World Precision Instruments; Sarasota, Florida, USA), operating at 0.5 ml/h. A voltage of 13 kV was applied between the blunt needle (0.4 mm diameter, 25 mm length) and the ground target which was positioned approximately in 17 cm distance to the needle tip. The scaffold was fixed on an aluminium foil enveloped petri dish cover by an electrical clamp. For the generation of the high voltage, the output of a “PS-2403D” laboratory power supply (Voltcraft; Wollerau, Switzerland) was set up by a custom build 25 kV transformer.

3.5.9 BMP-2 Release Study

To perform a cytokine release study with the bone scaffolds described in **Chapter 4.3**, the optimal rehydration volume of the scaffolds was determined to 60 µl. Using a stock solution containing 83,3 ng/µl rh-BMP-2 (recombinant human bone morphogenetic protein 2), each freeze dried scaffold was soaked with the objective to be loaded with 5 µg of BMP-2. For this task, a progressive loading procedure was elaborated:

The gamma radiation sterilised scaffolds are placed inside the wells of a 96 well plate, where 60 µl of the BMP stock solution were pipetted on each scaffold. Afterwards, the well plate was placed on an orbital shaker for 30 minutes of orbital shaking with 150 rpm. A manual compression of the lateral surface of each scaffold was performed with a spatula by exerting 0.7 N for 1 sec. The 96 well plate was transferred inside a desiccator, of ca. 2 l inner volume, coupled to a vacuum pump with a performance of 2 mbar and evacuated for 10 min using a "KNF Laboport" vacuum pump (Neuberger; Freiburg, Germany). After keeping the pump running for 1 min, the scaffolds were left to stay evacuated for 9 min with the pump switched off; the pump was shut off to avoid losing too much liquid by evaporation. In order to achieve a good loading result, no drying-agents should be present in the desiccator.

After loading, the scaffolds were immediately transferred into "Protein LoBind" sealable vials (Eppendorf; Hamburg, Germany) to perform the BMP-2 release study: The BMP-2 loaded scaffolds were subjected to lixiviation for 28 days in sterile PBS solution (137 mmol/l NaCl, 2.7 mmol/l KCl, 7 mmol/l $Na_2HPO_4 \cdot 2H_2O$, 1.5 mmol/l KH_2PO_4). Five scaffolds of each kind (anisotropic, isotropic and isotropic chondroitin sulphate containing bone scaffolds) were subjected to 0.5 ml PBS solution for each day until the next measuring point. The lixiviation was carried out at 37°C under shaking with 25 rpm. The supernatant was captured and replaced on the days 1, 2, 3, 4, 5, 7, 9, 11, 14, 17, 21 and 28.

The release was investigated[**] within 28 days using an enzyme linked immunosorbent assay (ELISA). Therefore, a "RayBio Human BMP-2 ELISA Kit" (Ray Biotech; Norcross, Georgia, USA) was used to measure the exchanged buffer samples. In brief, an antibody specific for human BMP-2 was used to immobilize the BMP-2 of standards and samples. With repetitive washing, a biotinylated anti-human BMP-2 antibody, a HRP-conjugated streptavidin and a TMB substrate solution are added subsequently to develop a colouring (measured at 450 nm) in proportion to the amount of bound BMP-2. The sample read out was conferred with the standards read out to yield cytokine concentrations. A standard deviation between the measured values was used as error.

[**] The ELISA test and read out was performed by Ms. Maria Aniolek, technical assistant at FMZ.

Each sample was measured in duplicate. With respect to the amount and reliability of steps involved, an ELISA Kit accuracy in the lower pg/ml range was doubtful. Therefore an accuracy level of 130 pg/ml was introduced, since the ELISA read out for duplicate measurements of the same samples returned zero or another numerical value below this level. Consequently only values above the introduced accuracy level are suitable for a closer interpretation of the results. Additionally, the BMP-2 retention was cumulatively displayed. Since the standard deviations of the ELISA measurements alone were too small to describe the inaccuracies involved in the entire process of loading and release, a 0.1 % tolerance of the total BMP-2 content was additionally considered for the initial amount of cytokine that was loaded to the scaffolds. Consequently the displayed measuring accuracies of the BMP-2 retention are represented cumulatively by the loading tolerance and standard deviations. (**Figure 4.26**)

3.5.10 X-Ray Diffraction (XRD)

With an X-ray Diffractometer "D5005" (Siemens; Karlsruhe, Germany) 2-theta scans of the samples were recorded in Bragg-Brentano geometry. Hereby, an acceleration voltage of 40 kV and an electron current of 30 mA were applied. An X-ray tube of the type "FK60-04x12" with copper anode served as radiation source. The sets of apertures and X-ray wavelengths used are listed in **Chapter 9 Table 1**.

The XRD diffractograms were recorded with the software “Diffracplus XRD Commander 2.4.1” at a resolution of 0.02 °. Since calcium phosphates show a high density of characteristic reflections especially in the a 2Θ angle range of 20 ° to 40 °, this angular range was used for the investigations. The data processing was performed using the software "EVA 10.0.1.0". Crystalline components were identified by the JCPDS substance database[263].

4 Results and Discussion

Parts of the following chapter have been originally written by the author and are published analogously in other text documents. In particular, fractions of the **Chapters 4.1, 4.4** and **4.5** are disclosed by the Patents EP 2788171 A2[27] and US 2014350331 A1[264].

4.1 Process Development - Directional Solidification

Despite intensive research, the current available solutions still do not allow the production of a physical or (bio) chemical hierarchical, monolithic structure with zones of different material compositions and continuous anisotropic pore structures. It is a well-known problem that subsequently joined materials often show a material failure at the contact points of different components[265]. This is of particular significance for materials with porosities in the micron range. Here, the porosities are mostly present in random distribution and therefore do not fit each other when individual components are assembled together. If the entire material is considered, this causes a decrease of the overall penetrability, which may affect the functionality significantly.

This problem is solved by the method according to the invention described in EP 2788171 A2[27], since multi layered but monolithic materials featuring continuous pore structures can be obtained: In the newly developed proceeding multiple flowable precursors are solidified inside a cryostructuring device; after ice crystal removal they are cross linked to a monolithic material. The precursors, which are arranged between temperature-controlled bodies and isolating bodies that may represent partial the desired shape of the material negatively, are directionally solidified entirely or partially. Various mutually different precursors can be combined to form a monolith. These precursors may consist out of solutions, dispersions, suspensions, gels or polymeric melts, which include sublimable additives. After cryo-structuring, the solidified additives are removed by sublimation under suitable pressure and temperature conditions. Thereby, a hierarchically build material is generated, which is entirely or partially penetrated by anisotropic pores.

A further consolidation of the resulting material can be performed by cross linking, sintering or infiltration with other materials or mixtures of materials. **Figure 4.1** is illustrating the main production steps of an osteochondral scaffold, which represents a more concrete example of the developed platform proceeding. A directional solidification of different precursors (e.g. collagen “solutions”), which are layered inside a cryostructuring device is leading to a controlled growth of aligned ice crystals. While the ice crystals penetrate the individual solution layers perpendicular to the planes of layering they push particulate constituents aside, forming channels of ice. The ice inside the cannels is removed by lyophilisation, leaving behind a continuous pore structure.

If a superficial layer with fibre orientation parallel to the surface is desired, polymer fibres may be deposited by electrostatic spinning (**Chapter 4.5.4**). In order to consolidate all layers as a monolithic structure, covalent cross linking by using activated carbodiimides is applied. In this cell-compatible "zero-length" cross linking covalent bonds are established between the collagen molecules without the incorporation of other substances or linkers.

After removing chemical residues of the cross linking by washing, the scaffold is freeze dried and subjected to gamma sterilization. Finally, the scaffold may be used for cell seeding or directly as off the shelf product for surgical implantation.

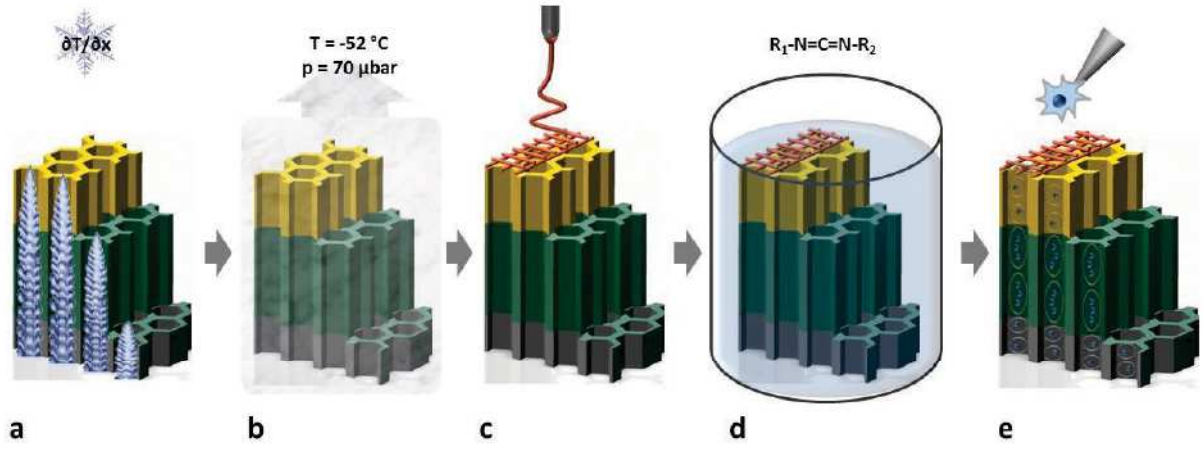

Figure 4.1: Schematic illustration of the process steps involved in the developed cryostructuring process for an osteochondral scaffold. a) Directional solidification, b) lyophilisation, optional: c) electrospinning of polymer fibres on the scaffold surface, d) covalent cross linking of multi layered precursors, e) cell seeding or implantation.

4.1.1 Development and Assembly of an Adjustable Cryostructuring Device

The development of a tuneable device, which was especially designed for the directional solidification of aqueous precursors, represented a crucial part for the practical realization of the process. Without such a device the precise control over ice crystal growth and thus, the porosity of the scaffolds would be impossible.

The generation of a controllable temperature gradient in a thermal well isolated environment represented the core requirement of the device, which lead together with a very broad application spectrum to the respective design decisions. In contrast to established freezing devices for directional solidification[14,23,29,182,183,242,246,249,253,266], were liquid nitrogen is used to generate a low temperature level, the developed device is based on electrical temperature control by usage of Peltier elements (PEs). Based on preliminary studies of the authors diploma thesis[26], the preferable temperature parameters for the creation of cell carrier matrices are to be reached more practically by the chosen method than by the established ones. Conventionally, one liquid nitrogen cooled metal body is heated up by a current-carrying wiring, from a basis temperature (towards – 273 °C) to the desired level[29,183,242,249,266]. In the developed device, two temperature-controllable bodies are thermally connected to an intermediate temperature reservoir (tempered between 5°C and -35 °C). The temperature-controllable bodies are heated or cooled to the necessary temperature levels and thus require a smaller temperature difference to be modulated.
The Adjustable Cryostructuring Device (ACD) was designed as a variable kit so that modifications, extensions or improvements can be made efficiently regarding resources of time, effort and costs. After several optimizations, it was possible to use the ACD for the preparation of different sample types with spatially resolved compositions and adjustable sample dimensions, pore sizes and orientations.

The basic operation principle of the ACD is depicted in **Figure 4.2** a): two Peltier elements (PE) are arranged opposing each other. In between them, flowable precursor materials may be arranged in a sample volume. A powerful thermal isolation around the sample volume is required for the generation of a directional external temperature gradient. The PEs are tempered at different temperature levels by electrical control, so that a directional temperature gradient is generated.

The absolute value of the external temperature gradient is dependent on temperature difference and distance of the respective PEs. If, for instance, the upper PE is brought to a higher temperature level than the lower one, the temperature gradient is build up from the upper to the downer PE. A front of solidification may now expand antiparallel to the direction of heat flow. Depending on the composition of the precursors and the strength of the heat flow, the solidification may manifest in an equiaxial, dendritic or columnar growth of solidified solvent.

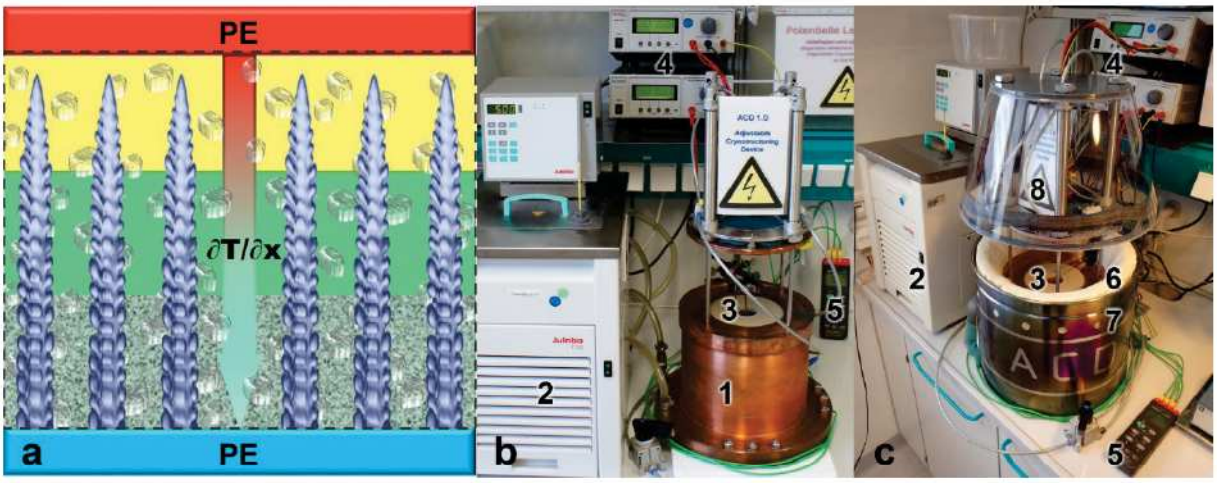

Figure 4.2: Operation principle and stages of development of the Adjustable Cryostructuring Device (ACD). a) A directional temperature gradient (∂T/∂x) is established between two differently tempered Peltier elements (red PE – higher temperature; blue PE - lower temperature). Ice crystals grow antiparallel to the temperature gradient through precursors (grey, green, yellow) inside the sample volume. b) Intermediate development stage of the ACD depicting the heat exchanging elements which are surrounded by an isolating housing in the final development stage (c).

An intermediate development stage of the ACD is documented in **Figure 4.2** b) revealing its major components: A stovepipe hat shaped copper unit (outer assembly group (OAG); **Figure 4.2** b) number 1) is responsible for the overall heat exchange. The OAG is connected to a "Julabo F32" cryostat (Julabo; Seelbach, Germany) (**Figure 4.2** b), c) number 2) by a piping system. The combination of both devices enables the generation of an intermediate cooling level while removing the heat that is generated inside the inner assembly group (IAG; **Figure 4.2** b), c) number 3), which is located inside the OAG. Two Programmable Power Supplies "PSP 12010" (Voltcraft; Wollerau Switzerland) (**Figure 4.2** b), c) number 4) enable the control of the PEs within the IAG.

To ensure a good accessibility for modifications of the IAG and a convenient sample production, the top of the OAG may be lifted up by four pneumatic driven cylinders “DNSU-20-160-PPS” (Festo; Esslingen; Germany). The temperatures of the PEs and the sample precursors can be monitored and recorded by temperature sensors, connected to a “K204 Datalogger” (Voltcraft; Wollerau Switzerland; **Figure 4.2** b), c) number 5).
In order to increase the performance and to avoid the unwanted deposition of condensed water, the ACD was further upgraded until its final configuration. The OAG was isolated by two custom polyurethane foam shells (**Figure 4.2** c) number 6) fit into an outer stainless steel cylinder (**Figure 4.2** c) number 7). The piping system between cryostat and OAG was isolated by tubular polyethylene foam isolations. To shield off air exchange and thus condensed water to the bare parts of the OAG, the top of the OAG and the pneumatic cylinders were augmented by an isolation sealed hood (**Figure 4.2** c) number 8) out of polyethylene and acrylic glass. The top, and the bottom part, as well as the outer housing of the OAG are grounded to the respective zero conductors of the DC power supplies. The current supply of the PEs and the temperature sensors run through an isolation sealed horizontal tunnel at the back of the OAG (**Figure 4.3** a), b)), which also allows an endoscopic monitoring of the cryostructuring process itself.

After multiple years of development, four major IAG configurations of the ACD were ready for use (**Figure 4.3** c) – f)) so that various different sample types and dimensions are accessible. For these configurations further sub-configurations, including diverse sample shaping moulds have been created. This facilitates the production of smaller as well as large samples, with one single device. Thereby, cell carrier matrices like a partial rat femur and a complete bovine meniscus may be produced.
An itemized plan of the ACD’s central components and their assemblage is depicted in **Figure 4.3**: A combination of the precisely fitting IAG and OAG is shown in **Figure 4.3** a) as a sectional image. The cupreous OAG comprises the IAG including the sample volume (red) in the centre, which is investigable through a horizontal service tunnel. Inside this tunnel run the current supply cables of the PEs as well as three temperature sensors. One sensor monitors the sample temperature, while two sensors record the PE surfaces that are facing the sample (orange sub channels).

The three central parts of the OAG are shown in **Figure 4.3** b). The main heat exchanger unit A1 is traversed by the cooling agent of the cryostat in order to be kept on an intermediate temperature. On top of A1 sits a ring shaped heat exchanger unit A2, which contains the IAG and is gaped to provide the service tunnel. The four (not depicted) pneumatic cylinders are screwed in here, to lift or close the top heat exchanger unit A3 for precursor fillings into the sample volume.

An exploded view of IAG main configurations can be found in **Figure 4.3** c) - f). Individual components of the IAG are representatively described for configuration f): The sample volume is located in the centre of the isolation unit I1 and is in thermal contact with the temperature-controlled bodies W1 and W2, mounted above and below the sample volume. Those parts are fit in the isolation units I1 and I2 and are thermally coupled to the PEs P1 and P2, which in turn are fixed by the isolation units I3 and I4. Temperature sensors run along channels in I2 and eventually W2 while the current wires of the PEs run inside of I4. While the isolation units are all made out of polyether ether ketone (PEEK), the temperature-controlled bodies are fabricated out of aluminium. For reasons of clarity the sample volume S is only depicted in **Figure 4.3** c).

Petri dishes may be placed inside the sample volume before the precursors are arranged inside to ensure a hygienic sample production with a low contaminant exposure. To enable the production of differently sized samples, sample volumes of 344 cm^3 (c), 14 cm^3 (d), 10 cm^3 (e) and 6 cm^3 (f) can be addressed with the IAGs depicted in **Figure 4.3**. A hardware based preset of the used temperature gradients may be selected by choosing the appropriate distance between the temperature-controllable bodies from 14 mm (**Figure 4.3** c), d)), 8 mm (**Figure 4.3** e)) and 5 mm (**Figure 4.3** f)).

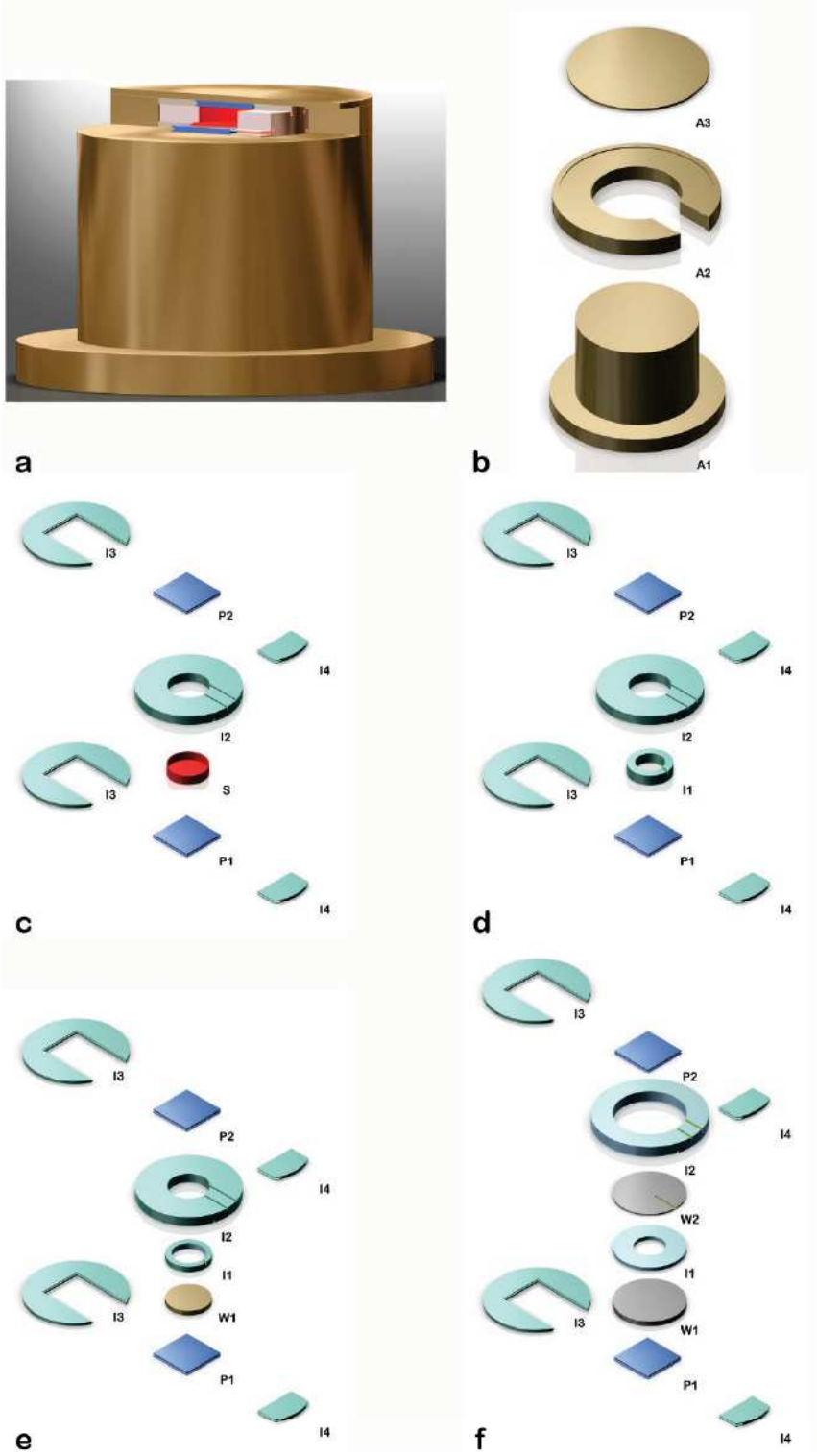

Figure 4.3: CAD images of Adjustable Cryostructuring Device with different configurations of the inner assembly group. a) Sectional image of combined central parts of inner and outer assembly group. The precisely fitting groups comprise the sample volume which is investigable through a horizontal service tunnel. b) Central parts of outer assembly group. Exploded view of main configurations of the inner assembly group with different maximum sample volumes: c) 344 cm^3, d) 14 cm^3, e) 10 cm^3 f) 6 cm^3. Further components of the device are not depicted.

During development, the OAG of the ACD was upgraded multiple times by improvement of isolation and variation of the cooling agent. The variation of the cooling agent had a considerable impact on the achievable (intermediate) temperatures of the OAG, being responsible for heat exchange. While temperatures of only 1 °C were practicable using pure water, the use of a 1:1 mixture of ethylene glycol and water enabled temperatures of -20 °C. By using “Thermal HY Baysilone-Oel M3” (Julabo; Seelbach, Germany) intermediate temperatures down to -27 °C could be established. Isolation optimizations of cooling agent piping systems and OAG were carried out in parallel to the change of cooling agents. A significant performance improvement of the ACDs accessible external temperature gradient from (1.3 ± 0.1) K/mm up to (9.0 ± 0.1) K/mm was achieved, which enabled the directional solidification of (collagenous) precursors in a highly controlled manner.

4.1.2 Process Evaluation by Fabrication of Cryostructured Alginate Scaffolds

The cryostructuring process of alginate solutions was analysed regarding temperature gradient, cooling rate and solidification rate. The pore sizes of the resulting scaffolds were determined for the top, the bottom and the cross section. Alginate was chosen as scaffold material due to a better availability and a lower economic significance than collagen. In order to get reproducible results efficiently, a temperature gradient working range where the ACD does not require thermal regeneration was chosen.

4.1.2.1 Scaffold Preparation

For the systematic investigation of cryostructured scaffolds, an alginate solution in deionized water was prepared by dissolution of 5.50 wt% Protanal LF 10/60, a low viscosity alginate with a mean G/M ratio of 70 % and mean molecular weight of 180 kDa (FMC Biopolymer; Drammen, Norway). In order to avoid the formation of alginate compound colloids, the alginate was added gradually under vortex appearance. 2.5 µg/ml Fungizone Amphotericin B (Invitrogen Life Technologies, Karlsruhe, Germany) was added as a precaution to prevent an eventual colonization by mould fungus.

The ACD was set up with the IAG depicted in **Figure 4.3** e) and the cryostat cooled the heat exchanging unit of the ACD to a temperature of -25 °C. A polished petri dish cover, with an inner diameter of 37 mm, (BioOne, Greiner, Germany) was placed in the centre of the cryostructuring unit and the PEs were supplemented with the current necessary, to generate the respective desired temperature gradients. When the cryostructuring unit of the ACD was near thermal equilibrium, 3 ml of the alginate solution were injected into the petri dish cover. The solution was frozen under the influence of a unidirectional outer temperature gradient. The temperature curves of the PEs and the solidifying solution were recorded.

After solidification, the specimens were transferred to a lyophilizator, where the sublimation of the frozen solvent was carried out for 18 h, at -52 °C and 70 µbar. The resulting porous alginate structure was further ionically crosslinked. Therefore, the structure was placed in a pressure vessel (**Figure 4.17**), which was evacuated until reaching an operating pressure of 100 mbar. 50 µl of 1 mol/l $CaCl_2$ solution was added per mg of specimen; 45 seconds after the infiltration of the material, the pressure vessel was vented. After 24 h reaction time, the scaffold was washed three times in distilled water.

4.1.2.2 Temperature curve evaluation

Temperature curves were recorded for scaffolds that were produced under varying external temperature gradients $\vec{\nabla} T$. The external temperature gradient was calculated according to:

$$\vec{\nabla} T = \frac{\partial T}{\partial \vec{x}} \cong \frac{|T_{pd} - T_{pu}|}{\vec{x}_u - \vec{x}_d}, \qquad (8)$$

with T_{pu} and T_{pd} being the temperatures, $\vec{x}_u$ and $\vec{x}_d$ being the position vectors of the upper and the lower tempered bodies (e.g. PEs), respectively. For the further evaluation, the external temperature gradient ratio perpendicular to the surface of the PEs was considered. A gradient range from 0.5 K/mm to 4.5 K/mm was investigated in steps of 0.5 K/mm; within each step the cryostructuring of five scaffolds was analysed.

A cooling rate, which is representing the cooling performance of the device, and a solidification rate, which stands for the temporal progression of solidification inside the precursors was determined. In order to generate discrete values for cooling rate and solidification rate a linear interpolation was performed between $t(T_0)$, the time when the sample reached a temperature of 0° C, and $t(T_*)$, the time when complete solidification was reached. The point of complete solidification was set according to the starting point of a 30 second time interval when the temperature of the frozen sample did not change any further (**Figure 4.4**). The linear interpolated solidification rate v_s and the linear interpolated cooling rate v_c were calculated according to the following formulas:

$$v_s = \frac{h*1{,}09}{t(T_*)-t(T_0)}\ ; \qquad v_c = \frac{T_*-T_0}{t(T_*)-t(T_0)}\ . \qquad (9;\ 10)$$

With h being the height of the freeze dried scaffold, considering a solidification conditioned, sample volume expansion of approximately 9 % at a confined sample radius.

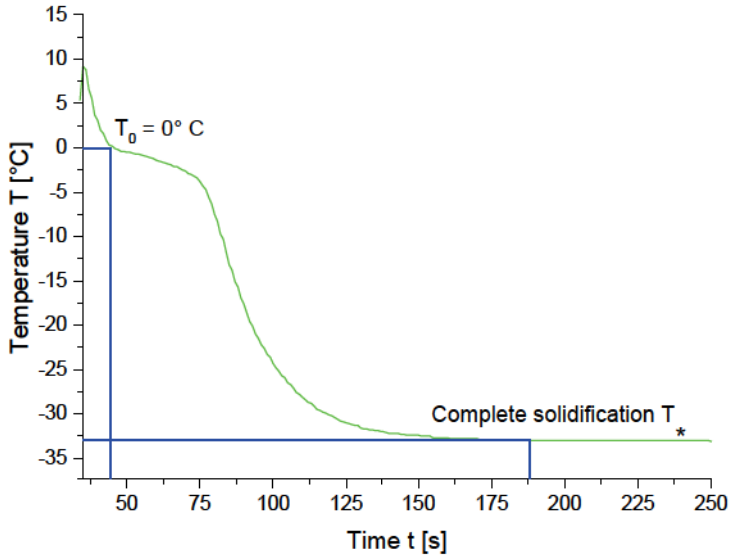

Figure 4.4: Exemplary temperature curve for $\vec{\nabla} T$ = 4.5 K/mm. Cooling rate and solidification rate have been determined by linear interpolation between 0° C (T_0) and the temperature of complete solidification (T_*).

The further temperature curve evaluation was performed by calculating the arithmetic average, for the linear interpolated cooling rate (**Figure 4.5** a)) and the corresponding linear interpolated solidification rate (**Figure 4.5** b)), out of five cryostructured scaffolds per temperature gradient step of 0.5 K/mm. The standard deviations of mean pore diameters and temperature gradients are displayed by error bars.

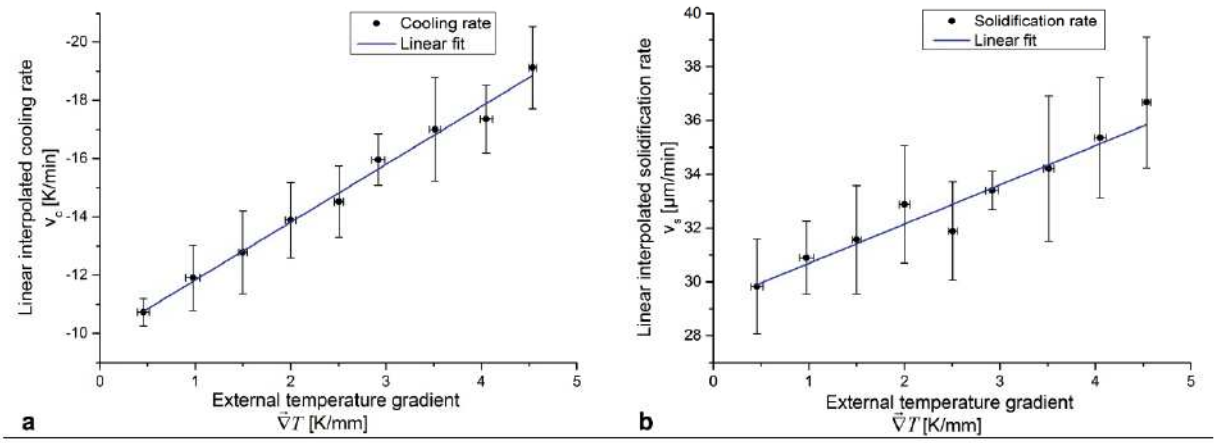

Figure 4.5: Linear interpolation of a) cooling rate and b) resulting solidification rate in dependency of the applied external temperature gradient.

After Fourier's law, the heat current density is directly proportional to the present temperature gradient. In case of the cooling rate, which is in turn directly proportional to heat current density, a linear dependency from the temperature gradient is resulting. On the other hand the linear temperature decrease during cryostructuring is obviously superimposed by the heat energy that is released due to the crystallization enthalpy (**Figure 4.4**). In order to determine a mean rate of solidification a linear interpolation was performed which led naturally to a linear dependency form the temperature gradient. Out of the slope of the linear fit in **Figure 4.5** a) properties of the ACD can be determined for the used experimental setup: An external temperature gradient increase of 1 K/mm is resulting in a cooling rate elevation of (- 1.900 ± 0.059) K/min.

Since the velocity of the ice front is an crucial parameter which determines the properties of the growing ice crystals, the dependency of the solidification rate from the external temperature gradient is of special interest. From considering the slope of the linear fit in **Figure 4.5** b) it can be seen that, for the current parameters, the linear interpolated solidification rate will increase about (1.46 ± 0.14) µm/min for each external temperature gradient increment of 1 K/mm.

4.1.2.3 Pore analysis

Image data processing of SEM images followed by statistical analysis was used to determine the pore sizes of scaffolds that were produced under varying external temperature gradients. Again, a gradient range from 0.5 K/mm to 4.5 K/mm was investigated in steps of 0.5 K/mm. Therefore, the central region was cut out of three scaffolds per step, and subjected to gold coating inside a gold sputtering unit with 25 mA sputter current. For each scaffold, SEM images of the top, the cross section and the bottom were captured with a Scanning Electron Microscope at 5 kV acceleration voltage (**Figure 4.6** a), b) and c)).
These pictures were analysed by the use of the software "ImageJ 1.43m". After threshold adjustment, pore masks (**Figure 4.6** d), e) and f)) were generated, which were used to determine area and diameter of each single pore. Because of irregularities of the gold coating in combination with disparities in the level of analogue photographic development, the threshold adjustments had to be carried out individually. Since the pores showed, perpendicular to the ice crystal growth direction an elliptic appearance, a short pore diameter (d_x) and long pore diameter (d_y) was determined (**Figure 4.9** a)). In average, over 600 Pores were analysed per image.

This data was further processed with the software "Origin Pro 8.5.1 G". Assuming, that higher pore areas are corresponding to higher pore diameters, both pore diameters and the pore areas were ordered by absolute value. Each pore area was normalized to the total pore area of the image and summed up iterative. Thus, a normalized pore area fraction was plotted in dependency of the short pore diameter (d_x) and long pore diameter (d_y), respectively. At a normalized pore area fraction of 0.5, a mean value of the pore diameters d_x and d_y was gained for each image. (**Figure 4.7**)

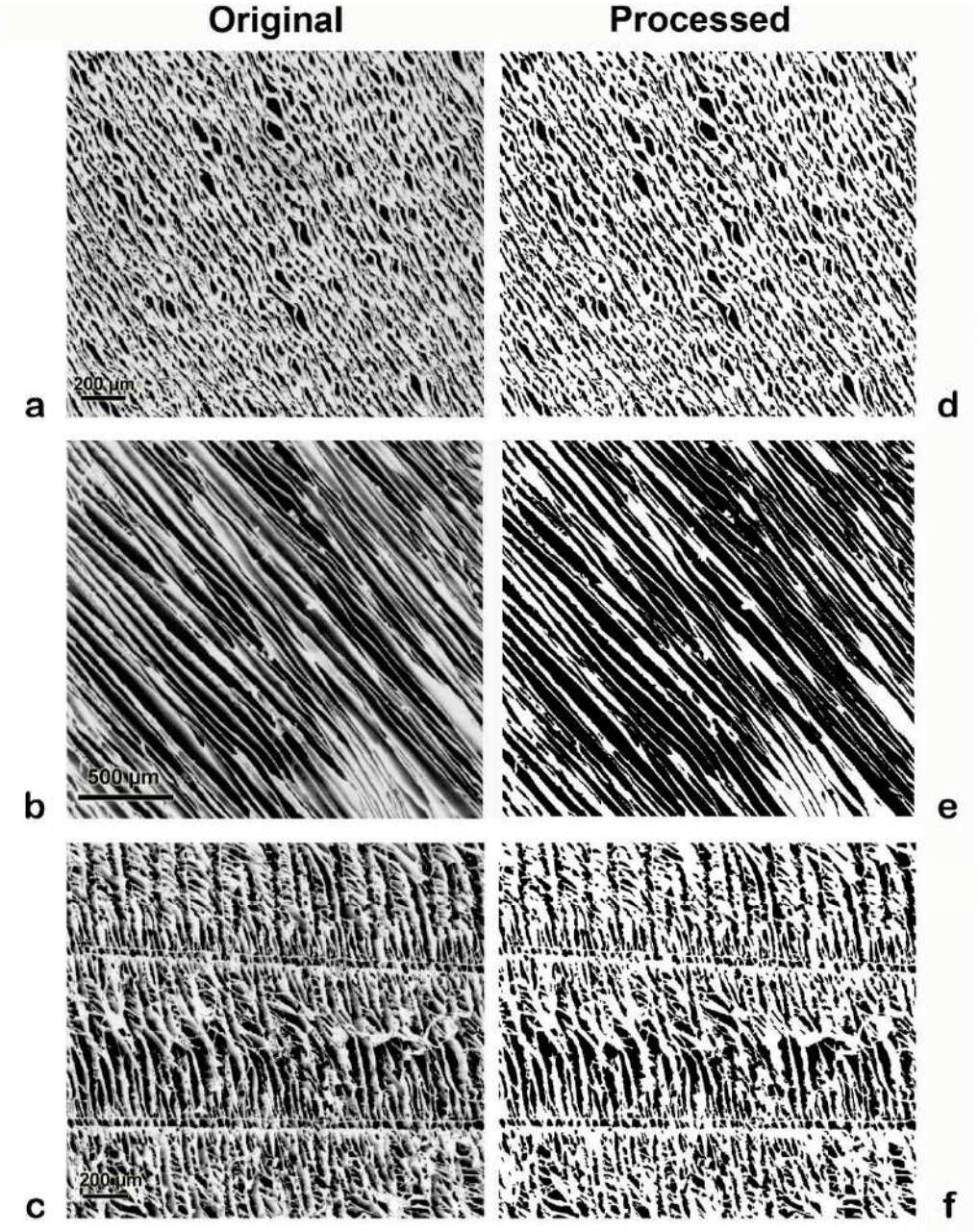

Figure 4.6: Image data processing. SEM images of the scaffolds (original) were analysed regarding their pore areas and diameters by threshold adjustment resulting in pore masks (processed). Exemplary results for a) top, b) cross section and c) bottom of the central scaffold region. The evaluation was carried out as described on page 68.

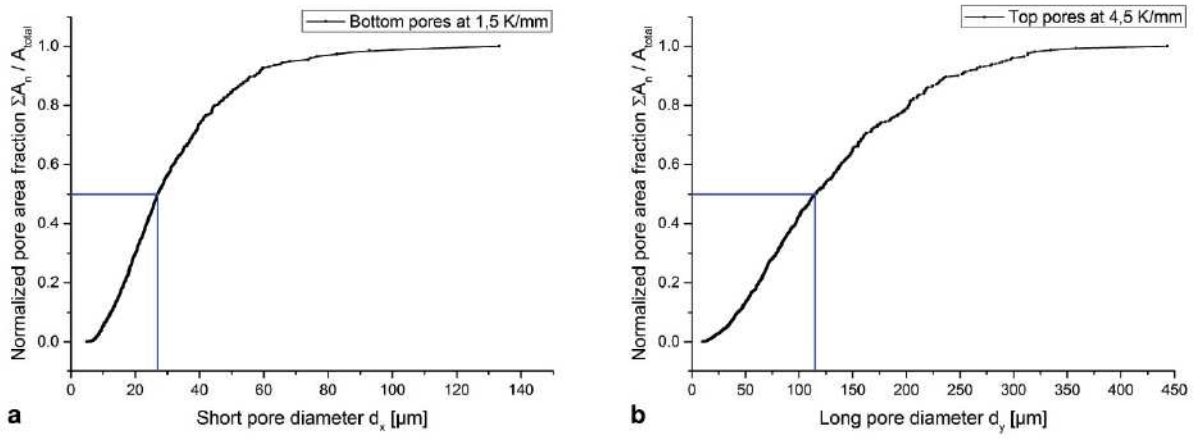

Figure 4.7: Exemplary determination of mean pore diameters by normalized pore area fraction. a) Short pore diameter of bottom pores, b) long pore diameter of top pores. For an illustration of the spatial orientation of short and long pore diameter see **Figure 4.9** a).

Exemplary SEM images of the scaffold pore structures are shown in **Figure 4.8**. Corresponding to the external temperature gradients ($\vec{\nabla} T$) which were applied during cryostructuring, the respective pore structures can be observed for the top, the cross section and the bottom pores.

On the top surface of the scaffolds, a few micrometres thin sheeting is open-worked by elliptic to spindle-shaped pores. While these pores show an irregular spatial orientation and stronger differing pore areas at lower values of $\vec{\nabla} T$, the spatial orientation as well as the pore areas are getting more uniform and the pore sizes are decreasing with higher values of $\vec{\nabla} T$.

In the cross sections, anisotropic spindle- to tube-shaped pores are stretching through the entire height of the scaffolds. Smaller temperature gradients are leading to a rather confused alignment of single domains where the pores run more or less parallel to each other in comparatively flatter angles to the scaffold surface. With increasing temperature gradients the pore orientation is moving until a perpendicular orientation to the scaffold surface, resulting in a highly ordered pore structure for high $\vec{\nabla} T$.

At the bottom of the scaffolds, a fine feather-like pore structure is established which is resulting from the initial crystallization processes at the beginning of cryostructuring. Inside the scaffold this structure is expanding only for a few micrometres before merging into the cross section pores. The pore size at the bottom of the scaffolds is increasing with incremental temperature gradients.

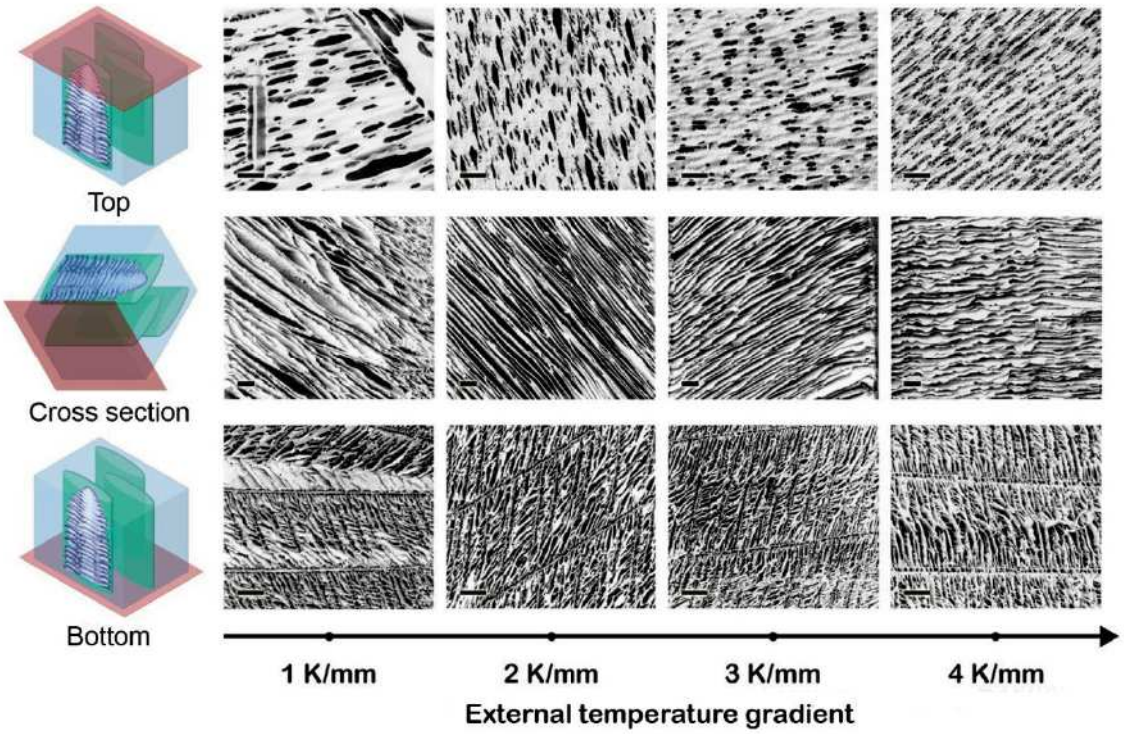

Figure 4.8: SEM images of exemplary pore structures for the top, the cross section and the bottom pores in dependency of the external temperature gradient used for their creation. (Scale bars: 200 µm)

After image data processing and evaluation, the arithmetic average of the pore diameters d_x and d_y was calculated for top and bottom images corresponding to the associated temperature gradient step (**Figure 4.7**). In case of the cross section images, only the short pore diameter could be obtained by this evaluation method. Besides preparative challenges, a reliable image data processing for a cross section of the long pore diameter appeared impossible because of the small contrast changes correlating with the comparably low depth of the pore elongation in d_x-direction which is impaired by the dendritic microstructure of the pore wall.

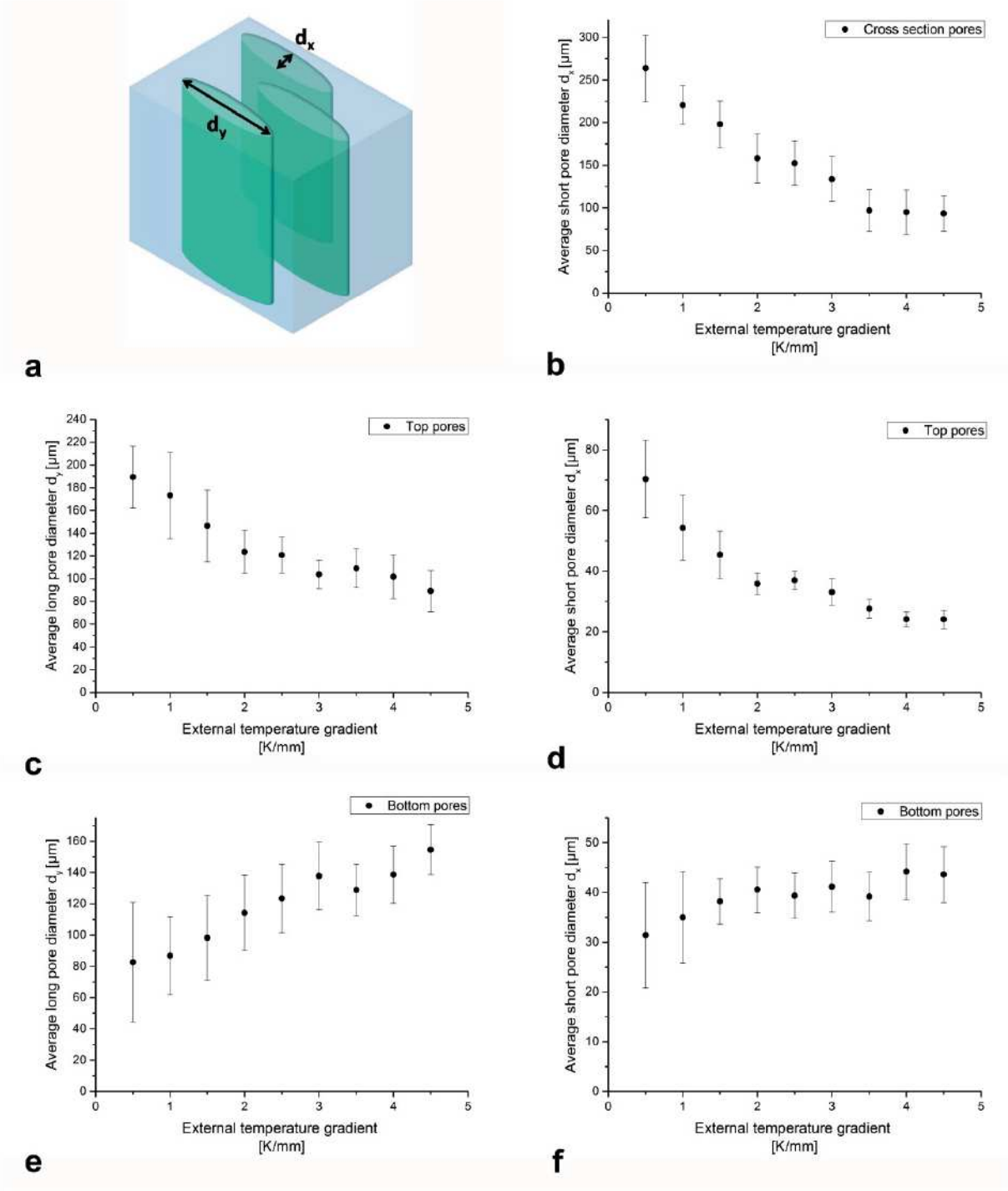

Figure 4.9: a) Schematic image of a porous scaffold showing the orientation of the measured pore diameters (d_x = short pore diameter; d_y = long pore diameter). Average pore diameters of the cross section (b)), top (c), d)) and bottom (e), f)) pores.

Summarized it can be observed that for an increasing external temperature gradient the diameters of top and cross section pores are decreasing while the diameters of bottom pores are increasing. Within the analysed working range, it can be roughly estimated that the final pore diameter decrease is nearly always about 50 %, while the increase is about 200 % of the initial pore diameter, respectively. Since the total pore homogeneity and anisotropy is increased with higher external temperature gradients and a short cross section pore diameter of about 80 µm is to be achieved at higher temperature gradients. Isotropic pore structures may be created by operating at low temperature gradients, while the production of (osteo)chondral scaffolds is best to be performed at elevated temperature gradient levels. For scaffolds with an meniscus microstructure lower external temperature gradients in between the afore mentioned ranges are the appropriate choice.

4.1.3 Optimization of Processing Steps

In order to achieve the material production in the final stages, as demonstrated in **Chapters 4.3, 4.4** and **4.5**, several years of development and optimization were required. Besides the successive augmentation of the ACD also optimization in the processing of precursors was crucial. The control over the freezing regimes inside the ACD enabled the formation of complex scaffold microstructures, like a meniscus mimetic fibre architecture (**Chapter 4.4**). A continuous propagation of anisotropic ice crystals through different layers of precursors, turned out to be a challenging task. Different cross linking methods have been evaluated before the most suitable solution was found.

4.1.3.1 Precursor Preparation

To apply the cryostructuring process in a way to yield an anisotropic pore structure, the precursors must feature a certain level of flowability. For the determination of the optimal concentrations of the respective precursor components, multiple concentration ranges had to be screened. For proof of principle, preliminary scaffolds have been produced by using alginate. Therefore concentrations (w/w) between 0.5 % and 6.0 % dissolved in water were evaluated regarding their cryostructuring potential.

Alginate solution represented a very convenient precursor material for directional solidification, regardless of the concentration used. The fact that the solubility of sodium alginate (Protanal LF 10/60 FT) in water, respectively the saturation level, is increasingly limited above a concentration of 5.0 % turned out to be the only real limitation. Since the mechanical stability of the resulting scaffolds is increasing together with the biopolymer content of the precursors, concentrations between 5.0 % and 5.5 % have been found to yield optimal results. Higher concentrations leaded to inhomogeneities caused by the aggregate formation of unsolved alginate.

As a measure of flowability, the temperature dependent viscosity of a 5.0 % alginate solution was compared to a 5.0 % alginate solution containing 5.0 % brushite. Therefore, rheological measurements during cooling from 20 °C to 0 °C were carried out to approximate the situation in the beginning of the cryostructuring process (**Figure 4.10** a)). Upon the addition of the plate shaped calcium phosphates the viscosity increases for a manifold. Especially at lower temperatures an exponential increase of the systems viscosity can be clearly observed.

To follow a biomimetic approach, collagen I represented the main structural constituent of the precursor materials of the final scaffolds. Collagen I material, derived as described in **Chapter 3.3.1** and dissolved in 0.5 mol/l acetic acid was investigated within a concentration range (w/w) of 0.1 % to 4.5 %. Suitable concentrations of acetic acid for the preparation of collagenous solutions have been already investigated by H. Schoof[252]. The viscos behaviour upon cooling of a 1.0 % collagen solution is depicted in **Figure 4.10** b). Within the investigated range from 20 °C to 0 °C a nearly linear increase can be observed for the progression of the viscosity.
While alginate solutions with concentrations in the range of 5 % still behave honey like regarding the flowability, collagen I solutions of about 1 % already behave like a gel. Although this fact represents important for the practical realisation of experiments, it is not predictable if only the measured viscosities are considered. The directional solidification of collagenous solutions was achievable up to concentrations of 4.0 %. Above this value, only an isotropic solidification was observable.

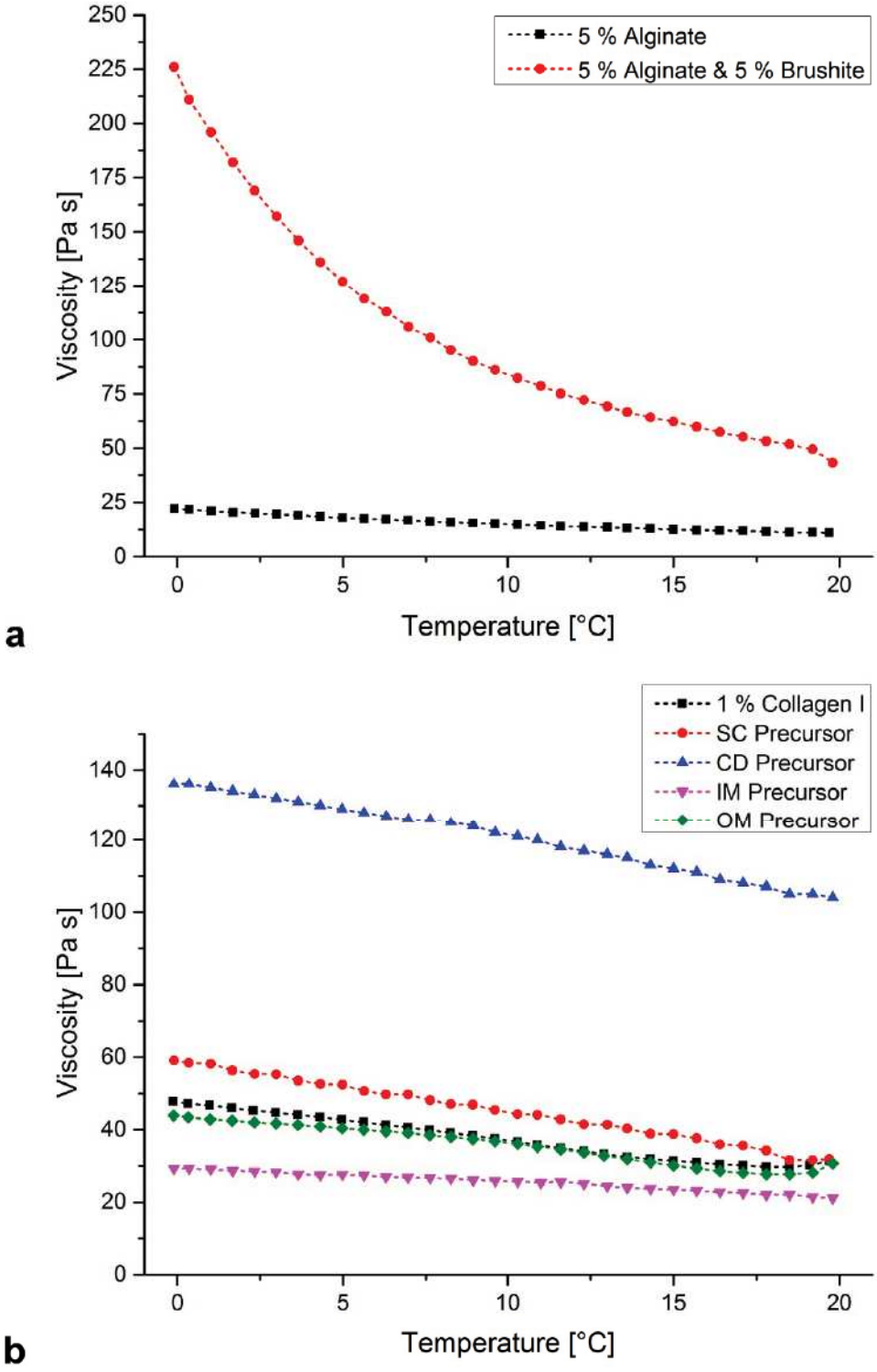

Figure 4.10: Viscosities of precursors. a) Alginate precursors show a significant increase of viscosity upon the addition of calcium phosphates. b) Collagen precursors exhibit varying viscosities according to their respective compositions SC, CD (**Chapter 4.5**) and IM, OM (**Chapter 4.4**).

Besides the collagen I, also collagen II, chondroitin sulphate, hydroxyapatite and brushite were employed for the precursor preparation. In these cases the precursor is not to be titled as solution or gel anymore. The precursor may be rather stated as dispersion, suspension, or slurry. Regarding these further ingredients it is of huge importance to consider if the components are to be seen as inert or active to some degree during precursor preparation. Hereby, the interaction with the collagen I is of main significance. Also the particle/aggregate size of the ingredients is a key feature, since larger particles may lead to significant disturbances during the directional crystal growth.

Calcium phosphates like brushite and hydroxyapatite are to be seen as inert particles, which interfere with the cryostructuring process only marginally within certain concentration limits. Depending on the particle size, the only relevant alteration, of the precursor represents the reduction of the flowability (**Figure 4.10** a)). For calcium phosphate crystals with a particle size below 60 µm, the formation potential of anisotropic crystals upon directional solidification is only slightly decreased if the dry weight of calcium phosphates does not exceed the dry weight of the main structural component.
The use of higher concentrations of inert particles is still possible, but a continuous anisotropic pore structure of the resulting materials is not to be expected anymore. Commonly the establishment of a dense and an isotropic zone will occur before an area where an anisotropic structure might be formed[152]. Structures of this quality maybe formed without a dispersing agent by using ceramic particles up to the fivefold dry weight of the biopolymer.

Collagen II in the used form of ground, purified cartilage particles represents as almost inert regarding the precursor alteration. With a collagen II particle size of 60 µm or lower, the swelling upon rehydration alters the precursor performance only marginally, as long as the dry weight of collagen II does not exceed the 1.5 fold of the dry weight of the collagen I. It is also possible to process anisotropic structured scaffold layers consisting entirely of collagen II (**Figure 4.16**). Therefore, also enzymatically treated collagen II, which could be obtained after pepsin digestion, was used. However, these scaffolds were extremely fragile to handle before cross linking and after the consolidation they still featured only a negligible stability.

Consequently, the used states of collagen II did not contribute sufficient structural integrity to the overall matrix structure. Because it would represent the most biomimetic approach, the fabrication of osteochondral scaffolds which only contain collagen II as structural component within the chondral zones would be highly desirable. Unfortunately, the mechanical requirements for prolonged cell culture or surgical implantation are not matched by the use of the available collagen II alone. Thus, collagen I represented the most suitable biopolymer for the creation of scaffolds that fulfil all the requirements. Additionally, collagen II was supplemented to the scaffolds, close to the maximal amount without disturbing the anisotropic pore formation. This way, the biological key signals of collagen II are still to be expected to affect invading stem cells while the mechanical performance of the scaffolds corresponds to the above mentioned requirements.

In order to mimic the different zonal compositions of the cartilagnious tissues, also GAGs were supplemented. The mutually repulsion of the, in hydrated state, negatively charged sulphate groups of GAGs in native cartilage represents a key component for the mechanical dampening function. This feature might be adequately transferred to the scaffolds by processing GAGs too.

Native meniscus tissue is known to feature different amounts of GAGs in the respective tissue zones. According to the literature, the GAG content, measured as cdw, accounts to 10 % for the inner and less than 1 % for the outer meniscus zone, respectively[115,121].

According to the investigations of Venn et al. considering the chemical composition of human articular cartilage[100,102], the respective zonal content of GAGs was determined. Based on this data, the sum of all GAGs was calculated to be approximately 20 % of cdw in the deep chondral zone and ca. 15 % cdw in the middle chondral zone. Inside native femoral head cartilage, the chondroitin sulphate content shows only a small variation with depth on a dry weight basis while keratan sulphate increases with distance from the articular surface[100]. However, for reasons of economic favourability, chondroitin sulphate sodium salt from bovine cartilage (Sigma-Aldrich; Munich, Germany) was chosen to be used as compensatory for all GAGs in the native tissues.

Therefore, the content of chondroitin sulphate was varied within the biological significant range of 0 % to 20 % cdw within the scaffold zones. In contrast to the previously mentioned precursor ingredients, chondroitin sulphate is to be considered as actively interacting with other components. The most dominant effect on the precursor behaviour is clearly the interaction with collagen I. Already after short stirring time during precursor preparation, a gelling of chondroitin sulphate together with collagen I could be observed. This leads to a local segregation of the gelified proteins from the solvent. Depending on the total concentration of the respective components, this might lead to a significant change of the flowability which may culminate in disabling the formation of an anisotropic crystal structure during directional solidification. If chondroitin sulphate is added in trace amounts ($1*10^{-2}$ % to $1*10^{-3}$ %) the mentioned local segregation leads to a lowered viscosity due to a relative increase of available solvent. Within the range of $1*10^{-1}$ % and above, the overall viscosity is increased for precursors featuring collagen I concentrations above 1 %. In this case, the gelification is dominating the effect of the released solvent. (**Figure 4.10** b))

In order to achieve an anisotropic solidification despite the employment of 20 % cdw of chondroitin sulphate the content of collagen I and consequently the total amount of precursor materials had to be reduced. Self-evidently this is lowering the overall mechanical performance of the scaffolds, since the increase in sulphate group repulsion alone will not compensate the associated loss of material, responsible for the structural integrity. But on the other hand the increase in availability of key signals to a biomimetic quantity may be able to improve the cellular response to the scaffold and thus the clinical relevant outcome.

Collagens and where required also GAGs and CaPs were stirred together with 0.5 mol/l acetic acid to produce a flowable mixture. During the stirring process, a considerable amount of air is incorporated within the precursors. Entrapped air bubbles lead locally to unwanted alterations of the microstructure during the cryostructuring process. For precursors which are closer related to solutions in their behaviour, a stirring under low pressure may be a sufficient way to overcome this problem. Low concentrated alginate solutions represent good examples for this behaviour.

For precursors being closer related to gels, like it is the case for most of the collagenous formulations used to produce the described scaffolds, this method is not adequately applicable. A centrifugation within a syringe as shown in **Figure 4.11** represented the most effective and practical method for degassing of the precursors. Therefore, the precursor was filled inside a 10 ml Luer-Lock syringe, which was augmented with a stabilization unit before it was cap-locked. The stabilization unit prevents a lateral displacement of the Luer-Lock/cap-lock junction and facilitates this way a higher operation safety. Before centrifugation, the system in transferred into a 50 ml centrifugation tube with a circular opening for the plunger of the syringe. After ensuring, that the plunger may not collide with inner parts (11180 setup) of the "3-16K" centrifuge (Sigma Laborzentrifugen; Osterode am Harz, Germany) the precursor was subjected to centrifugation with 4500 rpm for 5 minutes. This way, a highly effective degassing could be achieved since air of approximately half of the initial precursor volume could be separated from the precursor by centrifugation.

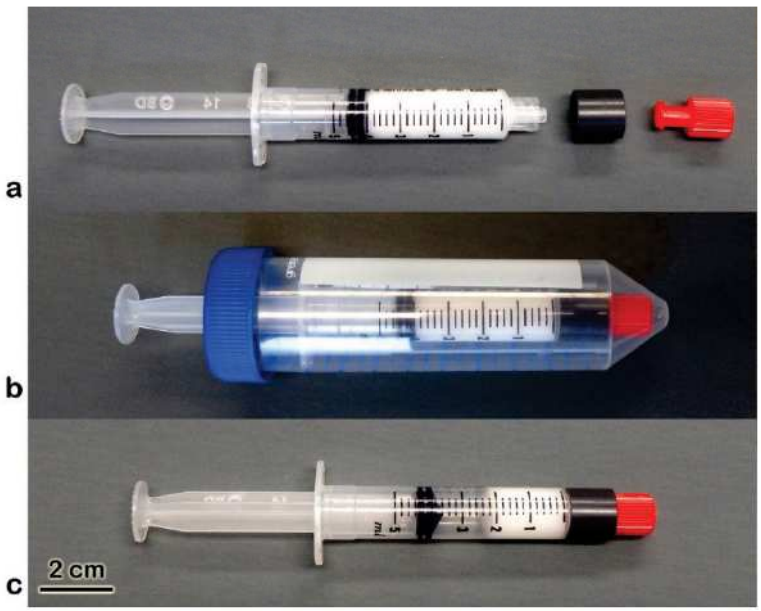

Figure 4.11: Centrifugation of precursors in syringe setup. a) A Luer-Lock syringe filled with precursor (white) is augmented with a stabilization unit (black) and cap-locked (red). b) The system in transferred in a centrifugation tube. c) After centrifugation, a highly effective degassing is achieved.

4.1.3.2 Cryostructuring of Collagenous Precursors

Due to the high potential of the directional solidification processes, a calculation of the parameters that would be needed to achieve specific structural sizes and alignments would be desirable to reduce time and resources of research. For precursors, that can be considered as “single component” materials like metal or metal alloy melts where the specific behaviour is already well-defined and understood, such calculations are reasonable and very usefully applied to the casting of metal materials[208,214,221].

The motivation to transfer the associated mathematical apparatus, designed for “single component” systems to “multi component” systems, which do not actively interact with each other, represents comprehensible. However, already the transition of these complex calculations to simpler “multi component” systems requires several approximations. Some assumptions, which would allow a convenient mathematical description of solidification processes upon temperature change, include the treatment of material parameters as constants to yield numerical values.

As presented in **Chapter 2.5.3** these parameters are mostly defined as functions of several other (e.g. temperature) dependent variables. Thus, the adequacy to use variables as constants remains a subject for debate for each specific parameter. During the cryostructuring process, the interaction of a huge variety of parameters influence the form of solidification: decrease in enthalpy upon cooling as well as enthalpy decrease on solidification (latent heat of fusion), external heat flux, heat capacities, diffusion properties, nucleation probabilities, changes in Gibbs energy upon interface formation etc. Depending on those, the liquidus temperature of the precursor and the slope in the temperature position diagraph determines an eventual constitutional undercooling of the precursor (**Chapter 2.5.2**). In the area of constitutional undercooling, crystallisation habits, the tip radius and the wetting angle of directional solidifying material(s) initiate the formation of solidification structures on small length scales.

An experimental determination of the respective parameter functions, for interacting precursor materials and for several distinct precursor compositions used in this study, itself would necessitate an enormous amount of research. However, bigger issues would have to be faced for deriving a new system that would allow a correct mathematical description of these highly complex multi component systems.

Even if both of the previously mentioned barriers would have been overcome, an experimental verification of the theoretical apparatus would still be inescapable. As a result of these considerations it was found to be most effective to evaluate the practically critical parameters by an empirical, experimental approach.

In order to investigate the behaviour of collagen during directional solidification, a 0.5 wt% collagen I solution was prepared, as described previously, using 0.5 mol/l acetic acid. The cryostructuring was carried out with varying external temperature gradients in order to monitor qualitatively the microstructural changes associated with different manifestations of ice crystal growth. **Figure 4.12** displays representative ice crystal morphologies of the collagen I precursors. All Images were captured using an "AxioCam ICc5" and further processed with "Zen Pro 2012 blue edition" (Carl Zeiss Microscopy; München, Germany).

Figure 4.12 a) depicts the common macroscopic appearance of directional solidifying collagen precursors. Like in all images of **Figure 4.12**, the solidification is propagating form the bottom to the top. Reasoned by the hexagonal crystallization behaviour of water, a lamellar solidification is established. The orientation of the visual plane corresponds to the cross section view depicted in **Figure 4.8** and the short pore diameter d_x explained in **Figure 4.9** a), respectively. During the ice crystal growth the very most of the non-aqueous components in the precursors are rejected from the growing crystal. A separation of crystalline water and in this case, of collagen I and acetic, acid is occurring. Dark lines in **Figure 4.12** a) indicate the accumulation of collagenous material in between the ice crystals. A homogenous crystallization may be achieved over a range of several mm.

A dependence of alignment and spacing between the ice crystals on the magnitude of external temperature gradients ($\vec{\nabla} T$ = "$\partial T/\partial x$") is captured in **Figure 4.12** b): Here, the typical dendritic crystallization behaviour which is commonly established under external temperature gradients in the range of $1^* 10^{1}$ K/mm can be exemplary observed. A front of needle like, primary crystals is penetrating the collagen precursor. Dendritic crystal structures are rising out of these primary crystals. Due to the plane of optical focus, only the dendritic structures pointing outward of the picture plane are visible. The temperature gradient on the left side of the image $\partial T/\partial x_L$ = (6.6 ± 0.8) K/mm bares a lower absolute value in the crystal growth direction compared to the one on the right side of the image $\partial T/\partial x_R$ = (8.3 ± 0.8) K/mm.

As observable, the spacing between the individual primary ice crystals is directly depending on the magnitude of applied temperature gradient. Together with an increasing absolute value in growth direction, the distance between the primary crystals in decreasing from λ_L = (72.5 ± 5.0) µm to λ_R = (38.6 ± 5.0) µm. This behaviour is consistent with the findings of **Chapter 4.1.2**. Together with the decrease in spacing, the alignment of the solidified water is increasing from left to right.

As visible in **Figure 4.12** c) a columnar morphology of the ice crystals is formed under high external temperature gradients in the range of 1* 10^2 K/mm. The crystal tip features a nearly elliptic shape and a smooth surface. While further crystal growth, the initial smoothness vanishes, since small manifestations of dendritic side branches build up. During videographic observation, the piling up of displaced collagen fibres is visible ahead of the moving ice front. Due to the opacity of the hydrated collagen I this effect does not show very well on non-motion pictures.

An insight in the nature of dendritic side branches is given in **Figure 4.12** d). Again, the plane of optical focus is on the dendritic structures, so that the primary crystals are not in focus. Nevertheless, a significant outgrowing of dendritic manifestations can be observed after a length distance of 60 - 80 µm from the tips. These show a hexagonal crystal growth with a planar geometry.

Being oriented parallel to the growth direction of the primary crystal tips, the lateral surface is corresponding to the basal plane of the hexagonal crystal lattice. In higher developed states of growth they branch out and fuse at the sides, being equivalent to prismatic surfaces, which finally leads to a lamellar solidification. All primary dendritic branches themselves also exhibit secondary dendritic side branches with the same planar geometry as the primary dendrites. Due to the cryoconcentration, the dendritic notches occasionally accumulate collagenous fibres, which are circumvented by the secondary dendritic crystals. These secondary dendritic crystals in turn fuse together behind the accumulated fibres, so that an entrapment may occur. After ice crystal removal, these structures will show as bridges between the respective scaffold lamellae.

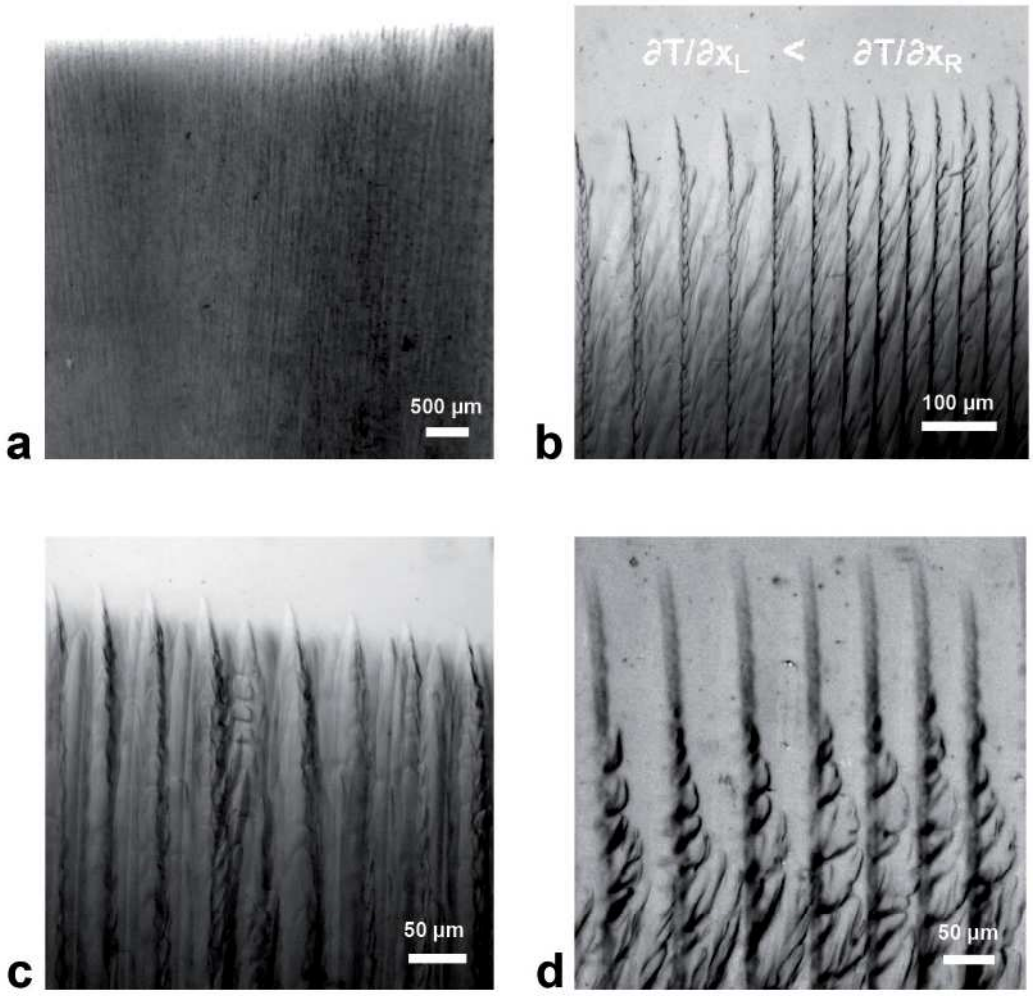

Figure 4.12: Ice crystal morphologies in collagen I precursors. a) Macroscopic appearance of lamellar solidification. b) Alignment and spacing between the ice crystals depend on external temperature gradients ($\partial T/\partial x$). A higher temperature gradient leads to a smaller spacing between the individual crystals and a higher alignment, respectively. c) A columnar morphology of the ice crystals is formed under high temperature gradients. d) Dendritic side branches lead to a lamellar solidification.

When **Figure 4.12** c) is compared to b) and d) a significant difference between the diameters of the early primary crystals is obvious. While the columnar ice crystals in c) expand to their maximal width already after ca. 200 µm, due to a higher temperature gradient, the dendritic crystals in a) b) and d) expand stepwise. This special feature of lamellar solidifying precursors shows especially well in alginate solutions: **Figure 4.13** a) depicts the solidification of a 3.0 % alginate solution (Protanal LF 10/60 FT). Here, the stepwise increasing lamellar solidification is clearly visible in three stages, where the intensifying darkening corresponds to a pronounced cryoconcentration caused by the gradual dendritic ice crystal growth.

During the very beginning of the cryostructuring process a thin initial layer of fishbone-like structured ice crystals is formed at the bottom of the precursor containing vessel (**Figure 4.13** b): Starting from points with the highest cooling, an interweaved and plane, crystal structure is formed inside a 0.5 wt% collagen I precursor. This mechanism corresponds to the appearance of the bottom structure in **Figure 4.8**. The primary crystals which dominate the rest of the directional solidification originate highly probable from dendritic side branches of these initial crystals.

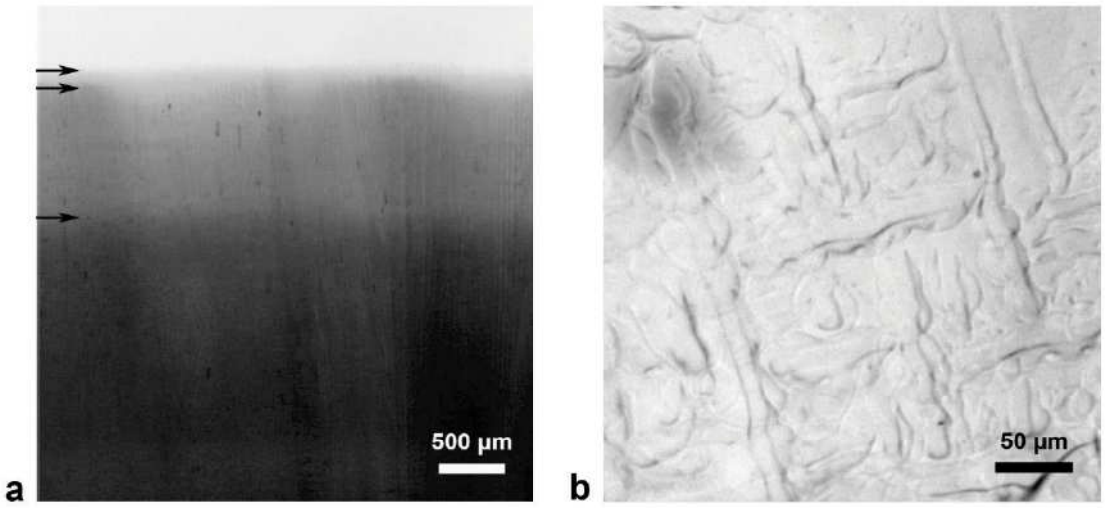

Figure 4.13: Special dendritic growth habits during directional solidification. a) Stepwise intensifying lamellar solidification in alginate solution, as indicated by black arrows on the right hand side. b) Fishbone-like structure in collagen precursor at initial stages of solidification (The darker part in the top left corner is owed to an air bubble as artefact).

After achieving control over the solidification microstructures, the processing of multiple precursors to form one monolithic scaffold was approached. Therefore, the method firstly was established with alginate precursors. Approximating the zonal variations of articular cartilage, three different precursors were prepared by using 4.0 wt% alginate (Protanal LF 10/60 FT). Furthermore, 4.0 wt% brushite was supplemented for the subchondral zone (SC), and for the deep (CD) and middle (CM) chondral zone, each 2.0 wt% of orange and blue pigments were added, respectively. The ACD was mounted with the IAG depicted in **Figure 4.3** e) and the cryostat cooled the heat exchanging unit of the ACD to a temperature of -21 °C. A polished petri dish cover (BioOne, Greiner, Germany), with an inner diameter of 37 mm, was placed in the centre of the cryostructuring unit.

The PEs were supplemented with the current necessary, to generate an outer temperature gradient of (4.313 ± 0.063) K/mm. When the cryostructuring unit of the ACD was near thermal equilibrium, 1.2 g of the SC precursor was injected into the petri dish cover to create the subchondral zone of the scaffold. Hereinafter, 1.7 g CD precursor and 1.1 g CM precursor were added subsequently to generate the deep and middle zone of the scaffold, respectively. The directional solidification was performed with a linear interpolated cooling rate of (-1.33 ± 0.13) K/min which led to a linear interpolated solidification velocity of (225 ± 11) µm/min. Afterwards, the combined precursors were lyophilized and further ionically crosslinked with 50 µl of 1 mol/l $CaCl_2$ solution per mg of sample.

As a summary of the aspects mentioned afore, **Figure 4.14** a) - c) shows a cryostructuring diagraph together with images of the resulting osteochondral scaffold. A temperature diagraph depicting the thermal precursor alteration during directional solidification is displayed in **Figure 4.14** a). In consistence with the following images the subsequent addition of precursors is colour-coded: grey = subchondral zone (SC), green = deep chondral zone (CD), yellow = middle chondral zone (CM).
The linear cooling of the SC precursor is superimposed by the latent heat which is generated from the fusion of liquid water to ice. Energy of motion is drawn from the water molecules when they take their place in the ice crystal lattice and released in the surrounding environment. In the very beginning of solidification, this may even lead to a temperature peak, which appears to be attributed to an equiaxial manifestation of solidification. Considering the resulting scaffold structures, featuring an entirely anisotropic pore structure, it seems more likely, that the generation of the initial fishbone-like structure (**Figure 4.13** b)) is causing a general warming of the precursor. This might look like an equiaxed solidification from the temperature diagraphs. But since these initial ice crystals feature a preferential growth direction in the plane perpendicular to the external temperature gradient, they may not be defined as equiaxial.
All generated thermal energy has to be removed by the heat flow which is induced by the external temperature gradient. Like described in **Figure 4.12** and **Figure 4.13** the lamellar solidification is progressing rather fast for the primary crystals, whereas the final structure is depended on the growth of dendritic side branches which requires more time to be carried out in completion.

This also shows in the temperature diagraph, where an intense amount of heat is generated in the beginning of the solidification. Afterwards, the slope of the temperature graph is decreasing again, but not to the extent that was shown before the solidification started.
When the temperature is approaching an equilibrium value, the addition of the next (CD) precursor is carried out. Due to the higher temperature of the precursor, in combination with the newly released heat of fusion, the slope of the graph is rapidly increasing. The processes mentioned afore proceed again, whereas the expression of the slope alteration is damped with each further layer of precursor. Hereinafter, the last (CM) precursor is applied, with the consequence of essentially analogue effects that have been described previously. In the end; the solidified multi zonal sample is left for the final ripening of ice crystals until thermal equilibrium is reached.

A photography (**Figure 4.13** b)) and a SEM image (**Figure 4.13** c)) depict the resulting pigmented scaffold. The pigmented colouring in **Figure 4.14** b) corresponds to the precursor composition as follows: white = subchondral zone (SC), orange = deep chondral zone (CD), blue = middle chondral zone (CM). As observable, no intermixing between the respective precursors is occurring. With the presented process, scaffolds having clinical relevant dimensions may be prepared since scaffolds with height and area of typical osteochondral defects may be created.

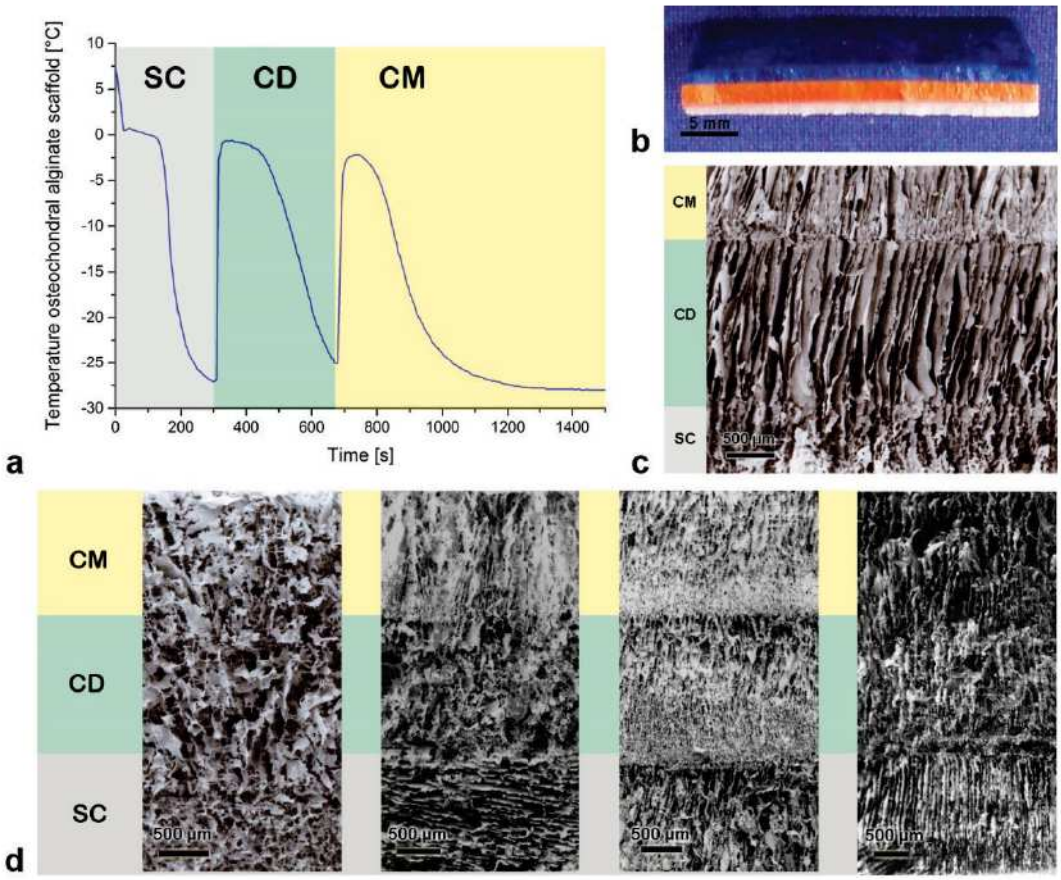

Figure 4.14: Evolution of multi-layered cryostructuring with osteochondral scaffolds. The respective scaffold zones may be distinguished by the coloured labelling: subchondral zone – SC/grey, deep chondral zone – CD/green and middle chondral zone – CM/yellow. The proof of principle was performed using alginate as precursor material by directional solidification according to the cryostructuring temperature diagraph a). The resulting pigmented scaffold is depicted as photography (b) and SEM image (c). Evolutionary steps, from early/left to late/right, of the multi-layered cryostructuring of collagenous precursors are depicted as SEM images (d) (See text for description).

As shown by **Figure 4.14** c), the monolithic osteochondral matrix features an entirely anisotropic pore structure with short pore diameters (d_x in **Figure 4.9** a)), or cross section pore widths, of ca. 80 µm. Details of **Figure 4.14** c) are depicted in **Figure 4.15** as SEM images: Continuous pores but a clearly identifiable interface are shown in the pore structure between middle (CM) and deep (CD) chondral zone (a)). With a roughness in the micron to sub-micron range the surface structure of the chondral zone lamellae represents rather smooth (b)). The interface between deep (CD) and sub- (SC) chondral zone is very fluent, but cross section pore diameters in the subchondral zone are smaller than in the deep chondral zone. Within the subchondral zone, a rough surface is created by lamellas with anchored off-standing plate shaped brushite crystals.

Although the consistency in pore size as well as the smoothness of the interfaces are not perfect yet, this osteochondral scaffold features, in mean, a preferable pore size for cell seeding and servers as proof of principle for the creation of multi zonal scaffolds by the presented method.

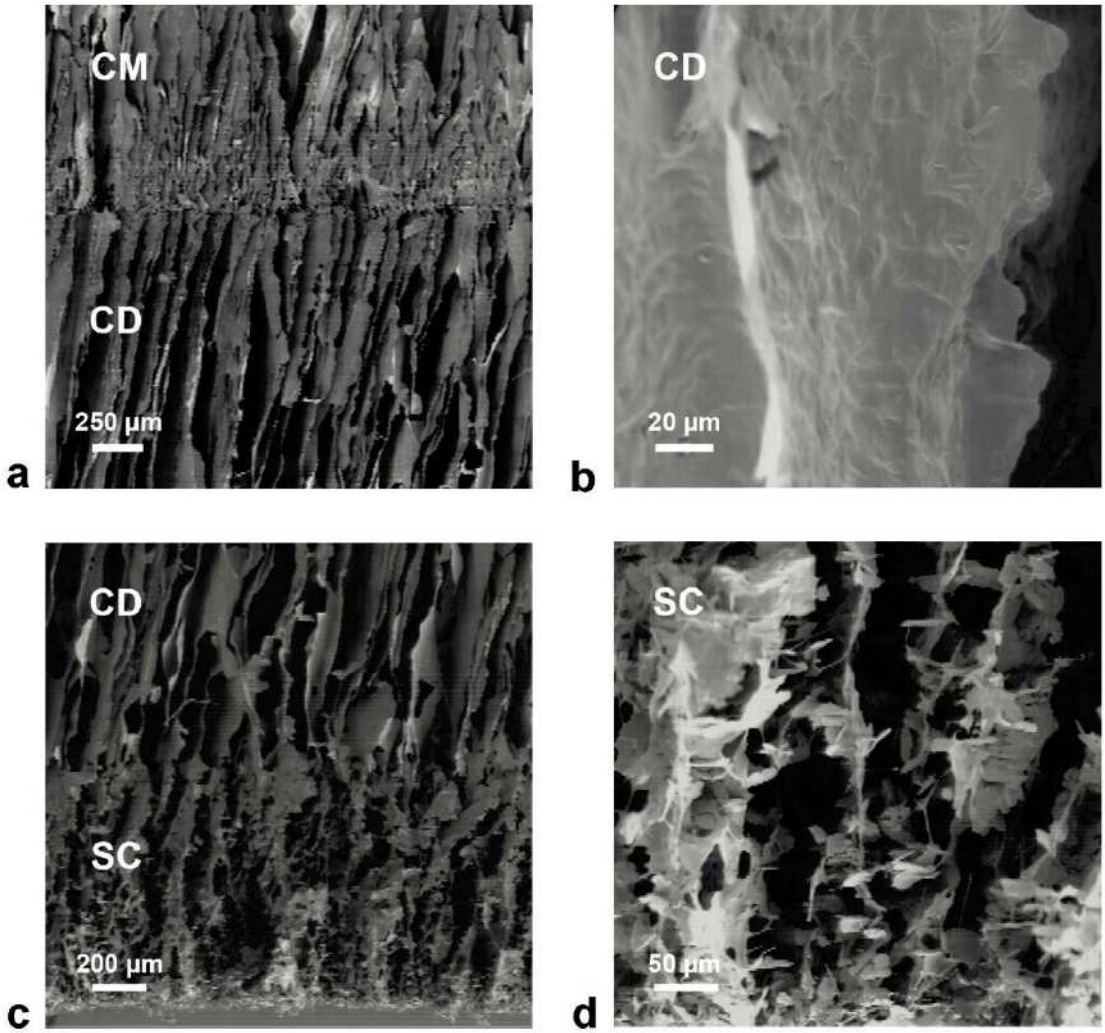

Figure 4.15: SEM images of osteochondral alginate scaffold details. a) Pore structure and interface of middle (CM) and deep (CD) chondral zone. b) Surface structure of chondral zone lamellae. c) Pore structure and interface of deep (CD) and sub- (SC) chondral zone. d) Off-standing plate shaped brushite crystals lead to a rough surface in the subchondral zone lamellas.

Since the presence of biomimetic key signals is suspected to influence seeded cells positively regarding their differentiation and matrix products, the next step consisted in transferring the method on collagenous precursors. In comparison to alginate, the anisotropic structuring of collagen precursors represented itself significantly more challenging.

Self-evidently a truly biomimetic composition of osteochondral scaffolds, with collagen II, XI and IX being the only present collagen phases in the chondral zones of the scaffold, would be desirable. Although the cryostructuring of a pure collagen II precursor could be demonstrated to be feasible with attractive pore sizes (**Figure 4.16** a)), the resulting scaffolds featured only a marginal initial stability. By the use of different cross linking methods (**Chapter 4.1.3.3**), the overall stability could be increased, but not to a level which would be relevant for the intended use as implant or matrix for in situ tissue engineering. Consequently, the incorporation of the not fully biomimetic collagen I within the chondral zone of osteochondral scaffolds represented the most suitable compromise that still fulfils the before mentioned requirements while contributing additional structural integrity.

Representative evolutionary steps, in the generation of multi-layered cryostructured collagenous precursors are depicted in **Figure 4.14** d). From left to right, stages of increased development are presented as SEM images. In the early times of process development an anisotropic pore structure could only be observed suggestively. Due to the immature stage of the ACD, the achievable external temperature gradients represented themselves too small to achieve a unidirectional pore structure with multi-layered collagenous precursors (first image in **Figure 4.14** d)). Upon further improvement of the ADC an anisotropic pore formation could be generated. In further earlier stages (second image in **Figure 4.14** d)) the directional pore formation succeeded within the subchondral zone, but not as intended with pores orthogonal to the layering. Also the ice crystal growth within the chondral zones represented only occasionally anisotropic. Both are to be explained by the still insufficient absolute value of the established temperature gradient. Following additional upgrades, the formation of continuous anisotropic pores parallel to the external temperature gradient was achieved. Due to insufficient process control, the pore sizes varied within the single zones (third image in **Figure 4.14** d)). Finally, after adaption of the precursor formulations, a continuous anisotropic pore structure with rather constant pore sizes could be realized (fourth image in **Figure 4.14** d)).

4.1.3.3 Cross Linking

In order to transform the cryostructured and lyophilized multi-layered constructs into decent scaffolds the process includes some form of consolidation after the structuring. This way a multi zonal but monolithic material can be generated. Therefore, wet chemical cross linking with and without spacer, as well as thermal cross linking was evaluated.

For prehardening of the fragile collagen II scaffolds prior to wet chemical cross linking a dehydrothermal treatment was carried out. By thermal removal of water from the collagen molecules, the formation of intermolecular crosslinks through condensation reactions either by esterification or amide formation may be achieved[72,185,186].
Therefore, the cryostructured, freeze dried scaffold was cured inside a vacuum oven "Vacutherm VT 6060 M-BL" (Heraeus; Waltham, Maine, USA). At a pressure below 10 µbar the cross linking temperature was varied between 90 °C and 120 °C, while the duration of the heat treatment was evaluated between 1 h and 3 h. If the dehydrothermal treatment is carried out at elevated temperatures for more than one hour, the whitish scaffold is transformed to a yellowish colour, indicating a thermal alteration of the collagenous structure. This might be avoided by curing the scaffold inside an aluminium foil envelope.
Resumed, a dehydrothermal treatment for 80 minutes with a temperature of 105 °C represented as the best compromise between unnecessary thermal degradation of the collagen and increased mechanical stability. The structural alteration induced by the dehydrothermal cross linking may be observed by comparison of **Figure 4.16** a) (untreated scaffold) with **Figure 4.16** b) (thermal treated scaffold). A "melting down" of smaller fragments, standing out of the main structure may be observed here.
However, since the beneficial feature of the cryostructuring process to employ non-denatured collagenous materials could be forfeited by the thermal treatment, it was preferred to employ also collagen I for a stable scaffold production and to spare the dehydrothermal treatment.

As mentioned in **Chapter 4.1.2**, alginate scaffolds were cross linked using a 1 mol/l $CaCl_2$ solution. This concentration was chosen based on previous investigations[26] by the author. To yield an increased mechanical stability of multi-layered alginate composite materials, a further cross linking step using diisocyanates may be applied (Stuckensen et al.[149]). Since the highly reactive isocyanate groups suit for a bonding of the amide and hydroxyl groups of collagens, they were used for a cross linking approach of the collagenous scaffolds too.

The concentration of the cross linking agent 1,6-hexamethylene diisocyanate (HMDI) was varied between 5.0 vol% and 10.0 vol% in acetone solution. The duration of cross linking was varied between 1 h and 5 h. Summarized, a submersion of the scaffold in 7.5 vol% HMDI for 80 minutes yielded the most promising results. Nonetheless the cross linking using HMDI was found to be afflicted with significant disadvantages:

Firstly, the submersion technique yields to an inhomogeneous increase of the mechanical stability. During the cross linking process, the HMDI is required to diffuse inside the porous structures of the scaffold. Since the reaction of the isocyanate groups is rather unspecific, the HMDI tends to accumulate more on the outside of the scaffold than in the inner areas. Consequently, the surface of the scaffolds is highly cross linked, while the interior gains only marginally in stability. Together with this effect comes an entanglement of the HMDI chains (**Figure 4.16** c)), which is leading to a subsequent blocking of the pore channels (**Figure 4.16** d)). The probability for an intensive web formation across a pore is rising together with increasing submersion exposure time and closeness to the scaffold surface. Consequently, the submersion in HMDI solution did not represent an appropriate way of cross linking, since the potential for cell colonialization and the mechanical performance is altered unfavourably.

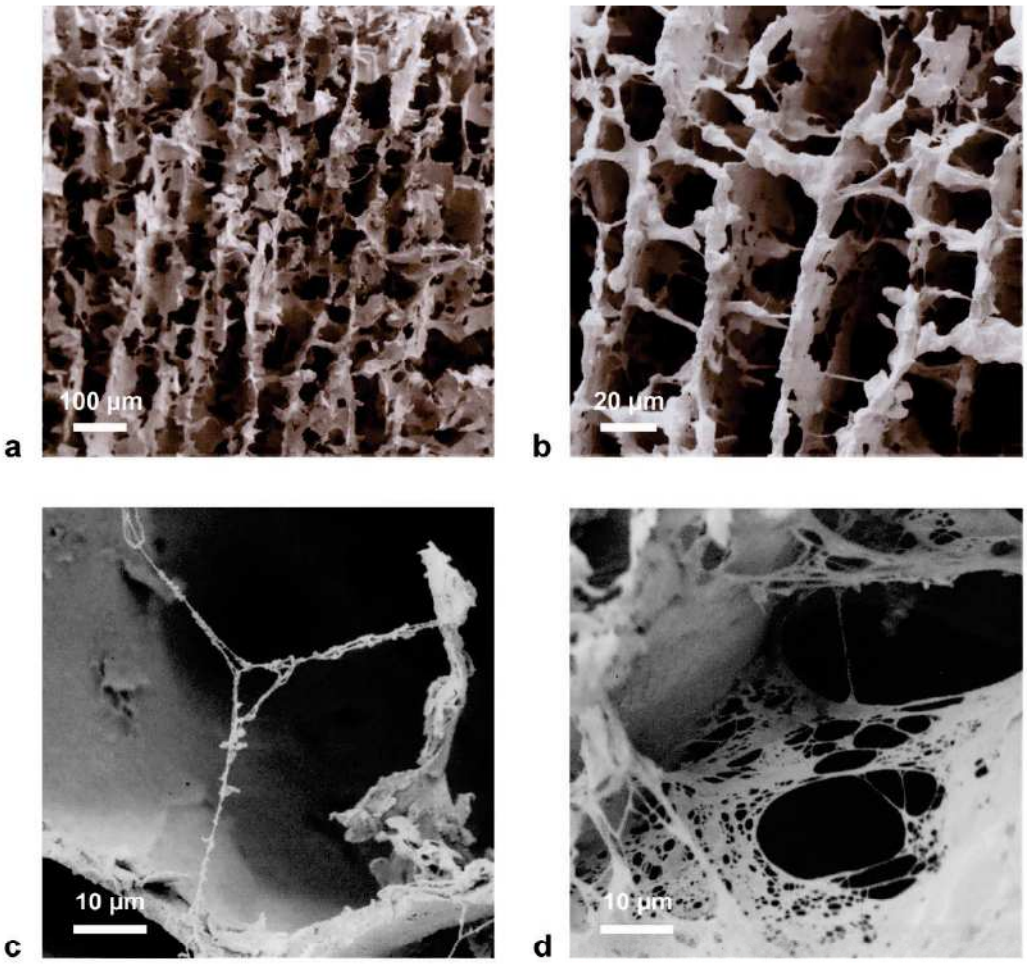

Figure 4.16: SEM images of collagen II scaffold cross sections. a) Anisotropic pore structure of pure collagen II scaffold. b) Dehydrothermal treated collagen II scaffold. c) 1,6-hexamethylene diisocyanate (HMDI) cross linking is leading to an entanglement of the cross linking polymers. d) Further HMDI cross linking leads to a blocking of the channel pores by web like structures.

By far the most promising results were attained by using carbodiimides for a wet chemical cross linking step. Carbodiimides belong to the class of zero-length cross linkers, since they do not remain as part of the bonding[192] and rely on a spatial closeness (about 1 nm) of the collagen molecules[267]. The cross link formation between collagens using 1-ethyl-3-(3-dimethylaminopropyl)-carbodiimide (EDC) evolves in multiple steps of a condensation reaction: After the activation of the carboxylic acid groups of glutamic or aspartic acid residues by EDC, 0-acylisourea groups are generated. After nucleophilic attack by free amine groups of lysine or hydroxylysine residues, crosslinks are formed between the collagens. Simultaneously, the EDC-related water-soluble compound 1-ethyl-3-(3-dimethylaminopropyl)urea is liberated (**Figure 2.7**)[191].

Some studies estimate / calculate / measure the number of carboxylic acid groups per alpha chain of collagen to approximate the optimal molar ratios for the cross linking. However, the most promising mechanical results in this thesis were achieved when the cross linking components were available in excess[191,268]. This might firstly to be attributed to the natural fluctuations of the state of collagens after the respective isolation treatments. Secondly, the reaction potential of EDC with GAGs that are naturally attached to collagen fibres is often not considered. Additionally to the collagen-collagen cross links described above, an amide formation between collagens and the carboxyl groups of GAGs is possible via activation by EDC[269]. Moreover, when GAGs are additionally supplemented to the collagenous precursors, an increased amount of EDC is required. In general, a further steric hindrance to the EDC cross linking upon the addition of supplements during the processing of the collagen scaffold may not be excluded.

Since a significant reduction of the EDC half-life in aqueous solutions is occurring under presence of phosphates[193], they were avoided within the cross linking solution. Alternatively, the system was buffered by 2-(N-morpholino)ethanesulphonic acid (MES). In order to suppress unwanted side reactions of the 0-acylisourea groups, N-hydroxysuccinimide (NHS) was added. On the one hand, water can act as a nucleophile and the hydrolysis of the 0-acylisourea group may result. On the other hand, the reactive 0-acylisourea group can perform an N-acyl shift and convert to a stable N-acylurea group. By supplementing NHS, the 0-acylisourea group may convert to a NHS-activated carboxylic acid group. Compared to the 0-acylisourea group, this activated carboxylic acid group is less vulnerable to hydrolysis at acidic pH values.[191]

The ranges of 5 - 40 mmol/l NHS, 50 - 250 mmol/l EDC und 100 - 350 mmol/l MES were screened for the best cross linking results. To ensure a reliable cross linking result for multiple precursor concentrations of different cross linkable materials (such as collagen I, collagen II and chondroitin sulphate) the cryostructured and lyophilized samples were subjected to 100 µl crosslinking solution per mg of scaffold. The most effective cross linking solution was achieved by dissolving 250 mmol/l MES, 120 mmol/l EDC and 25 mmol/l NHS inside a mixture of 40 vol% ethanol and 60 vol% H_2O.

Due to the possibility of air entrapment inside the scaffold pores upon submersion in cross linking solution, all kinds of wet-chemical cross linking were carried out inside a vacuum apparatus to avoid inhomogeneous results. The used setup of vacuum apparatus is depicted in **Figure 4.17**. In order to generate optimal cross linking results, the sample was placed at the bottom of the container in adequately sized petri dishes. By using a "KNF Laboport N 840.3FT.18" vacuum pump (Neuberger; Freiburg, Germany) the interior of the container was evacuated for 3 minutes to 8 mbar in order to remove the air from the scaffold pores before the pump was shut off. Cross linking solution was filled inside the separating funnel at the top of the apparatus. The afflux vessel was slightly opened, so that the solution could slowly drop down a spiral hose and gradually submerse the samples from the bottom to the top. After 3 minutes of incubation, the pressure vessel (**Figure 4.17** left) was gently vented and the sample was left 20 h for cross linking. By using this method, the common problem of collapsing pore structures during the wet chemical cross linking of collagenous cryostructured scaffolds could be avoided.

Figure 4.17: Vacuum apparatus for optimal cross linking results containing a meniscus scaffold.

After cross linking by carbodiimides an intensive washing procedure is mandatory. Since the EDC as well as the resulting substituted urea product are toxic to cells, they have to be removed from the scaffolds before they can be used for cell culture or implantation. Therefore, the scaffold was washed three times for one day, each in 100 ml distilled water per 100 mg of scaffold dry weight.

4.2 Precursor Materials and Processing Induced Alterations

Despite alginate and chondroitin sulphate, all materials used for the production of scaffolds by the developed cryostructuring process were self-produced or gained from natural materials which were further processed. In the following, a further insight on the characterization and eventual alteration during processing of the precursor materials is represented.

4.2.1 Collagens

As described in **Chapter 3.3.1** collagen I was isolated from the tendons of rat tails, while collagen II was derived after the processing of bovine knee cartilage. The inherent structure of the osteochondral tissue in a bovine tibia plateau is depicted in **Figure 4.18** a): The downer fifth of the picture shows the subchondral area where porous calcified bone matrix shows partially through the collagen I rich tissue of the beginning bone. The tidemark extends rippled at the interface between chondral and subchondral tissue. Above this, the collagen II based hyaline cartilage tissue of the chondral part expands for approximately 1 mm in height.
A closer insight in the structure of the chondral zone is depicted in **Figure 4.18** b): the extracellular matrix represents as a woolly structure of fibres with voids in the lower micron or sub-micron range. The bigger spheroid shaped slots with an expansion of about 10 µm represent the hollow chondrons, where the formerly living chondrocytes produced a dense matrix around them.
With respect to these circumstances, the limited migration potential of the cartilage synthesizing cells and thus the small self-healing capacity of articular cartilage becomes quite understandable. Regarding the overall spatial alignment of the collagenous fibres and the chondrons together, a preferential fibre direction from the bottom (facing the subchondral zone) to the top (facing the articular cartilage surface) can clearly be observed.

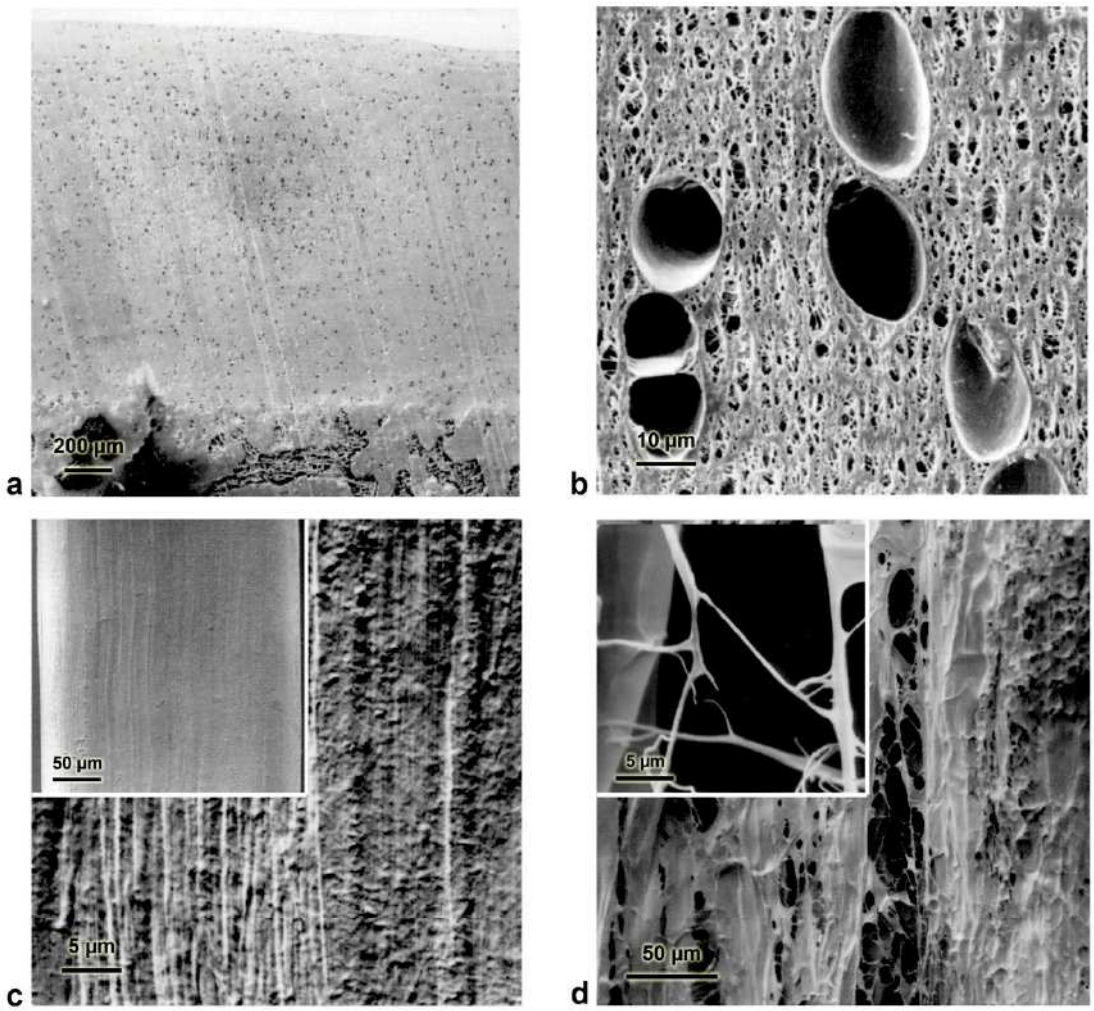

Figure 4.18: SEM images of collagenous tissues from bovine knee cartilage and murine tail tendon. a) Cross section of native osteochondral tissue in bovine tibia plateau. b) Detail image of a) revealing the structure of chondral tissue. c) Surface of native rat tail tendon. d) Rat tail tendon after acidic fractioning, depicting fractioned collagen fibrils in the (sub-) micron rage.

A surface of a native murine tendon is represented in **Figure 4.18** c). The pathway of the collagen I fibres can be divined inside a densely packed matrix: A preferable fibril orientation from the top to the bottom of the image indicates the main direction of fracturing during acidic treatment. When subjected to mild acidic fractioning (**Chapter 3.3.1**), the collagen fibrils separate along the indicated directions as exemplary shown in **Figure 4.18** d). Collagen I fibrils with diameters in the sub-micron or low micron range are derived by acidic fractioning. Among all used precursor materials they represent the most important ones regarding the structural integrity and mechanical performance of the scaffolds. The accessible resolution of the used "Digital Scanning Microscope 940" was not sufficient to illustrate the characteristic D banding pattern of the collagen fibrils.

In order to characterize the native, isolated and cryostructured collagenous materials Fourier Transform - Infrared Spectroscopy (FT-IR) measurements were carried out. The characteristic major amide bands in the IR spectra of collagen have been summarized by Yannas[72] and have been verified later on in literature [270-272].

The N-H stretching vibration (Amide A) is located in the interval between 3290 cm^{-1} and 3330 cm^{-1}. The stretching vibration of the C=O bond (Amide I) is to be found from 1640 cm^{-1} to 1660 cm^{-1}. A combination of the stretching vibration of the C-N bond with a bending vibration of the N-H bond (Amide II) represents from 1535 cm^{-1} to 1550 cm^{-1}. Between the wavenumbers 1230 cm^{-1} and 1270 cm^{-1} the C-C stretching vibrations combine with the stretching vibration of the C-N bond and the bending vibration of the N-H bond (Amide III).

As depicted in **Figure 4.19**, those four characteristic amide bands can be clearly identified in the FT-IR spectra described in **Chapter 4.5** (native bovine articular cartilage and rat tail tendon, isolated collagens I and II and cryostructured collagen I/II scaffolds before and after cross linking). Since no peak, where constancy in height, shape and maximal peak position could be guaranteed among all investigated samples, was identifiable within the FT-IR spectra, they could not be normalised and quantified.

However, a significant difference in the extinction levels correlated directly with the presumed density of the tested materials. While the dense native tendon and cartilage tissues show only low values of extinction in the investigated range, the isolated collagens exhibited medium levels. The highly porous cryostructured scaffolds displayed the lowest optical density.

Muyonga et al. [271] investigated fish collagens and gelatines by FT-IR and found a very obvious broadening of the N-H stretching vibration peak upon thermal denaturation. Such an evidence for denaturation could neither be found for the isolated precursor collagens nor for the cryostructured scaffolds investigated in **Figure 4.19**.

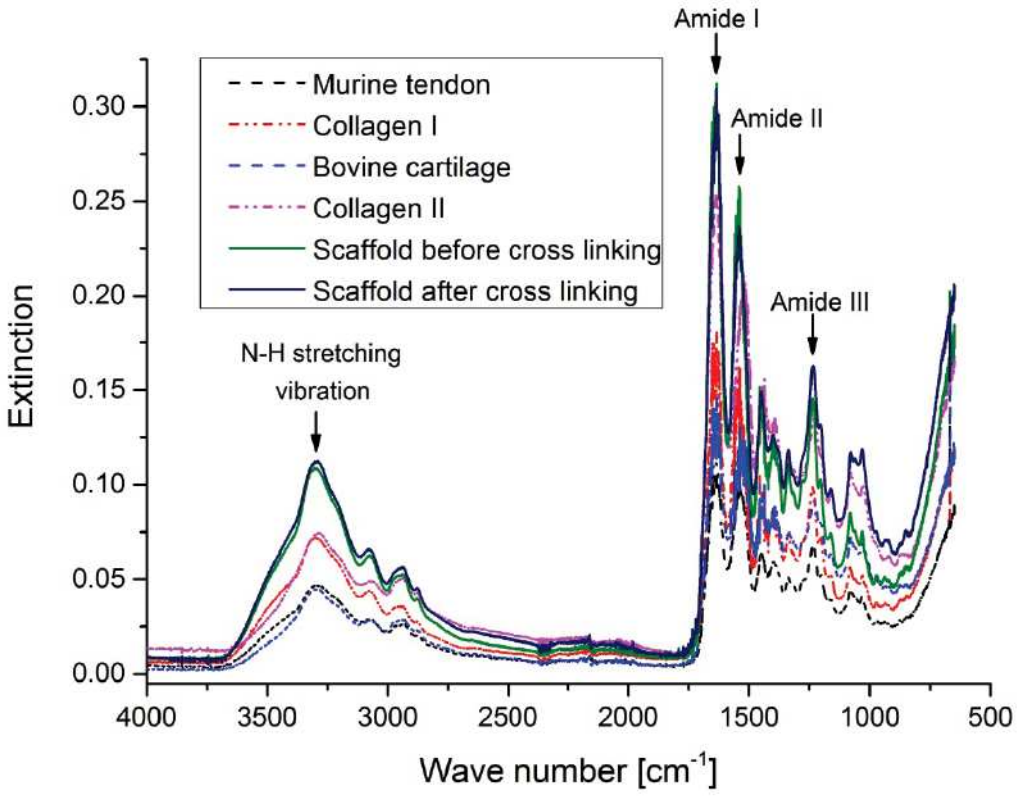

Figure 4.19: FT-IR spectra of native collagenous tissues, precursor collagens and resulting scaffolds. Considering the comparability of the respective samples, no significant changes in the relative peak heights and positions were observable.

An eventual denaturation of collagenous materials was studied by Sachlos et al.[272] using FT-IR measurements: By monitoring the wavenumber of the N–H stretching vibration, conclusions on the tertiary structure of collagen resp. on a denaturation of the collagen were drawn. A thermal denaturation was stated to lead to a lowered wavenumber of the N–H stretching vibration peak. Bovine achilles tendon collagen type I (Sigma-Aldrich) was thermally denatured for 1h with temperatures up to 80° C. FT-IR measurements with 20 scans at a resolution of 2 cm^{-1} were reported to show a decrease in the wavenumbers of peak positions up to 25 wavenumbers lower than the ones of native material.

In order to evaluate this finding, the same collagen I material (Bovine achilles tendon; Sigma-Aldrich; Germany) was subjected to temperatures up to 90°C for 2 h. The FT-IR measurements were performed with a larger number of scans and a higher resolution than in the named literature (**Chapter 3.5.7**).

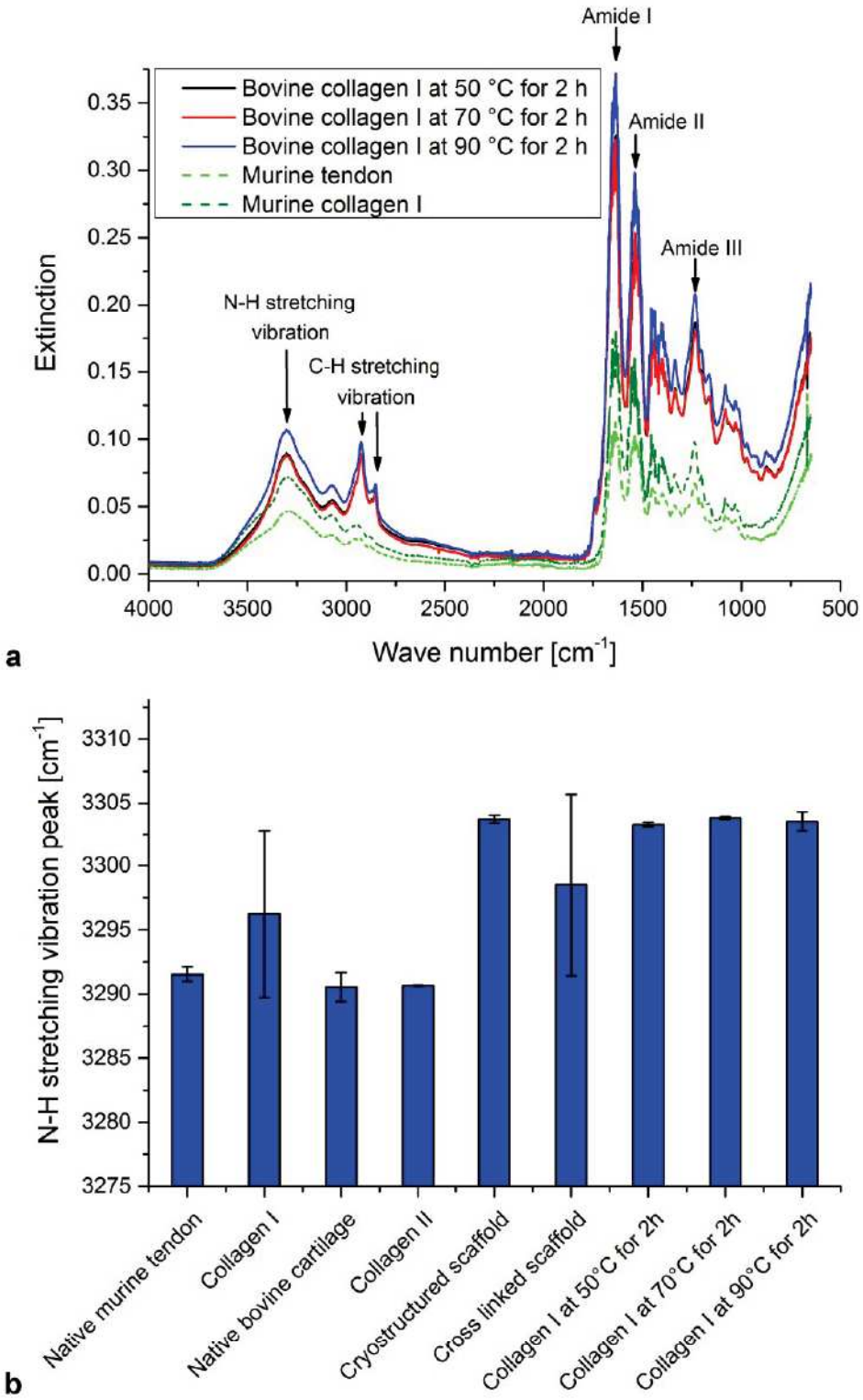

Figure 4.20: a) FT-IR spectra of native, isolated and thermally treated collagen I. All spectra show amide bands that are characteristic for collagen. A significant broadening of the N-H stretching vibration peak upon thermal treatment could not be observed. b) N-H stretching vibration peak positions of native collagenous tissues, precursor collagens, resulting scaffolds and thermally treated collagen.

The resulting spectra (**Figure 4.20** a)) show the amide bands that are characteristic for collagen. In comparison, bovine material obviously exhibited a stronger pronouncement of C-H stretching vibrations than murine material. The respective amide A peak positions of native collagenous tissues, precursor collagens, cryostructured scaffolds and thermally treated collagen were compared in **Figure 4.20** b).
Contrary to literature [272], the native materials showed peak positions with lower or comparable wavenumbers than the other tested materials. With consideration of the existent signal fluctuations, the existence of a denaturation related shift of the N-H vibration peak could not be verified.

Since insoluble native collagenous materials are generally problematic to investigate for signs of denaturation, FT-IR scans of the freeze dried tissues would represent a convenient characterization method. Regarding all FT-IR measurements, with respect to the comparability of the respective samples, no significant changes in the relative peak heights and positions were observable. Consequently, FT-IR spectroscopy could not be evaluated as an appropriate characterization method to perform an undoubtedly investigation of the eventual denaturation of collagenous materials.

4.2.2 Calcium Phosphates

Freeze dried calcium phosphates used for the precursor preparation were investigated by SEM. **Figure 4.21** a) depicts precipitated brushite with a clearly visible plate-like crystal morphology. A longitudinal extension of the brushite plates in the double-digit micron range is obvious. The elongated crystal shape indicates the bidental underlying growth mechanism. Due to mechanical stress during the production and purification procedure, the corners of the crystals are usually broken off and represent themselves in the form of fragments. These crystal fragments extend up to the single digit micron range. In addition, it can be observed that planar regions are fractured off the plate crystal surfaces. Some crystallites are even cleaved parallel to the surface. The thickness of these breakaway regions accounts typically for about 1 micron. Both phenomena are probably to be explained by the derogation of the crystals structural integrity by crystal water.

Since the fluid retentions in the crystals are layered parallel to the (010) plane within the crystal structure (**Figure 2.2** b), c)) they predetermine the propagation pathway of eventual fractures.

The sub-micron crystallites of the precipitated hydroxyapatite may be viewed in **Figure 4.21** b). The typical needle shape of hydroxyapatite crystals is embodied by a cuboid shape when regarded in detail. This corresponds well with the known prismatic growth habit; even though the hexagonal crystallisation system does not show in the established morphology. The usually square shaped basal area of the prisms occasionally also extends to a rectangular shape and thus to plate shaped crystals. The precipitates mainly consist out of cuboids with a diameter in the nanometre range. When they occasionally expand to a plate shape, the crystal diameter expands into the sub-micron range, too.

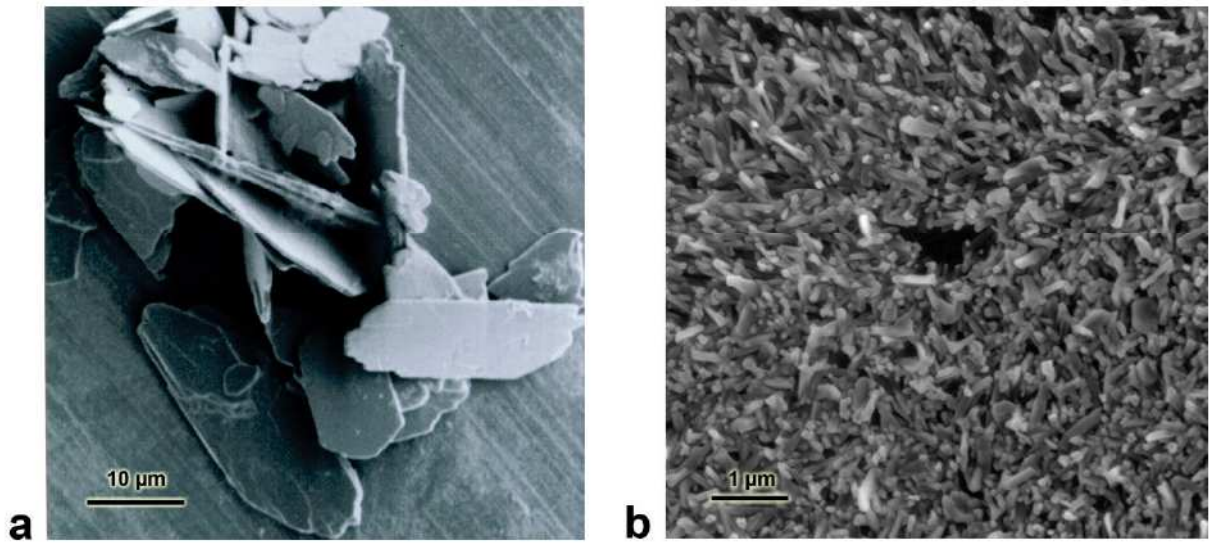

Figure 4.21: SEM images of synthetized calcium phosphates. a) Plate shaped brushite crystallites, b) cuboid shaped hydroxyapatite particles.

X-Ray Diffraction (XRD) patterns of the synthesised calcium phosphates and exemplary calcium phosphate containing scaffolds are collated in **Figure 4.22**. Each of the respective diffractograms has been indexed with the associated crystal reflections according to the JCPDS database[263]. The raw powders were measured in an arbitrary orientation of the crystallites, which led to an almost exact accordance to the respective reflection intensities of the database.

Figure 4.22 a) depicts the diffraction pattern of the brushite powder with a comparably sharp and intense signal. All the reflections of the raw powder were identifiable as brushite characteristic. The diffactogram of the used hydroxyapatite precipitates is displayed in **Figure 4.22** b). Due to the sub-micron crystal size, the respective peaks are wider and more overlapping than the ones for brushite. In addition, a higher scattering by multiple smaller surfaces leads to an overall lowered intensity than in case of the previously mentioned material. Nonetheless, a well consistence with the database was found for the characteristic reflections of the synthesized hydroxyapatite.

In order to compare the initial inorganic material compositions with the processed calcium phosphate containing scaffolds, and to detect an eventual conversion of the mineral phase, XRD diffractograms of the scaffolds were recorded. The XRD pattern of the subchondral zone of an osteochondral scaffold (**Chapter 4.5**) that was produced with brushite is shown in **Figure 4.22** c). The only pronounced reflections are represented by those characteristic to brushite. Consequently, even if conversion processes occur during the processing, the crystalline parts of the final scaffolds consist entirely of brushite.

Figure 4.22 d) depicts the diffractogram of an anisotropic bone scaffold (**Chapter 4.3**), produced with a hydroxyapatite containing precursor. The characteristic reflections of hydroxyapatite are identifiable. Furthermore the diffraction pattern of brushite is represented in the scan. At first this might seem to be surprising since the complete process is carried out at ambient conditions, but when all production steps are considered the conversion is elucidated:

For the precursor preparation, hydroxyapatite is mixed together with collagen I in 0.5 M acetic acid ($pH_{precursor} = 4.06 \pm 0.08$). After cryostructuring, the carbodiimide cross linking performed in acidic conditions too ($pH_{cross\ linking\ solution} = 4.21 \pm 0.08$). Considering the solubility properties of calcium phosphates, as regarded in **Figure 2.2**, the singular point, where hydroxyapatite becomes less stable than brushite or monetite is situated at a pH value of 4.2. Consequently, at acidic conditions below this singular point, brushite and monetite represent as the thermodynamically more stable phases. Whereas hydroxyapatite and brushite are about equally stable during the carbodiimide cross linking, the H_3O^+ concentration while the precursor fabrication is high enough to dissolve the hydroxyapatite.

No characteristic reflections of monetite could be identified in **Figure 4.22** d). Thus, it might be assumed, that the incorporation of H_2O in the crystal lattice of the re-precipitating calcium phosphates is energetically favoured during the process. This leads to the formation of brushite instead of monetite.

Both of the scaffold diffraction patterns in **Figure 4.22** c) and d) are superimposed by a stronger background signal due to the processed biopolymers and thus show a lower intensity, compared to the pure powders. Despite the presence of the biopolymers themselves, the structural state of the materials is also affecting the intensity of the background signal.

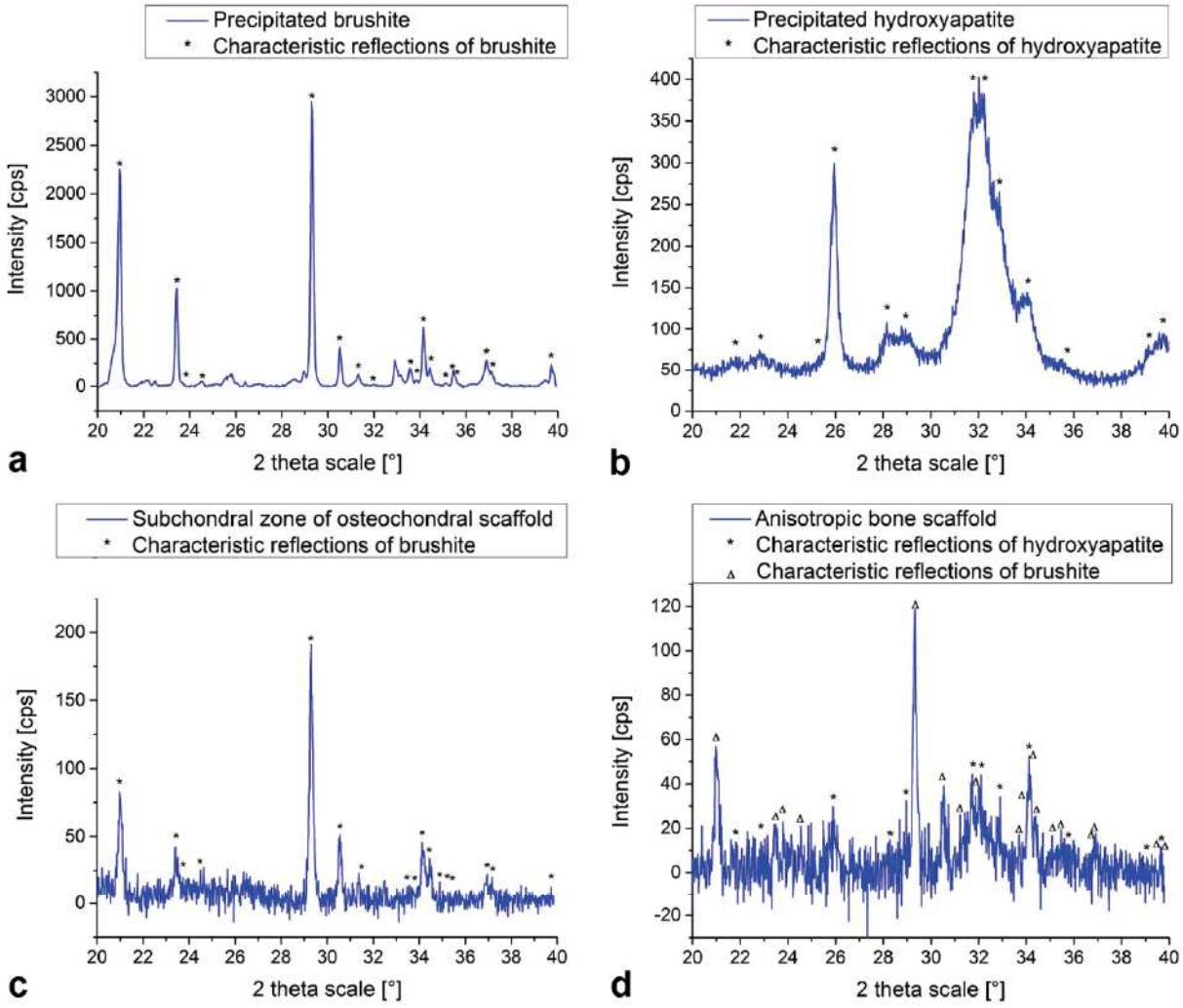

Figure 4.22: XRD diffractograms of synthesised calcium phosphates and exemplary calcium phosphate containing scaffolds. a) Brushite, b) hydroxyapatite, c) subchondral zone of osteochondral scaffold produced with brushite, d) anisotropic bone scaffold from hydroxyapatite precursor. Crystalline components were identified as brushite (PDF-No. 009-0077[263]) and hydroxyapatite (PDF-No 009-0432[263]).

While the powders of **Figure 4.22** a) and b) were conventionally prepared by compacting a smooth surface to the measuring plane, the anisotropic scaffolds of **Figure 4.22** c) and d) were both cut vertically and measured without applying a grinding process. The microstructured surfaces of the scaffolds were scanned within the measuring plane in order to examine the scaffolds for an eventual preferential orientation of the calcium phosphates by the anisotropic structure of the matrix.
As revealed by Stuckensen et al.[149], an anisotropic biopolymer matrix may induce a preferential spatial alignment of precipitating brushite crystals. The crystallographic orientation can be linked to the intensity of certain characteristic reflexes with the XRD diffractograms: Powders show a random orientation of the crystallites, whereas the respective reflection intensities match those of the database[263]. Brushite containing, anisotropic composite diffraction patterns may show a significant higher intensity of the (0 4 0) reflection (occurring at 23.3911°), in relation to the other occurring reflections. Since the (0 1 0) crystal plane is identical with the basal plane of the brushite crystal, the (0 4 0) crystal plane is an equivalent for the plate surface of the crystals. This would consequently indicate a preferred crystal orientation within the composite. A significant difference of the scaffolds reflections intensities from the intensities shown by powders could not be observed in the two theta scans of **Figure 4.22**. As a result, the induction of an anisotropic mineralization behaviour could not be observed for the cryostructured scaffolds.

4.3 Bone Scaffolds

For the production of cryostructured bone scaffolds, a collagenous suspension was prepared by suspending collagen I and hydroxyapatite, each 3.8 wt%, in 0.5 molar acetic acid. The suspension was degassed by centrifugation. The ACD was set up with the inner assembly group depicted in **Figure 4.3** d) and the cryostat cooled the heat exchanging unit of the ACD to a temperature of -25 °C.
A polished petri dish, with an inner diameter of 37 mm, (BioOne, Greiner, Germany) containing a silicon body with cylindrical moulds (diameter = 5 mm, height = 7 mm) was placed in the centre of the cryostructuring unit. The PEs were supplemented with the current necessary, to generate the respective desired outer temperature gradients. When the cryostructuring unit of the ACD was near thermal equilibrium, 1.4 ml of the suspension was injected into the moulds.

The precursor was frozen for 25 minutes under the influence of a unidirectional outer temperature gradient. Temperature curves of the PEs and the solidifying precursor were recorded. After solidification, the specimens were transferred to a lyophilizator, where sublimation of the frozen solvent was carried out for 18 h, at -52 °C and 70 µbar.

The resulting porous structure was further covalently cross linked with a carbodiimide solution containing 3/5 H_2O, 2/5 Ethanol, 200 mmol/l MES, 52 mmol/l EDC and 21 mmol/l NHS. Therefore, the structure was placed in a pressure vessel, which was evacuated until reaching an operating pressure of 100 mbar. 100 µl of a cross linking solution was added per mg of specimen; 45 seconds after the infiltration of the material, the pressure vessel was vented. Following 20 h reaction time, the scaffolds were washed three times in distilled water. Thereupon, the scaffolds were freeze dried again to yield cylindrical samples of 4 mm diameter and 6 mm height.

In order to investigate different scaffold attributes upon their benefit for bone regeneration three kinds of scaffolds were produced out of equal weight amounts of collagen I (**Chapter 3.3.1**) and sub-micron hydroxyapatite crystals (**Chapter 3.2.2**):

- Bone scaffolds with anisotropic channel pores, which propagate from one basis of the cylinder to the other. (ANI)
- Bone scaffolds with an isotropic, sponge like, pore structure that are randomly distributed among the matrix. (ISO)
- Bone scaffolds with isotropic pores containing 2/5 collagen I, 2/5 hydroxyapatite and 1/5 chondroitin sulphate. (ISOCS)

Although an entirely anisotropic pore structure (ANI scaffolds) does not reassemble the situation in a native bone, it could result in favourable results after implantation due to a higher facilitation of cell migration. Therefore, both isotropic types of scaffolds (ISO and ISOCS) recapitulate the structure of spongiosa bone tissue. Furthermore, the addition of the GAG chondroitin sulphate in the ISOCS scaffolds may increase the stiffness and present another kind of biological key stimulus to inherent cells.

Since the term critical size bone defect is defined as the size where the body cannot bridge the defect without further cell stimulating substances and scaffolding[273], the task to heal such a defect just by implantation of a scaffold is pretty ambitious. Reasoned by this, scaffolds were also loaded with the cytokine “recombinant human bone morphogenetic protein 2” (rh-BMP-2) for a further induction of bone growth. Scaffolds containing BMP-2 are commonly used as alternative to bone autografts[274]. Besides other attempts, BMPs are also delivered through collagen sponges[50,275]. The effective dose of BMPs needed for treatment is much higher than the physiological[276].
By using the cryostructured scaffolds the efficiency of existing BMP-2 treatments may be increased, since the sub-micron hydroxyapatite crystals represent a highly attractive binding site with a huge surface area. This way, the conventional leaching out of loaded cytokines like BMP-2 could be avoided. Thereby, the needed BMP-2 dose for a treatment of critical sized bone defects could be significantly reduced.

These three types of scaffolds have been fabricated with the following sets of experimental parameters: The anisotropic scaffolds (ANI) were cryostructured with an external temperature gradient of $\vec{\nabla} T$ = (4.750 ± 0.0357) K/mm. At a linear interpolated cooling rate of v_c = (-0.806 ± 0.093) µm/min the ice front propagated with a linear solidification velocity of v_s = (505 ± 30) µm/min. The isotropic scaffolds (ISO and ISOCS) were subjected to an external temperature gradient of $\vec{\nabla} T$ = (1.128 ± 0.0357) K/mm. The application of a linear interpolated cooling rate of v_c = (-0.393 ± 0.043) µm/min, led to a linear interpolated solidification velocity of v_s = (476 ± 27) µm/min.
Corresponding cryostructuring diagraphs are displayed in **Figure 4.23** a), where the typical thermal behaviour of an anisotropic structured scaffold may be compared with the two types of isotropic scaffolds. Since the cooling attributes of the isotropic bone scaffolds are coherent to each other only the graph for the ISOCS scaffolds is displayed representatively. Both types of samples first are cooled down linearly with the respective cooling rates, before the temperature diagraphs are superimposed by the latent heat, generated from the fusion water. In the beginning of solidification, this leads to a temperature peak in case of the anisotropic scaffolds.

Again, this appears to be attributed to an equiaxial manifestation of solidification. However, the generation of the initial ice structure at the bottom of the scaffold is causing a general warming of the precursor and thus only seems like an equiaxed solidification from the temperature diagraphs. Since these initial ice crystals feature a preferential growth direction in the plane, perpendicular to the external temperature gradient, they may not be defined as equiaxial.
Both, the anisotropic as well as the isotropic curves feature an inflection point during the further progressing of the graph. The existence of the inflection points is to be explained by the superposition of heat peaks. The initial heat peak, corresponding to the primary crystals, combines with a further heat peak, attributed to the secondary or higher ordered crystal growth, which requires more time to be carried out in completion. This behaviour is expressed more distinctly in case of the anisotropic scaffolds, since here the precursor reaches a lower temperature within a shorter time than the isotropic structured precursors.

The elementary composition of the resulting bone scaffolds was analysed by Energy Dispersive X-ray spectroscopy (EDX) (**Figure 4.23** b) - d)). Due the equivalent precursor compositions the spectra of ANI and ISO scaffolds reach similar values of ca. 40.4 wt% Carbon, ca. 11.2 wt% Nitrogen, ca. 23.6 wt% Oxygen and ca. 23.6 wt% Calcium and for the dominant peaks, while ca. 0.7 wt% Phosphor and ca. 0.4 wt% Sulphur have been detected for the minor peaks. The chondroitin sulphate containing ISOCS scaffolds reach values of ca. 27.7 wt% Carbon, 4.8 wt% Nitrogen 0.8 wt% Phosphor and 33.5 wt% Calcium. In contrast to the ANI and ISO scaffolds, the ISOCS scaffolds reach values of 31.5 wt% Oxygen and 1.6 wt% Sulphur, which correspond to a significant increase of the sulphate groups due to the addition of GAGs. As residues from the collagen isolation, also Sodium and Chloride were detected in all the captured EDX spectra.
Admittedly, EDX does not represent the most optimal method for analysing partially organic samples, but nonetheless the expected ranges of elementary compositions are matching with the measured ones. Since the sample coating was performed with a thin layer of carbon and platinum, a small fraction of the respective peak areas is to be attributed to the coating. This is of special importance for the Phosphor peak which is superimposed by the stronger Platinum peak with energetically close K_α radiations.

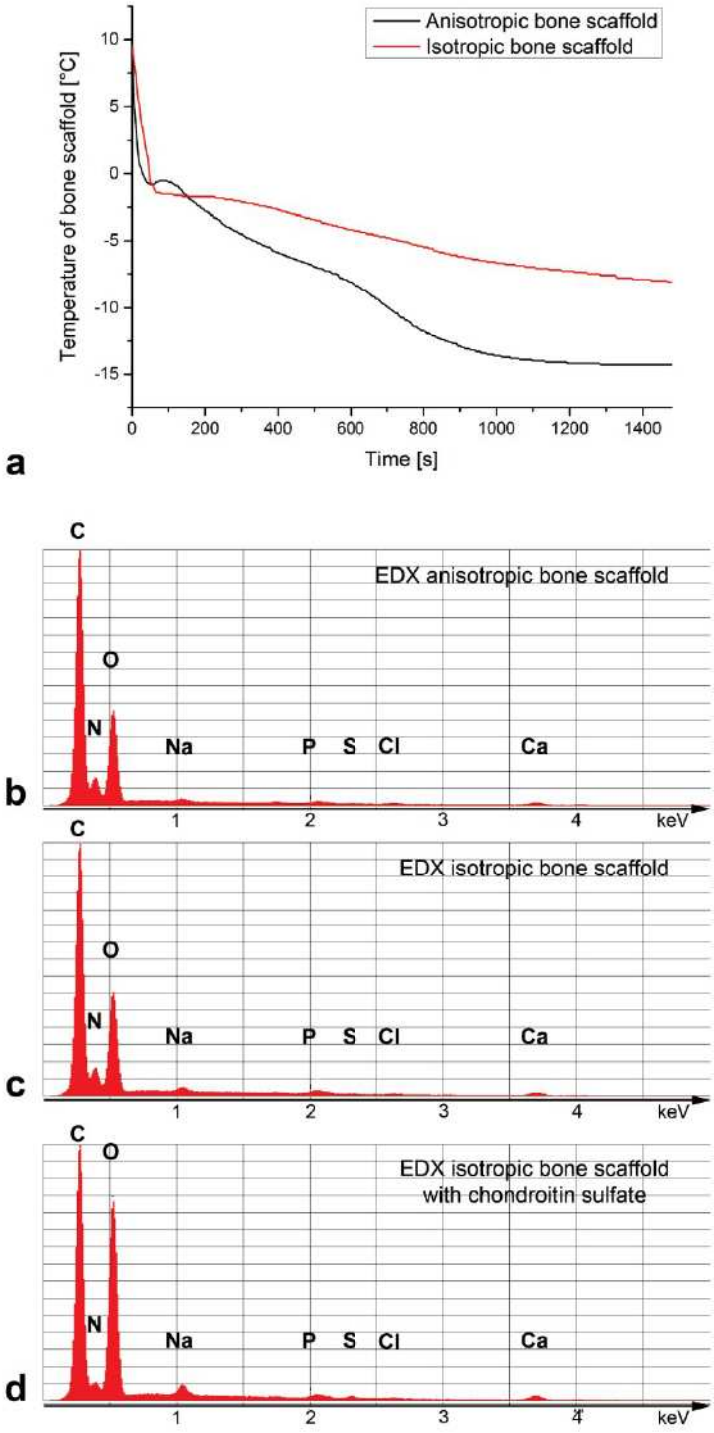

Figure 4.23: a) Temperature diagraphs during preparation of cryostructured anisotropic and isotropic bone scaffolds. c) - d) Energy Dispersive X-ray spectra of all three types of bone scaffolds.

The resulting bone scaffolds are depicted in **Figure 4.24**. All three types of cylindrical bone scaffolds (ANI, ISO and ISOCS), intended to fill a rat femur critical sized defect, are photographed in **Figure 4.24** a). Sub-micron hydroxyapatite crystals which are adhered to the inner scaffold surface are standing off the composite matrix structure and create a huge surface area (**Figure 4.24** b)).

A cross section through a wall between the pores is presented in **Figure 4.24** c). The ca. 0.5 µm thick walls consist of a homogeneous composite structure of collagen I, hydroxyapatite (and chondroitin sulphate in case of the ISOCS scaffolds). A random distribution of the cuboid shaped hydroxyapatite crystals is present. Cross sections, perpendicular to the basic surface of the cylinder samples, reveal the inner pore structure of all three types of scaffolds:

In case of the ANI scaffolds, a homogeneous, anisotropic aligned pore structure is present. Channel pores featuring small cross section pore widths of (65 ± 25) µm are supported by collagenous fibre pillars (**Figure 4.24** d)). **Figure 4.24** e) and f) give insights into the random pore structure of the isotropic scaffolds ISO and ISOCS, respectively. The spongy irregular shaped pores of the isotropic scaffolds are interconnected by randomly distributed and sized holes inside the pore walls. For the ISO scaffolds, the diameter accounts (88 ± 35) µm, and for the ISOCS scaffolds (93 ± 42) µm, respectively. Due to the gelification of collagen I with chondroitin sulphate[277], aggregates are produced, which lead to the formation of some bigger pores and thus, a slight increase of the mean pore diameter in case of the ISOCS scaffolds.

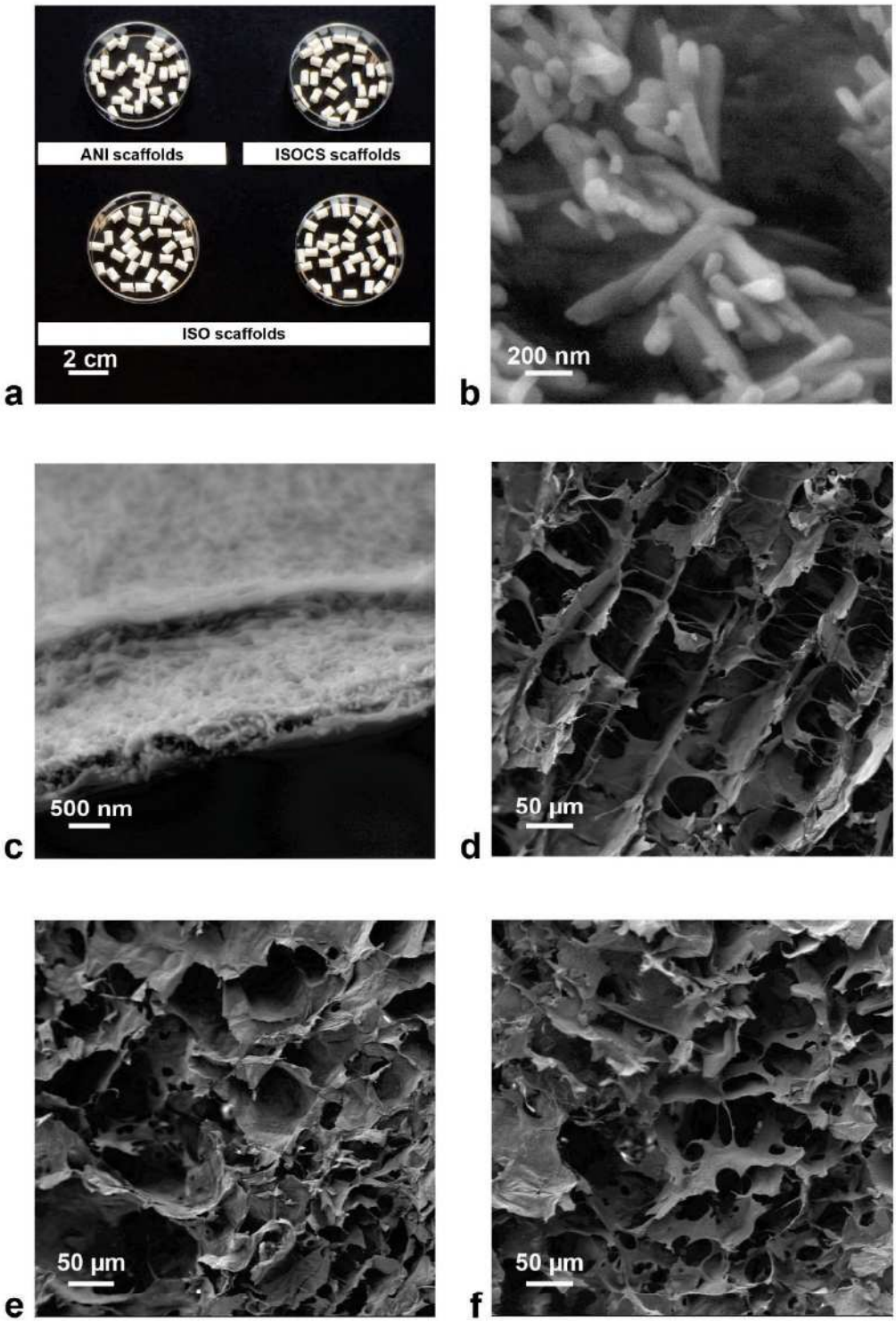

Figure 4.24: Cryostructured bone scaffolds. a) Photography of cylindrical bone scaffolds to fit a critical sized defect in a rat femur (Anisotropic bone scaffolds – ANI, isotropic bone scaffolds – ISO, isotropic chondroitin sulphate containing scaffolds - ISOCS). b) Sub-micron hydroxyapatite crystals are adhered to the inner surface of each scaffold type. c) Cross section of a typical lamellae revealing a homogeneous composite structure of collagen I and hydroxyapatite. d) – f) Cross sections of the different pore structures of ANI (d)), ISO (e)) and ISOCS (f)) scaffolds. (Images b) - f) captured by SEM)

Under physiological conditions, the degradation behaviour of bone scaffolds was analysed, like described in **Chapter 3.5.6**. Over a time span of 11 weeks, the scaffolds were evaluated in terms of change in residual mass, equilibrium water content and free water content like depicted in **Figure 4.25**:

The residual mass (m/mo) was determined as the percental relation between current and initial drained mass. Within the first 10 weeks all the bone scaffolds behaved similarly and showed a mean mass loss of (0.52 ± 0.13) % per day. During the 11th week the ISOCS scaffolds lost clearly more of their drained weight than the ANI and ISO scaffolds (**Figure 4.25** a)).

A calculation of the percental relation of water, which is still bound after draining, to the drained weight of the scaffolds, returned the equilibrium water content (EWC). Again, all the bone scaffolds behaved nearly the same and showed an average EWC loss of ca. (0.0595 ± 0.0059) % per day within weeks 1 to 10. Consistent with the loss of residual mass, the ISOCS scaffolds showed a distinct higher EWC loss after the 10th week (**Figure 4.25** b)). Since this behaviour was only observed for the chondroitin sulphate containing ISOCS scaffolds, it is likely to suspect that the connections upon gelation of collagen I and chondroitin sulphate are less stable towards degradation than the carbodiimide induced cross links.

Additionally, the free water content (FWC) was determined as the percental relation of loosely adhered water to the wet weight of the bone scaffolds. In average the FWC increased for about (0.389 ± 0.020) % per day. Due to the anisotropic channel pores, the ANI scaffolds were capable to release the loosely stored water more easily than the isotropic ISO and ISOCS scaffolds.

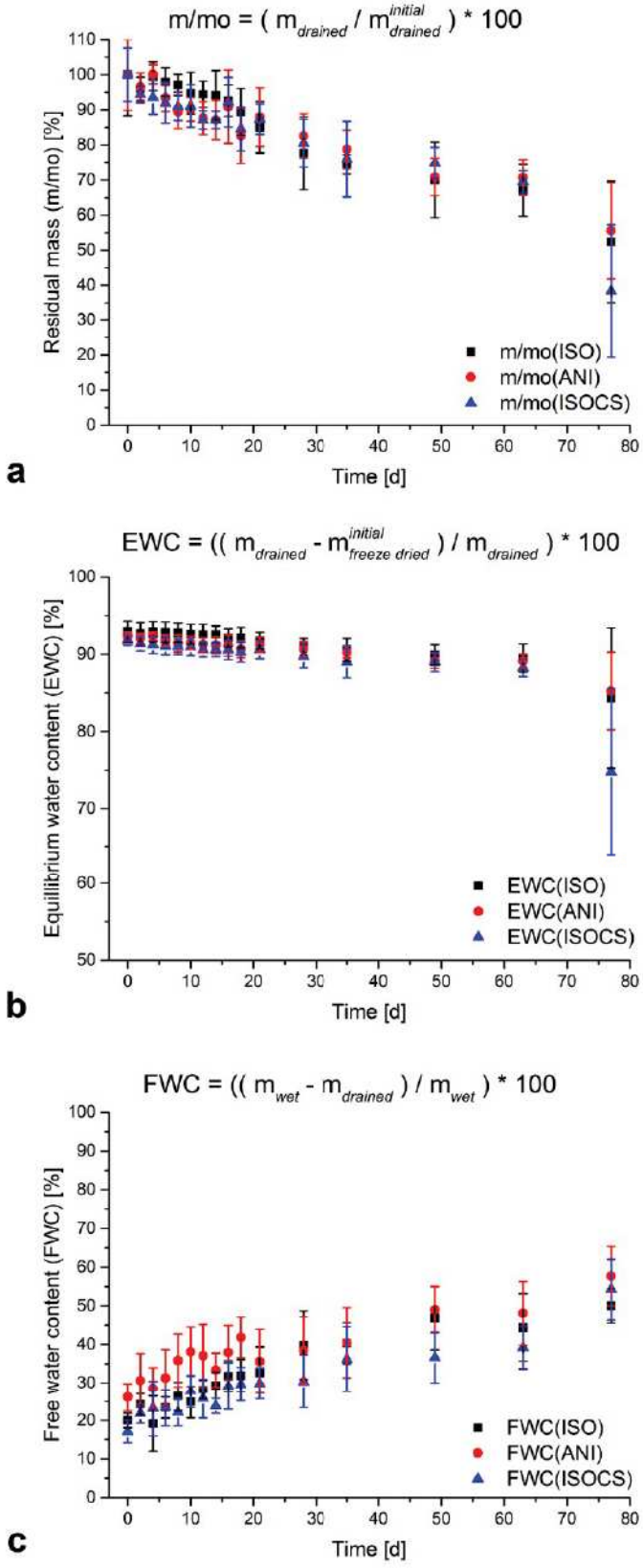

Figure 4.25: Degradation behaviour of the three types of bone scaffolds under physiological conditions (PBS at 37 °C under shaking with 25 rpm). a) Residual mass (m/mo). b) Equilibrium water content (EWC). c) Free water content (FWC).

Taken together, the degradation behaviour of the bone scaffolds under physiological conditions is moderate over a period of ten weeks. Thereby, the suitability for a prolonged cell culture or an *in vivo* implantation might be given. Admittedly, such a degradation model cannot recapitulate all the processes, which are to be expected *in vitro* or *in vivo* due to a lack of enzymes, cellular remodelling and liquid perfusion. After eleven weeks, the breakdown of the scaffold structure was clearly recognizable in form of a significant loss in structural integrity. Interestingly, the erosion culminated in a volume degradation, where the interior of the scaffolds was more altered than the outer shell. In case of the isotropic scaffolds, this was to be expected due to the limited diffusion potential of the cross linking agents. Nonetheless, the same processes occurred in case of the anisotropic scaffolds so that it can be concluded, that the carbodiimide based cross linking also yields slightly inhomogeneous results for high concentrated collagen precursors.

With the objective to load bone scaffolds with each 5 µg of rh-BMP-2 a progressive loading procedure was performed as described in **Chapter 3.5.10**. The rh-BMP-2 was produced inside modified Escherichia Coli Bacteria and kindly provided by Dr. Joachim Nickel (Department for Tissue Engineering and Regenerative Medicine, University of Würzburg, Germany).
A release study of the BMP-2 loaded scaffolds was performed, and evaluated according to **Chapter 3.5.10**. The resulting BMP-2 release and retention of all three types of bone scaffolds is displayed in **Figure 4.26**. For the ELISA kit, an accuracy level was set to 130 pg. Below this level the duplicate measurements returned zero or a numerical value. Therefore, the obtained values that are lower than the accuracy level should not be considered for a detailed interpretation.
The released amounts of BMP-2 per measuring day are depicted in **Figure 4.26** a). Only minimal amounts in the ng rage were released within the first two weeks. After this timespan the released cytokine was below the detection limit of the kit. Based on the cumulative release, the percental retention of the BMP-2 was calculated by assuming a successful initial loading of 5 µg rh-BMP-2 for each scaffold (**Figure 4.26** b)). Concluding it can be stated that, the BMP-2 release accounted ca. 0.022 % for the isotropic scaffolds (ISO), ca. 0.043 % for the anisotropic scaffolds (ANI) and ca. 0.089 % for the chondroitin sulphate containing isotropic scaffolds (ISOCS).

Calcium phosphates are known to bare a high binding potential to proteins like BMP-2[278]. Due to the use of sub-micron hydroxyapatite crystals for the generation of cryostructured bone scaffolds, a high surface area with attractive BMP-2 binding sites has been created, so that after all only less than 0.1 % of the initially loaded cytokine is released within 4 weeks.

The ISO scaffolds showed in relation to the ANI scaffolds a higher retention capability. In direct comparison with the ANI scaffolds, a leaching out of the BMP-2 is eased in case of the anisotropic pore structure, reasoned by the possibility of unhindered liquid flow and diffusion in the channel pores. The isotropic pores in turn present a higher hindrance to the distribution processes. In case of the ISOCS scaffolds, the “highest” release was detected although the absolute values were still very small. Nonetheless, an effect caused by the added chondroitin sulphate, which is lowering the retention capability of the scaffolds measurably, seems to exist. A possible explanation of this phenomenon may be represented by the gelification of the chondroitin sulphate together with collagen I during the precursor production: The BMP absorbing hydroxyapatite crystals are more likely to be encapsulated within the collagen-glycosaminoglycan gel. Thus, the BMP adhering sites of the calcium phosphates are not as present to the cytokine as it would have been the case without a further precursor gelification, which reduces the overall retention capability.

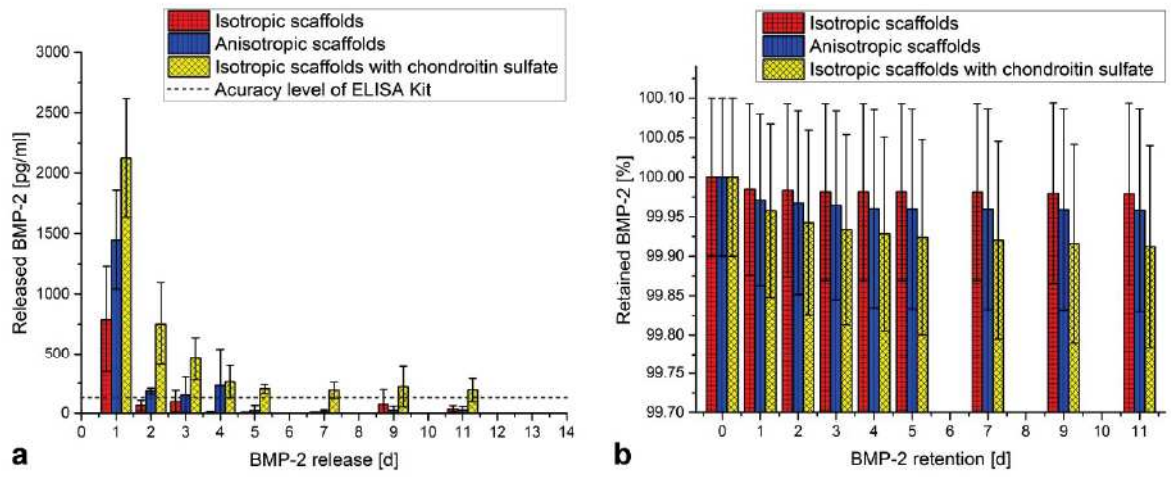

Figure 4.26: BMP-2 release and retention of bone scaffolds. a) Amounts of cytokine released within two weeks. Only values above the accuracy level of the used ELISA Kit are adequate for a significant interpretation. b) BMP-2 retention based on cumulative release. Only less than 0.1 % of the initially loaded BMP-2 is released during the investigated time span.

4.4 Meniscus Scaffolds

4.4.1 Ice Crystal Growth Angled to External Temperature Gradient

As shown in **Chapter 4.1.2** a variation of the temperature gradient may also be used to control the spatial alignment of the ice crystals and the resulting pore structure, respectively. By using smaller temperature gradients, also crystal growth directions which are angled to the external temperature gradient may be achieved (**Figure 4.8**). If the process is performed under borderline conditions of small external temperature gradients which still allow a directional solidification, an ice crystal growth propagating nearly perpendicular to the external temperature gradient can be achieved. Since this pore orientation reassembles the preferred fibre orientation in meniscus tissue in large, the process was tuned to work out with a composition approximating the one of native tissue. The cryostructuring process described in **Chapter 4.1.2** was performed with a collagenous precursor, containing 0.75 % collagen II, 1.75 % collagen I and 10 % of the collagenous dry weight (cdw) in chondroitin sulphate, which was solidified at an external temperature gradient of 4.8 K/mm. For collagen precursors, this absolute value is to be considered as low, since the anisotropic solidification of collagens requires higher temperature gradients than alginate precursors.

Cross section SEM images of the resulting scaffolds may be observed in **Figure 4.27**. An external temperature gradient, close to the borderline case of anisotropic solidification, was running from the top to the bottom of each displayed image, while the upper surface of the scaffold is located upwards. As observable in **Figure 4.27** a), the angle between the propagation direction of the anisotropic scaffold pores and the external temperature gradient moves towards 90 °. A complete perpendicular progression of the ice crystal growth to the temperature gradient is practically not realizable in the test conditions, since the initial crystal phases still originate at the bottom of the precursor containing vessel. Thus, as long as the solidification is intended to be anisotropic, always a slight angle will remain between the achievable structures and the temperature gradient vector.

A closer insight into the microscopic pore structure is given in **Figure 4.27** b). Intra-lamellar pillars support the nearly horizontally aligned lamellar pores. Since these processing conditions represent a borderline case in anisotropic crystal growth, the growth progress of individual ice crystals may occasionally break down. The negative imprint of an ice crystal tip where the growth has ceased is shown in **Figure 4.27** c). In direct comparison to ice crystal tips depicted in **Figure 4.12** c) a strong geometrical correlation is present since the surface of the tip imprint represents rotational elliptically and very smooth. On the right edge of **Figure 4.27** c) a rim is present below the tip imprint. This rim is originating from the primary dendritic growth processes as discussed in **Chapter 4.1.3.2**.

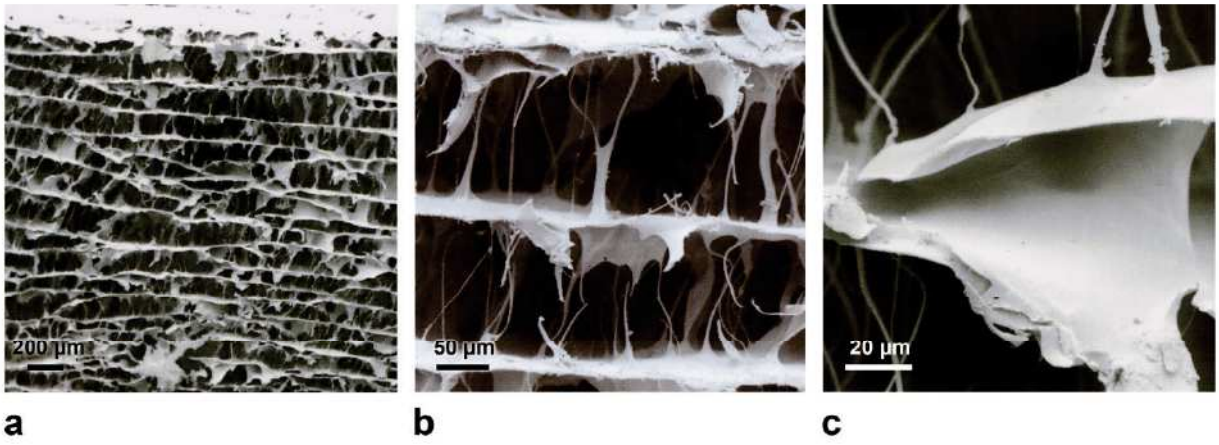

Figure 4.27: SEM images of scaffolds describing the borderline case of anisotropic solidification for low temperature gradients. a) The anisotropic scaffold pores proceed nearly perpendicular to the external temperature gradient which was running from the top to the bottom of the image. b) Lamellar pores that are supported by intra-lamellar pillars are formed. c) During this borderline case the growth of individual ice crystals may break down which results in negative shapes of the ice crystal tips.

Thus, also more complex pore architectures may be fabricated by the invented cryostructuring processing route, when the external temperature gradient is adjusted to the respective precursor composition. The next logical step consisted in combining the multi zonal approach with a tissue mimetic pore orientation. On top of this, also the production of complete meniscus scaffolds featuring an authentic shape and size was possible, since the ACD was designed to allow a scaffold production with clinical relevant dimensions. Consequently, the application of the afore mentioned principles may be used together with anatomically shaped scaffold moulds to create a novel biomimetic meniscus tissue engineering approach.

In order to shape the precursors during solidification inside the ACD, moulds or temperature controllable bodies may be used (**Figure 4.28** a), b) and literature[279]). These feature a negative imprint of the desired scaffold shape, in this case a meniscus, and may be fabricated out of metals (like Aluminium) or polymers (like Polytetrafluorethylene, Polyvinylsiloxane or Polystyrol).

Again, the proof of principle was performed by using pigmented 5.5 wt% alginate precursors (**Figure 4.28** c)) with a blue colouring for marking the inner meniscus zone (IM) and orange for the outer meniscus zone (OM). The cross section in the centre of **Figure 4.28** c) shows the successful tissue mimetic generation of continuous pores throughout both zones. Admittedly, the propagation of the pores did not work out as intended throughout all regions the complete meniscus scaffold in these early stages of development, but since the process functionality was generally proven, the transfer to collagenous precursors was approached.

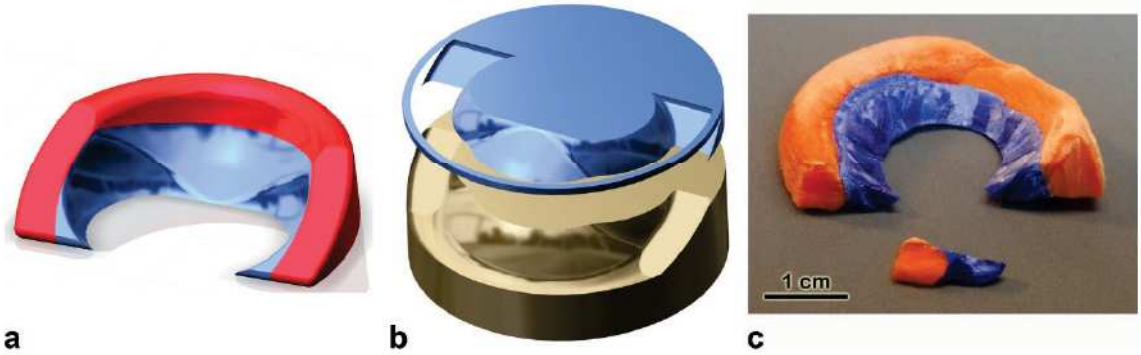

Figure 4.28: CAD design of bi-zonal meniscus scaffold (a) and temperature controllable bodies (b) to shape the precursors during solidification. The proof of principle was performed with pigmented alginate precursors (c).

4.4.2 Cryostructured Meniscus Scaffolds

According to the literature[116,118,121,127,280,281] it may be collated, that the extracellular matrix of native meniscus tissue is mainly build up out of an inner meniscus zone, consisting of ca. 3/5 collagen II, ca. 2/5 collagen I and ca. 10 % cdw in GAG and an outer meniscus zone consisting of collagen I with trace amounts (< 1 % cdw) of GAG. In order to find precursor compositions fulfilling the structural pore alignment after cryostructuring and biomimetic composition at the same time, the following ranges of protein concentrations have been screened: 1.80 % - 0.75 % collagen II, 1.75 % - 0.80 % collagen II and 0.25 % - 0.008 % cdw chondroitin sulphate as GAG.

Finally, the most successful results were achieved by preparing an inner meniscus precursor (IM) featuring 1.2 % collagen II, 0.8 % collagen I and 0.2 % chondroitin sulphate, together with an outer meniscus precursor (OM) consisting out of 1.0 % collagen I and 0.008 % chondroitin sulphate. Hereby, 0.5 mol/l acetic acid was used as solvent for each precursor.

For the preparation of the meniscus scaffolds, the ACD was mounted with the IAG depicted in **Figure 4.3** c) and the cryostat cooled the heat exchanging unit of the ACD to a temperature of -25 °C. A meniscus mould was used to generate the outer scaffold shape. The PEs were supplemented with the current necessary, to generate an outer temperature gradient of (2.464 ± 0.035) K/mm.

When the cryostructuring unit of the ACD was near thermal equilibrium, 5.0 ml of the OM precursor and subsequently 2.6 ml IM precursor was applied to create the outer and inner meniscus zone of the scaffold, respectively. The precursor preparation followed the procedure described in **Chapter 4.1.3.1**, while the directional solidification was performed with a linear interpolated cooling rate of (-0.322 ± 0.014) K/min which led to a linear interpolated solidification velocity of (195.9 ± 8.7) µm/min. Afterwards, the combined precursors were lyophilized and covalently cross linked by carbodiimides as mentioned in **Chapter 4.1.3.3**.

A graphical expression of the cryostructuring procedure can be observed in **Figure 4.29** a). The temperature diagraph is depicting the thermal precursor alteration during directional solidification upon the subsequent addition of both precursors (green = OM/outer meniscus zone and yellow = IM/inner meniscus zone) to yield a meniscus scaffold as shown in the inlay. The linear cooling of the OM precursor is superimposed by the heat of fusion which again shows in a small pseudo equiaxial manifestation of solidification. As described in **Figure 4.12** and **Figure 4.13** the lamellar solidification is progressing faster for primary crystals, whereas the final structure is depending on the slower growth of dendritic side branches. This corresponds to the temperature diagraph, where a bigger amount of heat is generated in the beginning of the solidification before the slope of the temperature graph is decreasing again. When the temperature is approaching an equilibrium value, the IM precursor is added and the mentioned processes proceed again.

In agreement with the CAD drawing, the resulting scaffold, as depicted in **Figure 4.29** b) is build up out of an inner meniscus zone (IM) and an outer meniscus zone (OM). Although both precursor materials appear whitish, the transition between both zones may be recognized as a change in the white intensity. Since the processed collagen II material is more dense and white appearing than the used collagen I material, the IM zone also appears more whitish than the OM zone. The anterior and the posterior horn of the meniscus scaffold have both been sectioned off to reveal the inner pore structure of the scaffold.

A higher magnification of the inner pore structure can be observed in **Figure 4.29** c). The pores inside the scaffold are propagating through both scaffold zones over large length scales, while approximating the preferential alignment of the collagenous fibres inside native meniscus tissue[122]. Due to the considerable mass of solidified OM precursor, the smaller mass of IM precursor was subjected to additional cooling during the cryostructuring process, which led to the formation of smaller cross section pore diameters in the IM zone than in the OM zone.

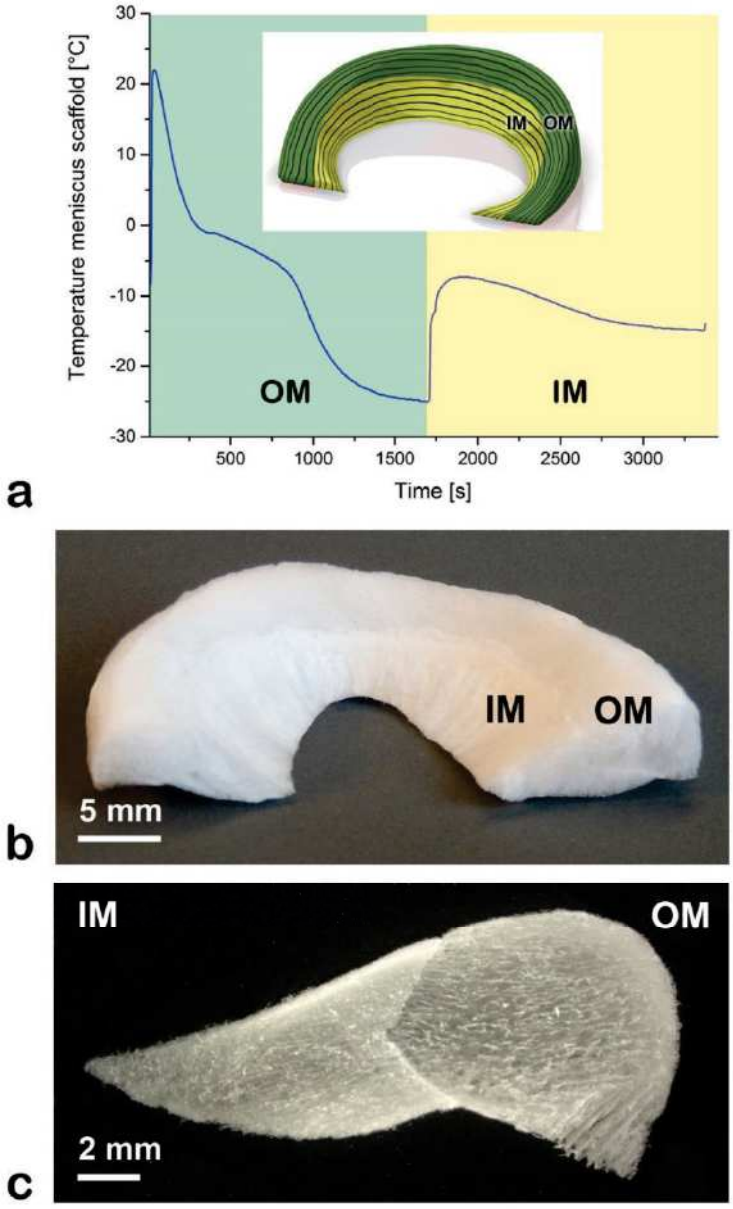

Figure 4.29: Biomimetic meniscus scaffold. a) Cryostructuring graph documenting the directional solidification of inner (IM) and outer (OM) meniscus precursors. Inlay: CAD image of meniscus scaffold indicating a preferential pore alignment through inner (IM) and outer (OM) meniscus zone. b) Photography of macroscopic meniscus scaffold featuring an authentic size and shape. c) Light microscopic image of a cross section revealing the tissue mimetic microstructure.

A closer insight into the scaffolds microstructure can be gained by consideration of cross section SEM images (**Figure 4.30**). Due to the differing pore sizes the interface between the finer IM and the comparably coarser OM zone is clearly recognizable. By using the above mentioned parameters, the process could be tuned to an extent, that the curved pathway of the ice crystals has not been interrupted upon their way through both precursors (**Figure 4.30** a)).

The mechanism behind this effect is revealed by **Figure 4.30** b). The interface between the right OM zone and the left IM zone is recognizable by off standing collagen smithereens. These resulted from the proteins that have been concentrated in front of the ice crystal tips during solidification. During addition of the IM precursor, areas which created the smithereens bared a higher temperature because the heat of fusion has been transmitted to them. Reasoned by a combination of these local surface temperature changes together with the mass correlated thermal resistance of the OM precursor a tip splitting of the ice crystals did occur on interface. The smaller cross section pore size in the IM zone was thus a consequence of a higher number of ice crystals which are additionally restrained inside a smaller volume than in the OM zone.

In **Figure 4.30** c) and d) the resulting pore structures for the IM and OM zone can be viewed in detail. In average, the cross section pore diameter accounts to (93 ± 21) µm for the IM zone and (248 ± 63) µm for OM zone. Within both areas, supporting pillars in between the lamella structures can be observed. Closer insights in this architecture can be gained on consideration of **Figure 4.30** e) and f). The waved lamellas feature a smooth surface within the multiple micrometre range. Since the pillar structures are only present in between two opposing lamellas and do not propagate through them, the creation mechanism is to be attributed to the dendritic crystallization during solidification of the precursors. Upon successive growth, the flat lateral surface of the lamellar ice crystals is pushing the solid precursor components aside. At the place where the primary dendritic sprouting originated, the pillars are created by the entrapment of collagenous material in between fusing secondary dendritic crystals. By inspection of a cross sectioned lamella, the laminated inner structure of sub-micron collagen layers becomes obvious. Thus, the growth progression of ice crystals seems to occur in intervals which yield a laminated lamella structure in sub-micron dimensions.

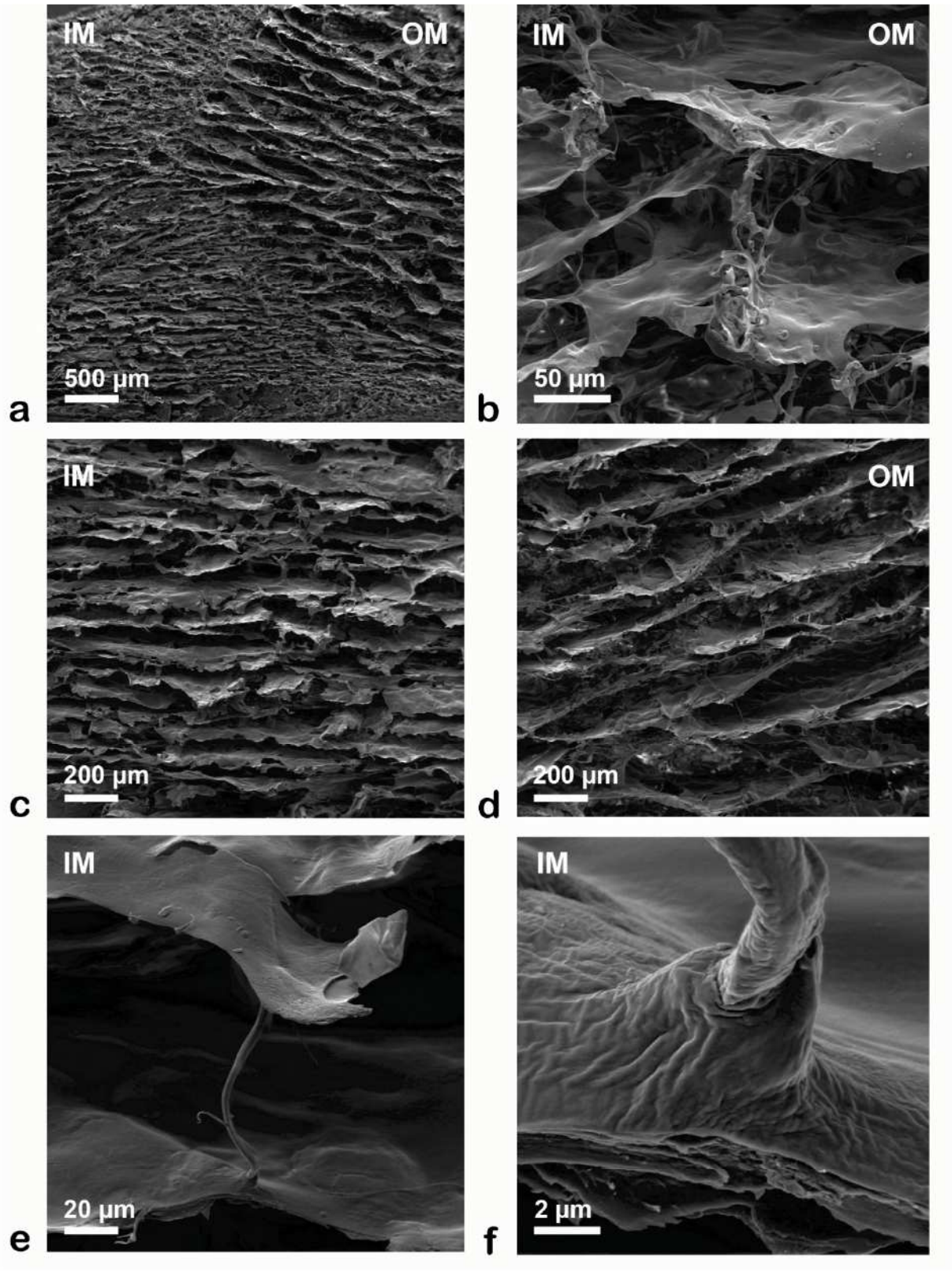

Figure 4.30: Microstructure cross section SEM images of meniscus scaffold. The pores extend continuously between the inner (IM) and outer (OM) meniscus zone (a)). On the interface between both zones, a tip splitting of the ice crystals (b)) leads to a shrinkage of the pore size from the OM (d)) to the IM (c)) zone. Supporting pillars are present in between opposing lamellas (e)), which are constituted from multiple sub-micron thick layers (f)).

If the surface structure of the lamellas in the respective zones is inspected even further, a distinct sub-micron to nanostructure shows up (**Figure 4.31** a), b)). Essentially, this structure may be described as combination of bulk material and nano-aggregates which form a wave like surface structure. Interestingly, both zones show differences in their respective nanostructures. While the height of the wave structures ranges within ca. 300 nm - 400 nm for the IM zone, the ones of the OM zone range within ca. 250 nm – 300 nm. Furthermore, the diameter of the spherical aggregates, which is visible from outside varies between ca. 10 nm - 150 nm for the IM zone and ca. 60 nm – 100 nm in case of the OM zone.

A possible explanation for these wave structures is again to be found in the mechanism of crystal growth during cryostructuring: Upon progressive crystal growth the non-solvent constituents of the precursors are piled up in front of the moving primary ice front and later on also in front of higher ordered crystal morphologies. When certain critical values of piled up mass, precursor flowability, friction and corresponding moving force of the growing ice crystals are reached, the material and ice crystal slip apart. This leaves an accumulation of material behind, which is further modified by equivalent later ripening processes during crystal growth. The differences in the height of the wave structures also correspond to the measured precursor viscosity (**Figure 4.10** b)). The comparably higher viscous OM precursor will slip earlier away from the ice crystals then the IM precursor, which is leading to smaller heights of the wave structures in the case of the OM zone.

EDX was used to analyse the elementary composition of the meniscus scaffold zones (**Figure 4.31** c) and d)). Surely, the accuracy that can be expected from analysing organic samples with EDX is limited, but still insights in composition and purity may be gained from this analysis. In consistency with the differing precursor compositions, the spectra of the meniscus zones reach values of ca. 52.8 wt% Carbon, ca. 18.8 wt% Nitrogen, ca. 21.4 wt% Oxygen and ca. 1.3 wt% Sulphur for the IM zone, while ca. 54.9 wt% Carbon, ca. 21.7 wt% Nitrogen, ca. 15.6 wt% Oxygen and ca. 0.7 wt% Sulphur have been detected for the OM zone. The further subdominant peaks for Sodium and Chloride are owed to residues originating from the saline storage during the collagen I isolation. A visible platinum peak is to be reasoned by the sample coating procedure.

Summarized it can be stated, that the differences between the spectra may dominantly be attributed to the variation of the Sulphur and Oxygen peaks. A pronounced presence of the sulphate groups in the IM zone was to be expected due to the addition of GAGs to the precursors.

EDX was also used to compare the chemical composition of the nanoaggregates with the one of the bulk material, but with respect to the expected measuring accuracy, no significant differences were observable. Therefore, a gelling of the collagen I together with the GAGs on a nanometre range seems not to be an appropriate explanation for the presence of the nanoaggregates. Although their true origin remains unclear, they are suspected to represent a feature of the collagen I since they are found inside both zones.

Obviously, these aggregates show up more prominently in the OM zone than in the IM zone, although they seem to be equally present in both zones. A potential explanation for this behaviour might be found in the density of the materials. To a high degree of likeliness the aggregates will exhibit a slightly increased density, compared to the bulk material. If now the ice crystals push against these small spherical bodies, they will more easily penetrate the less viscous IM zone which results in a lowered visibility. In case of the OM zone the relation of density and bulk material viscosity seems to be more counterbalanced, so that the aggregates show up better on the surface.

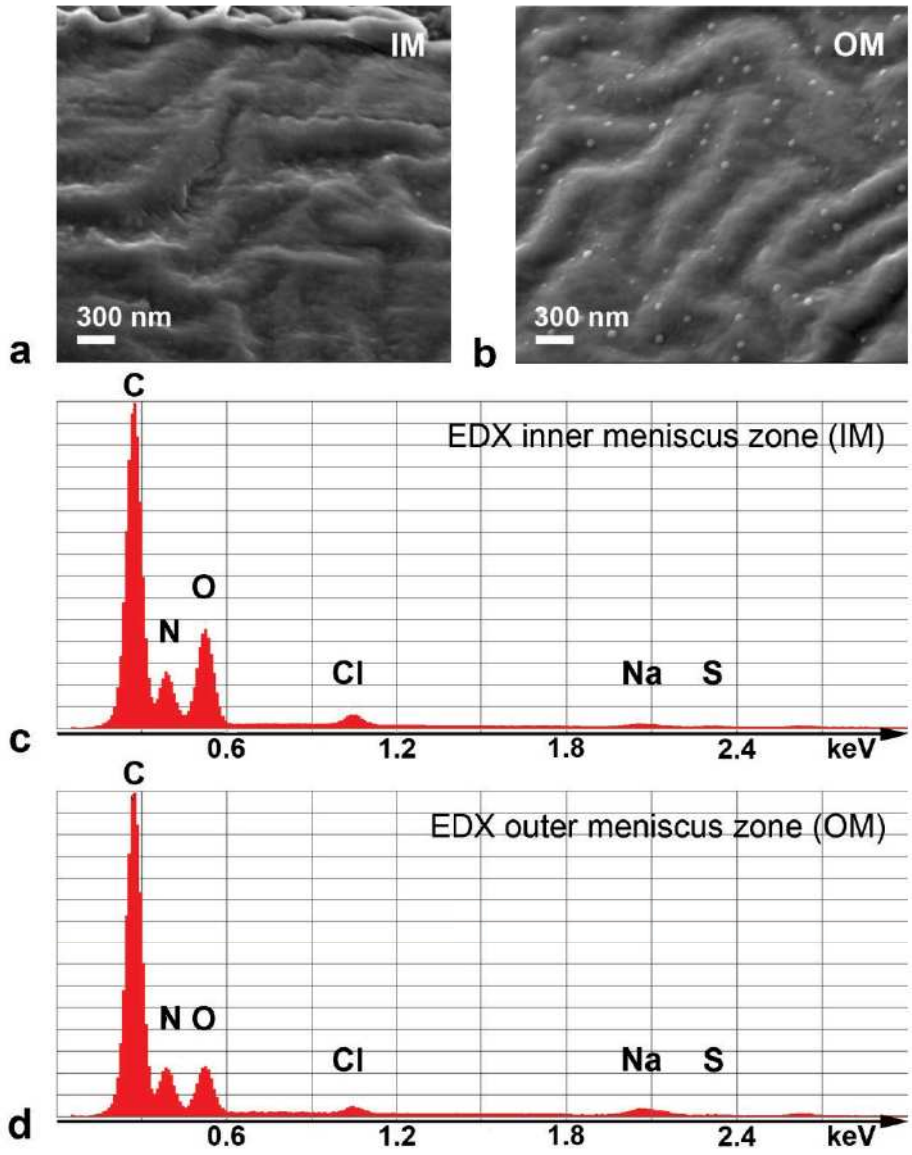

Figure 4.31: Nanostructure and elemental composition of meniscus scaffolds. Surface topographical nanostructure of lamellas in IM (a)) and OM (b)) captured by scanning electron microscopy (SEM). Energy Dispersive X-ray spectroscopy (EDX) of IM (c)) and OM (d)).

As described in **Chapter 3.5.6**, the degradation behaviour of the meniscus scaffolds was analysed during 30 days under physiological conditions. Therefore, cylindrical scaffolds which were consisting entirely out of the IM composition were compared with scaffolds produced only with the OM precursor and also with combined (ca. 50 % IM and ca. 50 % OM) meniscus scaffolds. The results in terms of change in residual mass (**Figure 4.32** a)), equilibrium water content (**Figure 4.32** b)) and free water content (**Figure 4.32** c)) were determined:

A percental relation between current and initial drained mass was set as the residual mass (m/mo) of the scaffolds. With respect to the limited measuring accuracy, all the meniscus scaffolds behaved similarly and showed, in mean, a mass loss of ca. (1.56 ± 0.10) % per day. The equilibrium water content (EWC) was calculated as the percental relation of water, which is still bound after draining, to the drained weight of the scaffolds. Again, all the meniscus scaffolds behaved nearly the same and showed a EWC loss of ca. (0.479 ± 0.041) % per day. Additionally, the free water content (FWC) was determined as the percental relation of loosely adhered water to the wet weight of the scaffolds. The daily increase of the FWC accounted in average to (0.389 ± 0.020) %. Thus, the scaffold mass and amount of bound water shrank with proceeding erosion while the quantity of soaked water increased.

Although the overall degradation of the meniscus scaffolds represents itself quite considerable, they still own enough structural integrity for cell culture. Due to the respective precursor compositions, the OM scaffolds always exhibited the highest loss of mass and EWC, since the collagen I concentration and the presence of gelation inducing GAGs was smaller in the OM precursor than in the IM precursor. The individual scaffolds, which lost up to ca. 50 % of their initial mass featured only a marginal handling stability when they reached this value. In case of the combined meniscus scaffolds, there was no preferential breakdown observable at the interface between both zones.

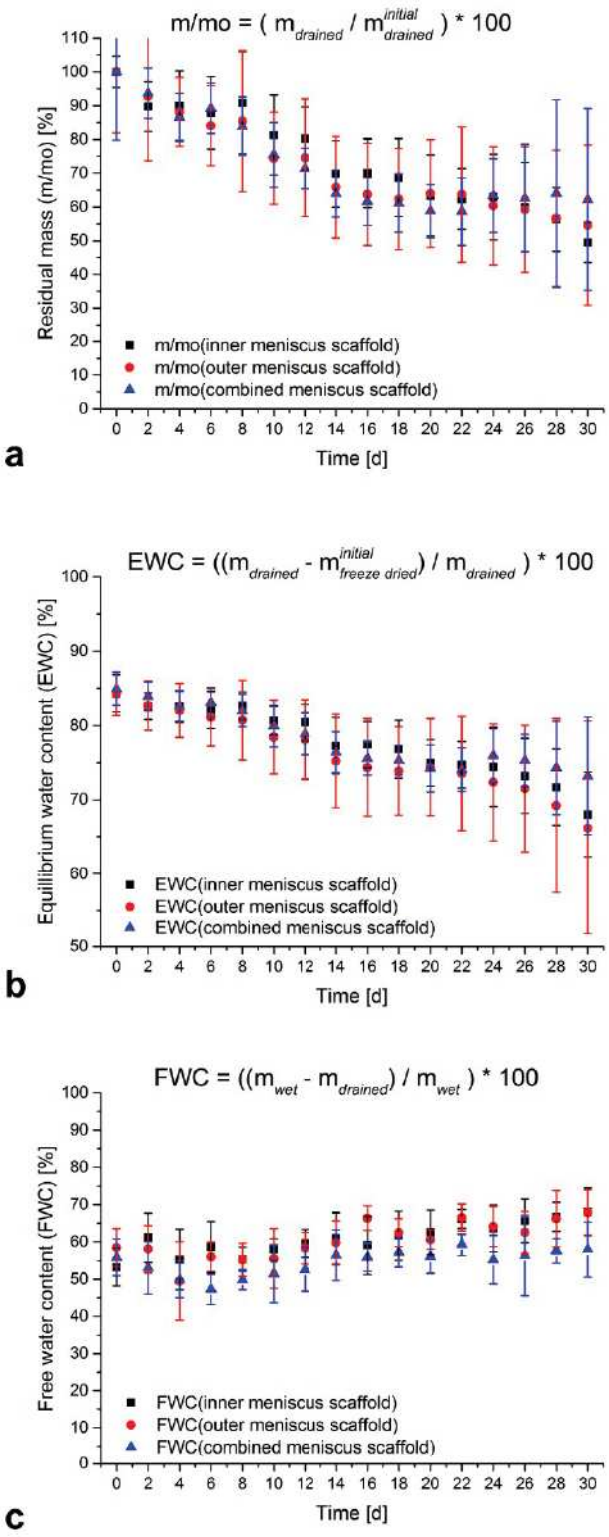

Figure 4.32: Degradation of meniscus scaffolds under physiological conditions (PBS at 37 °C under shaking with 25 rpm). a) Residual mass (m/mo). b) Equilibrium water content (EWC). c) Free water content (FWC).

4.5 Osteochondral Scaffolds

4.5.1 Strategy for Osteochondral Tissue Engineering

As shown in **Chapter 4.1.3.2**, the cryostructuring process may be tuned to yield multi-layered scaffolds with continuous pores proceeding parallel to the external temperature gradient. In order to generate tissue mimetic osteochondral scaffolds, the structure and composition of the native tissue should be considered, to develop an appropriate scaffold design (**Figure 4.33**).

Like depicted in the histological staining and the schematic drawing of native articular cartilage architecture, it may be divided up into three chondral zones which merge into a subchondral zone. Thereby, the chondral zone is mainly composed out of collagen II and GAGs. The concentration of GAGs in the chondral zone increases downwards, displayed in colour from red to yellow to green, until the subchondral zone is reached. This subchondral zone is consisting out of collagen I and calcium phosphates like hydroxyapatite. In the native tissue, the spheroid shaped chondrocytes and their organization are adapted to the specific requirements of each zone (s, m, and d). The spheroids in the scaffold design displayed in **Figure 4.33** c) symbolize cells with zone specific morphology.

A preferential alignment of collagen fibres inside the chondral zone proceeds orthogonal to the chondral surface inside the deep chondral zone, through the middle chondral zone, into the superficial chondral zone, where the fibres are arranged mostly parallel to the chondral surface. Since the deep chondral zone represents the most dominant zone of native tissue, in terms of volume fraction, the scaffold design uses predominantly an equivalent pore alignment. In order to mimic the fibre architecture of the superficial chondral zone too, fibres may be deposited in the scaffold surface by electrostatic spinning. In detail, a fibre alignment parallel to the joint surface can be achieved by using electrospun polymers.

For the reasons already mentioned in **Chapter 4.1.3.2**, a combination of collagen I and collagen II will lead to more promising results for the cryostructuring of the chondral zone, than the use of precursors featuring only collagen II. In order to mimic also the content of GAG in the respective chondral zones, the concentration of chondroitin sulphate (representing the GAGs) was successively increased downwards to the subchondral zone.

This subchondral zone is mainly containing hydroxyapatite in the native tissue, like the bone scaffolds described in **Chapter 4.3**. However, it was decided, to use the calcium phosphate phase brushite instead of hydroxyapatite to yield a completely resorbable/degradable scaffold. In contrast to hydroxyapatite, which features only a poor resorption potential *in vivo*, brushite may be dissolved and remodelled more easily. Thus, the subchondral zone of the scaffold was created by using precursors consisting of collagen I and brushite.

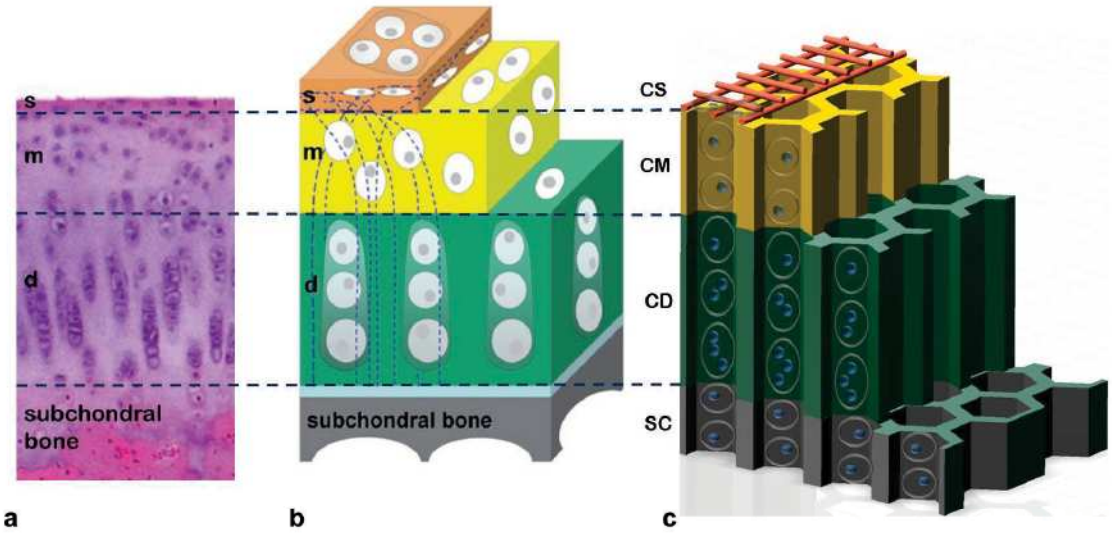

Figure 4.33: Comparison of native osteochondral tissue with scaffold design. a) Hematoxylin-eosin staining of articular cartilage (modified from literature [282]). b) Schematic drawing of zonal articular cartilage architecture[97]. The preferred collagen fibre alignment is indicated by the dashed blue lines. c) Design of cryostructured osteochondral scaffold. The chondral part of native tissue may be divided up into three zones (s = superficial zone, m = middle zone and d = deep chondral zone) which merge into the subchondral bone. In order to approximate the native tissue, the scaffold is mimicking its structure and composition. (CS = chondral superficial scaffold zone, CM = chondral middle scaffold zone, CD = chondral deep scaffold zone and SC = subchondral scaffold zone)

4.5.2 3D Powder Printing of Calcium Phosphates

With the aim to test the application of 3D Powder Printing for the suitability to be combined with the cryostructuring method, the inorganic component of the osteochondral scaffolds was produced as one monolithic piece. Porous cylindrical samples were prepared by printing of a CAD concept into tricalcium phosphate powder. Upon reaction with phosphoric acid coin like brushite samples were produced by hydraulic setting reaction. (**Chapter 3.2.3**)

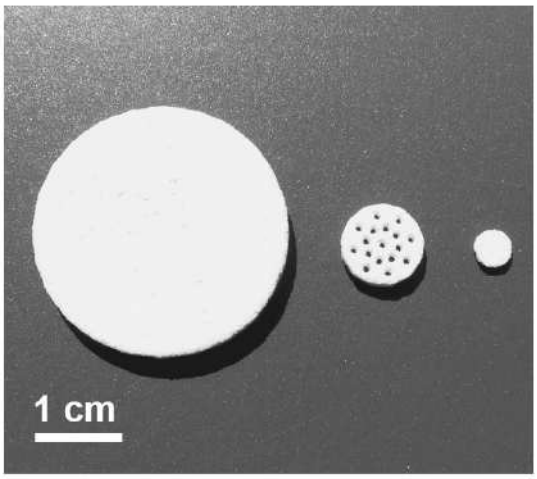

Figure 4.34: 3D printed calcium phosphate substrates in petri dish (left), 48 well (middle) and 96 well (right) formats.

In order to ensure a variable applicability, sample sizes to fit in 96 well, 48 well and petri dishes, with 3.3 cm diameter, were produced (**Figure 4.34**). The sample height corresponded to the diameter with 1 mm, 2 mm and 3 mm, respectively. These substrates could be successfully incorporated into the subchondral zone of osteochondral scaffolds, where they replaced the supplemented calcium phosphate powder. Although the massive structure was present within the subchondral zone, the creation of an anisotropic pore structure in the chondral zone was possible by application of the cryostructuring process.

Thereby, the stiffness of the native subchondral zone was approximated closer, than with the addition of calcium phosphate crystals. Unfavourably, the resulting osteochondral scaffolds showed no relaxation after extreme compression. When the hydrated scaffolds were heavily compressed, most of the water inside the pores was pressed out of the top opening of the pores. The internal porosity of the substrates was either not sufficient in permeability or blocked by biopolymers. Therefore, the channel like pores stayed collapsed after compression, since capillary forces prevented a re-expansion. In order to try to improve this deficit in relaxation potential, the substrates were designed to be perforated by channels with the smallest printable dimensions.

Reasoned by the printer resolution for the used tricalcium phosphate powder, 0.5 mm was found to represent the smallest printable channel size. Additionally, the fraction of channels to total volume, where the structural integrity of the substrates was not altered too much accounted only to 17 % (**Figure 4.34** 48 well format).

Because of the high brittleness of the calcium phosphate bodies before post hardening, a significant increase of this relation would not result in appropriate results. Based on the small channel to volume fraction, the overall effect of collapsed pores was improved, but not a level which would seem promising to create scaffolds that might be used clinically. Moreover, the migration potential of cells through the subchondral zone would be dramatically reduced in comparison to the permeable structure of subchondral zones that may be prepared by adding calcium phosphate powder to the precursors. Therefore, the latter method was chosen over the use of calcium phosphate substrates for the following experiments.

4.5.3 Osteochondral Scaffolds

In order to produce a scaffold featuring a consecutive pore structure while preferably mimicking the zonal composition of native tissue, as well as a beneficial pore size for cellular migration, multiple precursor compositions and cryostructuring conditions were tested. More precisely, the precursor concentrations were varied in the intervals 0.5 – 2.0 % for collagen I, 0 – 3.0 % for collagen II, 0 – 0.8 % for chondroitin sulphate and 0 – 1.8 % for brushite, while the external temperature gradient was changed in between 2 K/mm and 9 K/mm. After evaluation of numerous attempts, the following procedure was found yield the most promising results:

Prior to the cryostructuring, the precursors of the respective zones were prepared according to **Chapter 4.1.3.1**. For the SC precursor 1.2 % brushite and 1.2 % collagen I were used, while both chondral precursors CD and CM were produced from 1.8 % collagen II and 1.2 % collagen I. For the deep and middle chondral zone 15 % cdw and 5 % cdw chondroitin sulphate was supplemented, respectively.

Again, the directional solidification was carried out inside the ACD, which was mounted with the IAG depicted in **Figure 4.3** e). The cryostat temperature was set to -25 °C and the Peltier elements were supplied with the current necessary, to generate an external temperature gradient of $\vec{\nabla} T$= (8.300±0.062) K/mm. When the cryostructuring unit of the ACD was near thermal equilibrium, each 2.0 ml of the precursor were subsequently applied to create the three scaffold zones. In correspondence to the cryostructuring diagraph (**Figure 4.35** a)), the directional solidification was performed with a cooling rate of v_c = (-1.42 ± 0.22) µm/min which resulted in a solidification velocity of v_s = (511 ± 40) µm/min.

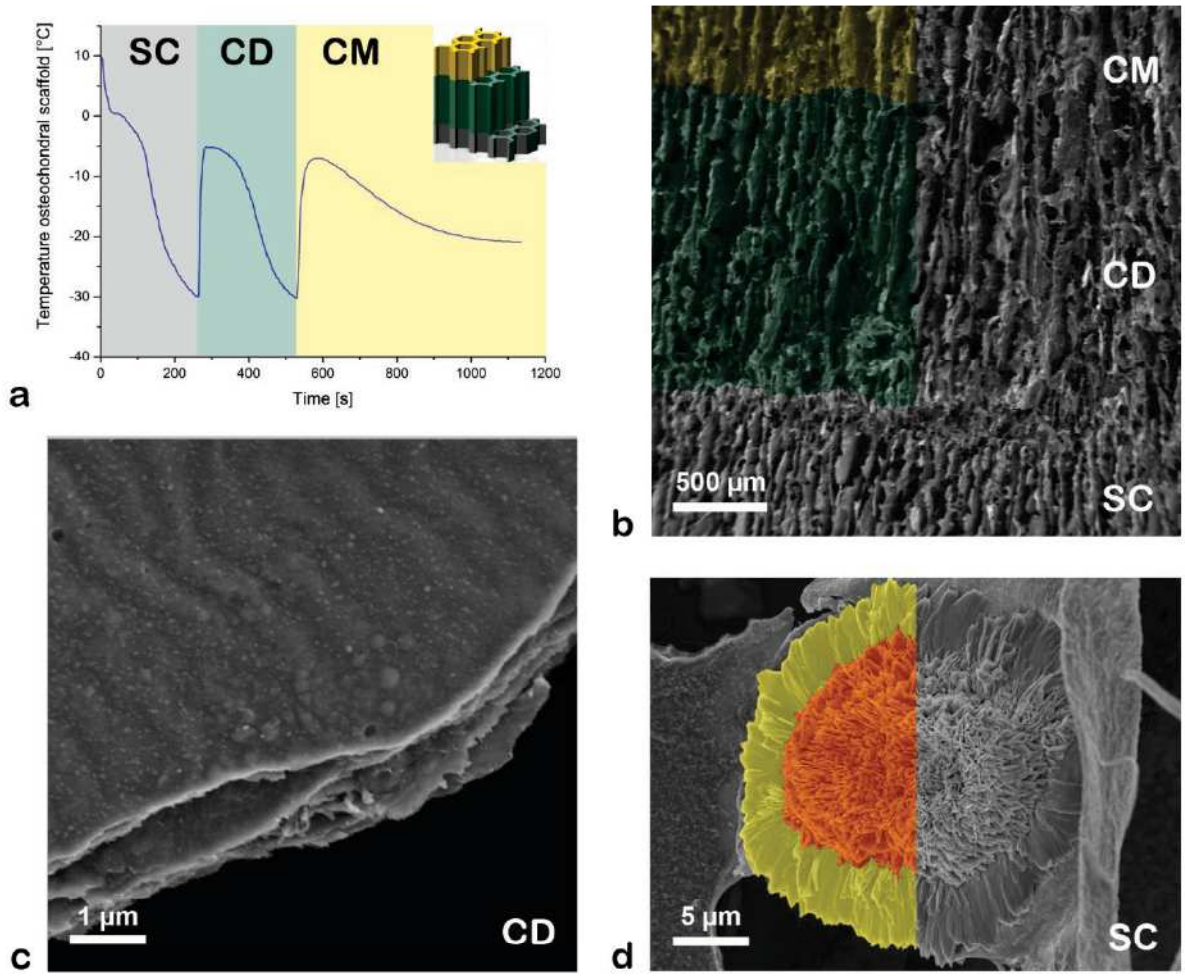

Figure 4.35: Cryostructuring diagraph and cross section SEM images of osteochondral collagen scaffold. a) Temperature progress during directional solidification. The respective scaffold zones may be distinguished by the coloured labelling: subchondral zone – SC/grey, deep chondral zone – CD/green and middle chondral zone – CM/yellow. b) Resulting osteochondral scaffold with fluent interfaces. c) Inner structure of lamella in deep chondral zone. d) A re-precipitation process during the scaffold production is influencing the crystal morphologies in the subchondral zone (bright yellow: residual brushite crystal; bright red: re-precipitated brushite crystallites). The left half of images b) and d) has been coloured to facilitate a differentiation between scaffold zones and crystal morphologies, respectively.

As depicted, the thermal precursor alteration during directional solidification upon the subsequent precursor addition (grey = SC/subchondral zone, green = CD/deep chondral zone and yellow = CM/middle chondral zone) yields an osteochondral scaffold as shown in the inlay. The linear cooling of each layer of precursor is superimposed by the heat of fusion. In the SC precursor this also shows in a small pseudo equiaxial manifestation of solidification. As described for **Figure 4.12** and **Figure 4.13**, the lamellar solidification is progressing faster for primary crystals, whereas the final structure is depending on the slower dendritic branch growth.

Correspondingly, a bigger amount of heat is generated in the beginning of the solidification, before the slope of the temperature graph is decreasing again in the temperature diagraph. When the temperature is approaching an equilibrium value, the next precursor may be added which leads again to the explained processes. Afterwards, the three precursors were lyophilized and covalently cross linked by carbodiimides (**Chapter 4.1.3.3**) to fabricate a monolithic structure.

SEM cross section images of the resulting osteochondral scaffolds are displayed in **Figure 4.35** b) –d) and **Figure 4.36**. Where necessary, the left half of the image has been coloured to facilitate a clear assignment of the respective scaffold zones or the crystallite structures. The tri-zonal but monolithic scaffold is penetrated by aligned pores, whereby the respective interfaces are blending smoothly into each other. As visible in **Figure 4.36** the zonal interfaces are barely detectable, even on a micrometer range. Collagenous smithereens like the ones that could be detected on the interface between inner and outer meniscus zone (**Chapter 4.4**) are only occasionally present. The consecutive lamellar pore structure is extending fluently throughout the entire osteochondral scaffold as it could not been realized before. The scaffold pores feature a mean diameter of (82 ± 25) µm in SC, (83 ± 29) µm in CD and (85 ± 39) µm in CM. They propagate perpendicular to the chondral surface, reassembling the dominant collagen fibre arrangement in native osteochondral tissue[94,97,174]. Thereby they facilitate a good nutrient supply and guidance for seeded cells.

Obviously, the mean pore diameter is increasing a little with the addition of each further zone. If the corresponding errors are compared among each other too, they demonstrate also an increase in the variation range of pore sizes. This is mainly to be attributed to single pores, which continuously grow larger than others. Consequently, the overall average diameter increases together with the respective deviations. The creation of single larger pores can be tracked to the interface between SC and CD, where obviously a fusion of ice crystals occurred in some cases.

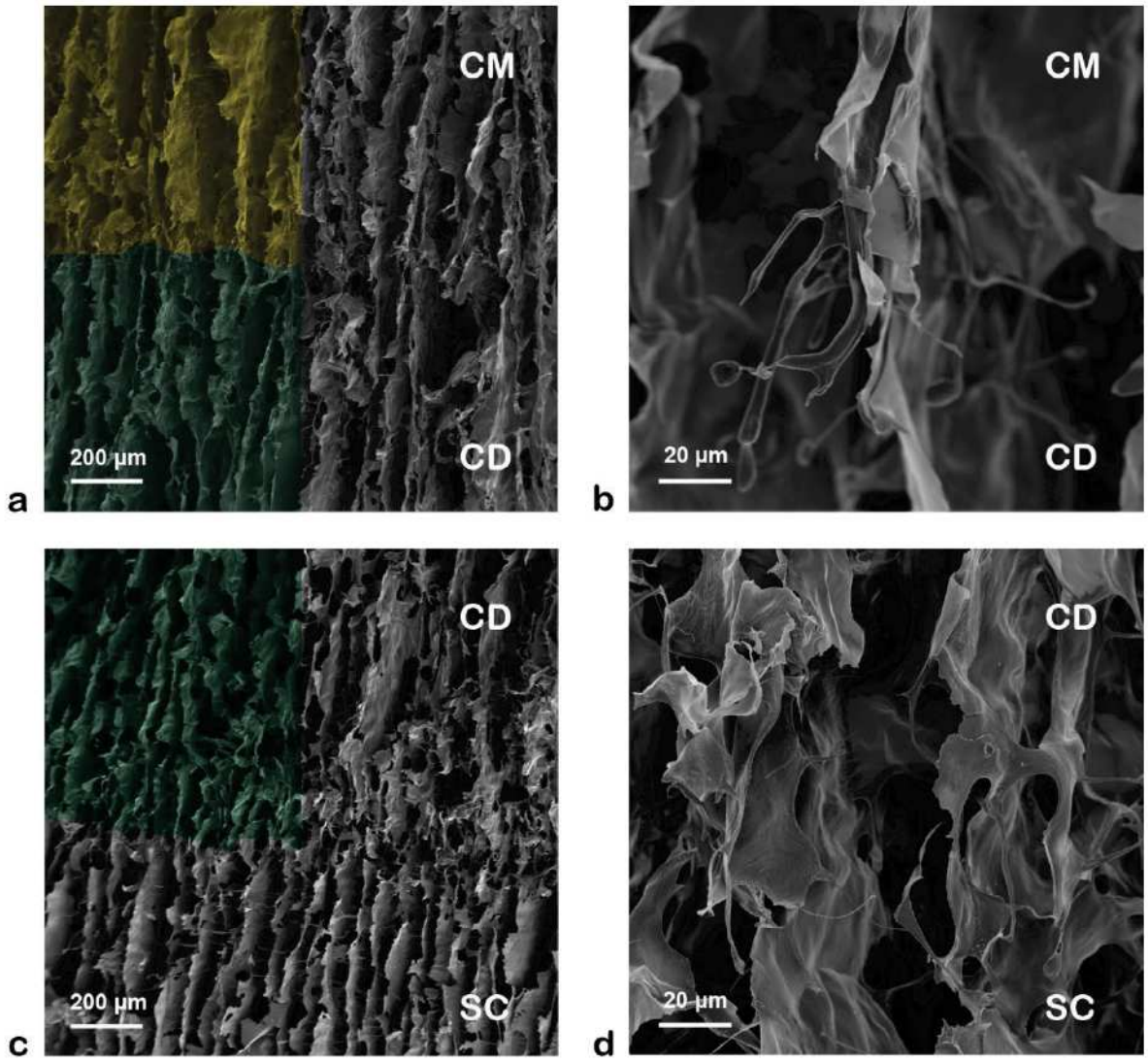

Figure 4.36: SEM cross section images of interfaces between osteochondral scaffold zones. a) Middle (CM) and deep (CD) chondral zone. b) Magnification of a). c) Deep (CD) and subchondral zone (SC). d) Magnification of c). The left halves of images a) and c) have been coloured to facilitate a differentiation of the scaffold zones.

Figure 4.35 c) depicts the surface as well as the inner structure of a lamella in the deep chondral zone. This surface is imposed by a sub-micron structure consisting out of larger waves and smaller aggregates. Furthermore, the sectioning of the lamella revealed a layered inner structure parallel to the lamella surface. Consequently, this laminated inner structure seems to be attributed to the growth progression of ice crystals which occurs in intervals (**Figure 4.13**). The sub-micron structure, found on the outer surface, is not present inside which is leading to the assumption, that it is created during later ripening processes.

In the subchondral zone, the mineralization of collagenous material with brushite crystals can be observed (**Figure 4.35** d)). Usually, these plate shaped crystals, which had been supplemented to the precursors, were arranged to lie flat on the lamellas by the action of ice crystals. Interestingly, the brushite crystals are altered during the preparation, so that new small crystal structures are generated. These are found in the centre of the flat brushite crystals, where they tend to point out of the surface. Thus a flower like crystal arrangement is created, which is indicated by the colouring in **Figure 4.35** d). The bright yellow coloured brushite crystal apparently was exposed to eroding processes, so that the initial smooth surface has been altered. In the centre of the brushite crystals, with an approximate diameter of 20 µm, smaller crystals, which have been formed during the cryostructuring process, are coloured in bright red.

A closer insight into the newly formed crystallites is given in **Figure 4.37** g). Basal diameters, in the range of ca. 0.5 µm – 2.0 µm, were measured for these plate shaped crystals. The elementary composition of the mentioned crystallites was analysed by EDX (**Figure 4.37** h)). The approximate weight percents of the main constituents Oxygen, Phosphate and Calcium accounted to 40.1 %, 24.1 % and 25.8 %. When the particular weight percents are divided by the molar masses of the corresponding elements a Ca : P : O relation around 1 : 1 : 4 is attained. This represents the composition of brushite ($CaHPO_4 \cdot 2H_2O$) or its anhydrous phase monetite. According to the XRD measurements of the subchondral zone (**Figure 4.22** c)), where brushite represented the only detectable calcium phosphate phase, the crystallites consist out of brushite. Reasoned by the SEM sample coating a peak of 9.9 wt% Carbon was detected, which may be used as “baseline” for the interpretation of the organic components of the scaffold zones.

The newly formed crystallites feature significantly smaller sizes than the crystals that have been supplemented to the precursor and are to be identified as brushite re-precipitates. Their origin is to be explained by the acidic conditions during the precursor preparation. Since the precursors are prepared by stirring in 0.5 mol/l acetic acid, the solubility of brushite is high (**Figure 2.2** a)) and the crystals are partly dissolved. Due to the gel like consistency of the precursor, the diffusion of ions away from the etched crystals is limited. During the cryostructuring process, the cryo-concentration of involved ions leads to a shift of the reaction equilibrium to the crystal phase, with the consequence of re-precipitating brushite crystallites.

Because they are predominately found in the centre of the etched crystals an epitactic growth mechanism might be suspected. Nonetheless, the spatial alignment of the crystallites basal planes ((010) crystal plane in **Figure 2.2** b)) is mostly not coherent with the one of the underlying crystal. Therefore, an epitactic mechanism seems not to represent the dominant mechanism behind the re-precipitation.

An observation of the sub-micron to nano scale surface structure of the different zones is displayed together with the chemical composition as determined by EDX in **Figure 4.37** a) - f). As indicated before, a wave structure of the bulk material is combined with spherical aggregates, which shows in the surface appearance of the CD and the CM zones. Both show rather comparable surfaces with wave structures of ca. 1 µm height and aggregates in the range of 30 nm - 120 nm for the CD zone and wave heights of approximately 1 - 2 µm and aggregates between 30 nm - 90 nm for the CM zone, respectively. These differences are again to be explained by the composition which reads: ca. 56.2 wt% Carbon, ca. 17.6 wt% Nitrogen, ca. 21.1 wt% Oxygen and ca. 1.2 wt% Sulphur for the CD zone and ca. 62.2 wt% Carbon, ca. 19.9 wt% Nitrogen, ca. 12.4 wt% Oxygen, ca. 0.8 wt% Sulphur for the CM zone. (**Figure 4.37** a) - d))

By comparison of the contents in Carbon and Nitrogen the limited accuracy of the EDX results for organic samples becomes obvious, since the only difference between the CD and the CM precursors consisted in varied amounts of added chondroitin sulphate. However, these varieties show in the EDX signals detected for Oxygen and Sulphur where a higher content, which is to be attributed to the sulphate groups of the GAG, was recorded for the CD zone.

In case of the SC zone, the previously discussed brushite crystals and crystallites are predominately found in discrete mineral “islands”. Apart from those, the remaining material is forming a unique surface structure of dominating aggregates stand out of wave structures, featuring a height in the sub-micron range. Diameters in the range of 90 nm - 210 nm were present for the aggregates. The elemental composition of ca. 28.9 wt% Carbon, ca. 10.6 wt% Nitrogen, ca. 24.1 wt% Oxygen, ca. 15.4 wt% Phosphor and ca. 15.8 wt% Calcium shows that the presence of calcium phosphates is not restricted to those island structures. (**Figure 4.37** e) - h))

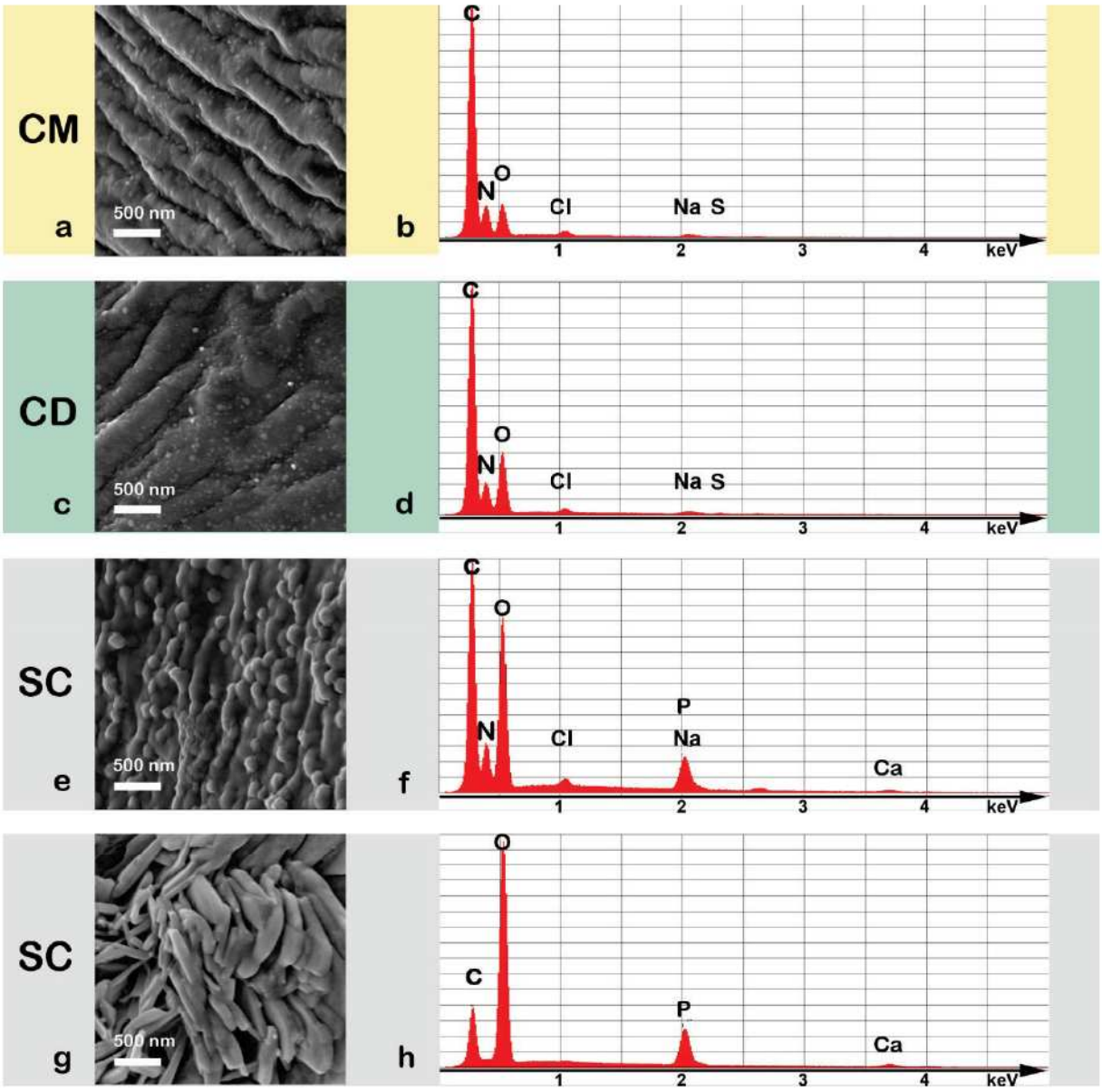

Figure 4.37: Nanostructure and composition of osteochondral scaffold zones. SEM images (a, c, e, g) and EDX spectra (b, d, f, h) of middle chondral zone (CM), deep chondral zone (CD) and subchondral zone (SC). Newly formed crystallites in SC (g)) show calcium to phosphate ratios (h)) that are coherent with X-Ray diffraction analysis of brushite and are therefore supposed to consist of re-precipitated brushite. The nanostructure of the bulk material in all zones (a), c) and e)) shows a combination of aggregates and wave like structures.

Although not visible from the outside, the bulk material is consisting of a brushite and collagen I composite. Since the SC zone represented the only zone where aggregate structures were mainly responsible for shaping the surface, it may be inferred that the aggregates represent themselves to be a feature of the collagen I. Possibly, some kind of mineralisation also occurred inside these aggregate structures. Sadly, their small size aggravates an analysis of single aggregates by EDX.

Such a small area would be quickly altered by the energy input so that the output signal would not be very reliable. However, the used EDX was accurate enough to map the threefold of the CM zone's GAG content in the CD zone. For the inorganic materials the EDX results were coherent with the expectations and the XRD results. In addition to the mentioned signals also minor peaks for Sodium, Chloride and Platinum have been detected in the EDX spectra. While the Platinum peak is to be attributed to the coating for the SEM sample preparation, the signals for Sodium and Chloride are to be assigned to residues originating from the collagen I isolation.
On comparison of the three surface structures it becomes apparent that the mechanism of crystal growth during cryostructuring and the measured precursor viscosity (**Figure 4.10** b)) alone are not sufficient to explain all details of the found structures. The difference in intensity of the waving between the two chondral zones is explainable by a higher structural integrity due to a pronounced gelation upon an increased addition of GAGs in the CD zone.

An overview of the scaffolds macroscopic appearance together with the 3D microstructure is revealed by **Figure 4.38**. The cylindrical scaffolds may be used as osteochondral plugs since they feature clinical relevant dimensions in terms of tissue thicknesses and area. In order to ease a differentiation of the subchondral zone from the more whitish appearing chondral zone, a black suture material is indicating the chondral zones CM and CD, while the subchondral zone SC is marked by a blue suture material.
By µ-CT acquisition the 3D microstructure was made visible. Hereby, the mineralized subchondral part may be identified more clearly due to the higher X-Ray absorbance of the calcium phosphates. A vertical section, depicted in **Figure 4.38** c), allows following the continuous propagation of the scaffold pores orthogonal to the scaffold surface. Within a horizontal section through the subchondral zone (**Figure 4.38** d)) the alignment of the spindle shaped pore structures is documented: During the cryostructuring process, the ice crystals align in domains of preferential directions. These domains seem to feature random sizes and orientations, but their boundaries always build polygonal areas of varying angels.

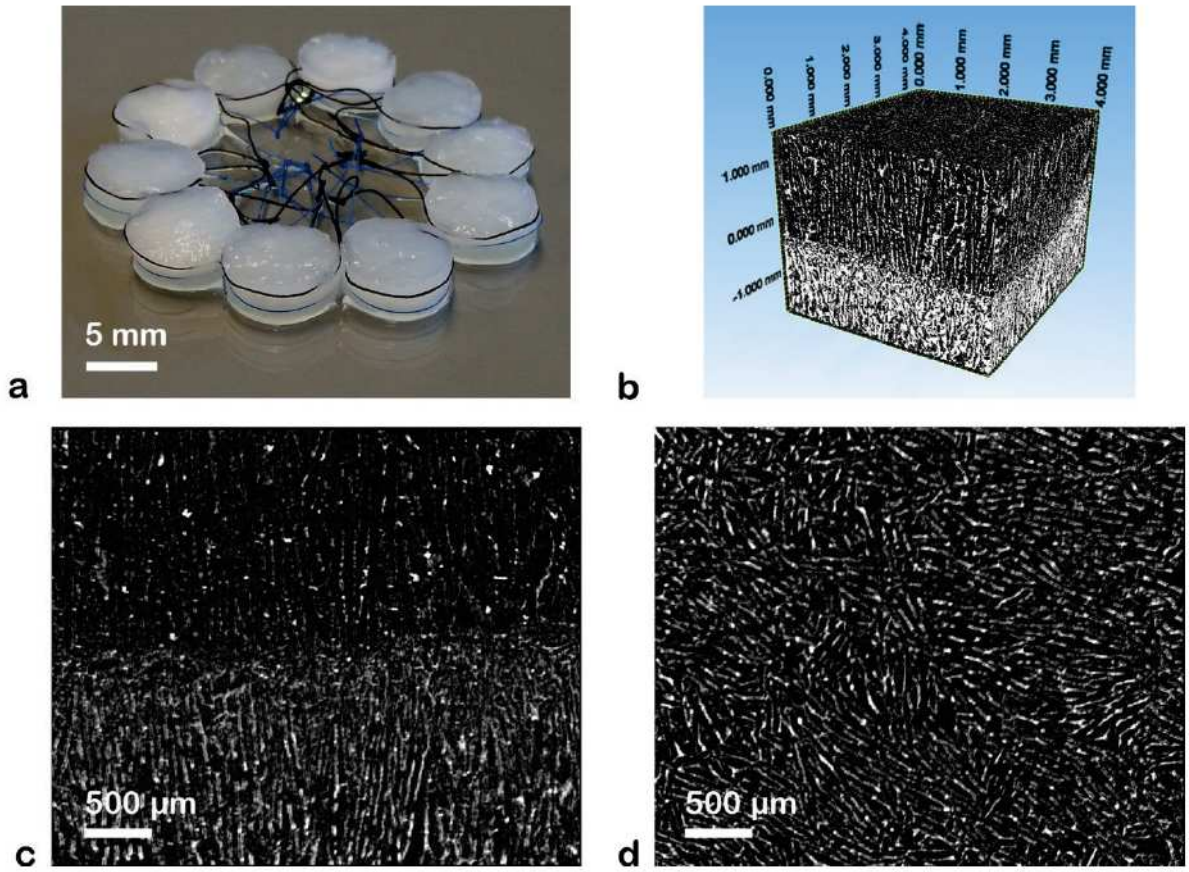

Figure 4.38: Macroscopic appearance and 3D microstructure of an osteochondral scaffold. a) Photography of cylindrical scaffolds with suture material marking the chondral (black suture material) and the subchondral (blue suture material) zone. b) – d) µ-CT images depicting mineralization and pore structure. Calcium phosphates in the subchondral zone lead to an increased signal. c) Vertical section through osteochondral scaffold. d) Horizontal section through subchondral zone.

Since it represents an important factor for *in vitro* and *in vivo* performance, the degradation behaviour of the osteochondral scaffolds was analysed during 30 days under physiological conditions (**Chapter 3.5.6**). By investigating chondral, subchondral and the osteochondral samples, the effect of individual zones on the overall scaffold can be extrapolated. Like for the other scaffold types, the changes in residual mass (**Figure 4.39** a)), equilibrium water content (**Figure 4.39** b)) and free water content (**Figure 4.39** c)) were determined:

Again, the residual mass (m/mo) was set as the percental relation between current and initial drained mass. The subchondral scaffold showed the smallest daily mass loss of ca. (0.393 ± 0.074) %. Chondral and osteochondral scaffolds behaved similarly and showed, in mean, a mass loss of ca. (0.80 ± 0.10) % per day. The percental relation of water, which is still bound after draining, to the drained weight of the scaffolds was calculated as the equilibrium water content (EWC).

In this case, the chondral scaffold featured the least capacity to bind water with a daily EWC loss of (0.125 ± 0.017) %, while the subchondral and osteochondral scaffolds behaved nearly similar by showing an EWC loss of ca. (0.106 ± 0.012) % per day. Furthermore, the free water content (FWC) was determined as the percental relation of loosely adhered water to the wet weight of the scaffolds. The daily increase of the FWC accounted in average to (0.363 ± 0.048) % for the chondral scaffold. With respect to the fluctuations in the data, the subchondral and osteochondral scaffolds yielded a comparable FWC value of ca. (0.47 ± 0.015) % per day.

The differences in the residual mass may be explained by the presence of calcium phosphates in subchondral scaffolds, which do not degrade as fast as the biopolymers. In case of the osteochondral scaffolds this effect does not seem to play a major role, although the mass loss is proceeding a little slower than for the chondral scaffolds. In contrast to this, the presence of calcium phosphates, which induce a higher surface area, influences the water binding capacity in a positive way for both the osteochondral and subchondral scaffolds. The effect of calcium phosphates seems to be dominating the effect resulting from the presence of sulphated GAGs on the EWC capacity. Despite slightly different values were obtained for the variating capacity of loosely bound water, the deviations fade out when the measuring accuracies are considered. Therefore, a discussion of the individual differences in alteration of the FWC does not appear reasonable.

In general, the scaffold mass and amount of bound water shrink with proceeding erosion while the quantity of soaked water is increasing. Featuring a moderate degradation, the osteochondral scaffolds represent themselves suitable for cell culture. Furthermore, the multi-zonal osteochondral scaffolds did not show a preferential breakdown at the interface between the zones.

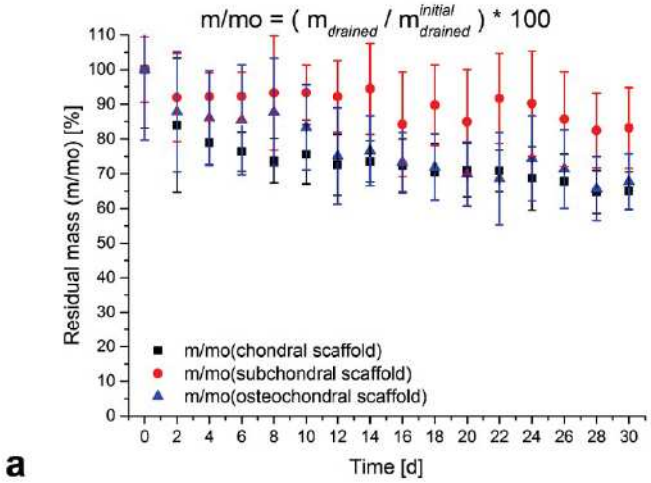

a

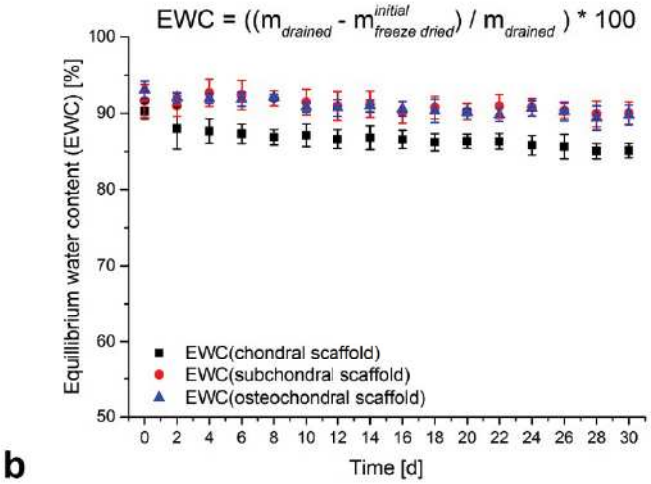

b

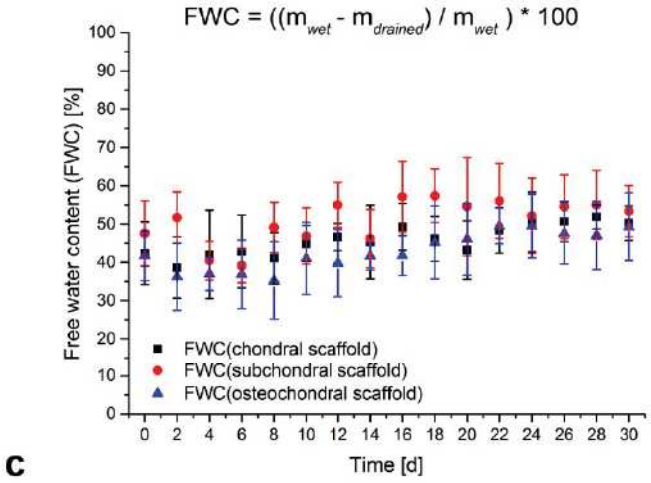

c

Figure 4.39: Degradation of osteochondral scaffolds under physiological conditions (PBS at 37 °C under shaking with 25 rpm). a) Residual mass (m/mo). b) Equilibrium water content (EWC). c) Free water content (FWC).

4.5.4 Preparation of Articular Cartilage Surface by Electrostatic Spinning

In order to realize a fibre alignment parallel to the chondral surface, electrostatic spinning of polymer solutions was applied on the top of the cryostructured osteochondral scaffolds to create the superficial chondral zone (CS in **Figure 4.33** c)). Under the influence of an electrostatic field, a charged polymer solution is accelerated and deposited on a target. During the flight phase, solvent evaporation leads to a transformation from a solution jet to small polymer threads which form a non-woven fabric on the scaffolds.
This way, a matrix consisting out of poly (D, L-lactide-co-glycolide) (PLGA) was deposited on the middle chondral (CM) zone of the scaffold. A tilted cross section view of the CS and CM zone is displayed in **Figure 4.40** a). To ease the zonal assignment, the left half of the image has been coloured. The red marked CS zone is consisting out of the polymeric fibres, while the yellow coloured CM zone represents the underlying cryostructured osteochondral scaffold. Like described in the scaffold strategy (**Chapter 4.5.1**), the fibre alignment of the CS zone proceeds parallel to the chondral surface and the consecutive cryostructured pores propagate orthogonal them. A more detailed image in top view is depicted in **Figure 4.40** b). The electrospun fibres, with a diameter in the micron to sub-micron range, are bridging the scaffolds top pores to form the chondral surface.

Thus, an osteochondral scaffold with zones of tissue mimetic microstructure alignment could be fabricated. Even if the polymeric fibres would be covalently attached to the underlying scaffold, the long term stability of the CS/CM interface remains questionable. During an application, where it is subjected to mechanical forces, the stability cannot be guaranteed, since the number of contact points is small in relation to the covered area. This may also be attributed to the scaffolds top surface, which is uneven on a micrometre scale. At the edges of the scaffold pores collagenous smithereens may stand out, where the polymeric jet entangles preferably because of electrical field peak effects. Consequently, the local adhesion area is to be considered as marginal.

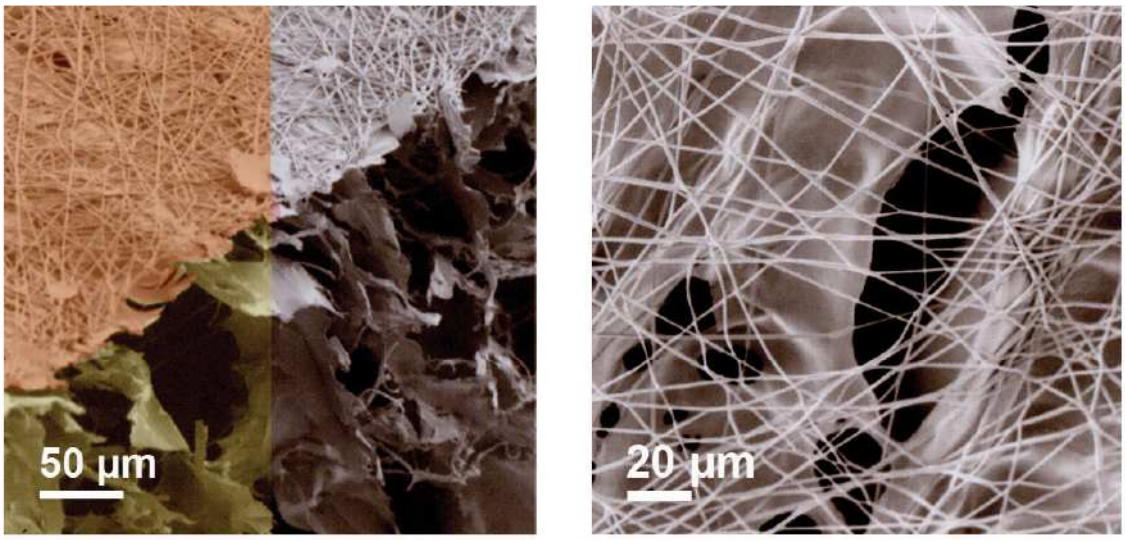

Figure 4.40: Electrospun polymers on osteochondral scaffold. a) Poly (D, L-lactide-co-glycolide) fibres as superficial chondral zone on osteochondral scaffold. The left half of the image has been coloured (red = polymer fibres/superficial chondral zone; yellow = middle chondral zone) to ease a zonal assignment. b) Electrospun fibres are bridging the scaffolds top pores.

4.6 Development of Mechanical Testing Procedure in Confined Compression

The mechanical properties of cell substrates were demonstrated to influence the fate of seeded stem cells significantly[283]. Additionally, the practical requirements to handling and *in vitro* / *in vivo* versatility have to be fulfilled. Therefore, the mechanical testing of scaffolds represents an important aspect to consider. Since unconfined compression testing of hydrogel scaffolds is limited in accuracy due to negligence of the occurring area change while compression, testing in confined conditions seems to be a suitable way to overcome this drawback.

Common dynamic mechanical analysis or unconfined compression measurements lack the mentioned inclusion of area change. For samples like osteochondral scaffolds, testing in confinement represents a better approximation of the scenario after implantation. This mentioned testing is typically performed using porous platens for compression and/or bedding together with a non-permeable confinement[109-114]. Although the according issues due to interdigitation between the sample surface and the porous filter remain a known problem, it is seldom addressed in the literature[25]:

The sample surface is only partially in contact with the solid part of the porous filter while the number of contact points and their total area is increasing with accumulating compression. To overcome these limitations a confined testing setup with massive compressing stamp and bedding in combination with a confinement that allows the displacement of liquids may be chosen.
Commonly measurements in confined compression are performed under the assumption of equilibrium conditions and yield the aggregate modulus; a measure of the tissues stiffness when all fluid flow has ceased. Since the clinical relevant conditions are far away from equilibrium state, a dynamic model was chosen for the evaluation, which allows the determination of the frequency dependent apparent elastic modulus of the system. Technically speaking the elastic modulus is only defined for homogeneous isotropic materials, but nonetheless allows a description of the apparent elastic modulus a comparison to established materials.

4.6.1 Experimental Setup

For each chondral, subchondral, osteochondral, inner meniscus and outer meniscus scaffolds, six cylindrical samples with a uniform diameter of 8 mm and a height of 2 - 3 mm were prepared using a hollow punch. In case of the anisotropic, isotropic and isotropic chondroitin sulphate containing bone scaffolds each five samples were tested with a uniform diameter of 4 mm and a height of 6 - 7 mm.
After storage in freeze dried state, they were rehydrated in phosphate buffered saline (PBS, **Chapter 3.5.5**) one hour prior to testing. The measurements were carried out in PBS at 25 °C using a “Eletroforce 3220” (Bose GmbH, Friedrichsdorf, Germany) with “Wintest 4.1” software. Due to a limitation of the “Wintest 4.1” software to record only 2000 data points per file, the used deformation protocols were carried out with fewer deformation cycles to achieve a better resolution of the captured data. The scaffolds were tested in elastic response inside a custom build confined compression setup coupled to a 2.45 N load cell. (**Figure 4.41)**
To ensure a testing in the elastic range, all measurements were performed within a deformation interval of 10 % of the initial scaffold height. Prior to the measurements, the samples were placed inside the confinement and the force transducer was driven inside the liquid until the sample surface was reached.

After taring of the load cell, the following deformation protocols were measured: linear compression with 0.15 mm/sec; cyclic compression with physiological frequencies of 0.2 Hz and 2 Hz and a high frequency of 20 Hz (each n=5); instantaneous compression with a square function (0.2 Hz, n=3).

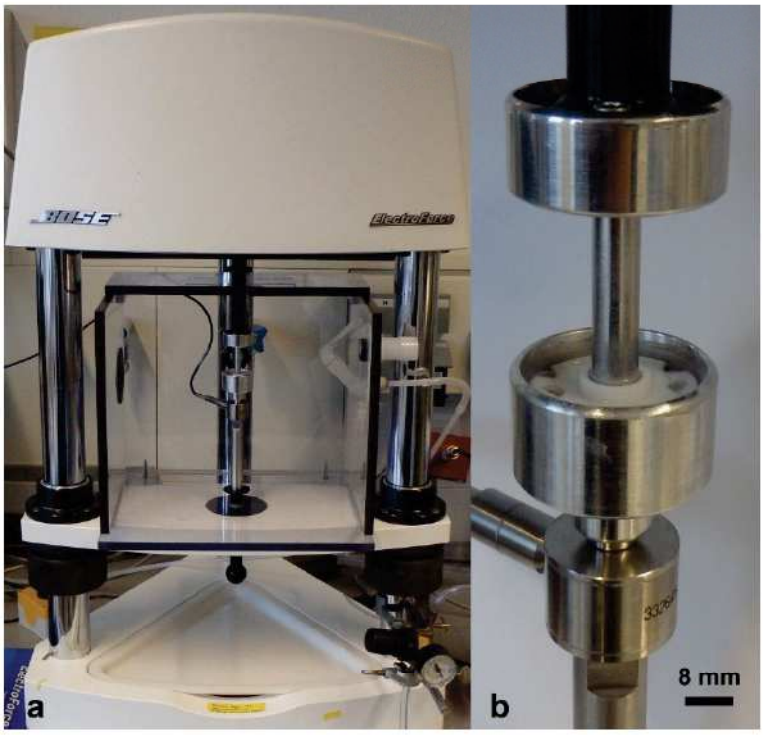

Figure 4.41: Custom build confined compression setup mounted to the mechanical testing device "Electroforce 3220". a) Entire measuring setup. b) Detail view of tight-fitting setup coupled to force transducer (top) and load cell (bottom).

4.6.1.1 Custom Build Confined Compression Setup

A compressing stamp, a confinement and a container represent the sub units that were used to assemble the confined compression setup. Both, the outer diameter of the cylindrical aluminium stamp and the inner diameter of the Teflon confinement correspond to the sample diameter of 8 mm for the osteochondral and meniscus scaffolds and 4 mm for the bone scaffolds, respectively. To enable a measurement of hydrogels in liquid environment, the confinement is fit inside the aluminium container which is filled up with PBS. The sample is placed inside the confinement and stimulated by the compressing stamp.

Figure 4.42 a) is illustrating the setup for an 8 mm sample diameter. While the upper part of the stamp may be connected to the force transducer of the mechanical testing device, the load cell may be screwed on the downside of the container. Channels with 0.2 mm depth in the bottom of the confinement facilitate liquid to be pressed out of the hydrogel samples. Thereby, a continuous exchange of liquid in the confinement and the reservoir is possible through notches in the outer edge of the confinement. (**Figure 4.42** b), c))

In order to ensure that the deviations through the channels in the confinement stay negligible, the sample height should be at least ten times the channel depth. Additional to this, the deformation during the tests is performed within 10 % of the initial sample height so that a confined measurement within the elastic response of the material is given. The friction between compressing stamp and confinement, as well as the shear forces upon liquid displacement represented to be negligible within the measuring accuracy.

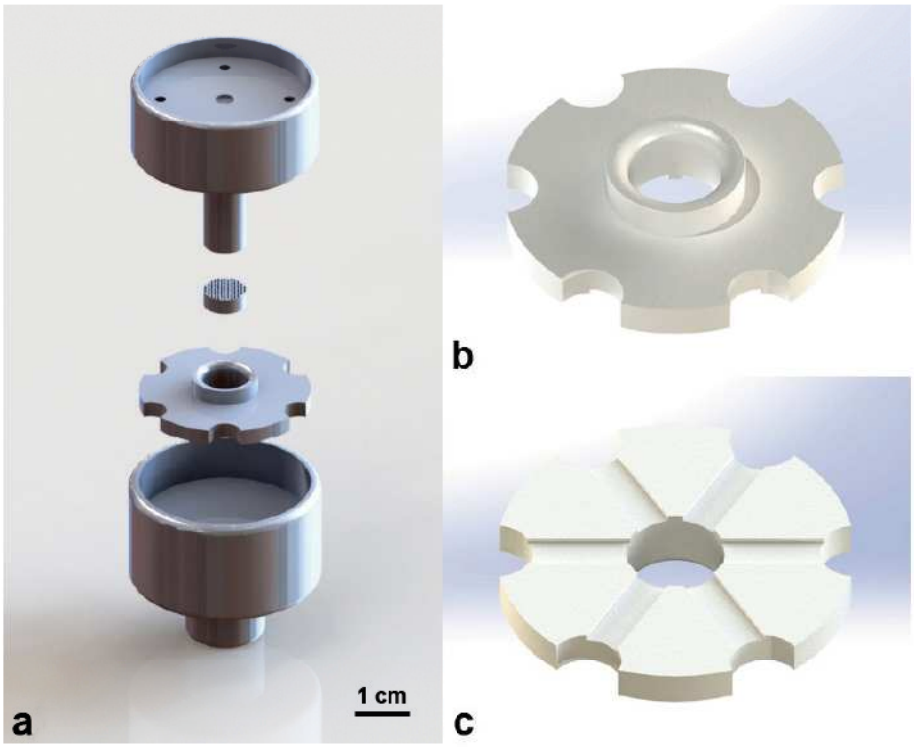

Figure 4.42: CAD design of custom build confined compression setup for 8 mm sample diameter. a) A cylindrical sample is placed inside of a confinement, which is set inside of a container filled with phosphate buffered saline. The sample is stimulated by a piston, which may be coupled to the force transducer of the testing device, while the container is mountable to the load cell. b), c) Top and bottom view of the confinement. A displacement of liquids is facilitated through small channels along the bottom of the confinement.

4.6.1.2 Data Evaluation

All parameters derived by the subsequent methods describe the states of laterally confined scaffolds in PBS as one system. To compare of the evaluation method of the used cyclic mechanical testing, also linear compression was addressed. Therefore, the samples were tested with the confined compression setup using a cross head speed of 0.15 mm/sec. The apparent elastic modulus was calculated as the slope of a linear fit in a compressive strain - elongation plot of the measured data (**Figure 4.44** a) and **Figure 4.45** a)). An analysis of the cyclic mechanical testing was performed according to the following implementations of **Figure 4.43**:

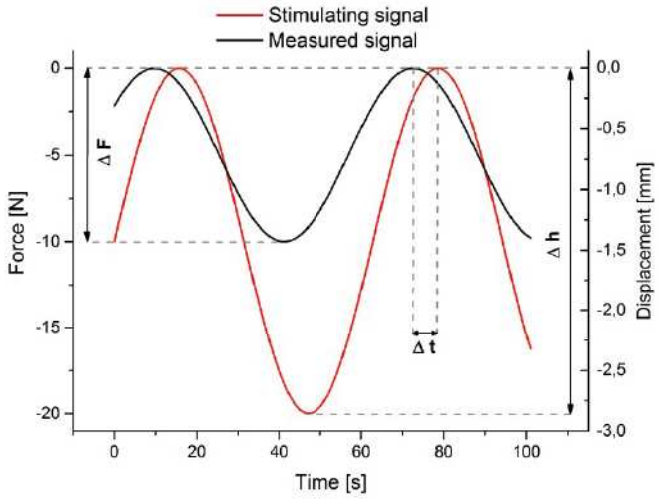

Figure 4.43: Theoretical dataset derived by cyclic mechanical compression. The stimulating and the measured signal are offset by a time shift interval Δt. The associated change in force (ΔF) and sample height (Δh) may be gained out of the measured and the stimulation signal, respectively.

The frequency f and time t depending behavior of the scaffolds forced, dampened oscillation during the cyclic mechanical testing in confined compression may be described by the complex approach

$$z(f,t) = C\, e^{i(2\pi f t+\delta)}, \qquad (11)$$

with amplitude C and phase shift angle δ. The time shift interval $\Delta t(f)$ and the oscillation duration $T = f^{-1}$ are related to $\delta(f,t)$ after the following equation:

$$\frac{\Delta t(f)}{T} = \frac{\delta(f,t)}{2\pi} \Leftrightarrow \delta(f,t) = 2\pi f \Delta t(f). \qquad (12)$$

Hereby, the dissipation factor $tan(\delta)$ may be calculated to express the relation of lost energy (viscous behavior) to stored energy (elastic behaviour) i.e. the dampening performance of the scaffolds inside the measuring setup. Thus, the complex apparent elastic modulus $E^*(f,t)$ is represented by:

$$E^*(f,t) = \frac{\sigma(f,t)}{\varepsilon(f,t)} = \frac{\sigma_{max}\, e^{i2\pi ft}}{\varepsilon_{max}\, e^{i(2\pi ft+\delta)}} = \frac{\sigma_{max}\, e^{i2\pi ft}}{\varepsilon_{max}\, e^{i2\pi ft}\, e^{i\delta}} = \frac{\sigma_{max}}{\varepsilon_{max}}\, e^{-i2\pi f\Delta t}. \quad (13)$$

In order to obtain the apparent elastic modulus $E(f,t)$ the real part of Equation (13) is considered using the previous equations together with the extrema definitions of input stress $\sigma_{max} = \Delta F/A$ and resulting sample strain $\varepsilon_{max} = \Delta h/h_0$:

$$E(f,t) = Re[E^*(f,t)] = Re\left[\frac{\sigma_{max}}{\varepsilon_{max}}\{\cos(-2\pi f\Delta t) + i\sin(-2\pi f\Delta t)\}\right]$$

$$= |E^*(f,t)|\, cos(-2\pi f\Delta t) = \frac{\frac{\Delta F}{A}}{\frac{\Delta h}{h_0}}\, cos(2\pi f\Delta t)\,. \quad (14)$$

Here, ΔF represents the input force and A the confined sample area while Δh and h_0 give the displacement and initial height of the sample, respectively.

Assuming that time and force are associated with the most significant inaccuracies of the measured signals the tolerances for the phase shift angle and apparent elastic modulus are derived by error propagation:

$$\sigma_\delta = \sqrt{\left(\frac{\partial\delta}{\partial\Delta t}\right)^2 \cdot {\sigma_{\Delta t}}^2} = \sqrt{(2\pi f)^2 \cdot {\sigma_{\Delta t}}^2}\,; \quad (15)$$

$$\sigma_E = \sqrt{\left(\frac{\partial E}{\partial\Delta F}\right)^2 \cdot {\sigma_{\Delta F}}^2 + \left(\frac{\partial E}{\partial\Delta t}\right)^2 \cdot {\sigma_{\Delta t}}^2}$$

$$= \sqrt{\left(\frac{\frac{1}{A}}{\frac{\Delta h}{h_0}} \cdot \cos(\delta)\right)^2 \cdot {\sigma_{\Delta F}}^2 + \left(\frac{\frac{\Delta F}{A}}{\frac{\Delta h}{h_0}} \cdot (-2\pi f \sin(\delta))\right)^2 \cdot {\sigma_{\Delta t}}^2}\,. \quad (16)$$

A determination of the scaffolds relaxation behaviour was performed by instantaneous compression using a square function (**Figure 4.47** a)). The relaxation time was set as the time interval between the initial force peak upon deformation and the force relaxation plateau. Thereby, the force relaxation plateau was set as the level which was reached when the signal noise was the only change in the detected force signal for 2 seconds.

4.6.2 Results of Developed Testing Method

Exemplary datasets of linear and cyclic measurements inside the confined compression setup are shown in **Figure 4.44** for an osteochondral scaffold and in **Figure 4.45** for an isotropic bone scaffold.

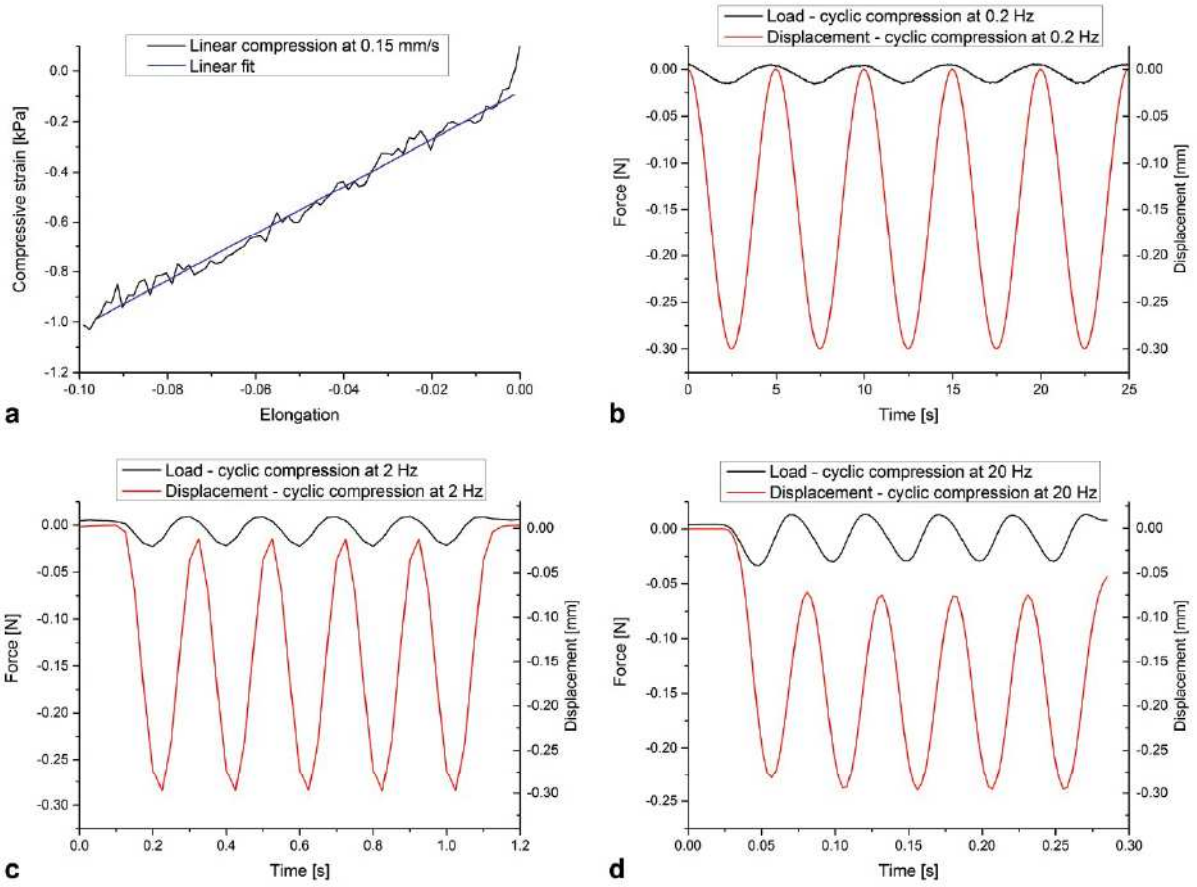

Figure 4.44: Exemplary datasets of a) linear compression with a cross head speed of 0.15 mm/sec and b), c), d) cyclic compression with 0.2, 2, and 20 Hz for an osteochondral scaffold with anisotropic pore structure aligned parallel to the compression direction.

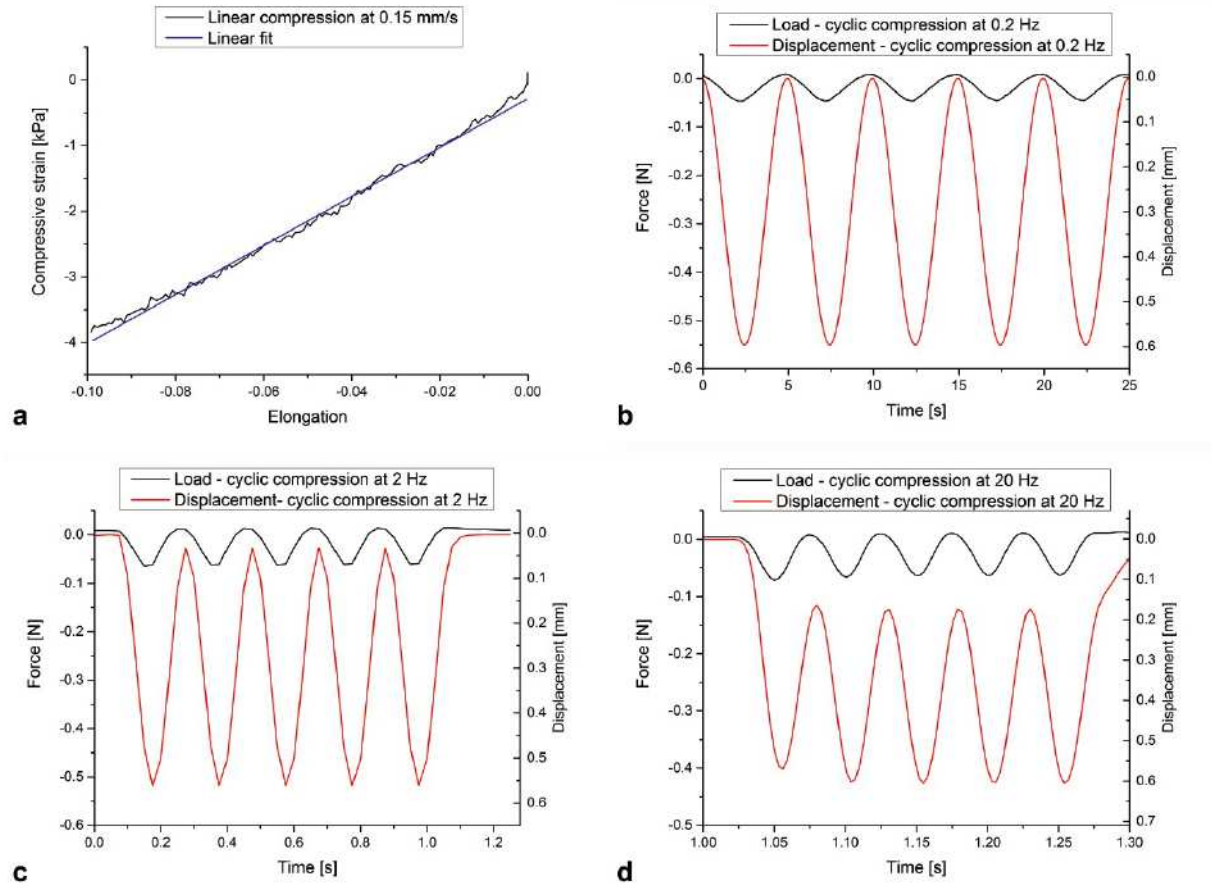

Figure 4.45: Exemplary datasets of a) linear compression with a cross head speed of 0.15 mm/sec and b), c), d) cyclic compression with 0.2, 2 and 20 Hz for a bone scaffold with isotropic pore structure.

Figure 4.44 a) and **Figure 4.45** a) show a representative compressive strain-elongation plot of the measured system derived from linear compression. The highly developed noise in the measured signal is owed to the high force resolution in the range of $1 \cdot 10^{-4}$ N. Within these tolerances, a linear progression of the stress-strain-behaviour was observed ensuring a measurement in the elastic deformation range.

Generic load-time-displacement graphs are displayed in **Figure 4.44** and **Figure 4.45** b), c), d). Apparently the extrema positions in the measured loads are always reached prior to the extrema positions in the displacement signal. This feature matches the behaviour of articular cartilage[284] and is to be attributed to the interplay of the pore structures in the scaffolds with the inherent liquid: Upon deformation, the migration of the, comparably incompressible, liquid is occurring considerably faster than the response of the scaffold material itself so that the super positioned response of the whole system is leading to the mentioned behaviour.

As to be expected, the time shift interval is decreasing, while the occurring force changes are increasing with incremental stimulating frequencies. Remarkably, the elastic response and structural integrity of the hydrated scaffolds was not even affected by measurements with frequencies as high as 20 Hz. In comparison with the osteochondral and meniscus scaffolds, the bone scaffolds reached approximately the two fold force values when the displacement distance was ca. doubled while staying within a 10 % deformation range.

Based on the datasets of linear and cyclic compression, the apparent elastic modulus as well as the dissipation factor were calculated as material parameters according to the previously stated equations (**Figure 4.46**):

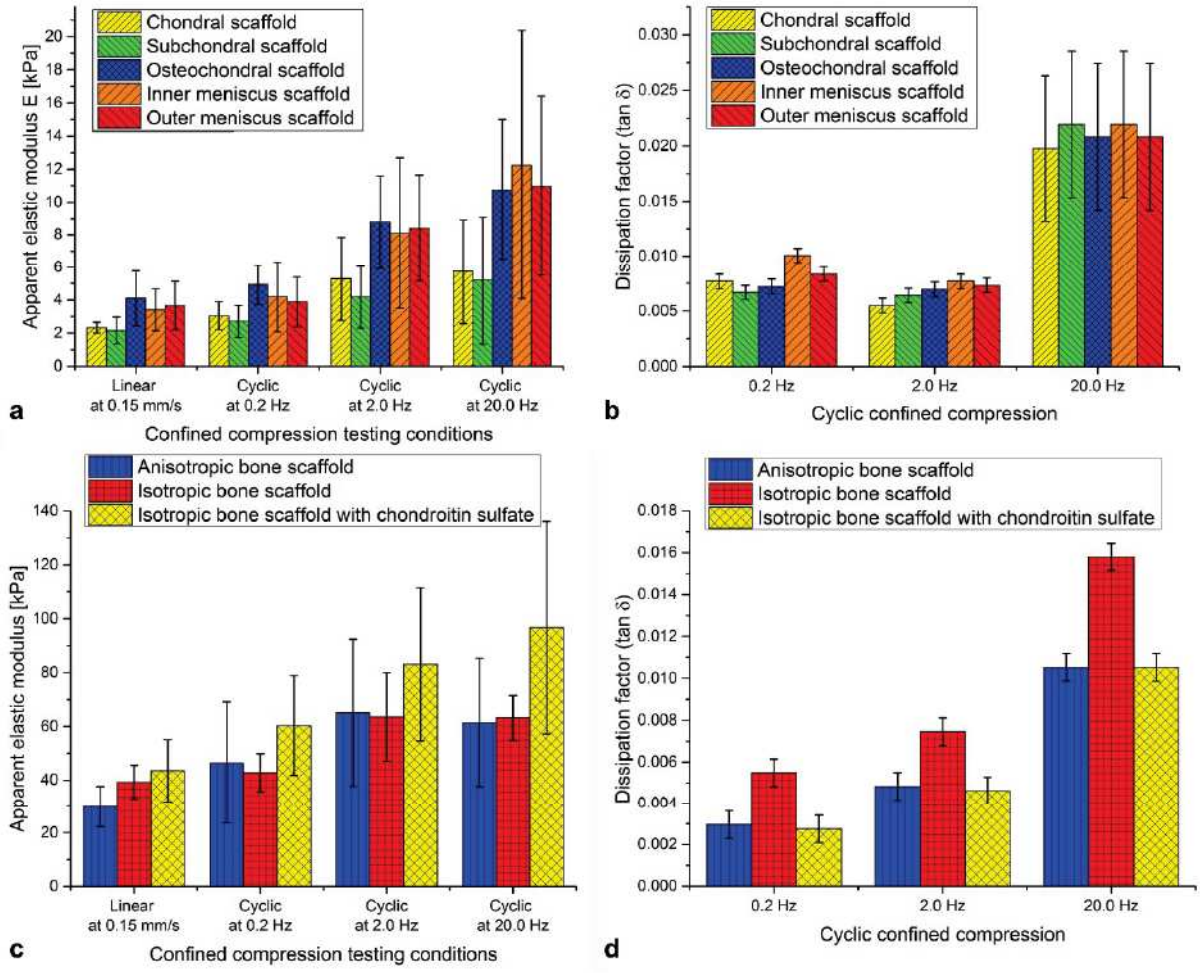

Figure 4.46: Resulting apparent elastic modulus for linear and cyclic compression and dissipation factor (relation of lost energy to stored energy) of osteochondral, meniscus (a), b)) and bone scaffolds (c), d)). (Testing parameters: 0.15 mm/sec, 0.2 Hz, 2 Hz and 20 Hz respectively; Error bars were derived by error propagation)

A resistance against elastic deformation for osteochondral and meniscus scaffolds is given by the apparent elastic modulus in **Figure 4.46** a): The average value of all tested scaffolds apparent elastic moduli accounted to (3.14 ± 0.85) kPa in linear compression, as well as (3.8 ± 0.9) kPa for 0.2 Hz, (7.0 ± 2.1) kPa for 2 Hz and (9.0 ± 3.2) kPa for 20 Hz of cyclic compression. Thus, a frequency depending behaviour of the apparent elastic modulus could be clearly observed.

With respect to the highly porous scaffolds used here, the material properties are more suitably to be compared with cartilage matrix structures rather than the entire cartilage tissue. Ateshian et al. investigated the compressive modulus of bovine articular cartilage of native and enzymatically proteoglycan removed samples in linear confined compression[114]. Values of (0.40 ± 0.20) MPa and (0.26 ± 0.15) MPa for immature and mature articular cartilage, as well as (8.7 ± 2.1) kPa and (40 ± 12) kPa for proteoglycan removed immature and mature articular cartilage were reported. In comparison with these results the value of (3.14 ± 0.85) kPa for linear compression represents approximately one third of the (8.7 ± 2.1) kPa compressive modulus which is reached by enzymatically treated immature articular cartilage. In relation to contrastable freeze dried collagen/GAG scaffolds, which reached a compressive modulus of 0.23 kPa[285], the scaffolds presented here feature a resistance against mechanical deformation that is improved for one order of magnitude.

Interestingly, the chondral and subchondral scaffolds always exhibited a lower elastic modulus than the osteochondral and meniscus scaffolds. A combination of the chondral and subchondral scaffolds to osteochondral scaffolds creates a further interface and thus an additional resistance for the liquid in the pores to pass. This difference between chondral / subchondral scaffolds and meniscus scaffolds may be explained by their approximated spatial alignment of the pore microstructure: while the pores of the chondral / subchondral scaffolds run parallel to the applied force the channels inside the meniscus scaffolds run perpendicular to it. Since in this measuring setup the liquid flow can mainly occur through the bottom channels of the confinement, it is to be achieved at a smaller force for the pores in direction of the external force than for the ones with perpendicular orientation. Apparently, the supportive effect of the pore walls in force direction is not contributing as much to the total resistance against deformation as the resistance of liquid flow inside the scaffolds.

Dampening properties of the osteochondral and meniscus scaffolds inside the measuring setup are expressed by the dissipation factor displayed in **Figure 4.46** b): Within one testing frequency all sorts of tested scaffolds showed a similar behaviour. While only less than 1 % of the exerted energy is lost under physiological frequencies this amount is increased to ca. 2 % under high frequencies as 20 Hz. In consequence 99 % of the energy is stored elastically under physiological frequencies, which proves the applicability of these scaffolds as dampening materials. For porcine articular cartilage tested in unconfined compression a dissipation factor of ca. 0.009 was reported [286]. Thus, the scaffolds potential of energy storage after compression reflects the one of native cartilage.

Figure 4.46 c) depicts the apparent elastic modulus for the bone scaffolds. In average, the bone scaffolds exhibited moduli of (37.6 ± 6.9) kPa in linear compression, together with (49.8 ± 9.3) kPa for 0.2 Hz, (70 ± 11) kPa for 2 Hz and (74 ± 20) kPa for 20 Hz of cyclic compression. Compared to the tested cartilage scaffolds the respective apparent elastic moduli of the bone scaffolds are each about one order of magnitude higher. Still, they are far away from the values that are reached by native bone tissues, but they approach the literature value of 60 kPa, which led to an “optimal” bone formation *in vivo*[159]. As reported in the literature, the elastic moduli of native bone tissues vary with origin[287] and sample geometry[288] of the tissues. While for cylindrical samples, comparable to those in this study, a value of ca. 1 GPa was determined by uniaxial compression[288], other sources refer to values from 2 GPa[289] up to ca. 17 GPa [287]. Again, a frequency depending behaviour of the apparent elastic modulus was obvious. With respect to the related errors, the bone scaffolds with isotropic and anisotropic pores showed comparable values.
Consequently a direct influence of the inherent pore structure on the resistance against mechanical deformation under the measuring conditions could not be observed. In contrast to this, an additional presence of GAGs in form of chondroitin sulphate inside the scaffolds leaded to notable higher values of the moduli in all testing conditions.
As measurable value for the dampening properties of bone scaffolds inside the measuring setup, the dissipation factor is shown in **Figure 4.46** d). Under physiological frequencies less than 0.8 % of the exerted energy is lost, which is increased to values below 1.7 % under high frequencies as 20 Hz.

This reflects the dissipation factor of native bone tissue, which is approximately ranging between 0.6 % and 1.1 %[290] within physiological frequencies. In this frequency range both, scaffolds and native bone tissue may store over 99 % of the energy elastically.
In comparison of the inherent pore structures, the anisotropic scaffolds reach significant lower values than the isotropic ones, which were found to be always bigger for at least 50 % of the anisotropic scaffolds value. This behaviour may be explained by the turbulent liquid streams within the different pore structures: For the anisotropic scaffolds, with their channel like pores parallel to the direction of displacement, the created turbulences lead to a smaller loss of energy than it is the case for the spongy pores of the isotropic scaffolds.

In the case of multi-layered scaffolds, the creation of a further interface in turn seems to lead to a considerable energy loss. Interestingly, the supplementation of 50 % cdw in chondroitin sulphate led to a complete compensation of the energy loss associated with the isotropic pore structure. This is because the negatively charged sulphate groups of the GAG increase the mutual electrostatic repulsion upon deformation and thus enlarge the amount of elastically stored energy to the level of the anisotropic pore structures.

As further parameter for the mechanical characterization, the relaxation time after spontaneous deformation was determined out of the load-time-displacement graphs of the scaffolds (**Figure 4.47**). Independent of the involved forces, the relaxation time showed comparable values for osteochondral and meniscus scaffolds as well as among bone scaffolds. These results were to be expected due to the respective similar composition of the main structural components. The fast relaxing osteochondral and meniscus scaffolds featured an average relaxation time of (0.613 ± 0.040) sec while an average value of (0.815 ± 0.077) sec was found for the bone scaffolds. In comparison to native human articular cartilage[113] and bovine cortical bone[291], this is a very quick relaxation since typical relaxation times for both tissues take around 100 seconds.

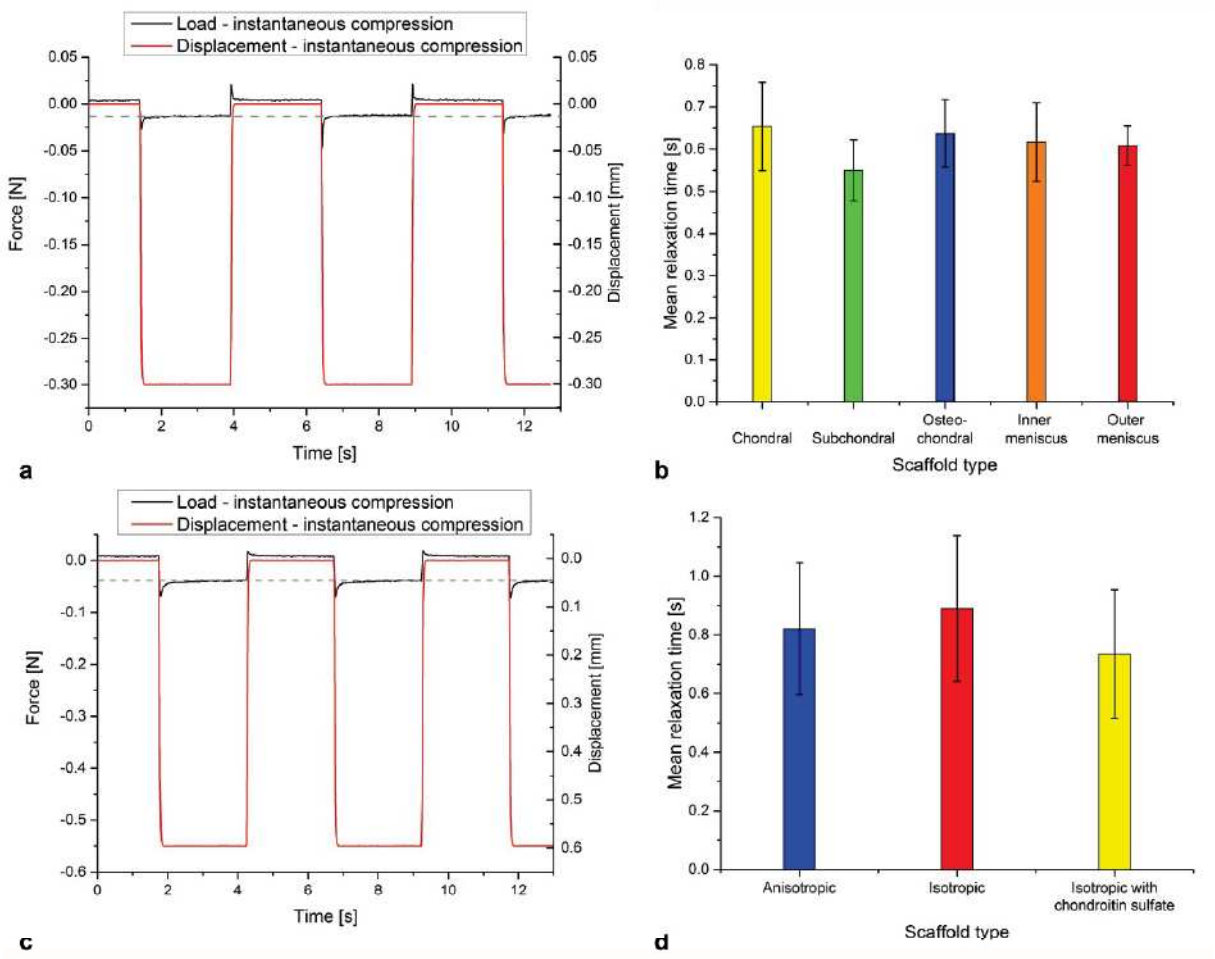

Figure 4.47: Exemplary dataset of instantaneous deformation by square function for an osteochondral scaffold (a)) and an isotropic bone scaffold (c)), respectively. Mean relaxation time of tested osteochondral, meniscus (b)) and bone (d)) scaffolds (error bars represent standard deviation).

4.7 Biological Results

By *in vitro* and *in vivo* application of the previously introduced scaffolds the following results were obtained. While the author of this thesis was responsible for design, creation and characterization of the scaffolds, the biological evaluation was carried out by collaboration partners: *In vivo* experiments were performed by Dr. José M. Lamo de Espinosa, Dr. Froilán Granero Moltó and Dr. Emma Muiños (Experimental Orthopaedics Laboratory, Cell Therapy Department of the Clínica Universidad de Navarra, Pamplona, Spain; Chair: Prof. Dr. Felipe Prósper) and by Dr. Ion Andreu (CEIT and TECNUN of the University of Navarra, San Sebastián, Spain).

In vitro culture was executed by M.Sc. Andrea Schwab and Markus Knauer (Department for Tissue Engineering and Regenerative Medicine of the University of Würzburg, Würzburg, Germany; Chair: Prof. Dr. Heike Walles). However, since the biological performance of the created materials represents a key feature regarding the intended application, the biological key findings are displayed within this thesis with permission of the originators.

4.7.1 Bone Scaffolds

A biological evaluation of the bone scaffold performance was carried out *in vivo* by using the scaffolds to fill a critical size defect in the femurs of Sprague-Dawly rats (female 10-12 weeks old). A femur segment of 5 mm length was removed with a dental burr and the bone was stabilized with a compression plate and four screws. Bone scaffolds with anisotropic and isotropic pore structure (ANI and ISO; **Chapter 4.3**) were employed in this study. The *in vivo* groups of the study (each n = 6) contained empty defects, bone scaffolds and bone scaffolds loaded with 5 µg recombinant human bone morphogenetic protein 2 (rh-BMP-2) (**Chapter 3.5.10**).

A radiographic monitoring of the healing progression was carried out at weeks 5, 7 and 10 after the surgery. Dr. Froilán Granero Moltó performed the radiographic evaluation of the defect region blindfolded through classification into three healing categories: A complete, continuous cortical bone represented the criterion for the highest category. The presence of a fracture line or a discontinuity in the cortical bone of a bridged defect led to a categorisation in the intermediate category. When the defect healing did not differ largely from the empty control, since no bone was formed to bridge the defect, the lowest category was chosen. These three categories correspond to a scoring of 0, 50 and 100 % in the radiographic healing evaluation displayed in **Figure 4.48** a): While all of the anisotropic scaffolds supplemented with BMP-2 showed a complete defect healing from week 5 on, the isotropic BMP-2 containing scaffolds showed in mean a slightly lowered, but still high, healing score. In case of the pure scaffold groups, a bridging of the defect with a fracture line could be observed. Interestingly, all isotropic scaffolds showed a bridging in week 5, which developed back in nearly all cases until week 10. In contrast to this, only half of the anisotropic scaffolds showed an equivalent behavior in the fifth week of the study, but afterwards the healing score mean value increased towards the tenth week.

After 10 weeks the assessed study duration was finished and the explanted femurs were characterized by µ-CT, histology and mechanical testing. Dr. Ion Andreu performed the mechanical characterization in torsion, which yielded the maximal torsional moment as depicted in **Figure 4.48** b): The defects treated with both types of BMP-2 loaded scaffolds attained nearly half of the mean torsional moment that was observed for intact femurs of the contralateral side. Without the employment of BMP-2 significantly lower values were obtained. While the application of the anisotropic scaffolds resulted in a mean torsional moment of one third of the ones that were exhibited by the use with BMP-2, the isotropic scaffolds only yielded one eighth of this value. Since individual samples of native tissues tend to show a divergent behavior, the values obtained for the intact and repaired femurs showed considerably large individual variations.

Representative µ-CT images of the explanted femurs confirmed the findings of the radiographic healing evaluation and the mechanical testing (**Figure 4.48** c)): Here, the X plane corresponds to the apical plane, which is oriented parallel to the bone compression plate. With an orthogonal orientation to the base of the bone compression plate, the Y plane is identical to a sagittal section. A 3D animation is showing a view of the plate averted side. As visible in the Y plane and 3D animation, an excessive bone growth was induced in the region that was altered by the bone compression plate. In agreement with the radiographic healing evaluation the best regeneration results were visible for the BMP loaded anisotropic scaffolds, while the BMP loaded isotropic scaffolds showed slightly lower, but still good results. An equivalent but more intense manifestation of this trend may be observed for the pure scaffolds. In most of the cases an incomplete bridging of the defect was present for the anisotropic scaffolds, but only poor bone growth could be found in case of the isotropic scaffolds.

Within the final healing evaluation of the explants, one defect that was treated with an anisotropic scaffold even healed without the application of BMP-2 (data not shown). Summarized, advances in the healing outcome could be assigned to the bone scaffolds featuring an anisotropic porosity since both types of scaffolds featured identical properties in all other aspects than the porosity.

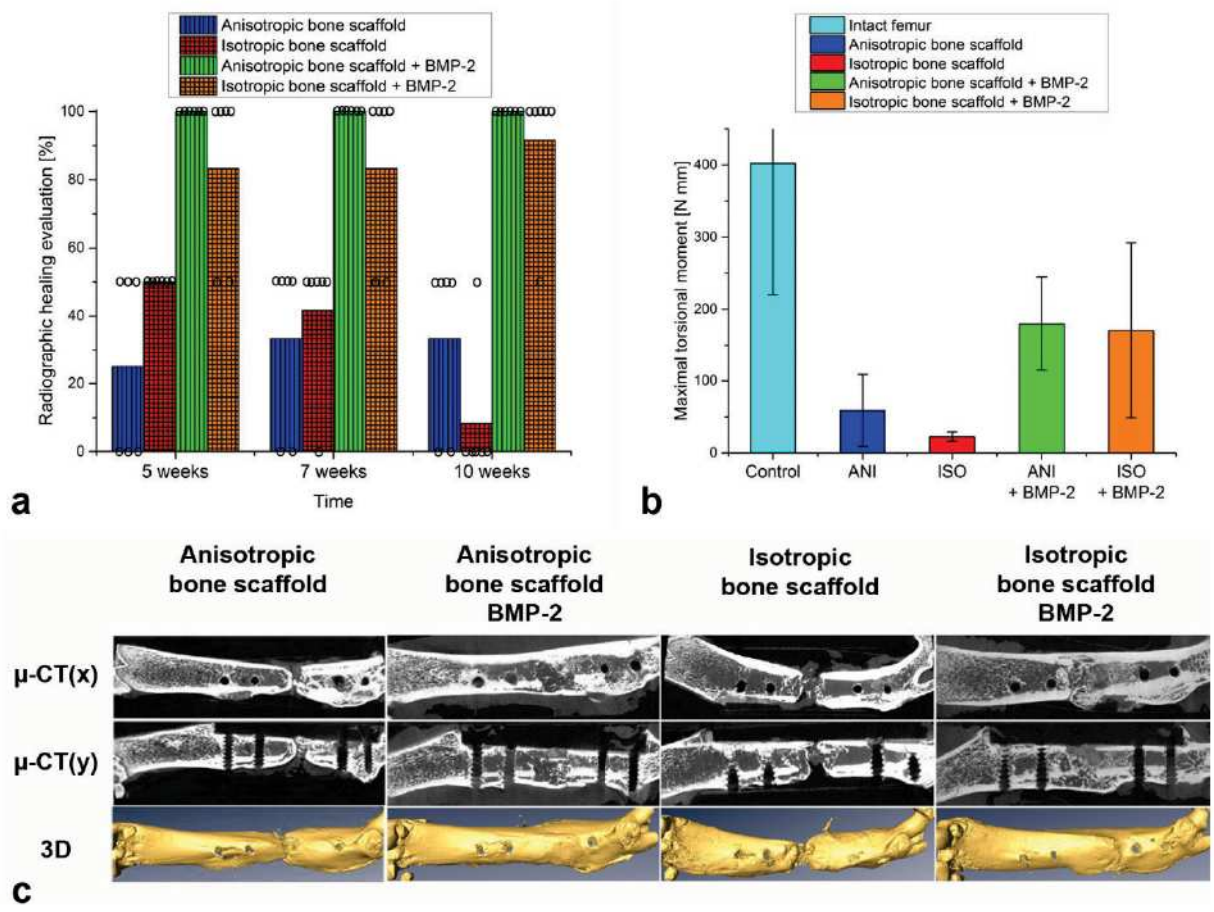

Figure 4.48: In vivo results for bone scaffolds. By employment of 5 µg BMP-2, good healing results could be observed regardless of the scaffolds porosity. On direct comparison of the porosities, advantages in bone healing could be demonstrated for an anisotropic scaffold pore structure. a) Radiography based evaluation of defect healing (100 % = bridged defect with intact cortical bone; 50 % = bridged defect with fracture line; 0 % = no bridging; Individual classifications that were used to determine the medium values are indicated by "o"). b) Mechanical characterization of explanted femurs by maximal torsional moment. c) Representative µ-CT sections and 3D animations of bone explants after 10 weeks.

Hematoxylin-Eosin stainings of the explants are displayed in **Figure 4.49**. Without BMP-2 only incomplete regeneration processes could be observed (**Figure 4.49** a), c)). A better healing appearance was visible in case of the anisotropic pore structure, which served as guidance for the migrating bone cells (**Figure 4.49** a2)). For the BMP-2 loaded scaffolds, good healing results were attained (**Figure 4.49** b), d)). In both cases, cortical bone (**Figure 4.49** b2), d2)) and trabecular bone (**Figure 4.49** b3), d3)) were generated. By comparison with literature [292], the hollow spherical structures may be identified as yellow bone marrow.

More trabeculae and lacunas are formed inside the isotropic scaffolds, which obviously showed a significant higher cell density. Interestingly, the anisotropic bone scaffolds still exhibited over all the highest healing quality, but a lower cell density when loaded with BMP-2.

Thus it can be suspected, that the anisotropic pore structure induces a better functionality of inherent cells than the isotropic pore structure. A presence of BMPs is known to induce the formation of bone tissue in non-skeletal implantation sites[293]. However, clinical results of BMP loaded collagen or hydroxyapatite / tricalcium phosphate scaffolds do not always show a significant increase in bone healing of critical sized defects when compared to the scaffolds alone[294]. The fast leaching out of BMP was presumed to cause these unsatisfying results for the above mentioned scaffolds[294]. According to literature [275], the opinion that a low release of BMPs over a long period of time does not lead to beneficial bone healing results, seems to be established. In contrast to this, the regeneration of a critical sized bone defect could be demonstrated by using anisotropically structured collagen I / hydroxyapatite scaffolds with a very high BMP retention capability.

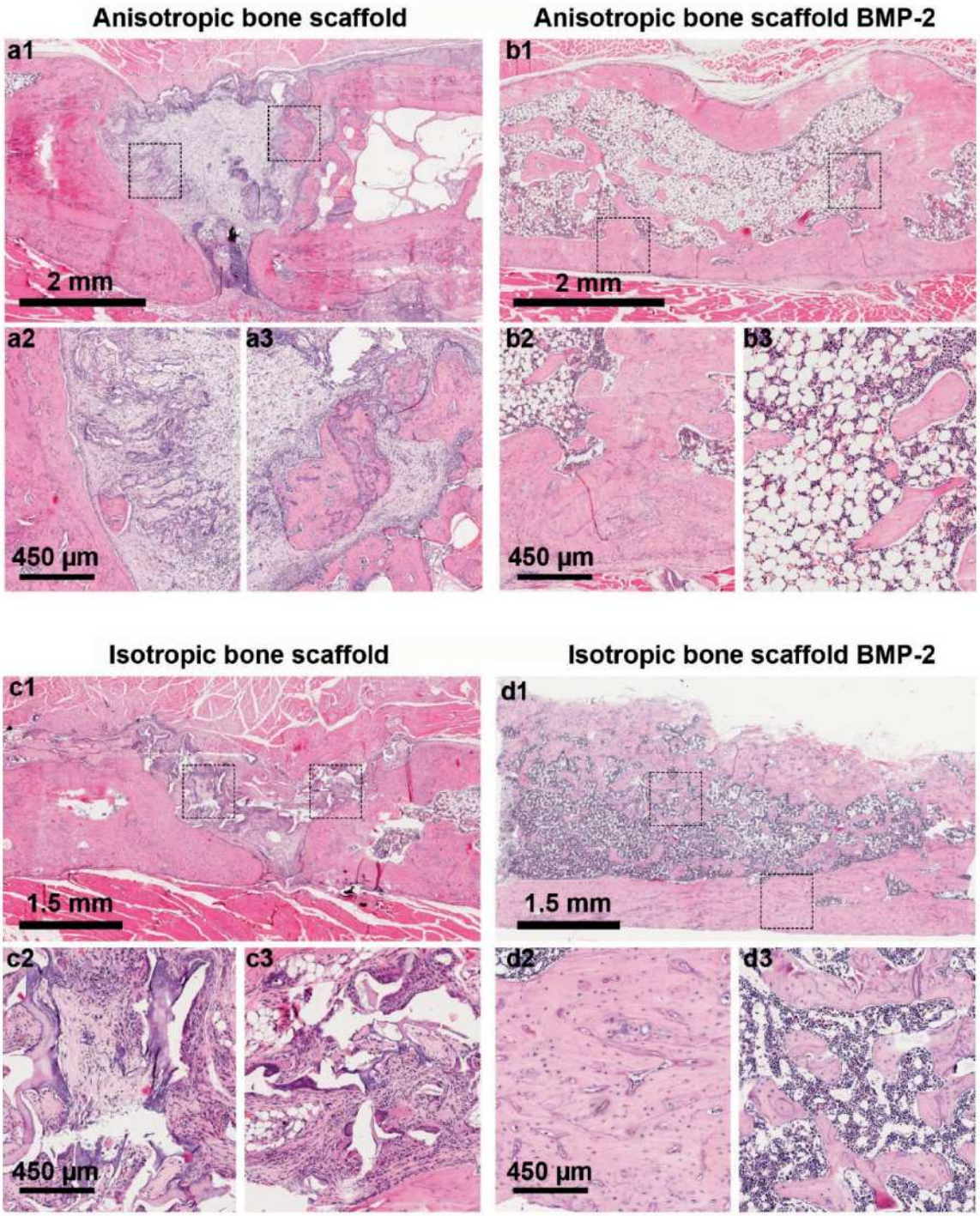

Figure 4.49: Hematoxylin-Eosin staining of bone scaffold treated defects after 10 weeks. Rectangles in a1-d1 indicate the approximate region of magnifications. If formed, the cortical bone is depicted in a2-d2 while the trabecular bone is represented by a3-d3. Without BMP-2 only meager regeneration processes could be observed (a), c)).The anisotropic pore structure served as guidance for the migrating bone cells (a2) and led to a better healing appearance. For the BMP-2 loaded scaffolds, good healing results, with cortical and trabecular bone, were generated (b), d)). Interestingly, the isotropic BMP containing scaffolds showed a higher cell density, but the anisotropic bone scaffolds exhibited over all a higher healing quality when loaded with BMP-2.

4.7.2 Cartilage Scaffolds

To evaluate the applicability of osteochondral and meniscus scaffolds for in situ tissue engineering, bi-layered scaffolds were subjected to static and perfusion cell culture with human mesenchymal stem cells (hMSCs). In order to ensure the comparability of both scaffold types the chondral zone of the osteochondral scaffold (CD) was fabricated using the same precursor composition as the inner zone of the meniscus scaffolds (IM): 2/5 collagen I, 3/5 collagen II and 10 % of the collagenous dry weight in chondroitin sulphate. The subchondral zone of the osteochondral scaffolds (SC) consisted out of equal amounts of collagen I and the bioresorbable calcium phosphate phase brushite ($CaHPO_4 \cdot 2H_2O$) while the outer meniscus zone (OM) was composed out of collagen I and 0.8 % of the collagenous dry weight of chondroitin sulphate. Both sorts of scaffolds were produced as presented in **Chapters 4.4** and **4.5**, respectively.

Thus, the constituents of the osteochondral scaffold match the key signals of native osteochondral tissue[97,100,101] in large, while the composition of the meniscus scaffolds truly represented the one of native tissue[116,117,121]. Admittedly, the hyaline cartilage of the native chondral zone does not contain collagen I. Both types of scaffolds were seeded with hMSCs under static and perfusion conditions. The static cell cultures were performed with scaffolds featuring a diameter of 8 mm and a height of ca. 3 mm inside 48 well plates.

For the perfusion cell culture, two types of bioreactors were used: In case of the osteochondral scaffolds a tube reactor was used with cylindrical scaffolds of 11 mm diameter and ca. 3 mm height. In between the tube connections, the hMSC seeded scaffold was mounted between two perforated polyether ether ketone (PEEK) plates where it was subjected to a flow of cell culture medium (**Figure 4.50** a)).Native meniscus tissue is surrounded by an outer partly vascularized structure[117,121,122]. Therefore, the perfusion cell culture of meniscus scaffolds featuring an authentic size and shape, was carried out inside a vascularizable tissue (**Figure 4.50** b)). This tissue, known as “BioVaSc” (BV) was derived from decellularized porcine jejunal segment and connected to a perfusion array. Within this setup, the meniscus scaffold has been precultured with hMSCs, while the BV was seeded by endothelial cells.

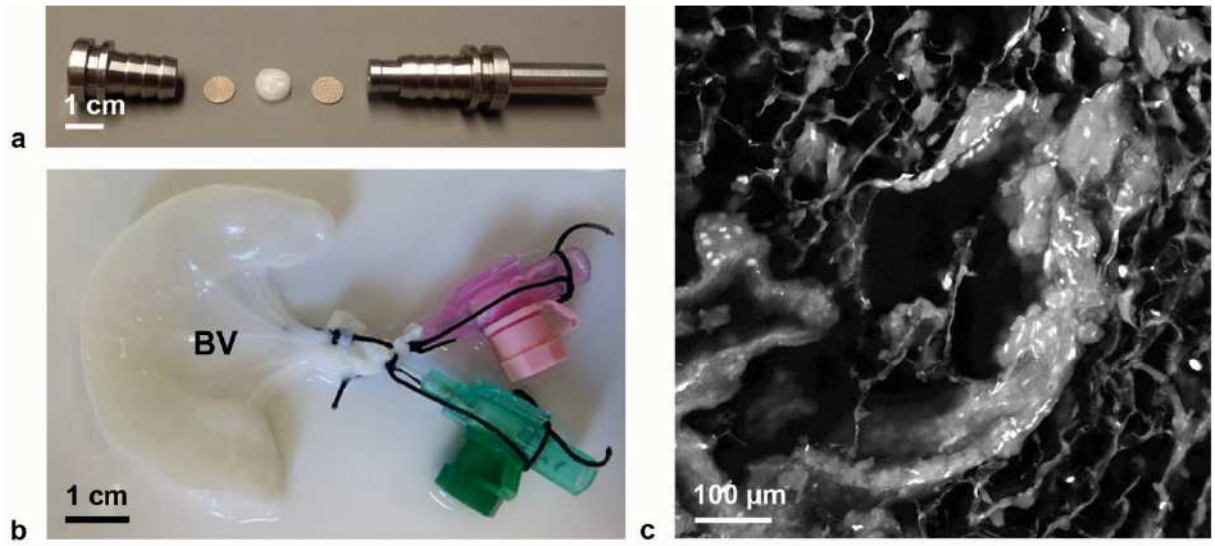

Figure 4.50: Used perfusion reactors for cell culture and cellular matrix remodelling. a) Tube perfusion reactor for osteochondral scaffolds in explosion view (the external tubing is not depicted). b) Meniscus scaffold inside vascularizable porcine jejuna segment (BioVaSc / BV) with connections for nutrient supply. c) Hoechst stain fluorescence image depicting matrix remodelling in horizontal cross section of hMSC seeded osteochondral scaffold.

The cellular response in terms of matrix remodelling processes is shown exemplary with immunohistological cross section stainings for collagen I, collagen II and aggrecan in **Figure 4.51**. Since the same trends were observable under static and perfusion conditions for both scaffold types, one example for each culture setup is shown. While the complete bi-layered meniscus scaffold (OM/IM) is sectioned together with the perfused vascularizable tissue (BV), the displayed osteochondral scaffold (CD/SC) was cultured under static conditions.

As a consequence of the collagenous material, which is still supposed to be in the native state, the scaffolds were very well accepted by the cells. Together with the consecutive anisotropic pore structure, this lead to an effective guidance of hMSCs deep inside the scaffold volume. Thereby, a huge advantage is represented, since most of the conventionally used 3D scaffolds lead only to a rather superficial cell colonialization.

Although other stainings would be more suitable to confirm these findings, the fact that the inner scaffold structure has been significantly remodelled by inherent cells, represents the indirect prove for a high cellular migration and activity. As proven with negative controls, the staining was specific to human extracellular matrix, since no staining was present for the scaffold matrix of animalistic origin (data not shown).

An impression of larger matrix remodelling processes may be gained upon consideration of **Figure 4.50** c): A horizontal cross section through the chondral zone of an osteochondral scaffold was stained with Hoechst, so that the cell DNA is fluorescing. The thin walls of the scaffold were seeded with matrix deforming cells. Accumulations of multiple cells lead to a pronounced matrix remodelling, creating spherical to stretched new matrix structures with thicker walls and dimensions in the rage of multiple 100 µm.

In case of the meniscus scaffolds, collagen I was generated throughout the entire matrix with the most dominant manifestation in the outer vascularizable tissue (BV). Remarkably, the distribution of collagen II and aggrecan represents the one found in native menisci[116-118], since both are expressed predominately in the inner meniscus zone (IM). In between BV, IM and OM a lumen is present which is to be attributed to the histological preparation (**Figure 4.51** a)). For the osteochondral scaffolds, collagen I was produced within the chondral zone (CD), but especially in the subchondral zone (SC). Interestingly, a pronounced synthesis of the chondrogenic matrix proteins collagen II and aggrecan was carried out by hMSCs in the chondral part of the scaffolds (CD) (**Figure 4.51** b)). All the displayed stainings have been unselectively modified in contrast to yield more comparable images.

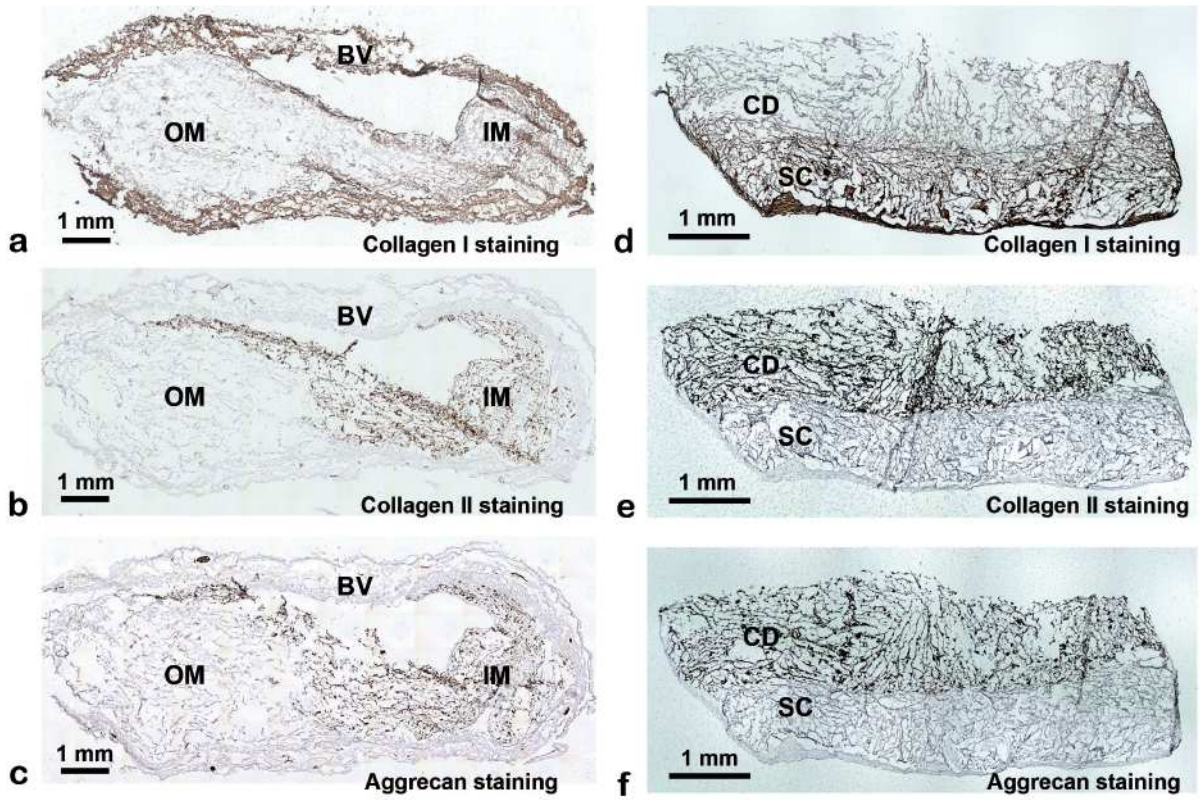

Figure 4.51: Immunohistological stainings of hMSC seeded, cross sectioned cartilage scaffolds (a), d): collagen I; b), e): collagen II; c), f): aggrecan). The bi-layered meniscus scaffolds (OM/IM) have been cultured inside a BioVaSc (BV) under perfusion conditions (a)-c)), while bi-layered osteochondral scaffolds (CD/SC) were cultured inside static cell culture. Like in native tissue, the cellular production of collagen II and aggrecan is more pronounced in the inner meniscus (IM) and the chondral zone (CD) than in the outer meniscus (OM) and the subchondral zone (SC), respectively.

Summarized, these findings demonstrate a tissue mimetic matrix remodelling in the respective tissue zones. Since collagen II and aggrecan constitute dominant protein structures which are characteristic for chondrogenic differentiation, these produced extracellular matrix proteins represent first signs for zone specific stem cell differentiation. Although further biological evaluation, like real time polymerase chain reaction (q-PCR), is needed to confirm these findings as true chondrogenic differentiation, the presented results already underline the unusual high suitability of these scaffolds for tissue engineering.

Commonly, an additional supplementation of growth factors or cytokines is required during cell culture to manipulate the cell faith in specific directions of differentiation. This is to a high degree of likeliness originating from the unnatural environment in which the cells are cultured. Interestingly, the presented tissue mimetic cartilage scaffolds seem to provide enough relevant properties and biological key signals, so that no additional growth factors are required to achieve these results.

In comparison to literature [295], the production of collagen II and GAGs was achieved before within the chondral zone of fibrin glued collagenous osteochondral scaffolds, but required the use of various growth factors (TGFβ-1, TGFβ-3 and FGF-2). In case of the meniscus scaffolds, the production of GAGs and collagen II was demonstrated in flat scaffolds of fibrin gel on small intestine submucosa with the use of growth factors (TGFβ-1 and IGF-1)[166]. Without the use of cytokines only smaller amounts of collagen I, collagen II and aggrecan were synthesized in complete meniscus scaffolds from layered collagen I fibre mats that were infiltrated with PLA/PLGA[168]. Thereby, the matrix production occurred by the cost of decreasing cell numbers during cell culture. However, these approaches could not recapitulate the native zonal structure of osteochondral and meniscus tissue.

4.8 Outlook on Further Applications

Parts of the following chapter are published analogously in the priority patent application DE 102011120488 and have been written by the author[296].

4.8.1 Variation of Precursor Materials

Although the use of collagenous materials is currently expected to yield the most promising results for biological cell carrier matrices, the inventive platform procedure may also be applied with a large number of further precursor materials to create a variety of 3D materials with defined microarchitectures. Therefore, numerous sublimable and non-sublimable materials may be contemplated for the precursor preparation, which are listed in claim 2 and 3 of PCT/EP2012/074980[296].
By using organic solvents, as sublimable precursor components, the application range for synthetic polymers, as non-sublimable materials, would be largely widened. Self-evidently, the use of conventional commercial freeze dryers would not be sufficient to induce a sublimation of organic solvents, so that other devices would be required. The method would be also applicable to create ceramic or metallic materials. Also the use of metalloids or non-metals and their oxidized states is possible. Therefore, these non-polymeric materials have to be processed in grind or powder form within the precursors. All non-polymeric, non-sublimable materials would require the use of a further phase to ensure the conservation of the structural integrity of the materials after solvent sublimation. The consolidation step would have to be adapted to the used precursor materials, so that the non-polymeric, non-sublimable materials are treated by sintering or infiltration. Consequently, the application possibilities of the general process are very broad, so that the production of collagenous bone and cartilage scaffolds for tissue engineering represents only a small fraction of the accessible application range.

4.8.2 Intervertebral Disc Scaffolds

In addition to cartilage scaffolds for osteochondral and meniscus engineering, also biomimetic scaffolds for the use in intervertebral disc defects may be produced by application of the inventive method. Although the quest for biomimetic solutions is the subject of intense research[297], no adequate replacement in the form of a monolithic support structure, with biomimetic composition and microstructure was achieved yet. The framework of the extracellular matrix of the native intervertebral disc consists essentially of an inner core, the nucleus pulposus, which is surrounded by fibrous lamellae that form the annulus fibrosus. Being structurally and mechanically isotropic, the nucleus pulposus contains a network of collagen type II and proteoglycans. From a simplified perspective, the annulus fibrosus consists out of a plurality of fins, which are made out of collagen type I in the outer part and out of type II collagen in the inner part.

In accordance with the native tissue, the intervertebral disc scaffold is composed out of the mentioned tissue components, which are combined to form a biomimetic monolithic carrier matrix. **Figure 4.52** a) visualizes the biomimetic scaffold strategy. An undirected network (reassembling the nucleus pulposus, NP in **Figure 4.52** a)) is produced by isotropic solidification and is located within two multi-ring-shaped structures (reassembling the annulus fibrosus). These two ring structures may be realized by anisotropic solidification of two compositions with lamellar structure (iAF and oAF in **Figure 4.52** a)). As a proof of principle, a lumbar disc-like support structure based on alginate can be observed in **Figure 4.52** b) and c) where several zones of different precursors form a monolith. A light micrograph of a top view of the outer portion of the ring matrix is shown in **Figure 4.52** b), revealing the anisotropic lamellae structure. A photograph of the macroscopic appearance is shown in **Figure 4.52** c). For illustration of the multi-zonal construction, individual regions were produced with coloured precursors (nucleus pulposus/NP - blue, inner annulus fibrosus/iAF - white and outer annulus fibrosus/oAF - orange). Possible future applications of these scaffolds are outlined as matrix for cell cultivation or even for a complete spinal disc replacement when used for matrix coupled cell transplantation.

4.8.3 Cell Culture under Mechanical Stimulation

Although many of the native tissue key signals are matched by the presented scaffolds, the approximation of the composition and microstructure alone cannot return all relevant cell stimulants that are found in the respective tissues. Therefore, the addition of a suitable mechanical stimulation to the cell culture conditions would represent a further step to approach the *in vivo* situation more closely. Additionally, this would illuminate the interesting question if different porosity arrangements may induce a specific shaped matrix remodelling of the seeded cells. Currently, a clear assignment of the larger remodelling structures to the spatial alignment of the scaffold pores is not easily possible (**Figure 4.51** and **Figure 4.50** c)). Since the stimulation exerted mechanical forces would be transmitted to the cells by the differently aligned matrix pores, a recognizable effect might be expected. Moreover, the bioreactor system currently used for the culture of osteochondral scaffolds (**Figure 4.50** a)) could easily be connected to a mechanical force transducer system, so that the used setup for cell culture would not have to be change significantly. The only modification needed would consist in a fixation of the perforated PEEK plates so that they always stay in place when the hollow cylinder piston is moving.

4.8.4 Influence of Cellular Behaviour by Tuning of Topographical Surface Structure

The manifestation of a certain sub-micron to nanostructure in form of a combination of waved bulk material and nano-aggregates was observed for both types of cartilage scaffolds. Since the surface topography in these length scales is known to influence cellular behaviour[133,298-300] the possibility to tune it to desired sizes also represents a highly interesting aspect for future investigations. A combination of piling up and slipping away of the cryo-concentrated precursors was hypothesized to be the creation mechanism of these pore surface structures. Referring to this, the differences in expression of surface structures seem to be directly connected to the solidification velocities. On comparison of the sub-micron to nanostructures found in osteochondral and meniscus scaffolds it may be concluded, that higher solidification velocities lead to smaller heights of the topographical structures, while lower ones yield higher structures.

Consequently, a controlled tuning of the solidification velocity by adjustment of external temperature gradient and precursor composition would enable the steered formation of surface topographies. Thereby, the cryostructuring processing route may provide a further parameter to control migration, adhesion, proliferation and differentiation properties of seeded cells and thus the clinical relevant outcome.

4.8.5 Electrospinning

As a modification for the osteochondral scaffolds, the electrospun poly (D, L-lactide-co-glycolide) fibres representing the superficial chondral zone (**Chapter 4.5.4**) could be covalently bound to the underlying structure. This may be achieved by the functionalization with amphiphilic macromolecules generated from star-shaped poly (ethylene) oxides, where the covalent bonding may be expressed by the action of isocyanate groups, terminating the star shaped molecules[11]. Thereby, the non-specific adsorption of proteins could be greatly minimized. Additionally, it would be possible to bind Proteoglycan 4, alias lubricin, covalently to allow a use as sliding layer on the cartilage surface.
Another possible endorsement would consist in the realization of the superficial chondral zone by electrospinning of collagen solutions. If applied directly after the lyophilisation processing step, remaining moisture residues of the spinning solution could soften the top of the underlying scaffold. This way, both collagenous materials might “melt” together before they are cross linked by the carbodiimide method described in **Chapter 4.1.3.3**. Thereby, a stronger coupling between the superficial and middle chondral zone could be achieved.

4.8.6 Filter Materials

Since porous materials are used in various application areas for filtering particles from liquids or gases, the invented production method, may also be applied to create filter elements. This way, a solid retention, which comprises different components in individual zones, each having specific affinities regarding the retainable substances, can be produced. Hereby, an internal pore structure is extending through all different composite areas.

Figure 4.52 d) depicts a CAD representation of a filter material while **Figure 4.52** e) shows photography of a segment for dual material retention. The inner and the outer material segment contain different colour pigments, representative of various materials with high affinities for the retainable substances. Since the cryostructuring method allows to process a huge variety of materials together with defined porosities, both may be adjusted to an optimal material retention. Additionally, the nano-topography of the inner surface may be tuned to increase the area of interaction (**Figure 4.31** and **Figure 4.37**). By the use of multiple retention stages, the overall effectivity/capacity and thus the operating life may be increased in comparison to conventional filter systems.

4.8.7 Material for Multistage Catalysis in Continuous Chemical Reactions

In chemical engineering different solid catalysts, arranged one behind the other, are used in a reactor for certain implementation processes. Using the described cryostructuring method, heterogeneous solid catalysts could be produced in which various catalysts or catalyst systems are mutually combined to form a monolith. The multistage catalyst may comprise a plurality of zone penetrating porosity with defined pore diameters in the micrometre range.

Figure 4.52 f) illustrates a schematic representation of the basic design for a multi-stage, heterogeneous solid state catalyst. The colour coded zones represent a plurality of stages where different catalysts or catalyst systems may be included in each. **Figure 4.52** g) shows a proof of principle where the pigments represent multiple catalytic systems, penetrated by a continuous pore structure in the sub millimetre range. Thereby, diverse steps of chemical reactions could be carried out while passing reactants through the continuous pore structure. Again, the control over pore diameter and inner surface could be advantageously used to fit the appropriate reaction time of processes. These kinds of multi-stage catalysts could be favourably applied where the chemical reactions proceed rapidly and individual reaction products feature only a short-term stability.

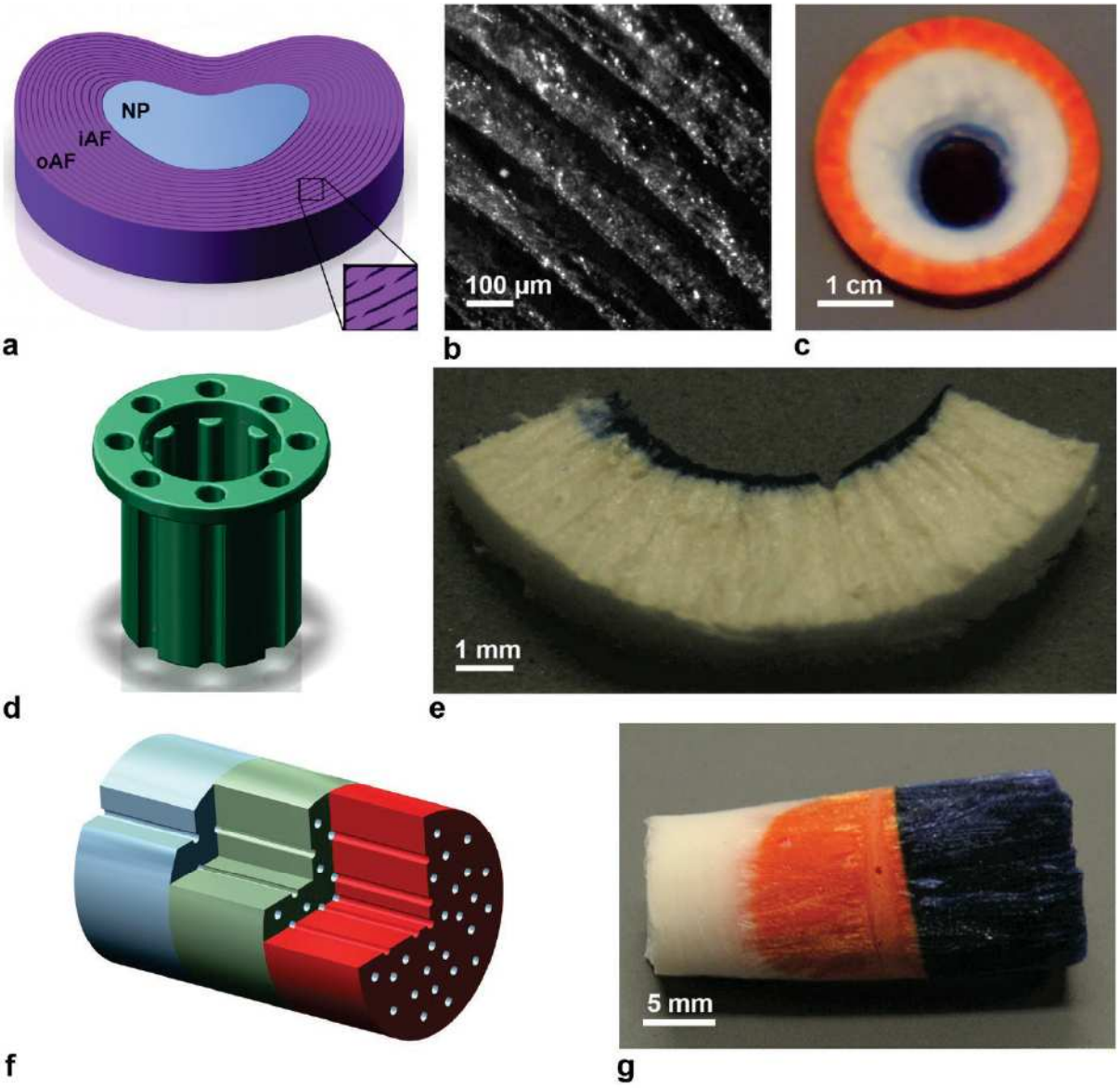

Figure 4.52: Outlook: Creation of intervertebral disc scaffolds, filter materials and multi stage catalysts and by application of the cryostructuring process. a) CAD design, b) light microscopic detail of top view on ring lamellas and c) photography of intervertebral disc scaffold (oAF/orange = outer anulus fibrosus; iAF/white = inner anulus fibrosus; NP/Blue = nucelus pulposus). d) CAD design and e) photography of section through a dual filter material. f) CAD design and g) photography of tri-zonal solid stage catalyst.

5 Conclusion

5.1 Development of a Directional Solidification Process and Device

A new platform procedure based on the directional solidification of flowable precursors was developed at the Department for Functional Materials in Medicine and Dentistry, without accessible prior knowledge. A solution, which was so far unknown by the prior art, is presented by the inventive process, since it enables the fabrication of multi-zonal monolithic materials, featuring consecutive pores proceeding orthogonal to the zonal interfaces. Furthermore, the use of one platform process to generate multiple biomaterials represents in economic compliance with recent advanced therapy medicinal product (ATMP) regulations[301]. The University of Würzburg filed marketable outcomes in the patents WO 2013/083844 A2[279], EP 2788171 A2[27] and US 2014350331 A1[264].

This new directional solidification process facilitates the formation of materials, composed out of zones with different material compositions, which are penetrated by aligned anisotropic pores. The spatial orientation of the pores may also run angled to the interfaces between the respective zones of the material. An entirely monolithic material is obtained since the consolidation processing step is carried out after the “cryostructuring” process, where joining of the material zones and the pore formation are taking place simultaneously. The resulting materials bare especially desired properties for medical scaffolds. A fully biomimetic zonal composition may be realized together with aligned pore structures, facilitating cellular acceptance and ingrowth. Spatial alignment and size of the scaffold pores may be controlled during fabrication. Due to the low processing temperatures, native sensitive components should be able to be processed without protein denaturation. This increases the potential use of the technique significantly, since many other scaffold production procedures involve harsher circumstances.

In order to apply the procedure, a custom made Device (ACD) was developed, designed with CAD software and assembled. Inside the device heat is pumped to flow through the inner assembly group. Thereby, an electrical controllable crystal growth of solidifying solvents or dispersing phases may be achieved in the sample volume. This way, a high control over spatial alignment and size of the crystals was possible, while producing a material with zonal compositions and custom shape.

The ACD may work without thermal regeneration in an external temperature gradient interval from 0 to 4.5 K/mm, where a continuous production of medical scaffolds is possible. Within a working range up to 9.0 K/mm the device may also be used for reproducible processing when a regeneration interval is allowed in between the cryostructuring of several scaffolds. After multiple upgrades, the ACD now represents a powerful, versatile and easy to maintain tool for scaffold fabrication. In contrast to other machines that are designed for directional solidification[23,241,246], the ACD allows the direct measurement of temperature changes in the solidifying precursors which enables a better assignment of freezing parameters to the resulting morphologies.

5.2 Precursor Materials and Processing Induced Alterations

Essential raw materials for the cryostructuring of collagenous precursors were independently produced and isolated, respectively. As mineral phase for all bone replacement precursors, the calcium phosphates brushite and hydroxyapatite were attained by precipitation reactions. An identification of the precipitated materials as the intended ones was performed by evaluation of characteristic reflections in X-Ray Diffraction (XRD) scans. In case of the bone scaffolds a partial conversion of hydroxyapatite to brushite could be observed, which was explained by the pH dependent solubility under the conditions of precursor preparation.

Native articular cartilage and tendon tissues were investigated by Scanning Electron Microscopy (SEM). The proceedings for the isolation of collagen I and II from murine and bovine tissue sources were established in the Department for Functional Materials in Medicine and Dentistry. This included practical methods for harvesting of collagenous tissue from murine tendons and bovine articular cartilage as well as working instructions for the purification and fractioning of the collagens. Additionally, a purification protocol of literature [262] was established in a modified form.

A characterization of native, isolated and cryostructured collagenous materials was performed by Fourier Transform - Infrared Spectroscopy (FT-IR) measurements. By comparison to investigations in the literature, FT-IR turned out not to represent the most suitable method to investigate a protein denaturation of collagenous materials.

Unfortunately, the predominant insolubility in mild aqueous solutions aggravates the characterization by other methods heavily. Nonetheless, no protein denaturation could be detected for the isolated and cryostructured collagenous materials by FT-IR. Since none of the processing steps is carried out in harsh conditions regarding protein denaturation and no denaturation could be detected, the purified collagens are supposed to be still in their native conformation.

5.3 Evaluation and Optimization of the Cryostructuring Process

The performances of the ACD and the produced materials have been systematically investigated by using alginate precursors. Structural aspects were evaluated by SEM image data processing together with material production parameters that were obtained by analysis of cryostructuring temperature profiles. With variation of the external temperature gradient, via electrical regulation of the Peltier elements (PEs), the pore size of the resulting scaffolds may be tuned relatively precise. This is consistent with the expectation, that by regulating the cooling rate of the ACD, the solidification rate of the used precursor is directly proportional manipulated, which in turn is affecting the size of the growing ice crystals.
An increase in availability of key signals to a biomimetic quantity was hypnotized to improve the cellular response to the scaffold and thus the clinical relevant outcome. Therefore, the optimization of the precursor processing to achieve specific microstructures by using tissue mimetic compositions represented a crucial task. In order to tune the scaffold production to the final stages, several years of development and optimization of the process were required.

Ice crystal growth
To understand the microstructural changes associated with different manifestations of ice crystal growth, the behaviour of collagenous precursors was investigated. Various precursor compositions were rheologically analysed, regarding viscosity alterations upon cooling. A consideration of the viscosities alone represented to be not as important as the effects resulting from the interaction of single precursor components. In addition, mechanisms behind the establishment of different crystallization morphologies were connected to outer experimental parameters.

Within the established theory for pure substances, the anisotropic ice crystal growth is thought to originate from perturbances at a morphological unstable solid liquid interface. In contrast to this, the dominant anisotropic crystallization for the used precursors was observed to originate from fishbone-like structured ice crystals at the bottom of the precursor containing vessel (**Figure 4.13** b)). Since these structures were formed at first, the anisotropic crystal structure was concluded to rise from dendritic side branches of these initial crystals. The results of the systematic investigations carried out in **Chapter 4.1.2** confirmed this conclusion.

Although the crystallisation does not originate from a visible solid liquid interface which becomes morphological unstable, this does not necessarily mean that similar perturbances are not involved in the crystal morphology. The morphology of the fishbone-like structure might be attributed to a sort of “steady wave” within the undercooled liquid zone. Such a phenomenon could have induced a preferential growth of the observed initial structures in an interweaved pattern. Nonetheless, these initial structures were only influencing the first few micrometres of the sample height. Afterwards, the solidification regime changed to an anisotropic lamella like crystal growth, which stayed dominant until the top of the sample was reached. This change is subjected to be attributed to the rise of dendritic side branches from the initial structures, which develop to the “primary crystals” represented by the lamella like dendritic crystals.

Experimental Parameters and Resulting Solidification Morphologies

Based on temperature curve evaluation and pore size analysis of all scaffolds that were produced by the use of collagenous precursors, a summarizing chart illustrating the dependency-trends of different solidification morphologies was created (**Figure 5.1**). Here, the absolute values in direction of the PE induced heat flow (defined as x-direction) of the vector variables solidification rate (“v_S”) and external temperature gradient (“$\vec{\nabla} T$”) are considered. Both are connected with the resulting morphologies of crystal growth inside collagenous precursors.

These types of variables represent crucial attributes that depend on the precursor compositions as well as the processing parameters. Together, they yield more information than the cooling rate, since the physical relevant information is included in the function of solidification velocity. Self-evidently, v_s represents as a function of $\vec{\nabla} T$ and is also influenced by the different individual precursor compositions.

Consequently, such a comparison may rather be used to visualize trends than to read out numerical values, since various precursor compositions were included in the chart. In general, the solidification crystal size is increasing with lower v_s while the degree of spatial alignment is increasing with $\vec{\nabla} T$, in an interdependent manner:

A plane ice front might be expected for $\vec{\nabla} T \rightarrow 0$ under theoretical assumptions of pure substances. In the reality of experiments, the high number of precursor components contains numerous crystallization nuclei, where small thermal fluctuations lead to an equiaxed ice crystal growth. This leads to an isotropic solidification, which is to be expected for low $\vec{\nabla} T$ as depicted by equiaxed ice crystals in the greyish area in the left side of the chart. Scaffolds with a spongy microstructure, like isotropic bone scaffolds, were created by working inside this regime.

The degree of spatial alignment is increasing with $\vec{\nabla} T$ until the isotropic solidification regime ends. Now the driving force, transmitted by $\vec{\nabla} T$, is high enough to induce a preferential crystal growth direction, so that the boundary case of anisotropic solidification is reached. For the aqueous collagen precursors, these processing conditions result in a dendritic ice crystal morphology. A small blueish area indicates this freezing regime in **Figure 5.1**, where low v_s meet intermediate to low values of $\vec{\nabla} T$. Here, an anisotropic ice crystal growth nearly orthogonal to $\vec{\nabla} T$ may be established, which was applied to create scaffolds with a meniscus like microstructure.

If the values of v_s and $\vec{\nabla} T$ increase further, the anisotropic spatial alignment approaches successively an antiparallel proceeding to $\vec{\nabla} T$ which is indicated by the intensifying greenish area depicted in the right upper section of **Figure 5.1**. Hereby, the crystal diameters get smaller while the angle to the $\vec{\nabla} T$ vector lowers. This form of solidification was applied to create osteochondral scaffolds. In order to yield constant consecutive pore diameters when multiple precursors are combined, a stronger expression of v_s and $\vec{\nabla} T$ during the cryostructuring process turned out to be beneficial.

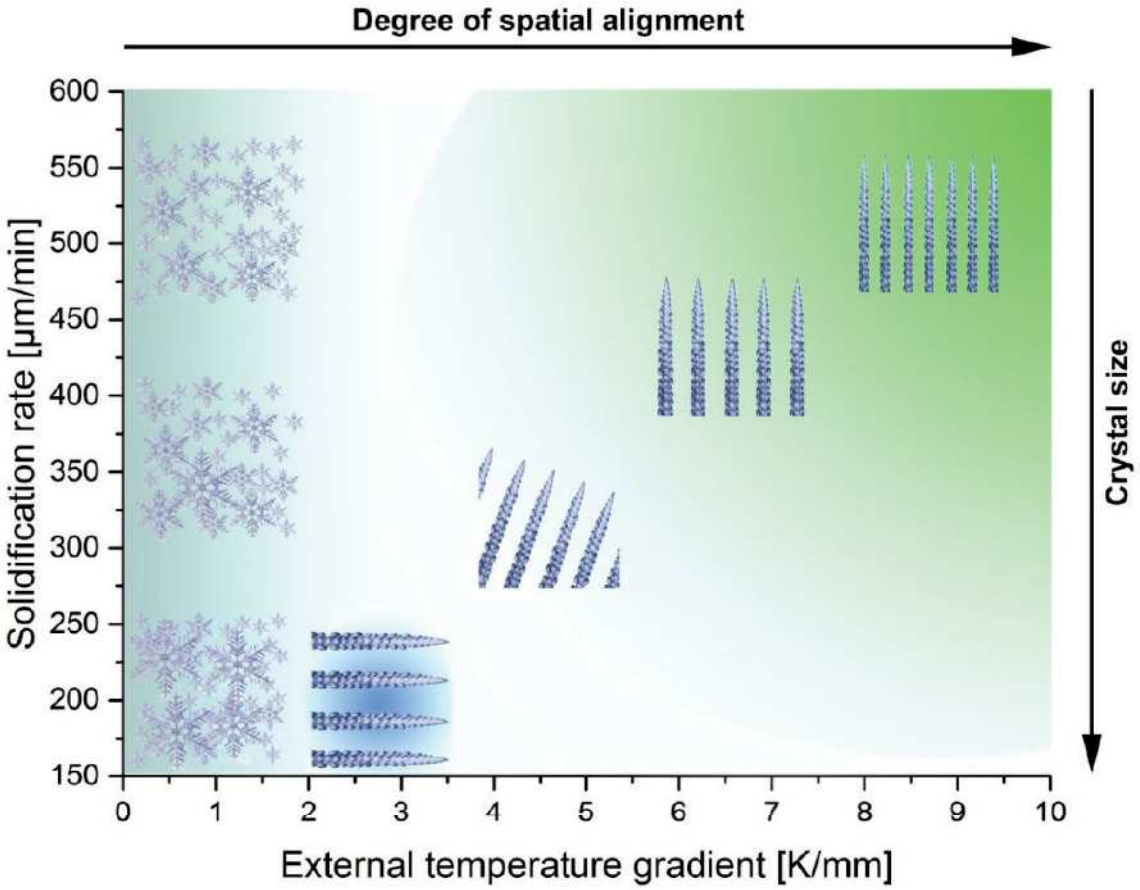

Figure 5.1: Dependency-trends of solidification morphologies from solidification rate (v_s) and external temperature gradient ($\vec{\nabla} T$) for collagenous precursors. The crystal size is increasing with lower v_s while the degree of spatial alignment is increasing with $\vec{\nabla} T$, interdependently. For low $\vec{\nabla} T$, an isotropic solidification is to be expected (greyish area). Due to compositional differences, different values of v_s are attainable for similar values of $\vec{\nabla} T$. In the boundary case of anisotropic solidification, for low v_s together with low to intermediate values of $\vec{\nabla} T$, an anisotropic ice crystal growth nearly orthogonal to $\vec{\nabla} T$ may be established (small blueish area). For increasing values of v_s and $\vec{\nabla} T$ the anisotropic spatial alignment approaches an antiparallel proceeding to $\vec{\nabla} T$ while the crystal diameters get smaller (greenish area).

Multi-layered Cryostructuring

After undergoing an evolutionary process, the multi-layered cryostructuring of osteochondral scaffolds could be successfully transferred from alginate to collagenous precursors featuring a tissue mimetic zonal composition and consecutive anisotropic pores. This transfer was enabled by a combination of process optimization steps together with adjusted precursor compositions.

Cross Linking

Additionally, the wet chemical cross linking with 1,6-hexamethylene diisocyanate (HMDI) and 1-ethyl-3-(3-dimethylaminopropyl)-carbodiimide (EDC), as well as dehydrothermal cross linking was evaluated for collagenous scaffolds. The use of HMDI turned out yield undesirable results, since the cross linking lacked in homogeneity over the entire scaffold and pores were partially closed by web-like polymer accumulations. Thermal cross linking was able to improve the stability of fragile scaffolds. But since the stability was not sufficient for the intended applications and an unbeneficial thermal alteration of the protein structures could not be excluded, the more promising route of carbodiimide cross linking was pursued further. A formulation for an EDC cross linking solution was found, which resulted in a high scaffold stability. By applying the cross linking with gentle supplementation of EDC solution inside a reduced pressure apparatus the common problem of pore collapse during wet chemical cross linking could be avoided.

5.4 Cryostructured Scaffolds

Due to the versatility of the cryostructuring process, medical cell carrier matrices for bone, articular cartilage and meniscus tissue engineering could be developed. All together feature suitable scaffold dimensions and shapes. Additionally, the material composition was biomimetically inspired so that also characteristic spatial material distributions inside the respective tissues are matched. Furthermore, the control over the freezing regime allowed the creation of various microstructures, which are mimicking the native tissue structures.

Bone Scaffolds

Three types of cylindrical bone scaffolds, fitting to fill out critical size defects in rat femurs, were produced out of collagen I and hydroxyapatite precursors. The bone scaffolds differed in pore structure and composition: Scaffolds with anisotropic channel pores, which propagate from one basis of the cylinder to the other (ANI) were created. Additionally, scaffolds featuring an isotropic, sponge like, pore structure (ISO) that is randomly distributed among the matrix and scaffolds with isotropic pores containing chondroitin sulphate (ISOCS) were fabricated.

Since a healing of critical size defects will per definition[302] not occur during the natural lifetime of an animal, further support in form of scaffolds and/or cell stimulants is required. Therefore, the bone morphogenetic protein (BMP) retention/release capacity of cryostructured bone scaffolds was evaluated by ELISA:
For all three types of scaffolds, only minimal amounts in the ng rage were released within the first two weeks. After 11 weeks, the BMP-2 release accounted to ca. 0.022 % for the ISO scaffolds, ca. 0.043 % for the ANI scaffolds and ca. 0.089 % for the ISOCS scaffolds. Due to the presence of sub-micron hydroxyapatite crystals on the inner pore walls of the bone scaffolds, a high surface area with attractive BMP binding sites has been created. Consequently, only less than 0.1 % of the initially loaded cytokine was released within 4 weeks, which proves an excellent BMP retention potential of the scaffolds.

Meniscus Scaffolds

If the cryostructuring process was performed under borderline conditions of anisotropic solidification, an ice crystal growth propagating nearly perpendicular to the external temperature gradient could be achieved. This pore orientation reassembles the preferred fibre orientation in meniscus tissue in large. Thus, the process was successfully tuned to work out with precursor compositions approximating the one of native meniscus tissue.
By processing precursors of collagen I, collagen II and chondroitin sulphate in fully biomimetic mass ratios, bi-zonal scaffolds were produced. Being composed out of an inner (IM) and outer (OM) meniscus zone, they were fabricated either in a cylindrical shape, for the cell culture in well plates, or in an authentic meniscus size and shape for a cell co-culture inside a vascularizable tissue. The pores inside the scaffolds were propagating through both scaffold zones over large length scales. Interestingly, they even approximated the preferential alignment of the collagenous fibres inside native meniscus tissue in case of complete meniscus scaffolds.

Osteochondral Scaffolds

By application of the cryostructuring process on three varying precursors consisting out of collagen I, collagen II, brushite and chondroitin sulphate, tri-zonal osteochondral scaffolds were created:

One mineralized subchondral zone (SC), was covered by two chondral zones (CD and CM), which were imitating the gradual glycosaminoglycan (GAG) distribution found in native osteochondral tissue. The anisotropic pore structure proceeded consecutively to the respective zones and perpendicular to the scaffold surface.

Furthermore, the possibility of combining the cryostructuring process with substrates fabricated by 3D Powder Printing of calcium phosphates, to resemble the subchondral zone, was evaluated. Although this joint venture excursus yielded stable, anisotropically structured scaffolds, the performance of those in practical application under higher compression turned out to be limited. The calcium phosphate substrates featured an inherent porosity as well as an additional pore structure, printed from CAD design. Both were not sufficient to ensure a proper re-erection of stronger compressed anisotropic pores. Therefore, the osteochondral scaffolds were further processed by using calcium phosphate powders in the subchondral zone.

An overview of the scaffolds macroscopic appearance together with the 3D microstructure was attained by µ-CT investigations. Here, the pore propagation pathways and morphologies could be expressed more holistically than it was possible with single section areas, as for instance in electron microscopic investigations.

To fulfil a biomimetic inspired strategy, where structural and compositional properties of the native osteochondral tissue are matched by the scaffolds, electrostatic spinning of polymer solutions was applied. A matrix consisting out of poly (D, L-lactide-co-glycolide) was deposited on the top of the middle chondral zone (CM) of the scaffold to create the superficial chondral zone (CS). By this, the native fibre alignment, parallel to the joint surface was mimicked. Thus, an osteochondral scaffold with four zones of tissue mimetic microstructure alignment could be fabricated.

Pore sizes, Morphologies and Topographical Structures

Since the process deals with the production of materials with special microstructures as a main feature, the investigation of the resulting matrices by SEM represented one of the most suitable characterization methods. An investigation of the ANI bone scaffolds revealed a uniform, anisotropic aligned pore structure, featuring diameters of (65 ± 25) µm. The ca. 0.5 µm thick walls consisted of a homogeneous composite

and were supported among themselves by collagenous fibre pillars. In addition, an insight in the pore structure of the ISO and ISOCS scaffolds showed spongy irregular shaped pores that were interconnected by randomly distributed and sized holes inside the pore walls. The pore diameter accounted to (88 ± 35) µm for the ISO scaffolds and (93 ± 42) µm for the ISOCS scaffolds, respectively.

For the meniscus scaffolds, differing pore sizes between the finer IM and the comparably coarser OM zone were clearly recognizable. But nonetheless, the process could be tuned to an extent, that the curved pathway of the ice crystals was not interrupted through both precursors. The mechanism behind this effect was discussed based on solidification properties. Respective pore diameters accounted to (93 ± 21) µm for the IM zone and (248 ± 63) µm for OM zone. Again, supporting pillars were observed in between the lamella structures and the mechanism leading to the deviation in the zone's pore sizes was argued.

In case of the osteochondral scaffolds, the respective zonal interfaces were barely detectable, even on a micrometre range. The tri-zonal but monolithic matrix was penetrated by an aligned, consecutive lamellar pore structure, which was extending fluently throughout the entire osteochondral scaffold. Channel pores, with diameters of (82 ± 25) µm in SC, (83 ± 29) µm in CD and (85 ± 39) µm in CM, were propagating perpendicular to the zonal surfaces. All in all, they were reassembling the dominant collagen fibre arrangement in native osteochondral tissue. By analysis of the SC zone, the results of re-precipitation processes were found and the underlying mechanism was explained.

Concluding it can be stated that a wider range of pore sizes was finding its application in the respective scaffolds. Pore sizes may be tuned to approach a desired value of ca. 80 µm with only smaller deviations of ca. 5 µm throughout multiple scaffold zones. If an anisotropic pore structure baring wider angles to the external temperature gradient is desired, the pore sizes naturally approach higher values. The angle is coupled with the external temperature gradient which is in turn affecting the pore size. In the case of higher concentrated precursors, bigger temperature gradients are needed to attain an anisotropic structure, which results in comparably smaller pore sizes. The addition of GAGs in 20 % cdw increased the pore diameters of isotropic scaffolds slightly, but measurable. For anisotropic scaffolds, the addition of 15 % cdw in GAG did not lead to effects that are to be considered significant, with respect to the measuring accuracy.

Both types of cartilage scaffolds were exhibiting a certain sub-micron to nanostructure, resulting from a combination of waved bulk material and nano-aggregates. In case of the meniscus scaffolds, the height of the wave structures ranged within ca. 300 nm - 400 nm for the IM zone and ca. 250 nm - 300 nm for the OM zone, while the diameter of the spherical aggregates varied between ca. 10 nm - 150 nm for the IM zone and ca. 60 nm - 100 nm in case of the OM zone. The osteochondral scaffolds showed aggregates, with diameters in the ranges of 90 nm - 210 nm, 30 nm - 120 nm and 30 nm - 90 nm together with wave structures of < 1 µm, ca. 1 µm and ca. 1 µm - 2 µm approximate heights for the SC, CD and CM zones, respectively.

A creation mechanism of the sub-micron to nanostructure was hypothesized, which was referring to a combination of piling up and slipping aside of the cryo-concentrated precursors. On consideration of that, the differences in expression of the wave structures seemed to be directly connected to the solidification velocities: Higher solidification velocities lead to higher wave structures, while lower ones yield lower wave structures. Since the surface topography in these length scales is known to influence cellular behaviour, the possibility to tune it to desired sizes represents an additional very promising feature of the cryostructuring processing route.

Cryostructuring Diagraphs

Temperature diagraphs depicting the thermal precursor alteration during directional solidification were recorded and evaluated for the different scaffold types. This allowed drawing conclusions from the cryostructuring parameters to the resulting scaffold morphologies. The subsequent addition of precursors together with the superpositioned cooling of the device and the generated heat of fusion are shaping the recorded temperature profiles characteristically. Different stages and forms of solidification were explained by the progression of the respective cryostructuring diagraphs. With evaluation of the parameters for external temperature gradient, solidification velocity and cooling rate, a reproducible regulation of the created solidification microstructures was enabled.

Scaffold Compositions and Degradation Behaviour

Elementary compositions of the respective scaffold zones were determined by EDX. Although, this method may not be optimal to analyse organic components, it was sufficient to map the presence of calcium phosphates and GAGs in the single scaffold zones.

The degradation behaviour represents an important factor for scaffolds intended for *in vitro* and *in vivo* applications. Mechanical support[5], remodelling capabilities[98] and degradation by products[133] are of huge importance for the cellular response to the material. An evaluation of residual mass (m/mo), equilibrium water content (EWC) and free water content (FWC) gave an insight of the degradation under physiological conditions:

While the bone scaffolds showed a mean daily mass loss of (0.52 ± 0.13) %, the meniscus scaffolds lost ca. (1.56 ± 0.10) % and the osteochondral scaffolds lost ca. (0.57 ± 0.21) % of the drained mass per day. The EWC of the bone scaffolds exhibited a loss of ca. (0.0595 ± 0.0059) % per day, while the meniscus scaffolds lost ca. (0.479 ± 0.041) % and the osteochondral scaffolds lost ca. (0.100 ± 0.030) % each day. In average, the FWC increased daily (0.389 ± 0.020) % for the bone scaffolds, (0.407 ± 0.078) % and (0.434 ± 0.060) % for the meniscus and osteochondral scaffolds, respectively.

In general, the scaffold mass and amount of bound water shrunk with proceeding erosion while the quantity of soaked water was increasing. The multi-zonal scaffolds did not show a preferential breakdown at the interface between the zones, which is to be attributed to the high quality of the interfaces on a microscopic level. A distinct lower rate of degradation was observable in case of the mineralized scaffolds that is to is to be reasoned by the comparably higher stability of the calcium phosphates against degradation. Due to the different cryostructuring conditions, varying pore architectures and pore sizes were produced. Larger pore sizes led to a greater extend of degradation progression, which is explainable by the increased circulation potential of liquids inside the scaffold pores. On consideration of all scaffold's pore sizes and degradation profiles, it was concluded, that the degree of degradation is directly proportional to the pore size.

An erosion of the bone scaffolds culminated in a volume degradation, where the interior of the scaffolds was more altered than the outer shell. This process was not that present in case of both types of cartilage scaffolds, so that this difference might be attributed to the inclusion of a higher amount of sub-micron hydroxyapatite crystallites in the bone scaffolds. However, it can be concluded too, that the carbodiimide based cross linking also yields slightly inhomogeneous results for high concentrated hydroxyapatite collagen precursors.
The degradation behaviour of all the scaffolds represented to be moderate under physiological conditions. Thereby, the suitability for a prolonged cell culture or an *in vivo* implantation might be given. Admittedly, such a degradation model cannot recapitulate all the processes which are to be expected *in vitro* or *in vivo* due to a lack of enzymes, cellular remodelling and liquid perfusion. Although the degradation properties reflect the known behaviour of biodegradable polymeric scaffolds for tissue engineering applications[303], they still bare room for optimisation.

Summarized, the invented process facilitated the fabrication of scaffolds that may address defects in multiple parts of the musculoskeletal system. This extent in mimicking of native tissue's structural properties in combination with spatial resolved tissue compositions exceeds the ones of conventional scaffolds, produced by state of the art methods. Since the whole production process takes place only at low temperatures, even temperature-sensitive active ingredients such as antibiotics and growth factors could be added to the different zones of the support structures. Thus, a new production method was conceptualized, optimized and implemented, whereby the fabrication of scaffolds that allow a testing of the key hypothesis (**Chapter 1**) was enabled.

5.5 Development of Mechanical Testing in Confined Compression

A new setup and evaluation method for confined compression measurements of hydrogels was developed. By working around the use of porous platens for compression or bedding, the well-known problem of interface alteration, associated conventional confined compression testing methods could be solved. The measuring setups were custom designed for different sample dimensions using CAD software.

A straight forward evaluation method was worked out to yield values for the apparent elastic moduli and the relation of lost to elastically stored energy (tan δ). Many other existing evaluation methods for confined compression experiments are limited in their actual practical applicability due to multiple approximations and boundary conditions. In contrast to these, the presented method is only deduced from progression of a complex wave function together with elementary definitions.

Osteochondral, meniscus and bone scaffolds were mechanically tested and evaluated with a custom build confined compression setup. An average linear compression value of (3.14 ± 0.85) kPa for apparent elastic moduli of cartilage scaffolds correlated with known values for enzymatically treated articular cartilage. The apparent elastic moduli of the bone scaffolds were about one order of magnitude higher than the moduli of osteochondral and meniscus scaffolds. However, the bone scaffolds exhibited, in mean, a linear compression module of (37.6 ± 6.9) kPa, which was significantly lower than known values for native bone tissue.
Within the present testing conditions, the additional interfaces present in multi-layered scaffolds led to higher apparent elastic moduli than the ones that could be reached by comparable monolayer scaffolds. Consequently, the implementation of a multi-layering in the invented production method was leading to an improved compressive behaviour of the scaffolds. The form of the scaffolds inherent pore structure (anisotropic and isotropic pores) seemed not to have a significant influence on the resistance against mechanical deformation under the measuring conditions. In contrast to this, an additional presence of GAGs in form of chondroitin sulphate inside the scaffolds leaded to notable higher values of the moduli in all testing conditions.

An analysis of the dissipation factor revealed a very similar behaviour of elastic energy storage to native articular cartilage and bone tissue. Under physiological frequencies less than 1.0 % and 0.8 % of the exerted energy was lost case of the bone and cartilage scaffolds, respectively. Thus, the scaffolds potential of energy storage after compression reflects the ones of native cartilage and bone. The anisotropic scaffolds showed significant lower values for energy loss than the isotropic ones. Interestingly, the supplementation of 50 % cdw in GAGs was sufficient to compensate of the energy loss associated with the isotropic pore structure.

The fast relaxing scaffolds featured an average relaxation time of (0.613 ± 0.040) sec and (0.815 ± 0.077) sec for the cartilage and bone scaffolds, respectively. Therefore, the relaxation time of the scaffolds was found to be four orders of magnitude faster than typical values for articular cartilage and cortical bone tissue. Since the investigated mechanical properties of the scaffolds mimicked mostly the behaviour of cartilage and bone tissues, another beneficial key signal which might be recognized by inherent cells is presented. Additionally, the fast relaxation behaviour and the high energy storage potential would benefit a use of the scaffolds in dynamic cell culture conditions.

Interestingly, all kinds of produced scaffolds were able to withstand cyclic compression with un-physiological frequencies as high as 20 Hz, without a loss in structural integrity. Although the behaviour of the scaffolds energy storage is matching the ones of the respective native tissues, the elastic modulus represents to be orders of magnitude lower than the values of these. If the fact is considered, that the scaffold volume consists predominantly out of pores that shall allow a proper cell seeding, whereas the constituents of the musculoskeletal system are much more dense, this is little surprising.

However, the influence of matrix stiffness on cellular behaviour is still a matter of discussion in the literature[304]. On the one hand, the stiffness of planar hydrogel matrices was demonstrated to influence stem cell adhesion and differentiation pathways[305] in the absence of protein tethering effects and porosity[306]. On the other hand, the alteration of cellular behaviour was shown to be independent on the changes in mechanical behaviour, since it rather relies on the binding of collagen I to integrins[307]. The mechanical properties of the matrix surely represent an important factor which is sensed by cells, but the cell fate is also influenced by the complexity of additional factors like chemical functionality, adhesivity, nanostructure and degradability of the matrix[133].

5.6 Biological Scaffold Performance

The cryostructuring process was applied to create bone scaffolds form collagen I and hydroxyapatite with anisotropic and isotropic pore structure. When loaded with BMP-2 a healing of critical sized defects in rat femurs could be demonstrated, despite their low cytokine release potential would be conventionally rated as unbeneficial[275]. While the trabecular bone features an isotropic appearance, the structure of cortical bone is rather to be seen as anisotropic. Despite this fact, no preferential formation of one of the mentioned tissue types could be attributed to the specific porosity anisotropic or isotropic scaffolds.
However, as shown by radiographic healing evaluation, torsion testing, µ-CT and haematoxylin eosin stainings, an anisotropic scaffold pore structure led to advantageous healing outcomes. In direct comparison between the anisotropic and isotropic pore structure, the oriented pores induced a more sustainable bridging of the defect and overall a more preferable healing impression. Interestingly, the cell density in the isotropic explants was found to be significantly higher, but apparently the functionality of the immigrated cells was expressed more pronounced inside an anisotropic pore structure. If these effects are to be attributed to the directionality of pore structure alone, or if the pore size and topographical microstructure of the scaffolds represent dominating effects remains to be clarified within further investigations.

Moreover, osteochondral and meniscus scaffolds with clinical relevant dimensions and properties were produced by unidirectional cryostructuring of hydrogel precursors. Despite being monolithic matrices, zones of varying composition were combined within the scaffolds, thus featuring at the same time an adapted material composition and continuous micropores, respectively. While the constituents of the osteochondral scaffolds matched the key signals of native osteochondral tissue[97,100,101] in large, the meniscus scaffolds featured an entirely biomimetic composition[116,118,121,127,280,281]. When subjected to static and perfusion cell culture, first signs for tissue mimetic zonal specific stem cell differentiation could be observed. By comparison of similar pore sizes, the cellular infiltration and distribution induced by the fabricated scaffolds represented to be superior to results of other literature[308], where only a limited holistic cellular infiltration could be observed.

A combination of tissue mimetic pore orientation and zonal composition presumably induced a zone specific matrix remodelling of the inherent cells like it is found inside the native tissues. In contrast to the bone scaffolds, no additional cytokines have been supplemented to influence the differentiation pathway during cell culture of cartilage scaffolds. This represents a further step towards biomimetic tissue engineering, which might guide the way to the formation of functional tissue, and thus eventually a true regeneration of cartilage.

Concluding it can be stated, that an anisotropic pore structure resulted in a higher functionality of immigrated cells which finally led to advantageous healing outcomes. Furthermore, the mimicking of local compositions of musculoskeletal tissues in combination with a consecutive anisotropic porosity that approaches the ones of native tissue structures was demonstrated to induce zone specific matrix remodelling in stem cells. Additionally, clues for a zone specific chondrogenic stem cell differentiation were attained without the supplementation of growth factors.
Consequently, the hypothesis, that an increased approximation of the hierarchically compositional and structurally anisotropic properties of musculoskeletal tissues would lead to an improved cellular response and thus presumably a better healing quality, could be confirmed. A direct transfer of the insights gained within this thesis to clinical regenerative therapies could also lead to improved results for cell free in situ tissue engineering approaches.

6 Summary

The key hypothesis of this work represented the question, if mimicking the zonal composition and structural porosity of musculoskeletal tissues influences invading cells positively and leads to advantageous results for tissue engineering. Conventional approaches in tissue engineering are limited in producing monolithic “scaffolds” that provide locally variating biological key signals and pore architectures, imitating the alignment of collagenous fibres in bone and cartilage tissues, respectively. In order to fill this gap in available tissue engineering strategies, a new fabrication technique was evolved for the production of scaffolds to validate the hypothesis.

Therefore, a new solidification based platform procedure was developed. This process comprises the directional solidification of multiple flowable precursors that are “cryostructured” to prepare a controlled anisotropic pore structure. Porous scaffolds are attained through ice crystal removal by lyophilisation. Optionally, electrostatic spinning of polymers may be applied to provide an external mesh on top or around the scaffolds. A consolidation step generates monolithic matrices from multi zonal structures. To serve as matrix for tissue engineering approaches or direct implantation as medical device, the scaffold is sterilized.

An Adjustable Cryostructuring Device (ACD) was successively developed; individual parts were conceptualized by computer aided design (CAD) and assembled. During optimisation, a significant performance improvement of the ACDs accessible external temperature gradient was achieved, from (1.3 ± 0.1) K/mm to (9.0 ± 0.1) K/mm. Additionally, four different configurations of the device were made available that enabled the directional solidification of collagenous precursors in a highly controlled manner with various sample sizes and shapes.

By using alginate as a model substance the process was systematically evaluated. Cryostructuring diagraphs were analysed yielding solidification parameters, which were associated to pore sizes and alignments that were determined by image processing. Thereby, a precise control over pore size and alignment through electrical regulation of the ACD could be demonstrated.

To obtain tissue mimetic scaffolds for the musculoskeletal system, collagens and calcium phosphates had to be prepared to serve as raw materials. Extraction and purification protocols were established to generate collagen I and collagen II, while the calcium phosphates brushite and hydroxyapatite were produced by precipitation reactions.

Besides the successive augmentation of the ACD also an optimization of the processing steps was crucial. Firstly, the concentrations and the individual behaviour of respective precursor components had to be screened. Together with the insights gained by videographic examination of solidifying collagen solutions, essential knowledge was gained that facilitated the production of more complex scaffolds. Phenomena of ice crystal growth during cryostructuring were discussed. By evolutionary steps, a cryostructuring of multi-layered precursors with consecutive anisotropic pores could be achieved and successfully transferred from alginate to collagenous precursors. Finally, very smooth interfaces that were hardly detectable by scanning electron microscopy (SEM) could be attained. For the used collagenous systems, a dependency relation between adjustable processing parameters and different resulting solidification morphologies was created.

Dehydrothermal-, diisocyanate-, and carbodiimide- based cross linking methods were evaluated, whereby the “zero length” cross linking by carbodiimide was found to be most suitable. Afterwards, a formulation for the cross linking solution was elaborated, which generated favourable outcomes by application inside a reduced pressure apparatus. As a consequence, a pore collapse during wet chemical cross linking could be avoided.

Complex monolithic scaffolds featuring continuous pores were fabricated that mimicked structure and respective composition of different areas of native tissues by the presence of biochemical key stimulants. At first, three types of bone scaffolds were produced from collagen I and hydroxyapatite with appropriate sizes to fit critical sized defects in rat femurs. They either featured an isotropic or anisotropic porosity and partly also contained glycosaminoglycans (GAGs). Furthermore, meniscus scaffolds were prepared by processing two precursors with biomimetic contents of collagen I, collagen II and GAGs. Here, the pore structures were created under boundary conditions, which allowed an ice crystal growth that was nearly orthogonal to the external temperature gradient. Thereby, the preferential alignment of collagen fibres in the natural meniscus tissue could be mimicked.

Those scaffolds owned appropriate sizes for cell culture in well plates or even an authentic meniscus shape and size. Finally, osteochondral scaffolds, sized to either fit well plates or perfusion reactors for cell culture, were fabricated to mimic the composition of subchondral bone and different cartilage zones. Collagen I and the resorbable calcium phosphate brushite were used for the subchondral zone, whereas the cartilage zones were composed out of collagen I, collagen II and tissue mimetic contents of GAGs. The pore structure corresponded to the one that is dominating the volume of natural osteochondral tissue.

Energy dispersive X-ray spectroscopy (EDX) and SEM were used to analyse the composition and pore structure of the individual scaffold zones, respectively. The cross section pore diameters were determined to (65 ± 25) µm, (88 ± 35) µm and (93 ± 42) µm for the anisotropic, the isotropic and GAG containing isotropic bone scaffolds. Furthermore, the meniscus scaffolds showed pore diameters of (93 ± 21) µm in the inner meniscus zone and (248 ± 63) µm inside the outer meniscus zone. Pore sizes of (82 ± 25) µm, (83 ± 29) µm and (85 ± 39) µm were present inside the subchondral, the lower chondral and the upper chondral zone of osteochondral scaffolds. Depending on the fabrication parameters, the respective scaffold zones were also found to feature a specific micro- and nanostructure at their inner surfaces.

Degradation studies were carried out under physiological conditions and resulted in a mean mass loss of (0.52 ± 0.13) %, (1.56 ± 0.10) % and (0.80 ± 0.10) % per day for bone, meniscus and osteochondral scaffolds, respectively. Rheological measurements were used to determine the viscosity changes upon cooling of different precursors. Micro computer tomography (µ-CT) investigations were applied to characterize the 3D microstructure of osteochondral scaffolds. To obtain an osteochondral scaffold with four zones of tissue mimetic microstructure alignment, a poly (D, L-lactide-co-glycolide) mesh was deposited on the upper chondral zone by electrostatic spinning. In case of the bone scaffolds, the retention / release capacity of bone morphogenetic protein 2 (BMP-2) was evaluated by an enzyme linked immunosorbent assay (ELISA). Due to the high presence of attractive BMP binding sites, only less than 0.1 % of the initially loaded cytokine was released. The suitability of combining the cryostructuring process with 3D powder printed calcium phosphate substrates was evaluated with osteochondral scaffolds, but did not appear to yield more preferable results than the non-combined approach.

A new custom build confined compression setup was elaborated together with a suitable evaluation procedure for the mechanical characterisation under physiological conditions. For bone and cartilage scaffolds, apparent elastic moduli of (37.6 ± 6.9) kPa and (3.14 ± 0.85) kPa were measured. A similar behaviour of the scaffolds to natural cartilage and bone tissue was demonstrated in terms of elastic energy storage. Under physiological frequencies, less than 1.0 % and 0.8 % of the exerted energy was lost for bone and cartilage scaffolds, respectively. With average relaxation times of (0.613 ± 0.040) sec and (0.815 ± 0.077) sec, measured for the cartilage and bone scaffolds, they respond four orders of magnitude faster than the native tissues. Additionally, all kinds of produced scaffolds were able to withstand cyclic compression at un-physiological frequencies as high as 20 Hz without a loss in structural integrity.

With the presented new method, scaffolds could be fabricated whose extent in mimicking of native tissues exceeded the one of scaffolds producible by state of the art methods. This allowed a testing of the key hypothesis: The biological evaluation of an anisotropic pore structure *in vivo* revealed a higher functionality of immigrated cells and led finally to advantageous healing outcomes. Moreover, the mimicking of local compositions in combination with a consecutive anisotropic porosity that approaches native tissue structures could be demonstrated to induce zone specific matrix remodelling in stem cells *in vitro*. Additionally, clues for a zone specific chondrogenic stem cell differentiation were attained without the supplementation of growth factors.

Thereby, the hypothesis that an increased approximation of the hierarchically compositional and structurally anisotropic properties of musculoskeletal tissues would lead to an improved cellular response and a better healing quality, could be confirmed. With a special focus on cell free in situ tissue engineering approaches, the insights gained within this thesis may be directly transferred to clinical regenerative therapies.

7 Zusammenfassung

Die Schlüsselhypothese dieser Arbeit bestand darin zu überprüfen, ob eine Nachahmung der zonalen Zusammensetzungen und Porenstruktur muskulo-skelettaler Gewebe einwandernde Zellen beeinflusst und zu vorteilhafteren Ergebnissen im Tissue Engineering führt. Obwohl bereits zahlreiche konventionelle Ansätze existieren, so sind diese in ihrem Vermögen spezielle Zellträgermatrices („Scaffolds“) herzustellen limitiert. Insbesondere können dabei lokal variierende biologische Schlüsselreize nicht mit einer Porenstruktur, welche die Ausrichtung der Kollagenfasern in Knochen- und Knorpelgeweben imitiert, kombiniert werden. Um diese Lücke in den verfügbaren Tissue Engineering Strategien zu schließen, wurde ein neues Verfahren entwickelt. Dieses erlaubte die Herstellung monolithischer Scaffolds, welche eine Validierung der Hypothese ermöglichten.

Das neue Plattform-Verfahren basiert auf der gerichteten Erstarrung mehrerer fließfähiger Vorstufen, um somit eine kontrollierte anisotrope Porenstruktur vorzubereiten. Ein Entfernen der erstarrten Lösungsmittel durch Lyophilisation führt zu porösen Scaffolds. Optional besteht die Möglichkeit, Polymere mittels elektrostatischem Verspinnen als umhüllendes Vlies zu inkorporieren. Nach einem Vernetzungsschritt resultieren monolithische Matrices, bestehend aus mehreren Zonen mit unterschiedlichen Zusammensetzungen. Vor einer Verwendung als Tissue Engineering Matrix oder implantierbares Medizinprodukt erfolgt eine Sterilisation. Hierfür wurde ein “Adjustable Cryostructuring Device“ (ACD) entwickelt, einzelne Bauteile mit Computer Aided Design entworfen und zu einer Apparatur montiert. Die Optimierung der Anlage ermöglichte eine signifikante Erhöhung des verfügbaren externen Temperaturgradienten von (1.3 ± 0.1) K/mm auf (9.0 ± 0.1) K/mm. Außerdem erlauben vier unterschiedliche Konfigurationen des ACD die gerichtete Erstarrung von kollagenen Vorstufen in einer besonders kontrollierten Art und Weise bei einer Vielzahl an Probengrößen und Formen.
Die systematische Evaluation des Prozesses erfolgte mit Alginat als Modell-Substanz. Aus den zeitlichen Verläufen der Gefrierstrukturierung resultierten Erstarrungsparameter, die mittels Bildverarbeitung den entstandenen Porengrößen und -ausrichtungen zugeordnet wurden. Dies demonstrierte eine präzise Kontrolle der Ergebnisse durch elektrische Ansteuerung der ACD.

Zur Erzeugung von Rohmaterialien war eine Etablierung von Extraktions- und Aufreinigungsprotokollen für Kollagen I und Kollagen II notwendig, während eine Herstellung der Calciumphosphate Bruschit und Hydroxylapatit mittels Präzipitations-Reaktionen verlief. Neben der sukzessiven Verbesserung des ACD, stellte auch die Optimierung einzelner Prozessschritte wichtige Aspekte dar. Die Untersuchung und Diskussion des Verhaltens einzelner Vorstufenkomponenten sowie der Erstarrungs-phänomene von Kollagenlösungen führte zu einem Verständnis welches die Produktion von komplexeren Scaffolds zuließ. Somit war es auch möglich eine Abhängigkeitsrelation der einstellbaren Prozessparameter zu den resultierenden Erstarrungsmorphologien der verwendeten Kollagensysteme abzuleiten.

Die Gefrierstrukturierung von mehreren Lagen unterschiedlicher Vorstufen konnte erfolgreich von Alginat- auf Kollagenvorstufen transferiert werden. Nach einer Optimierung der jeweiligen Grenzflächenübergänge, waren diese selbst mittels Rasterelektronenmikroskopie kaum noch zu erkennen. Eine Evaluierung von dehydrothermal-, diisocyanat- und carbodiimid- basierten Quervernetzungs-methoden zeigte die vorteilhaftesten Ergebnisse für die Vernetzung durch Carbodiimide. Zusätzlich wurde eine Zusammensetzung der Vernetzungslösung ermittelt, welche beim Einsatz in einer Unterdruckapparatur einen Porenstrukturkollaps durch nasschemische Vernetzung vermeidet.

Eine erweiterte Kontrolle der Gefrierprozesse erlaubte es Struktur und Zusammensetzung verschiedener Zonen nativer Gewebe durch eine monolithische Zellträgermatrix mit durchgängiger Porenstruktur und biochemischen Schlüsselreizen nachzuahmen. Zuerst wurden drei Arten von Knochenscaffolds aus Kollagen I und Hydroxylapatit hergestellt, die Defekten kritischer Größe in Rattenoberschenkel-knochen entsprachen. Diese zeichneten sich durch eine isotrope oder eine anisotrope Porenstruktur aus und enthielten teilweise Glycosaminoglycane (GAGs). Weiterhin erfolgte die Produktion von Meniskusscaffolds aus zwei Vorstufen mit biomimetischen Anteilen an Kollagen I, Kollagen II und GAGs. Dabei verlief die Gefrierstrukturierung unter Grenzbedingungen, welche ein nahezu senkrechtes Eiskristallwachstum zu dem äußeren Temperaturgradienten erlaubten. Somit konnte der bevorzugte Verlauf von Kollagenfasern in nativem Meniskusgewebe nachgeahmt werden. Die Scaffolds waren entweder passend für „Well Plates“ der Zellkultur bemaßt oder besaßen sogar Form und Größe von authentischen Menisken.

Zuletzt wurden osteochondrale Scaffolds hergestellt, deren Zusammensetzung den jeweiligen Bereichen von Subchondralzone und verschiedenen Gelenkknorpelzonen entsprach. Kollagen I und die bioresorbierbare Calciumphosphatphase Bruschit fanden Verwendung in der Subchondralzone, während die Knorpelzonen aus Kollagen I, Kollagen II und entsprechenden biomimetischen Anteilen an GAGs bestanden. Außerdem bildete die Scaffoldporenstruktur die Volumendominierende in natürlichem Osteochondralgewebe nach, wobei die Dimensionierungen der Scaffolds Well Plates oder Perfusionsreaktoren der Zellkultur angepasst waren.

Mittels energiedispersiver Röntgenspektroskopie und Rasterelektronenmikroskopie erfolgte die Analyse von Zusammensetzung und Porenstruktur der jeweiligen Scaffoldzonen. Die Größe der Porenquerschnitte betrug (65 ± 25) µm, (88 ± 35) µm und (93 ± 42) µm für die anisotropen, die isotropen und die GAG-haltigen isotropen Knochenscaffolds. Die Meniskusscaffolds besaßen Porendurchmesser von (93 ± 21) µm in der inneren Meniskuszone und (248 ± 63) µm innerhalb der äußeren Meniskuszone. Im Falle der osteochondralen Scaffolds wurden Porengrößen von (82 ± 25) µm, (83 ± 29) µm und (85 ± 39) µm in der subchondralen, der unteren chondralen und der oberen chondralen Zone gemessen. In Abhängigkeit von den Prozessparametern zeigten die inneren Oberflächen der jeweiligen Scaffoldzonen eine spezifische Mikro- und Nanostruktur.

Eine Prüfung des Degradationsverhaltens unter physiologischen Bedingungen ergab einen mittleren Massenverlust von (0.52 ± 0.13) %, (1.56 ± 0.10) % und (0.80 ± 0.10) % pro Tag für die Knochen-, Meniskus- und osteochondralen Scaffolds. Die Untersuchung der Viskositätsveränderungen während der Abkühlung unterschiedlicher Vorstufen geschah mit rheologischen Messungen. Weiterhin wurde die 3D Mikrostruktur von osteochondralen Matrices mit Mikro Computer Tomographie charakterisiert. Um einen osteochondralen Scaffold mit vier Zonen gewebeähnlich ausgerichteter Mikrostruktur zu erhalten, konnte die Scaffoldoberfläche durch ein elektroversponnenes Poly (D, L-Lactid-co-Glycolid) Vlies modifiziert werden.

Ein „enzyme linked immunosorbent assay“ (ELISA) diente zur Evaluation des Rückhalte- bzw. Freisetzungsverhaltens von „bone morphogenetic protein 2“ (BMP-2) in Knochenscaffolds. Bedingt durch die hohe Präsenz von attraktiven BMP Bindungsstellen betrug die freigesetzte Menge des initial beladenen Zytokins nur weniger als 0.1 %.

Die Eignung einer Kombination des Gefrierstrukturierungsprozesses mit 3D gedruckten Calciumphosphatsubstraten wurde anhand von osteochondralen Scaffolds überprüft, aber zeigte keine vorteilhafteren Resultate als die nicht kombinierte Vorgehensweise.
Für die mechanische Charakterisierung unter physiologischen Bedingungen konnte ein neues Test-Setup mitsamt Auswertungsverfahren entwickelt werden. Die gemessenen Elastizitätsmoduln betrugen (37.6 ± 6.9) kPa für Knochen- und (3.14 ± 0.85) kPa für Knorpelscaffolds. Da unter physiologischen Frequenzen nur weniger als 1.0 % der eingebrachten Energie verloren ging, entsprach die Fähigkeit der Zellträgermatrices zur elastischen Energiespeicherung dem von natürlichem Knochen- und Knorpelgewebe. Bei mittleren Relaxationszeiten von (0.613 ± 0.040) sec und (0.815 ± 0.077) sec für Knorpel- und Knochenscaffolds reagieren diese vier Größenordnungen schneller als die nativen Gewebe. Außerdem waren alle produzierten Matrices dazu in der Lage zyklischen Kompressionen bei unphysiologisch hohen Frequenzen von 20 Hz zu wiederstehen, ohne an struktureller Integrität zu verlieren.

Mit dem vorgestellten neuen Verfahren konnten Scaffolds hergestellt werden, deren Ausmaß in der Nachahmung nativer Gewebe mit etablierten Methoden nicht erreichbar war und welche eine Überprüfung der Schlüsselhypothese erlaubten: Die biologische Evaluation einer anisotropen Porenstruktur *in vivo* zeigte eine höhere Funktionalität eingewanderter Zellen, was zu vorteilhafteren Heilungsergebnissen führte. Darüber hinaus demonstrierte eine Imitation der lokalen Zusammensetzungen in Kombination mit einer durchgängigen anisotropen Porenstruktur, welche an diejenige in nativen Geweben angenähert ist, eine Induktion von zonenspezifischer Matrixremodellierung von Stammzellen *in vitro*. Außerdem waren Hinweise auf eine zonale chondrogene Stammzelldifferenzierung ohne eine gesonderte Zugabe von Wachstumsfaktoren zu beobachten.
Somit konnte die Hypothese, dass eine verbesserte Nachahmung der hierarchischen Zusammensetzung und anisotroper Struktur von muskuloskelettalen Geweben zu einer optimierten zellulären Reaktion und somit einer besseren Heilungsqualität führt, bestätigt werden. Mit einem speziellen Fokus auf zellfreies in situ Tissue Engineering, könnten die Erkenntnisse dieser Arbeit direkt für klinische Therapien eingesetzt werden.

8 Acknowledgment

First of all, I would like the thank Prof. Dr. Jürgen Groll for the supervision and financial support of my thesis as well as for the creative freedom he granted me in its conception. For his valuable lessons on specific topics, but also on general life in university and industry, I am thankful. By his guidance, he succeeded in replacing too much perfectionism with efficiency. Furthermore I really appreciated the opportunities to visit conferences and attain the related experiences.

Moreover, I want to thank Prof. Dr. Uwe Gbureck for all the years of supervision and the opportunity to manifest my own research approaches as thesis theme. I am grateful for all the interesting discussions we shared on scientific and continuative topics. Particularly, his exceptional care and permanent kindness made my time during the thesis very pleasant.

Additionally, I would like to enunciate my thanks to Prof. Dr. Frank A. Müller (Otto-Schott-Institute for Materials Research, Friedrich-Schiller-University of Jena) for complying my request to take the position of an external thesis reviewer and examiner of my thesis defence.

To Mr. Harald Hümpfer and Mr. Anton Hofmann I want to express my appreciation for the discussion on the construction of the Adjustable Cryostructuring Device. Without the excellently made, custom build parts of the device, the experimental part of this thesis could not have been realized in the present quality.

For various discussions about biological topics I would like to acknowledge Dr. Andrea Ewald. Additionally, I also want to thank Dr. Jörg Teßmar for his steady support and the improvement of all kinds of administrative issues. Furthermore, I want to thank Ms. Isabell Biermann for many years of being a very helpful contact person for everyday issues in the laboratory. Ms. Maria Aniolek is to be acknowledged for her endeavours with the ELISA measurements.

Moreover, I thank for the support that I received from other research facilities: Dr. Gregor Lang (Chair for Biomaterials, University of Bayreuth) helped me noticeably with the operation of the Electroforce. Mr. Werner Stracke (Fraunhofer Institute for Silicate Research, Würzburg) is to be acknowledged for his very motivated analysis with SEM and EDX. Dr. Joachim Nickel (Department for Tissue Engineering and Regenerative Medicine, University of Würzburg) provided rh-BMP-2 and advises for its use. Dr. Guntram Schwarz (Chair of Chemical material synthesis, University of Würzburg) is to be thanked for the introduction and the possibility to use the rheometer.

Furthermore, I want to express my thanks to Prof. Felipe Prósper Cardoso, Dr. Froilán Granero Moltó, Dr. Emma Muiños, Dr. José M. Lamo de Espinosa (Experimental Orthopaedics Laboratory & Cell Therapy Department, Clínica Universidad de Navarra, Pamplona, Spain) and Dr. Ion Andreu (CEIT & TECNUN, Universidad de Navarra, San Sebastián, Spain) for the accommodative collaboration as well as the performance and evaluation of in vivo experiments. Additionally, I appreciated the good care of Dr. Froilán Granero Moltó, Dr. Emma Muiños during my stay in Pamplona.

Farther, I would like to acknowledge Prof. Dr. Heike Walles, M.Sc. Andrea Schwab, Markus Knauer, Dr. Franziska Ehlicke and Dr. Jenny Reboredo (Department for Tissue Engineering and Regenerative Medicine, University of Würzburg) for the cooperative research. In addition, I thank M.Sc. Andrea Schwab and Markus Knauer for the execution and evaluation of the in vitro culture.

Nonetheless, I would like to express my gratitude towards all my colleagues for a very pleasant time during the PhD thesis. Especially my esteemed office colleagues Dipl.-Ing. Tobias Schmitz, Dipl.-Ing. Tomasz Jüngst, Dr. Karl-Heinz Heffels, M.Sc Ilona Zilkowski, M.Sc Sarah Bertlein, Dipl.-Chem. Simone Stichler and Dipl.-Chem Julia Blöhbaum enriched my daily life considerably. Last but not least, I thank Dipl.-Chem. Michael Schmitz for the helpful proof reading of this thesis.

9 References

1. Mow VC, Ratcliffe A, Poole AR. Cartilage and diarthrodial joints as paradigms for hierarchical materials and structures. *Biomaterials* 1992, **13**(2): 67-97.

2. Reznikov N, Shahar R, Weiner S. Bone hierarchical structure in three dimensions. *Acta Biomater.* 2014, **10**(9): 3815-3826.

3. Place ES, Evans ND, Stevens MM. Complexity in biomaterials for tissue engineering. *Nat. Mater.* 2009, **8**(6): 457-470.

4. Tibbitt MW, Anseth KS. Hydrogels as Extracellular Matrix Mimics for 3D Cell Culture. *Biotechnol. Bioeng.* 2009, **103**(4): 655-663.

5. Hollister SJ. Porous scaffold design for tissue engineering. *Nat. Mater.* 2005, **4**(6): 518-524.

6. Steinert AF, Rackwitz L, Gilbert F, Ulrich N, Tuan RS. Concise Review: The Clinical Application of Mesenchymal Stem Cells for Musculoskeletal Regeneration: Current Status and Perspectives. *Stem Cells Trans. Med.* 2012, **1**(3): 237-247.

7. Malda J, Visser J, Melchels FP, Jüngst T, Hennink WE, Dhert WJA, *et al.* Engineering Hydrogels for Biofabrication. *Adv. Mater.* 2013, **25**(36): 5011-5027.

8. Lutolf MP. Spotlight on hydrogels. *Nat. Mater.* 2009, **8**(6): 451-453.

9. Shayegan M, Forde NR. Microrheological Characterization of Collagen Systems: From Molecular Solutions to Fibrillar Gels. *PLOS ONE* 2013, **9**(7): e70590.

10. Sun J-Y, Zhao X, Illeperuma WRK, Chaudhuri O, Oh KH, Mooney DJ, *et al.* Highly stretchable and tough hydrogels. *Nature* 2012, **489**(7414): 133-136.

11. Grafahrend D, Heffels K-H, Beer MV, Gasteier P, Möller M, Boehm G, *et al.* Degradable polyester scaffolds with controlled surface chemistry combining minimal protein adsorption with specific bioactivation. *Nat. Mater.* 2010, **10**(1): 67-73.

12. Hochleitner G, Jüngst T, Brown TD, Hahn K, Moseke C, Jakob F, *et al.* Additive manufacturing of scaffolds with sub-micron filaments via melt electrospinning writing. *Biofabrication* 2015, **7**(6): 1-10.

13. Hochleitner G, Hümmer JF, Luxenhofer R, Groll J. High definition fibrous poly (2-ethyl-2-oxazoline) scaffolds through melt electrospinning writing. *Polymer* 2014, **55**(20): 5017–5023.

14. Schoof H, Apel J, Heschel I, Rau G. Control of Pore Structure and Size in Freeze-Dried Collagen Sponges. *J. Biomed. Mater. Res., Part A* 2001, **58**(4): 352-357.

15. Jungst T, Smolan W, Schacht K, Scheibel T, Groll J. Strategies and Molecular Design Criteria for 3D Printable Hydrogels. *Chem. Rev.* 2015.

16. Holzapfel BM, Reichert JC, Schantz J-T, Gbureck U, Rackwitz L, Nöth U, *et al.* How smart do biomaterials need to be? A translational science and clinical point of view. *Adv. Drug Del. Rev.* 2013, **65**(4): 581–603.

17. Lutolf MP, Hubbell JA. Synthetic biomaterials as instructive extracellular microenvironments for morphogenesis in tissue engineering. *Nat. Biotechnol.* 2005, **23**(1): 47-55.

18. Schacht K, Jüngst T, Schweinlin M, Ewald A, Groll J, Scheibel T. Biofabrication of Cell-Loaded 3D Spider Silk Constructs. *Angew. Chem.* 2015, **54**(9): 2816–2820.

19. Ristovski N, Bock N, Liao S, Powell SK, Ren J, Kirby GTS*, et al.* Improved fabrication of melt electrospun tissue engineering scaffolds using directwriting and advanced electric field control. *Biointerphases* 2015, **10**(1): 1-10.

20. Zhang Q, Lu H, Kawazoe N, Chen G. Pore size effect of collagen scaffolds on cartilage regeneration. *Acta Biomater.* 2014, **10**(5): 2005-2013.

21. Archer R, Williams DJ. Why tissue engineering needs process engineering. *Nat. Biotechnol.* 2005, **23**(11): 1353-1135.

22. Heschel I. Pore size of collagen scaffolds with anisotropic pore structure. DGBM annual meeting; 2010.

23. Schoof H, Bruns L, Fischer A, Heschel I, Rau G. Dendritic ice morphology in unidirectionally solidified collagen suspensions. *J. Cryst. Growth* 2000, **209**(1): 122-129.

24. Rieppo J, Hirvonen J, Korhonen RK, Laasanen MS, Helminen HJ, Jurvelin JS. Comparison of the equilibrium response of articular cartilage in unconfined compression, confined compression and indentation. *J. Biomech.* 2002, **35**(7): 903-909.

25. Buschmann MD, Soulhat J, Shirazi-adl A, Jurvelin JS, Hunziker EB. Confined compression of articular cartilage: Linearity in ramp and sinusoidal tests and the importance of interdigitation and incomplete confinement. *J. Biomech.* 1998, **31**(5): 171-178.

26. Stuckensen K. Synthese anisotrop strukturierter mineralischer Biopolymer-Matrizes. Dipl.-Ing thesis, Würzburg, 2010.

27. Stuckensen K, Gbureck U, Groll J, inventors; Patent EP2788171A2 - Production of materials having an anisotropic structure. 2012.

28. Jakob F, Ebert R, Ignatius A, Matsushita T, Watanabe Y, Groll J*, et al.* Bone tissue engineering in osteoporosis. *Maturitas* 2013, **75**(2): 118-124.

29. Wegst UGK, Bai H, Saiz E, Tomsia AP, Ritchie RO. Bioinspired structural materials. *Nat. Mater.* 2015, **14**(1): 23-36.

30. Hing KA. Bone repair in the twenty-first century: Biology, chemistry or engineering? *Phil. Trans. R. Soc. Lond. A* 2004, **362**(9): 2821-2850.

31. J.K. G, Arnold JS, Cohn SH. Composition of Trabecular and Cortical Bone. *Anat. Rec.* 1964, **149**(3): 325-332.

32. Reznikov N, Shahar R, Weiner S. Three-dimensional structure of human lamellar bone: The presence of two different materials and new insights into the hierarchical organization. *Bone* 2014, **59**(2): 93-104.

33. Magal RA, Reznikov N, Shahar R, Weiner S. Three-dimensional structure of minipig fibrolamellar bone: Adaptation to axial loading. *J. Struct. Biol.* 2014, **186**(2): 253-264.

34. Wang Y, Euw SV, Fernandes FM, Cassaignon S, Selmane M, Laurent G, *et al.* Water-mediated structuring of bone apatite. *Nat. Mater.* 2013, **12**(12): 1144-1153.

35. LeGeros R. Calcium Phosphate-Based Osteoinductive Materials. *Chem. Rev.* 2008, **108**(6): 4742–4753.

36. Albrektsson T, Johansson C. Osteoinduction, osteoconduction and osseointegration. *Eur. Spine J.* 2001, **10**(2): 96-101.

37. Murugan R, Ramakrishna S. Development of nanocomposites for bone grafting. *Composites Sci. Technol.* 2005, **65**(15): 2385–2406.

38. Bohner M, Gbureck U, Barralet JE. Technological issues for the development of more efficient calcium phosphate bone cements: A critical assessment. *Biomaterials* 2005, **26**(33): 6423–6429.

39. LeGeros R, Chohayeb A, Shulman A. Apatitic calcium phosphates: possible dental restorative materials. *J Dental Res* 1982, **61**(1): 343.

40. Brown W, Chow L. A new calcium phosphate setting cement. *J Dental Res* 1983, **62**(1): 672.

41. Müller FA, Gbureck U, Kasuga T, Mizutani Y, Barralet JE, Lohbauer U. Whisker-Reinforced Calcium Phosphate Cements. *J. Am. Ceram. Soc.* 2007, **90**(11): 3694–3697.

42. Geffers M, Groll J, Gbureck U. Reinforcement Strategies for Load-Bearing Calcium Phosphate Biocements. *Materials* 2015, **8**(5): 2700-2717.

43. Hofmann MP, Mohammed AR, Perrie Y, Gbureck U, Barralet JE. High-strength resorbable brushite bone cement with controlled drug-releasing capabilities. *Acta Biomater.* 2008, **5**(1): 43-49.

44. Gbureck U, Barralet JE, Spatz K, Grover LM, Thull R. Ionic modification of calcium phosphate cement viscosity. Part I: hypodermic injection and strength improvement of apatite cement. *Biomaterials* 2004, **25**(5): 2187–2195.

45. Barralet JE, Grover LM, Gbureck U. Ionic modification of calcium phosphate cement viscosity. Part II: hypodermic injection and strength improvement of brushite cement. *Biomaterials* 2004, **25**(11): 2197–2203.

46. Gbureck U, Hölzel T, Klammert U, Würzler K, Müller FA, Barralet JE. Resorbable Dicalcium Phosphate Bone Substitutes Prepared by 3D Powder Printing. *Adv. Funct. Mater.* 2007, **17**(18): 3940-3945.

47. Habibovic P, Gbureck U, Doillon CJ, Bassett DC, Blitterswijk CAV, Barralet JE. Osteoconduction and osteoinduction of low-temperature 3D printed bioceramic implants. *Biomaterials* 2008, **29**(7): 944-953.

48. Vorndran E, Klammert U, Ewald A, Barralet JE, Gbureck U. Simultaneous Immobilization of Bioactives During 3D Powder Printing of Bioceramic Drug-Release Matrices. *Adv. Funct. Mater.* 2010, **20**(10): 1585-1591.

49. Yuan H, Li Y, de Bruijn J, K dG, Zhang X. Tissue responses of calcium phosphate cement: a study in dogs. *Biomaterials* 2000, **21**(12): 1283–1290.

50. Geiger M, Li RH, Friess W. Collagen sponges for bone regeneration with rhBMP-2. *Adv. Drug Del. Rev.* 2003, **55**(12): 1613-1629.

51. LeGeros RZ. Biodegradation and bioresorption of calcium phosphate ceramics. *Clin. Mater.* 1993, **14**(1): 65-88.

52. Chow LC. Calcium phospahte cements. *Monogr Oral Sci. Basel* 2001, **18**(1): 148-163.

53. Tamimi F, Sheikh Z, Barralet J. Dicalcium phosphate cements: Brushite and monetite. *Acta Biomater.* 2011, **8**(2): 474–487.

54. Ohta M, Tsutsumi M. The relationship between the morphology of brushite crystals grown rapidly in silica gel and its structure. *J. Cryst. Growth* 1982, **56**(1): 652-658.

55. Tamimi F, Kumarasami B, Doillon CJ, Gbureck U, Le Nihouannen D, Cabarcos EL, *et al.* Brushite-collagen composites for bone regeneration. *Acta Biomater.* 2008, **4**(5): 1315–1321.

56. Oliveira C, Georgieva P, Rocha F, Ferreira A, Feyo de Azevedo S. Dynamical model of brushite precipitation. *J. Cryst. Growth* 2007, **305**(1): 201-210.

57. Abbona F, Angela MF. Crystal habit and growth conditions of brushite, CaHPO4 2H2O. *J. Cryst. Growth* 1993, **131**(3): 331-346.

58. Abbona F. The initial phases of calcium and magnesium phosphates precipitated from solutions of high to medium concentrations. *J. Cryst. Growth* 1986, **74**(3): 581–590.

59. Grover LM, Gbureck U, Wright AJ, Tremayne M, Barralet JE. Biologically mediated resorption of brushite cement in vitro. *Biomaterials* 2006, **27**(10): 2178-2185.

60. Ivanova TI, Frank-Kamenetskaya OV, Kol'tsov AB, Ugolkov VL. Crystal Structure of Calcium-Deficient Carbonated Hydroxyapatite. Thermal Decomposition. *J. Solid State Chem.* 2001, **160**(2): 340–349.

61. Dorozhkin SV. Calcium orthophosphate-based biocomposites and hybrid biomaterials. *J. Mater. Sci.* 2009, **44**(9): 2343-2387.

62. Döbelin N, Luginbühl R, Bohner M, Cells B. Synthetic Calcium Phosphate Ceramics for Treatment of Bone Fractures. *CHIMINA* 2010, **64**(10): 723-729.

63. Ewald A, Helmschrott K, Knebl G, Mehrban N, Grover LM, Gbureck U. Effect of cold-setting calcium- and magnesium phosphate matrices on protein expression in osteoblastic cells. *J. Biomed. Mater. Res., Part B* 2011, **96B**(2): 326-332.

64. Koutsopoulos S. Synthesis and characterization of hydroxyapatite crystals: a review study on the analytical methods. *J. Biomed. Mater. Res.* 2002, **64**(4): 600-612.

65. Hayek E, W. Bohler JL. Hydrothermalsynthese von Calcium-Apatiten. *Z. anorg. allg. Chem.* 1958, **295**(1): 241-246.

66. Gomez-Morales J, Torrent-Burgués J, Boix T, Fraile J, Rodriguez-Clemente R. Precipitation of stoichiometric hydroxyapatite by a continuous method. *Cryst. Res. Technol.* 2001, **36**(1): 15-26.

67. Rodríguez-Clemente R, López-Macipea A, Gómez-Moralesa J, Torrent-Burguésb J, Castañoc VM. Hydroxyapatite precipitation a case of nucleation-aggregation-agglomeration-growth mechanism. *J. Eur. Ceram. Soc.* 1998, **18**(9): 1351-1356.

68. Vijayalakshmi Natarajan U, Rajeswari S. Influence of calcium precursors on the morphology and crystallinity of sol-gel-derived hydroxyapatite nanoparticles. *J. Cryst. Growth* 2008, **310**(8): 4601-4611.

69. Stötzel C, Müller FA, Reinert F, Niederdraenk F, Barralet JE, Gbureck U. Ion adsorption behaviour of hydroxyapatite with different crystallinities. *Colloids Surf. B. Biointerfaces* 2009, **74**(1): 91-95.

70. Kheir E, Shaw D. Management of articular cartilage defects. *Orthop. Trauma* 2009, **23**(4): 266-273.

71. Cook JL. The Current Status of Treatment for Large Meniscal Defects. *Clin. Orthop. Relat. Res.* 2005, **435**(1): 88-95.

72. Yannas IV. Collagen and Gelatin in the Solid State. *J. Macromol. Sci., Part C* 1972, **7**(1): 49-106.

73. Fratzl P. *Collagen - Structure and Mechanics*. Springer, 2008.

74. Bosman FT, Stamenkovic I. Functional structure and composition of the extracellular matrix. *J. Pathol.* 2003, **200**(4): 423-428.

75. Nelson D, Cox M. *Lehringer Biochemie*, 4th edn. Springer Verlag: New York, 2009.

76. Fessler JH, Doege KJ, Duncan KG, Fessler L. Biosynthesis of Collagen. *J. Cell. Biochem.* 1985, **28**(1): 31-37.

77. Silver FH, Freeman JW, Seehra GP. Collagen self-assembly and the development of tendon mechanical properties. *J. Biomech.* 2003, **36**(10): 1529-1553.

78. Hay ED. Extracellular Matrix. *J. Cell Biol.* 1981, **91**(1): 205-223.

79. Orgel JPRO, Persikov AV, Antipova O. Variation in the Helical Structure of Native Collagen. *PLOS one* 2014, **9**(2): 1-11.

80. Bruns RR, Trelstad RL, Gross J. Cartilage Collagen: A Staggered Substructure in Reconstituted Fibrils. *Science* 1973, **181**(4096): 269-271.

81. Knapp DM, Barocas VH, Moon AG. Rheology of reconstituted type I collagen gel in confined compression. *J. Rheol.* 1997, **41**(5): 971-993.

82. Kadler KE, Holmes DF, Trotter JA, Chapman JA. Collagen fibril formation. *Biochem. J.* 1996, **11**(1): 1-11.

83. Kato YP, Christiansen DL, Hahn RA, Shieh S-J, Goldstein JD, Silver FH. Mechanical properties of collagen fibres: a comparison of reconstituted and rat tail tendon fibres. *Biomaterials* 2003, **10**(1): 38-42.

84. Mendler M, Eich-bender SG, Vaughan L, Winterhalter KH. Cartilage Contains Mixed Fibrils of Collagen Types II, IX, and XI. *Cell* 1989, **108**(1): 191-197.

85. Fithian D, Kelly M, Mow V. Material Properties and Structure-Function Relationships in the Menisci. *Clin. Orthop. Relat. Res.* 1990, **252**(1): 19-31.

86. Mansour JM. *The Mechanics and Pathomechanics of Human Movement, Chapter 5: Biomechanics of Cartilage*, 1st edn. Lippincott Williams and Wilkins: Philadelphia, 2003.

87. Roughley PJ. The structure and function of cartilage proteoglycans. *Eur. Cells Mater.* 2006, **12**(1): 92-101.

88. Pieper JS, Oosterhof A, Dijkstra PJ, Veerkamp JH, Kuppevelt THV. Preparation and characterization of porous crosslinked collagenous matrices containing bioavailable chondroitin sulphate. *Biomaterials* 1999, **20**(9): 847-858.

89. Bruckner P, van Der Rest M. Structure and Function of Cartilage Collagens. *Microsc. Res. Tech.* 1994, **28**(5): 378-384.

90. Compert WD, Veis A. The Mechanism of Nucleation for in vitro Collagen Fibril Formation. *Biopolymers* 1977, **16**(10): 2113-2131.

91. Cui F-z, Li Y, Ge J. Self-assembly of mineralized collagen composites. *Mater. Sci.* 2007, **57**(1-6): 1-27.

92. Poole AR, Kojima T, Yasuda T, Mwale F, Kobayashi M, Laverty S. Composition and Structure of Articular Cartilage. *Clin. Orthop. Relat. Res.* 2001, **1**(391): 26-33.

93. Benninghoff A. *Form und Bau der Gelenkknorpel in Ihren Beziehungen zur Funktion*, vol. 1st. Anatomisches Institut zu Kiel: Kiel, 1925.

94. Schumacher BL, Su J-l, Lindley KM, Kuettner KE, Cole ADAA. Horizontally Oriented Clusters of Multiple Chondrons in the Superficial Zone of Ankle, but Not Knee Articular Cartilage. *Anat. Rec.* 2002, **248**(4): 241-248.

95. Temeno JS, Mikos AG. Review: tissue engineering for regeneration of articular cartilage. *Biomaterials* 2000, **21**(5): 431–440.

96. Sharma B, Williams CG, Kim TAEK, Sun D, Malik A, Khan M, *et al.* Designing Zonal Organization into Tissue-Engineered Cartilage. *Tissue Eng.* 2007, **13**(2): 405-414.

97. Klein TJ, Rizzi SC, Reichert JC, Georgi N, Malda J, Schuurman W, *et al.* Strategies for Zonal Cartilage Repair using Hydrogels. *Macromol. Biosci.* 2009, **9**(11): 1049-1058.

98. Hutmacher DW. Scaffolds in tissue engineering bone and cartilage. *Biomaterials* 2000, **21**(24): 2529-2543.

99. Kurkijärvi JE, Nissi MJ, Rieppo J, Töyräs J, Kiviranta I, Nieminen MT, *et al.* The zonal architecture of human articular cartilage described by T2 relaxation time in the presence of Gd-DTPA2−. *Magn. Reson. Imaging* 2008, **26**(5): 602-607.

100. Venn M, Maroudas A. Chemical composition and swelling of normal and osteoarthrotic femoral head cartilage. *Ann. Rheum. Dis.* 1977, **36**(2): 121-129.

101. Stockwell RA, Scott JE. Distribution of acid glycosaminoglycans in human articular cartilage. *Nature* 1967, **215**(1): 1376-1378.

102. Venn MF. Variation of chemical composition with human femoral head cartilage age. *Ann. Rheum. Dis.* 1978, **37**(2): 168-174.

103. Kempson GE, Freeman MAR, Swanson SAV. Tensile properties of articular cartilage. *Nature* 1968, **220**(1): 1127-1128.

104. Maik Schulz R, Bader A. Cartilage tissue engineering and bioreactor systems for the cultivation and stimulation of chondrocytes. *Eur. Biophys. J.* 2007, **36**(4): 539-568.

105. Panseri S, Russo A, Cunha C, Bondi A, Di A, Patella S, *et al.* Osteochondral tissue engineering approaches for articular cartilage and subchondral bone regeneration. *Knee Surg. Sports Traumatol. Arthrosc.* 2011, **20**(6): 1182-1191.

106. Vinatier C, Guicheux J, Daculsi G, Layrolle P, Weiss P. Cartilage and bone tissue engineering using hydrogels. *Bio-Med. Mater. Eng.* 2006, **16**(4): 107-113.

107. Frenkel SR, Di Desare PE. Scaffolds for Articular Cartilage Repair. *Ann. Biomed. Eng.* 2004, **32**(1): 26-34.

108. Chiang H, Jiang C-C. Repair of Articular Cartilage Defects. *J. Formosan Med. Assoc.* 2009, **108**(2): 87-101.

109. Mow VC, Holmes MH, Lai WM. Fluid transport and mechanical properties of articular cartilage: a review. *J. Biomech.* 1984, **17**(5): 377-394.

110. Ateshian GA, Warden WH, Kim JJ, Grelsamer RP, Mow VC. Finite deformation biphasic material properties of bovine articular cartilage from confined compression experiments. *J. Biomech.* 1997, **30**(11): 1157-1164.

111. Armstrong CG, Mow VC. Variations in the intrinsic mechanical properties of human articular cartilage with age, degeneration, and water content. *J. Bone Jt. Surg.* 1982, **64**(1): 88-94.

112. Schinagl RM, Gurskis D, Chen AC, Sah RL. Depth-Dependent Confined Compression Modulus of Full-Thickness Bovine Articular Cartilage. *J. Orth. Res.* 1997, **15**(4): 499-506.

113. Huang C-Y, Stankiewicz A, Ateshian GA, Mow VC. Anisotropy, inhomogeneity, and tension–compression nonlinearity of human glenohumeral cartilage in finite deformation. *J. Biomech.* 2005, **38**(4): 799-809.

114. Guterl CC, Hung CT, Ateshian GA. Electrostatic and non-electrostatic contributions of proteoglycans to the compressive equilibrium modulus of bovine articular cartilage. *J. Biomech.* 2010, **43**(7): 1343-1350.

115. Ghosh P, Taylor T. The knee joint meniscus. A fibrocartilage of some distinction. *Clin Orthop Relat Res.* 1987, **224**(11): 52-63.

116. Cheung HS. Distribution of type I, II, III and V in the pepsin solubilizized collagens in bovine menisci. *Connect. Tissue Res.* 1987, **16**(4): 343-356.

117. Makris EA, Hadidi P, Athanasiou KA. The knee meniscus: Structure function, pathophysiology, current repair techniques, and prospects for regeneration. *Biomaterials* 2011, **32**(30): 7411-7431.

118. Chevrier A, Nelea M, Hurtig MB, Hoemann CD, Buschmann MD. Meniscus Structure in Human, Sheep, and Rabbit for Animal Models of Meniscus Repair. *J. Orth. Res.* 2009, **27**(9): 1197-1203.

119. Kambic HE, McDevitt CA. Spatial organization of types I and II collagen in the canine meniscus. *J. Org. Chem.* 2005, **23**(1): 142-149.

120. Melrose J, Smith ÆS, Cake ÆM. Comparative spatial and temporal localisation of perlecan , aggrecan and type I , II and IV collagen in the ovine meniscus : an ageing study. *Histochem Cell Biol* 2005, **124**(3): 225-235.

121. Fox AJS, Bedi A, Rodeo SA. The Basic Science of Human Knee Menisci: Structure, Composition, and Function. *Sports Health* 2012, **4**(4): 340-351.

122. Petersen W, Tillmann B. Collagenous fibril texture of the human knee joint menisci. *Anat. Embryol.* 1998, **197**(4): 317-324.

123. Nakano T, Dodd CM, Scott PG. Glycosaminoglycans and Proteoglycans from Different Zones of the Porcine Knee Meniscus. *J. Orth. Res.* 1997, **15**(2): 213-220.

124. Verdonk PCMMD, Forsyth RG, Wang J, Almqvist KF, Verdonk R, Veys EM, *et al.* Characterisation of human knee meniscus cell phenotype. *Osteoarthr. Cartilage* 2005, **13**(7): 548-560.

125. Longo UG, Loppini M, Forriol F, Romeo G, Maffulli N, Denaro V. Advances in Meniscal Tissue Engineering. *Stem Cells Int.* 2012, **2012**(1): 1-11.

126. Katsuragawa Y, Saitoh K, Tanaka N, Wake M, Ikeda Y, Furukawa H, *et al.* Changes of human menisci in osteoarthritic knee joints. *Osteoarthr. Cartilage* 2010, **18**(9): 1133-1143.

127. Sun Y, Mauerhan DR, Kneisl JS, Norton HJ, Zinchenko N, Ingram J, *et al.* Histological Examination of Collagen and Proteoglycan Changes in Osteoarthritic Menisci. *Open Rheumatol. J.* 2012, **6**(1): 24-32.

128. Mikos AG, Herring SW, Ochareon P, Elisseeff J, Lu HH, Kandel R, *et al.* Engineering Complex Tissues. *Tissue Eng.* 2006, **12**(12): 3307-3339.

129. Orthoworld. The Orthopaedic Industry Annual report: 2009 - 2010; 2010.

130. Cypher TJ, Grossman JP. Biological Principles of Bone Graft Healing. *Foot Ankle Surg.* 1996, **35**(5): 413-417.

131. Chen FH, Rousche KT, Tuan RS. Technology Insight: adult stem cells in cartilage regeneration and tissue engineering. *Nat. Clin. Pract. Rheum.* 2006, **2**(3): 373-382.

132. Yang S, Leong K-F, Du Z, Chua C-K. Review: The Design of Scaffolds for Use in Tissue Engineering. Part I. Traditional Factors. *Tissue Eng.* 2001, **7**(6): 679-689.

133. Murphy WL, McDevitt TC, Engler AJ. Materials as stem cell regulators. *Nat. Mater.* 2014, **13**(756): 547-557.

134. Badylak SF, Freytes DO, Gilbert TW. Extracellular matrix as a biological scaffold material: Structure and function. *Acta Biomater.* 2009, **5**(1): 1-13.

135. Han WM, Heo S-J, Driscoll TP, Delucca JF, McLeod CM, Smith LJ, *et al.* Microstructural heterogeneity directs micromechanics and mechanobiology in native and engineered fibrocartilage. *Nat. Mater.* 2016, **15**(1): 1-11.

136. Augst AD, Kong HJ, Mooney DJ. Alginate Hydrogels as Biomaterials. *Macromol. Biosci.* 2006, **6**(8): 623-633.

137. Drury JL, Mooney DJ. Hydrogels for tissue engineering: scaffold design variables and applications. *Biomaterials* 2003, **24**(24): 4337-4351.

138. Bank RA. Implanted materials: Larger is stealthier. *Nat. Mater.* 2015, **14**(5): 558–559.

139. Bonino CA, Krebs MD, Saquing CD, In S, Shearer KL, Alsberg E, *et al.* Electrospinning alginate-based nanofibers: From blends to crosslinked low molecular weight alginate-only systems. *Carbohydr. Polym.* 2011, **85**(1): 111-119.

140. Bhattarai BN, Li Z, Edmondson D, Zhang M. Alginate-Based Nanofibrous Scaffolds: Structural, Mechanical, and Biological Properties. *Adv. Mater.* 2006, **18**(11): 1463-1467.

141. Nakamuraay K, Nishimuraa Y, Hatakeyamab T, Hatakeyamab H. Thermal properties of water insoluble alginate films containing di- and trivalent cations. *Thermochim. Acta* 1995, **267**(1): 343-353.

142. Kuo CK, Ma PX. Ionically crosslinked alginate hydrogels as scaffolds for tissue engineering: Part 1. Structure , gelation rate and mechanical properties. *Biomaterials* 2001, **22**(6): 511-521.

143. Gelinsky M, Eckert M, Despang F. Biphasic, but monolithic scaffolds for the therapy of osteochondral defects. *Int. J. Mat. Res.* 2007, **98**(8): 749-755.

144. Smidsrod O, Skjak-Braek G. Alginate as immobilization matrix for cells. *Trends Biotechnol.* 1990, **8**(3): 71-78.

145. Khairou KS, Al-Gethami WM, Hassan RM. Kinetics and mechanism of sol–gel transformation between sodium alginate polyelectrolyte and some heavy divalent metal ions with formation of capillary structure polymembranes ionotropic gels. *J. Membr. Sci.* 2002, **209**(6): 445–456.

146. Braccini I, Perez S. Molecular Basis of Ca2+-Induced Gelation in Alginates and Pectins : The Egg-Box Model Revisited. *Biomacromolecules* 2001, **2**(7): 1089-1096.

147. Thiele H. Geordnete Kristallisation. Nucleation und Mineralisation. *J. Biomed. Mater. Res.* 1967, **1**(1): 213-238.

148. Thiele H. *Histolyse und Histogenese*, vol. 1st. Akademische Verlagsgesellschaft Frankfurt am Main, 1967.

149. Stuckensen K, Ewald A, Groll J, Gbureck U. In situ formation of multilayer biocomposite with anisotropic crystal orientation. *Mater. Lett.* 2014, **120**(4): 111-114.

150. Treml H, Kohler H-H. Coupling of diffusion and reaction in the process of capillary formation in alginate gel. *Chem. Phys.* 2000 **252** (6): 199–208.

151. Thumbs J, Kohler H-H. Capillaries in alginate gel as an example of dissipative structure formation. *Chem. Phys.* 1996, **208**(11): 9-24.

152. Deville S, Saiz E, Tomsia AP. Freeze casting of hydroxyapatite scaffolds for bone tissue engineering. *Biomaterials* 2006, **27**(32): 5480-5489.

153. Gelinsky M, Welzel PB, Simon P, Bernhardt A. Porous three-dimensional scaffolds made of mineralised collagen: Preparation and properties of a biomimetic nanocomposite material for tissue engineering of bone. *Chem. Eng. J.* 2008, **137**(1): 84-96.

154. Ishaug-Riley SL, Crane-Kruger GM, Yaszemski MJ, Mikos AG. Three-dimensional culture of rat calvarial osteoblasts in porous biodegradable polymers. *Biomaterials* 1998, **19**(15): 1405–1412.

155. Niemeyer P, Krause U, Fellenberg J, Kasten P, Seckinger A, Ho AD, *et al.* Evaluation of Mineralized Collagen and α-Tricalcium Phosphate as Scaffolds for Tissue Engineering of Bone Using Human Mesenchymal Stem Cells. *Cells Tissues Organs* 2004, **177**(2): 68–78.

156. Mygind T, Stiehler M, Baatrua A, Li H, Zou X, Flyvbjerg A, *et al.* Mesenchymal stem cell ingrowth and differentiation on coralline hydroxyapatite scaffolds. *Biomaterials* 2007, **28**(6): 1036–1047.

157. Lie RH, Wozney JM. Delivering on the promise of bone morphogenetic proteins. *Trends Biotechnol.* 2001, **19**(7): 255-265.

158. Yasko AW, Lane JM, Fellinger EJ, Rosen V, Wozney JM, Wang EA. The healing of segmental bone defects, induced by recombinant human bone morphogenetic protein (rhBMP-2). A radiographic, histological, and biomechanical study in rats. *J. Bone Jt. Surg. (Am.)* 1992, **74**(5): 659-670.

159. Huebsch N, Lippens E, Lee K, Mehta M, Koshy ST, Darnell MC, *et al.* Matrix elasticity of void-forming hydrogels controls transplanted-stem-cell-mediated bone formation. *Nat. Mater.* 2015, **14**(9): 1269–1277.

160. Harley BA, Lynn AK, Wissner-Gross Z, Bonfield W, Yannas IV, Gibson LJ. Design of a multiphase osteochondral scaffold III: Fabrication of layered scaffolds with continuous interfaces. *J. Biomed. Mater. Res., Part A* 2010, **92**(3): 1078-1093.

161. Tampieri A, Sandri M, Landi E, Pressato D, Francioli S, Quarto R, *et al.* Design of graded biomimetic osteochondral composite scaffolds. *Biomaterials* 2008, **29**(26): 3539-3546.

162. Tampieri A, Pressato D, De Luca C, inventors; Patent EP1858562B1 - Cartilaginiform and osteochondral substitute comprising multilayer structure and use thereof. 2006.

163. Dhollander AAM, Liekens K, Almqvist KF, Verdonk R, Lambrecht S, Elewaut D, *et al.* A Pilot Study of the Use of an Osteochondral Scaffold Plug for Cartilage Repair in the Knee and How to Deal With Early Clinical Failures. *Arthroscopy* 2012, **28**(2): 225–233.

164. Frosch K-H, Balcarek P, Walde T, Wachowski M, Stürmer KM. Kann die Entnahmemorbidität bei der autologen Knorpel-Knochen-transplantation (OCT) durch die Implantation von TruFit-Zylindern reduziert werden? Der Unfallchirurg - Abstracts der 59. Jahrestagung 2010 der Norddeutschen Orthopädenvereinigung e.V.; 2010; Hamburg; 2010.

165. Gastel JA, Muirhead WR, Lifrak JT, Fadale PD, Hulstyn MJ, Labrador DP. Meniscal tissue regeneration using a collagenous biomaterial derived from porcine small intestine submucosa. *Arthroscopy* 2001, **17**(2): 151–159.

166. Tan Y, Zhang Y, Pei M. Meniscus Reconstruction Through Coculturing Meniscus Cells with Synovium-Derived Stem Cells on Small Intestine Submucosa - A Pilot Study to Engineer Meniscus Tissue Constructs. *Tissue Eng., Part A* 2010, **16**(1): 67-79.

167. Mueller SM, Shortkroff S, Schneider TO, Breinan HA, Yannas IV, Spector M. Meniscus cells seeded in type I and type II collagen - GAG matrices in vitro. *Biomaterials* 1999, **20**(8): 701-709.

168. Bahcecioglu G, Buyuksungur A, Kiziltay A, Hasirci N, Hasirci V. Construction and in vitro testing of a multilayered, tissue-engineered meniscus. *J. Bioact. Compatible Polym.* 2014, **29**(3): 235-253.

169. Kohn L, Lorenz S, Hinterwimmer S. Meniskusimplantate - Was hat sich bewährt. *Arthroskopie* 2011, **24**(1): 42-47.

170. Stone KR, Rodkey WG, Webber R, McKinney L, Steadman JR. Meniscal regeneration with copolymeric collagen scaffolds. *American Journal of Sports Medicine* 1992, **20**(2): 104-111.

171. Stone KR, inventor Patent WO8900413A1 - Prostetic Meniscus. 1989.

172. Klompmaker J, Jansen HWB, Veth RPH, Nielsen HKL, de Groot JH, Pennings AJ. Porous Implants for Knee Joint Meniscus Reconstruction: A Preliminary Study on the Role of Pore Sizes in Ingrowth and Differentiation of Fibrocartilage. *Clin. Mater.* 1993, **14**(1): 1-11.

173. Huey DJ, Hu JC, Athanasiou KA. Unlike Bone, Cartilage Regeneration Remains Elusive. *Science* 2012, **338**(6109): 917-921.

174. Hunziker EB. The Elusive Path to Cartilage Regeneration. *Adv. Mater.* 2009, **21**(32): 3419-3424.

175. Brien FJO, Harley BA, Yannas IV, Gibson LJ. The effect of pore size on cell adhesion in collagen-GAG scaffolds. *Biomaterials* 2005, **26**(4): 433-441.

176. Puetzer JL, Petitte JN, Loboa EG. Comparative Review of Growth Factors for Induction of Three-Dimensional In Vitro Chondrogenesis in Human Mesenchymal Stem Cells Isolated from Bone Marrow and Adipose Tissue. *Tissue Eng., Part B Rev.* 2010, **16**(4): 435-444.

177. Giezen TJ, Mantel-Teeuwisse AK, Straus SMJM, Schellekens H, Leufkens HGM, Egberts ACG. Safety-Related Regulatory Actions for Biologicals Approved in the United States and the European Union. *J. Am. Med. Assoc.* 2008, **300**(16): 1887-1896.

178. Chrastil J, Low J, Whang PG, Patel AA. Complications Associated With the Use of the Recombinant Human Bone Morphogenetic Proteins for Posterior Interbody Fusions of the Lumbar Spine. *Spine* 2013, **38**(16): E1020–E1027.

179. Somoza RA, Welter JF, Correa D, Caplan AI. Chondrogenic Differentiation of Mesenchymal Stem Cells: Challenges and Unfulfilled Expectations. *Tissue Eng., Part B* 2014, **20**(6): 596-608.

180. Cunniffe GM, Brien FJO. Collagen scaffolds for orthopedic regenerative medicine. *JOM* 2011, **63**(4): 66,73.

181. Levingstone TJ, Matsiko A, Dickson GR, Brien FJO, Gleeson JP. A biomimetic multi-layered collagen-based scaffold for osteochondral repair. *Acta Biomater.* 2014, **10**(5): 1996-2004.

182. Deville S, Saiz E, Nalla RK, Tomsia AP. Freezing as a Path to Build Complex Composites. *Science* 2006, **311**(5760): 515-518.

183. Bouville F, Maire E, Meille S, Moortèle BVD, Stevenson AJ, Deville S. Strong, tough and stiff bioinspired ceramics from brittle constituents. *Nat. Mater.* 2014, **13**(3): 1-7.

184. Weadock K, Olson RM, Silver FH. Evaluation of collagen crosslinking techniques. *Biomater. Artif. Cell* 1983, **11**(4): 293-318.

185. Yannas IV, Tobolsky AV. Cross-linking of gelatine by dehydration. *Nature* 1967, **215**(7): 509-510.

186. Haugh MG, Jaasma MJ, Brien FJO. The effect of dehydrothermal treatment on the mechanical and structural properties of collagen-GAG scaffolds. *J. Biomed. Mater. Res., Part A* 2008, **89**(2): 363–369.

187. Weadock KS, Miller EJ, Bellincampi LD, Zawadsky JP, Dunnl MG. Physical crosslinking of collagen fibers: Comparison of ultraviolet irradiation and dehydrothermal treatment. *Biomed. Mater.* 1995, **29**(11): 1373-1379.

188. Hennink WE, Nostrum CFV. Novel crosslinking methods to design hydrogels. *Adv. Drug Del. Rev.* 2012, **54**(Supplement): 223–236.

189. Schwetlick K, Noack R. Kinetics and catalysis of consecutive isocyanate reactions. Formation of carbamates, allophanates and isocyanurates. *J. Chem. Soc., Perkin Trans.* 1995, **2**(1): 395-402.

190. Damink LHHO, Dijkstra PJ, Van Luyn MJA, Wachem PBV, Nieuwenhuis P, Feijen J. Crosslinking of dermal sheep collagen using hexamethylene diisocyanate. *J. Mater. Sci. Mater. Med.* 1995, **6**(7): 429-434.

191. Damink LHHO, Dijkstra PJ, Luyn MJAV, Wachem PBV, Nieuwenhuis P, Feijen J. Cross-linking of dermal sheep collagen using a water-soluble carbodiimide. *Biomaterials* 1996, **17**(8): 765-773.

192. Lee JM, Edwards HHL, Pereira CA, Samii SI. Crosslinking of tissue-derived biomaterials in 1-ethyl-3-(3-dimethylaminopropyl)-carbodiimide (EDC). *J. Mater. Sci. Mater. Med.* 1996, **7**(9): 531-541.

193. Gilles MA, Hudson AQ, Borders CLJ. Stability of water-soluble carbodiimides in aqueous solution. *Anal. Biochem.* 2004, **184**(2): 244-248.

194. Pieper JS, Hafmans T, Veerkamp JH, Kuppevelt THV. Development of tailor-made collagen-glycosaminoglycan matrices: EDC/NHS crosslinking, and ultrastructural aspects. *Biomaterials* 2000, **21**(6): 581-593.

195. Grossenbacher KA, McDuffie SM. Conductive cooling of lava: columnar joint diameter and stria width as functions of cooling rate and thermal gradient. *J. Volcanol. Geotherm. Res.* 1995, **69**(1-2): 95-103.

196. Budkewitsch P, Robin P-Y. Modelling the evolution of columnar joints. *J. Volcanol. Geotherm. Res.* 1994, **59**(3): 219-239.

197. Wanqi J. Progress of Solidification Researches and the Applications in Materials Processing *J. Mater. Sci. Technol.* 2001, **17**(5): 575-576.

198. Boswell JH, inventor Patent EP1452251B1 - Mould for component casting using a directional solidification process. 2004.

199. Deus P, Koi H, Sauermann H, Metzing P, inventors; Patent DD272669A1 - Anordnung zur Erzeugung von Temperaturfeldern für die Durchführung der gerichteten Kristallisation von Schmelzen. 1988.

200. Bauer M, Winkel K, Toebbens DM, Mayer E, Loerting T. Hexagonal ice transforms at high pressures and compression rates directly into “doubly metastable” ice phases. *J. Chem. Phys.* 2009, **131**(224514): 1-8.

201. Nada H, Furukawa Y. Anisotropy in growth kinetics at interfaces between proton-disordered hexagonal ice and water: A molecular dynamics study using the six-site model of H2O. *J. Cryst. Growth* 2005, **283**(1-2): 242-256.

202. Watkins M, Pan D, Wang EG, Michaelides A, Vandevondele J, Slater B. Large variation of vacancy formation energies in the surface of crystalline ice. *Nat. Mater.* 2011, **10**(8): 1-5.

203. Matsumoto M, Saito S, Ohmine I. Molecular dynamics simulation of the ice nucleation and growth process leading to water freezing. *Nature* 2002, **416**(3): 409-413.

204. Asthana R, Tewari SN. The engulfment of foreign particles by a freezing interface. *J. Mater. Sci.* 1993, **28**(20): 5414-5425.

205. Blackford JR. Sintering and microstructure of ice: a review. *J. Phys. D Appl. Phys.* 2007, **40**(21): 335-385.

206. Chen AS-h, Morris SW. On the origin and evolution of icicle ripples. *New J. Phys.* 2013, **15**(103012): 1-18.

207. Güémez J, Fiolhais C, Fiolhais M. Reproducing Black' s experiments: freezing point depression and supercooling of water. *Eur. J. Phys.* 2002, **23**(12): 83-91.

208. Glicksman ME. *Principles of Solidification*, 1st edn. Springer Verlag: New York, 2011.

209. Oxford H, Angell CA. Supercooled Water - Two phases? *Nat. Mater.* 2014, **13**(7): 673-675.

210. Rein P, Ruiz-montero MJ. Numerical calculation of the rate of crystal nucleation in a Lennard-Jones system at moderate undercooling. 1996, **104**(24): 9932-9947.

211. Mishima O, Stanley HE. The relationship between liquid, supercooled and glassy water. *Nature* 1998, **396**(11): 329-335.

212. Lambert FL. Entropy Is Simple, Qualitatively. *Journal of Chemical Education* 2002, **79**(10): 1241-1246.

213. Rutter JW, Chalmers B. A prismatic substructure formed during solidification of metals. *Canadian Journal of Physics* 1953, **31**(1): 15-39.

214. Kurz W, Fischer DJ. *Fundamentals of Solidification*, 3rd edn. Trans Tech Publications: Switzerland, 1992.

215. Mullins WW, Sekerka RF. Morphological Stability of a Particle Growing by Diffusion or Heat Flow. *Journal of Applied Physics* 1963, **34**(2): 323-329.

216. Mullins WW, Sekerka RF. Stability of a Planar Interface During Solidification of a Dilute Binary Alloy. *Journal of Applied Physics* 1964, **35**(2): 444-451.

217. Sekerka RF. Morphological stability. *J. Cryst. Growth* 1968, **3**(4): 71-81.

218. Mangers H, Blank E. Gerichtete Erstarrung. Verfahren zur Herstellung anisotroper Werkstoffe mit hoher Gefügeperfektion. *Materialwiss. Werkst.* 1980, **57**(1): 367-373.

219. Peppin SSL, Worster MG, Wettlaufer JS, A PRS. Morphological instability in freezing colloidal suspensions. *Proc. R. Soc. A* 2007, **463**(2079): 723-733.

220. Hunt JD. Steady State Columnar and Equiaxed Growth of Dendrites and Eutectic. *Mater. Sci. Eng.* 1984, **65**(1): 75-83.

221. Coriell SR, McFadden GB, Sekerka RF. Cellular growth during directional solidification. *Annu. Rev. Mater. Sci.* 1985, **15**(1): 119-145.

222. Heyer H. Neuere Untersuchungen zur Kinetik des Kristallwachstums. *Angew. Chem.* 1966, **78**(2): 130-141.

223. Ishiguro H, Rubinsky B. Mechanical Interactions between Ice Crystals and Red Blood Cells during Directional Solidification. *Cryobiology* 1994, **31**(5): 483-500.

224. Hunt JD. Pattern formation in solidification. *Sci. Technol. Adv. Mater.* 2001, **2**(6): 147-155.

225. Gránásy L, Pusztai T, Börzsönyi T, Warren JA, Douglas JF. A general mechanism of polycrystalline growth. *Nat. Mater.* 2004, 3(1): 645-650.

226. Viskanta R, Bianchi MVA, Critser JK, Gao D. Solidification Processes of Solutions. *Cryobiology* 1997, **34**(4): 348-362.

227. Hu XW, Li SM, Chen WJ, Gao SF, Liu L, Fu HZ. Primary dendrite arm spacing during unidirectional solidification of Pb – Bi peritectic alloys. *J. Alloys Compd.* 2009, **484**(1-2): 631-636.

228. Fan J, Li X, Su Y, Guo J, Fu H. Dependency of microhardness on solidification processing parameters and microstructure characteristics in the directionally solidified Ti–46Al–0.5W–0.5Si alloy. *J. Alloys Compd.* 2010, **504**(1): 60-64.

229. Eshraghi M, Felicelli SD, Jelinek B. Three dimensional simulation of solutal dendrite growth using lattice Boltzmann and cellular automaton methods. *J. Cryst. Growth* 2012, **354**(1): 129-134.

230. Wang Z, Li J, Wang J, Zhou Y. Phase field modeling the selection mechanism of primary dendritic spacing in directional solidification. *Acta Mater.* 2012, **60**(5): 1957-1964.

231. Stolze C, Janoschka T, Schubert US, Müller FA, Flauder S. Directional Solidification with Constant Ice Front Velocity in the Ice-Templating Process. *Adv. Eng. Mater.* 2016, **18**(1): 111-120.

232. Angell CA, Oguni M, Sichina WJ. Heat capacity of water at extremes of supercooling and superheating. *J. Phys. Chem.* 1982, **88**(6): 998-1002.

233. Moore EB, Molinero V. Structural transformation in supercooled water controls the crystallization rate of ice. *Nature* 2011, **479**(7374): 506-508.

234. Bertolini D, Cassettari M, Salvetti G. Anomalies in the latent heat of solidification of supercooled water. *Chem. Phys. Lett.* 1985, **119**(6): 553-555.

235. EngineeringToolBox. Thermal and thermodynamic properties of ice - density, thermal conductivity and specific heat at temperatures from 0 to -100 °C. http://www.engineeringtoolbox.com/ice-thermal-properties-d_576.html; 2016.

236. Rabin Y. The effect of temperature-dependent thermal conductivity in heat transfer simulations of frozen biomaterials. *CryoLetters* 2000, **21**(1): 163-170.

237. Fricke J, Borst WL. *Energie: Ein Lehrbuch der physikalischen Grundlagen*, 2nd edn. R. Oldenburg Verlag: München, 1984.

238. Deville S, Saiz E, Tomsia AP. Ice-templated porous alumina structures. *Acta Mater.* 2007, **55**: 1965-1974.

239. Megerlin F. Geometrisch eindimensionale Wärmeleitung beim Schmelzen und Erstarren. *Forsch. Ing-Wes.* 1968, **34**(2): 40-46.

240. Russo J, Romano F, Tanaka H. New metastable form of ice and its role in the homogeneous crystallization of water. *Nat. Mater.* 2014, **13**(5): 4-6.

241. Munch E, Franco J, Deville S, Hunger P, Saiz E, Tomsia AP. Porous Ceramic Scaffolds with Complex Architectures. *JOM* 2008, **60**(6): 54-58.

242. Deville S. Freeze-Casting of Porous Biomaterials: Structure, Properties and Opportunities. *Materials* 2010, **3**(3): 1913-1927.

243. Deville S. Freeze-Casting of Porous Ceramics : A Review of Current Achievements and Issues. *Adv. Eng. Mater.* 2008, **10**(3): 155-169.

244. Deville S, Maire E, Bernard-granger G, Lasalle A, Bogner A, Gauthier C, *et al.* Metastable and unstable cellular solidification of colloidal suspensions. *Nat. Mater.* 2009, **8**(12): 966-972.

245. Deville S, Saiz E, Nalla RK, Tomsia AP. Strong Biomimetic Hydroxyapatite Scaffolds. *Adv. Sci. Technol.* 2006, **49**(10): 148-152.

246. Munch E, Saiz E, Tomsia AP, Deville S. Architectural Control of Freeze-Cast Ceramics Through Additives and Templating. *J. Am. Ceram. Soc.* 2009, **92**(7): 1534-1539.

247. Flauder S, Heinze T, Müller FA. Cellulose scaffolds with an aligned and open porosity fabricated via ice-templating. *Cellulose* 2014, **21**(1): 97-103.

248. Flauder S, Gbureck U, Müller FA. ß-TCP Scaffolds with an Interconnected and Aligned Porosity Fabricated via Ice-Templating. *Key Eng. Mater.* 2013, **529-530**(Chapter II): 129-132.

249. Flauder S, Gbureck U, Müller FA. Structure and mechanical properties of β-TCP scaffolds prepared by ice-templating with preset ice front velocities. *Acta Biomater.* 2014, **10**(12): 5148-5155.

250. Flauder S, Sajzew R, Müller FA. Mechanical Properties of Porous β-Tricalcium Phosphate Composites Prepared by Ice-Templating and Poly(ε-caprolactone) Impregnation. *ACS Appl. Mater. Interfaces* 2015, **7**(1): 845-851.

251. Podorozhko EA, Kurskaya EA, Kulakova VK, Lozinsky VI. Cryotropic structuring of aqueous dispersions of fibrous collagen: influence of the initial pH values. *Food Hydrocolloids* 2000, **14**(2): 111-120.

252. Schoof H. Verfahren zur Herstellung gefriergetrockneter Kollagenschwämme mit definierter Porenstruktur. 2000.

253. Heschel I, Rau G, inventors; Patent DE19751031A1 - Verfahren zur Herstellung poröser Strukturen. 1999.

254. Heimburg DV, Zachariah S, Heschel I, Ku H, Schoof H, Hafemann B, *et al.* Human preadipocytes seeded on freeze-dried collagen scaffolds investigated in vitro and in vivo. *Biomaterials* 2001, **22**(5): 429-438.

255. Kroehne V, Heschel I, Schügner F, Lasrich D, Bartsch JW, Jockusch H. Use of a novel collagen matrix with oriented pore structure for muscle cell differentiation in cell culture and in grafts. *J. Cell. Mol. Med.* 2008, **12**(5a): 1640-1648.

256. Bozkurt A, Deumens R, Beckmann C, Damink LO, Schügner F, Heschel I, *et al.* In vitro cell alignment obtained with a Schwann cell enriched microstructured nerve guide with longitudinal guidance channels. *Biomaterials* 2009, **30**(2): 169–179.

257. Bozkurt A, Brook GA, Moellers S, Lassner F, Sellhaus B, Weis J, *et al.* In Vitro Assessment of Axonal Growth Using Dorsal Root Ganglia Explants in a Novel Three-Dimensional Collagen Matrix. *Tissue Eng.* 2007, **13**(12): 2971-2979.

258. Pot MW, Faraj KA, Adawy A, van Enckevort WJP, van Moerkerk HTB, Vlieg E, *et al.* Versatile Wedge-Based System for the Construction of Unidirectional Collagen Scaffolds by Directional Freezing Practical and Theoretical Considerations. *ACS Appl. Mater. Interfaces* 2015, **7**(16): 8495–8505.

259. Moseke C. Biomineralisation von Knochengewebe unter dem Einfluss von Metallionen. Münster, 2003.

260. Fratzl P. Position-Resolved Small-Angle X-ray Scattering of Complex Biological Materials. *J. Appl. Crystallogr.* 1997, **30**(1): 765-769.

261. Hollander AP, Pidoux I, Reiner A, Rorabeck C, Boume R, Poole AR, *et al.* Damage to Type II Collagen in Aging and Osteoarthritis Starts at the Articular Surface, Originates Around Chondrocytes, and Extends into the Cartilage with Progressive Degeneration. *J. Clin. Invest.* 1995, **96**(6): 2859-2869.

262. Damink LO, Bunde NL, Heschel I, inventors; Patent DE10157182A1 - Verfahren zur Behandlung von Materialien biologischen Ursprungs und Elastin Produkt. 2003.

263. Jcpds. International Center for Diffraction Data, Powder Diffractionfile. 1990.

264. Stuckensen K, Gbureck U, Groll J, inventors; Patent US2014350331A1 - Production of materials having an anisotropic structure. 2014.

265. Grote KH, Feldhusen J. *Dubbel - Taschenbuch für den Maschinenbau*, 22th edn. Springer: Berlin, 2007.

266. Tomsia AP, Saiz E. Nature-inspired bone regeneration scaffolds by ice-templating. *World Biomaterial Congress 2012 - Meeting Abstracts* 2012: 94720-94720.

267. Haugh MG, Murphy CM, McKiernan RC, Altenbuchner C, Brien FJO. Crosslinking and Mechanical Properties Significantly Influence Cell Attachment, Proliferation, and Migration Within Collagen Glycosaminoglycan Scaffolds. *Tissue Eng., Part A* 2011, **17**(9): 1201-1208.

268. Shepherd JH, Ghose S, Kew SJ, Moavenian A, Best SM, Cameron RE. Effect of fiber crosslinking on collagen-fiber reinforced collagen-chondroitin-6-sulfate materials for regenerating load-bearing soft tissues. *J. Biomed. Mater. Res., Part A* 2013, **101A**(1): 176-184.

269. Hanthamrongwit M, Reid WH, Grant MH. Chondroitin-6-sulphate incorporated into collagen gels for the growth of human keratinocytes the effect of cross-linking agents and diamines. *Biomaterials* 1999, **17**(2): 775-780.

270. Camacho NP, West P, Torzilli PA, Mendelsohn R. FTIR Microscopic Imaging of Collagen and Proteoglycan in Bovine Cartilage. *Biopolymers* 2001, **62**(1): 1-8.

271. Muyonga JH, Cole CGB, Duodu KG. Fourier transform infrared (FTIR) spectroscopic study of acid soluble collagen and gelatin from skins and bones of young and adult Nile perch (Lates niloticus). *Food Chem.* 2004, **86**(8): 325-332.

272. Sachlos E, Reis N, Ainsley C, Derby B, Czernuszka JT. Novel collagen scaffolds with predefined internal morphology made by solid freeform fabrication. *Biomaterials* 2003, **24**(8): 1487-1497.

273. Sheikh Z, Javaid MA, Hamdan N, Hashmi R. Bone Regeneration Using Bone Morphogenetic Proteins and Various Biomaterial Carriers. *Materials* 2015, **8**(4): 1778-1816.

274. Lee SS, Huang BJ, Kaltz SR, Sur S, Newcomb CJ, Stock SR*, et al.* Bone regeneration with low dose BMP-2 amplified by biomimetic supramolecular nano fibers within collagen scaffolds. *Biomaterials* 2013, **34**(2): 452-459.

275. Bessa PC, Casal M, Reis RL. Bone morphogenetic proteins in tissue engineering: the road from laboratory to clinic, part II (BMP delivery). *J. Tissue Eng. Regen. Med.* 2008, **2**(1): 81-96.

276. Gautschi OP, Frey SP, Zellweger R. Bone morphogenetic proteins in clinical applications. *Aust. N. Z. J. Surg.* 2007, **77**(8): 626-631.

277. Gelman RA, Blackwell J. Interaction between collagen and chondroitin-6-sulfate. *Connect. Tissue Res.* 1973, **2**(1): 31-35.

278. Ruhe PQ, Boerman OC, Russel FGM, Spauwen PHM. Controlled release of rhBMP-2 loaded poly (DL-lactic-co-glycolic acid)/calcium phosphate cement composites in vivo. *J. Controlled Release* 2005, **106**(1-2): 162-171.

279. Stuckensen K, Gbureck U, Groll J, inventors; Patent WO2013/083844A2 - Production of materials having an anisotropic structure. 2013.

280. Sanchez-adams J, Willard VP, Athanasiou KA. Regional variation in the mechanical role of knee meniscus glycosaminoglycans. *J. Appl. Physiol.* 2011, **111**(6): 1590-1596.

281. Herwig J, Egner E, Buddecke E. Chemical changes of human knee joint menisci in various stages of degeneration. *Ann. Rheum. Dis.* 1984, **63**(1): 635-640.

282. Articular Cartilage. http://www.vetmed.vt.edu/education/Curriculum/VM8054/Labs/Lab7/CASES/OCD/ARTICULAR%20CARTILAGE%20A.jpg; 2015

283. Eyckmans J, Chen CS. Stem cell differentiation - Sticky mechanical memory. *Nat. Mater.* 2014, **13**(6): 542-543.

284. Soltz MA, Ateshian GA. Interstitial Fluid Pressurization During Confined Compression Cyclical Loading of Articular Cartilage. *Biomed. Eng.* 2000, **28**(2): 150-159.

285. Al-Munajjed AA, Plunkett NA, Gleeson JP, Weber T, Jungreuthmayer C, Levingstone T, *et al.* Development of a Biomimetic Collagen-Hydroxyapatite Scaffold for Bone Tissue Engineering Using a SBF Immersion Technique. *J. Biomed. Mater. Res.* 2009, **90**(2): 584-591.

286. Gu W, DiDonato D, Reuben P, Howell D, Cheung H. Dynamic mechanical loading increases metalloproteinase levels in articular cartilage. *46th Annual Meeting of the Orthopaedic Research Society* 2000: 650-650.

287. Reilly D, Burstein A, Frankel V. The elastic modulus for bone. *J. Biomech.* 1974, **7**(7): 271-275.

288. Keaveny T, Borchers R, Gibson L. Trabecular bone modulus and strength can depend on specimen geometry. *J. Biomech.* 1993, **26**(8): 991-1000.

289. Keaveny T, Guo X, Wachtel E, McMahon T, Hayes W. Trabecular bone exhibits fully linear elastic behavior and yields at low strains. *J. Biomech.* 1994, **27**(9): 1127-1136.

290. Yeni YN, Christopherson GT, Turner AS, Les CM, Fyhrie DP. Apparent viscoelastic anisotropy as measured from nondestructive oscillatory tests can reflect the presence of a flaw in cortical bone. *J. Biomed. Mater. Res., Part A* 2004, **69**(1): 124-130.

291. Shepherd TN, Zhang J, Ovaert TC, Roeder RK, Niebur GL. Direct comparison of nanoindentation and macroscopic measurements of bone viscoelasticity. *J. Mech. Behav. Biomed. Mater.* 2012, **4**(8): 2055-2062.

292. Visser R, Arrabal PM, Becerra J, Rinas U, Cifuentes M. The effect of an rhBMP-2 absorbable collagen sponge-targeted system on bone formation in vivo. *Biomaterials* 2009, **30**(11): 2032-2037.

293. Urist MR. Bone: Formation by Autoinduction. *Science* 1965, **150**(3698): 893-899

294. Nguyen PD, Lin CD, Allori AC, Schachar JS, Ricci JL, Saadeh PB, *et al.* Scaffold-Based rhBMP-2 Therapy in a Rat Alveolar Defect Model: Implications for Human Gingivoperiosteoplasty. *Plast. Reconstr. Surg.* 2009, **124**(6): 1829-1839.

295. Daniels AU, Scotti C, Wirz D, Wolf F, Schaefer DJ, Bu V, *et al.* Biomaterials Engineering human cell-based, functionally integrated osteochondral grafts by biological bonding of engineered cartilage tissues to bony scaffolds. *Biomaterials* 2010, **31**: 2252-2259.

296. Stuckensen K, Gbureck U, Groll J, inventors; Priority Patent Application DE 102011120488 - Herstellung anisotrop strukturierter Werkstoffe. Germany. 2011 08.12.2011.

297. Nerurkar NL, Elliott DM, Mauck RL. Mechanical design criteria for intervertebral disc tissue engineering. *J. Biomech.* 2010, **43**(6): 1017-1030.

298. McMurray RJ, Gadegaard N, Tsimbouri PM, Burgess KV, McNamara LE, Tare R, *et al.* Nanoscale surfaces for the long-term maintenance of mesenchymal stem cell phenotype and multipotency. *Nat. Mater.* 2011, **10**(8): 637-644.

299. Dalby MJ, Gadegaard N, Oreffo ROC. Harnessing nanotopography and integrin–matrix interactions to influence stem cell fate. *Nat. Mater.* 2014, **13**(6): 558-569.

300. Watt FM, Huck WTS. Role of the extracellular matrix in regulating stem cell fate. *Nat. Rev. Mol. Cell Biol.* 2013, **14**(8): 467-473.

301. Brévignon-Dodin L, Singh P. ATMP in practice Towards a new industry landscape in tissue engineering. *J. Commerc. Biotechnol.* 2009, **15**(1): 59–65.

302. Spicer PP, Kretlow JD, Young S, Jansen JA, Kasper K, Mikos AG. Evaluation of bone regeneration using the rat critical size calvarial defect. *Nat. Protoc.* 2012, **7**(9): 1918-1929.

303. Freed LE, Vunjak-Novakovic G, Biron RJ, Eagles DB, Lesnoy DC, Barlow SK, *et al.* Biodegradable Polymer Scaffolds for Tissue Engineering. *Nat. Biotechnol.* 1994, **12**(1): 689 - 693.

304. Kumar S. Stiffness does matter. *Nat. Mater.* 2014, **13**(10): 918-920.

305. Engler AJ, Sen S, Sweeney HL, Discher DE. Matrix Elasticity Directs Stem Cell Lineage Specification. *Cell* 2006, **126**(4): 677-689.

306. Wen JH, Vincent LG, Fuhrmann A, Choi YS, Hribar KC, Taylor-weiner H, *et al.* Interplay of matrix stiffness and protein tethering in stem cell differentiation. *Nat. Mater.* 2014, **13**(1): 979-987.

307. Chaudhuri O, Koshy ST, Branco C, Shin J-W, Verbeke CS, Allison KH, *et al.* Extracellular matrix stiffness and composition jointly regulate the induction of malignant phenotypes in mammary epithelium. *Nat. Mater.* 2014, **13**(1): 970-978.

308. Murphy CM, Haugh MG, Brien FJO. The effect of mean pore size on cell attachment, proliferation and migration in collagen–glycosaminoglycan scaffolds for bone tissue engineering. *Biomaterials* 2010, **31**(3): 461-466.

10 Appendix

Apertures and filters	
Aperture	2 mm
Scatter aperture	2 mm
Ni-Filter	Elimination of k_β radiation
Detector aperture	0.2 mm
X-Ray wavelengths	
$k_{\alpha 1}$	1.541 Å
$k_{\alpha 2}$	1.544 Å
k_β	1.392 Å

Table 1: Apertures, filters and X-Ray wavelengths of XRD measurements.

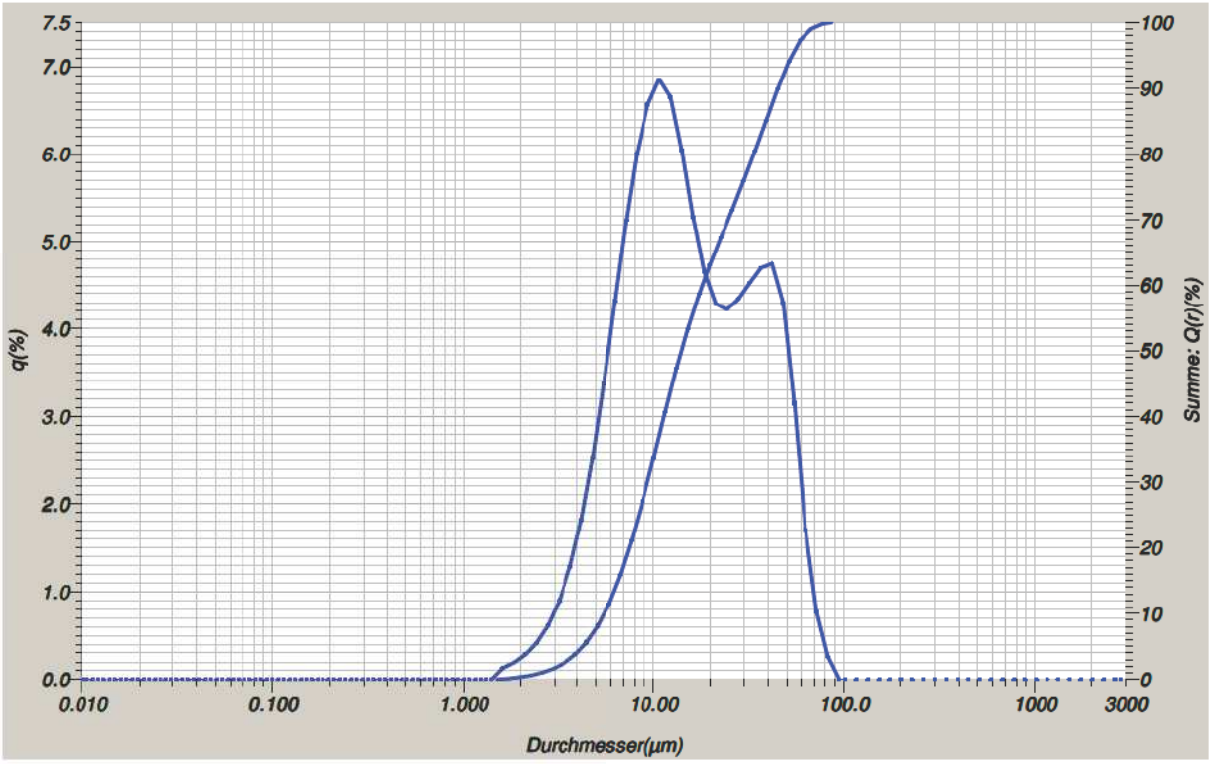

Figure 9.1: Particle size distribution of collagen II after cryogenic fracturing. The measurement was performed by Retsch (Haan, Germany) using a laser scattering particle size distribution analyser LA-950 in volume distribution resulting in a bimodal particle size distribution. (D10 value ca. 5 µm, D50 value ca. 14 µm, D90 value ca. 45 µm)